

Multifunctional Ligand Design for Modulating Protein Stability and Aggregation for Cancer Treatment

by

Jessica Jennifer Miller

B.Sc. (Hons.), Mount Allison University, 2014

Thesis Submitted in Partial Fulfillment of the
Requirements for the Degree of
Doctor of Philosophy

in the
Department of Chemistry
Faculty of Science

© Jessica Miller 2020
SIMON FRASER UNIVERSITY
Spring 2020

Copyright in this work rests with the author. Please ensure that any reproduction or re-use is done in accordance with the relevant national copyright legislation.

Approval

Name: Jessica Jennifer Miller

Degree: Doctor of Philosophy (Chemistry)

Title: Multifunctional Ligand Design for Modulating Protein Stability and Aggregation for Cancer Treatment

Examining Committee:

Chair: Robert A. Britton
Professor

Tim Storr
Senior Supervisor
Associate Professor

David J. Vocadlo
Co-Supervisor
Professor

Charles J. Walsby
Supervisor
Associate Professor

Erika Plettner
Supervisor
Professor

Roger Linington
Internal Examiner
Associate Professor

Justin Wilson
External Examiner
Assistant Professor
Department of Chemistry and Chemical Biology
Cornell University

Date Defended/Approved: March 30th, 2020

Abstract

Referred to as the “guardian of the genome”, p53 is the most frequently mutated protein in cancer and accounts for over 50% of cancer diagnoses. p53 regulates the cellular network by signaling for the activation of various pathways including apoptosis and cell cycle arrest to avoid propagation of damaged cells. Consequently, in 50% of cancer diagnoses, single point mutations render the protein inactive, prohibiting its antiproliferative response and allowing for accumulation of damaged cells. The majority of mutations are localized to the DNA-binding domain, a domain that contains a Zn²⁺ ion that is essential for proper protein folding and function. These mutations typically affect the proteins’ tertiary structure, resulting in a loss or alteration of Zn-binding which can lead to unfolding and enhanced aggregation. As an overexpressed and tumour-specific target, the past two decades have seen considerable dedication to the development of small molecules that aim to restore wild-type function in mutant p53. Previous efforts have been monofunctional in design, targeting specific characteristics of a given p53 mutant including thermal denaturation, aggregation, or loss of zinc.

This thesis explores small molecule design strategies to restore wild-type function in mutant p53. Considering the multifaceted nature of p53 mutants, a multifunctional approach was employed to simultaneously target various characteristics. Chapter 2 features a bifunctional scaffold targeting zinc loss and thermal denaturation. The utility of this scaffold in increasing intracellular zinc and restoring transcriptional function in mutant p53-Y220C is described. Modifications to the ligand scaffold to extend the structures into subsite cavities of this mutant are explored in Chapter 3. These modifications increased the cytotoxicity of the ligands and restored apoptotic activity, however, resulted in a loss in their ability to serve as zinc metallochaperones. Lastly, a combination of fragments targeting zinc loss and protein aggregation found success in restoring wild-type function in mutant p53 in Chapter 4. These studies highlighted the possible advantages of halogenation in modulating mutant p53 aggregation, as an iodinated scaffold limited mutant p53 aggregation and restored wild-type function. This work represents a foundation to simultaneously target the multiple characteristics of p53 mutants and provides important information for drug design moving forward.

Keywords: p53; cancer; multifunctional ligands; Zn metallochaperones; protein aggregation; apoptosis

To Melissa – you will always be my inspiration. RIP sweet angel.

Acknowledgements

First and foremost, I need to thank my parents, Karen and Gary. From the very beginning, you have emphasized the importance of education and consistently provided me with both unwavering support and the tools necessary to succeed. You instilled in me from a young age that no goal was unattainable and have taught me the value of hard work. For that, I am eternally grateful, and I hope that I have made you proud. To my sister Lee-Ann, thank you for sticking it out through my teenage years and still remaining one of my best friends – I can't begin to explain how much it has meant to me to have a sister like you. To my nieces Harper and Lucy, I can't wait to watch you grow up – may you always chase your dreams and know that you are loved beyond measure.

To my senior supervisor Tim Storr, you have set the bar for what a professional, yet caring supervisor should exemplify. You have afforded me numerous opportunities throughout my graduate degree including conferences, collaborations, and a research trip to France, which have all positively contributed to my growth as a scientist. Your mentorship has had a lasting impact on me and will be truly missed. To my co-supervisor David Vocadlo, thank you for welcoming me into your group and introducing me to the field of chemical biology – I felt at home within your group and can't thank you enough for your words of encouragement over the years.

A significant portion of the work presented in this thesis would not have been possible had I not met Dr. Gaiddon at Pacifichem in 2015. Thank you for expressing interest in my research project, and for establishing a continuing collaboration with our group. The three months I spent in your lab in 2018 sparked my interests in cellular imaging and has had a major influence on my research interests moving forward. To Anaïs B. and Christophe, thank you for your patience when teaching me everything I needed to know about cellular biology and for your continuing research efforts on the collaborative work contained in this thesis. Finally, to Gilles and Anaïs C., thank you for making me feel at home in France by singing Shania Twain in the lab everyday.

To my committee members Prof. Charles Walsby and Prof. Plettner, thank you for taking the time to serve on my committee and for your helpful suggestions and advice over the years. To Prof. Plettner, I extend a special thanks for your support of women in science – the department greatly benefits from your efforts. To Prof. Warren, thank you for taking

the time to share with me your knowledge and experience in protein expression – this is a valuable skill that I will carry with me throughout the rest of my career as a scientist.

My graduate degree would not have been the same if it weren't for the friendships I established within my group and within the department at SFU. To Khrystyna, I thank you for your treasured friendship and for everything you do for the group. I hope that we will stay friends long into the future – you are truly the measure of what it means to give without expectation, and I am lucky to have you in my life. To Janaina and Luiza, thank you for your friendship and the many scientific discussions we've had – protein aggregation seems more interesting when discussed among friends. To Diego, grad school wouldn't have been nearly as entertaining if you hadn't joined our group – thank you for all the fun we've had, and I look forward to our continued friendship. Curtis, thank you for the coffee dates, lunch dates, and nights spent eating junk food and playing Spyro. I'm realizing that our friendship largely revolves around food, but I wouldn't have it any other way. Finally, Rhea – I am so glad you asked if I wanted help carrying my books in first year when I was on crutches. That was the beginning of a lifelong friendship that I wouldn't change for anything. Even though you continuously drag me to climb mountains that I have no business climbing, I promise to keep struggling behind you for many years to come.

To my friends outside of SFU, thank you for being my outlet and keeping me sane. To Jess, Eric, and Tom – the nights spent over beers and boardgames will remain some of my most treasured memories in grad school. To Rebecca, you have been by my side since we were just six-year-old kids, and since then have grown up at each other's side. We've experienced the best and worst of times together, and your continued support and friendship has been an invaluable influence in my life.

Finally, Ryan Clarke. It's not easy to put into words the impact it has when someone comes into your life and changes it forever. You've been a constant source of inspiration in my life, and I am forever in awe of your passion and drive to succeed. Grad school has been a roller coaster full of ups and downs, but it has all been worth it because of you. Thank you for being my biggest support system and my best friend, and I can't wait to start this new chapter with you.

Table of Contents

Approval.....	ii
Abstract.....	iii
Dedication.....	iv
Acknowledgements.....	v
Table of Contents.....	vii
List of Tables.....	xi
List of Figures.....	xii
List of Acronyms.....	xxi
Chapter 1. Introduction.....	1
1.1. Cancer.....	1
1.2. Anti-Cancer Therapy.....	2
1.2.1. General Cytotoxic Agents.....	2
1.2.2. Targeted Chemotherapeutics.....	4
1.3. p53 Structural biology.....	5
1.3.1. Discovery.....	5
1.3.2. The p53 Family.....	6
1.3.3. Structural Organization.....	7
1.3.4. Regulatory Mechanism.....	10
1.3.5. Activation and Biological Response.....	10
1.4. Mutant p53 and Cancer.....	14
1.4.1. Contact and Structural Mutations.....	15
1.4.2. Mutant p53 and Aggregation.....	17
1.5. Therapeutic Intervention of p53 Malfunction.....	18
1.5.1. Inhibition of the p53-MDM2 Interaction.....	18
1.5.2. Restoration of Wild-type p53 Function.....	21
Protein Refolding via Cysteine Modification.....	21
Thermal Stabilization of Mutant p53.....	22
Modulating Mutant p53 Aggregation.....	24
Restoring Zinc-Binding in Mutant p53.....	25
1.6. Thesis Synopsis.....	30
Chapter 2. Multifunctional Compounds for the Activation of Mutant p53 in Cancer.....	34
2.1. Introduction.....	34
2.2. Results and Discussion.....	37
2.2.1. Ligand Design and Synthesis.....	37
2.2.2. Molecular Docking.....	39
2.2.3. Zinc Binding Affinities for L1-L5.....	42
2.2.4. Increasing Intracellular Zn ²⁺ in Cancer Cells.....	47
2.2.5. <i>In Vitro</i> Cytotoxicity.....	49
2.2.6. Apoptotic Effects of L4 and L5 in Human Gastric Cancer Cell Lines.....	54

2.2.7.	Transcriptional Upregulation of p53 Targets	57
2.3.	Summary	60
2.4.	Experimental	61
2.4.1.	Materials and Methods	61
2.4.2.	Synthesis.....	61
2.4.3.	Molecular Modeling	66
2.4.4.	X-ray Structure Determination of L4.....	66
2.4.5.	Stability Constant Determination.....	67
2.4.6.	Increasing Intracellular Levels of Zn ²⁺ in the p53-Y220C Cell Line NUGC3 ..	67
2.4.7.	<i>In Vitro</i> Cytotoxicity – NCI-60 Screening	68
2.4.8.	<i>In Vitro</i> Cytotoxicity – Stomach Cancer Cell Lines	68
2.4.9.	Western Blot Analysis.....	68
2.4.10.	Site-Directed Mutagenesis	69
2.4.11.	Protein Expression and Purification.....	69
2.4.12.	Surface Plasmon Resonance.....	70
2.4.13.	Immunoprecipitation.....	70
2.4.14.	Upregulation of p53 Transcription Factors by RT-qPCR.....	71
2.4.15.	Silencing of p53 in NUGC3 Cells Using siRNA.....	71

Chapter 3. Ligand Modifications for Targeting Subsite Cavities in Mutant p53-Y220C 72

3.1.	Introduction.....	72
3.2.	Results and Discussion	74
3.2.1.	Ligand Design and Synthesis	74
3.2.2.	Molecular Docking	78
3.2.3.	Zinc Binding Affinities for L5-P and L5-O	80
3.2.4.	Monitoring Intracellular Zn ²⁺ Levels in Cancer Cells.....	84
3.2.5.	<i>In Vitro</i> Cytotoxicity.....	86
3.2.6.	Apoptotic Effects of L5-P and L5-O in Human Gastric Cancer Cell Lines.....	88
3.2.7.	Interaction Between L6/L7 and Mutant p53.....	90
3.3.	Summary	91
3.4.	Experimental	93
3.4.1.	Material and Methods	93
3.4.2.	Synthesis.....	93
3.4.3.	Molecular Modeling	98
3.4.4.	Stability Constant Determination.....	98
3.4.5.	<i>In Vitro</i> Cytotoxicity – Stomach Cancer Cell Lines	99
3.4.6.	Monitoring Intracellular Levels of Zn ²⁺ in the p53-Y220C Cell Line NUGC3 ..	99
3.4.7.	Western Blot Analysis.....	100
3.4.8.	Site-Directed Mutagenesis.....	100
3.4.9.	Protein Expression and Purification	101
3.4.10.	Native Mass Spectrometry	101

Chapter 4. Bifunctional Ligand Design for Modulating Mutant p53 Aggregation in Cancer 102

4.1.	Introduction.....	102
4.2.	Results and Discussion	105
4.2.1.	Ligand Design and Synthesis	105
4.2.2.	Zinc Binding Affinities for L6 and L7.....	106
4.2.3.	Increasing Intracellular Zn ²⁺ in Cancer Cells	111
4.2.4.	Effects of L6 and L7 on Mutant p53 Aggregation	113
4.2.5.	Interaction Between L6/L7 and Mutant p53.....	117
4.2.6.	Restoration of p53 Function.....	119
4.2.7.	<i>In Vitro</i> Cytotoxicity	123
4.2.8.	Apoptotic Effects of L6 and L7 in Human Gastric Cancer Cell Lines	126
4.2.9.	Cytotoxicity in Non-Cancerous Intestinal Organoids	131
4.3.	Summary	136
4.4.	Experimental	137
4.4.1.	Materials and Methods	137
4.4.2.	Synthesis.....	138
4.4.3.	X-ray Structure Determination of L6 and L7	140
4.4.4.	Stability Constant Determination.....	141
4.4.5.	Increasing Intracellular Levels of Zn ²⁺ in the p53-Y220C Cell Line NUGC3141	141
4.4.6.	Site-Directed Mutagenesis.....	142
4.4.7.	Protein Expression and Purification	142
4.4.8.	Light Scattering.....	143
4.4.9.	Transmission Electron Microscopy	143
4.4.10.	Immunofluorescence (A11, ThT, and AIF).....	143
4.4.11.	Native Mass Spectrometry	144
4.4.12.	Immunoprecipitation.....	145
4.4.13.	Western Blot Analysis	145
4.4.14.	RNA Extraction and RT-qPCR	146
4.4.15.	<i>In Vitro</i> Cytotoxicity – NCI-60 Screening	146
4.4.16.	<i>In Vitro</i> Cytotoxicity – Stomach Cancer Cell Lines.....	146
4.4.17.	Organoid Culture and Immunofluorescence	147
4.4.18.	Organoid Survival Assay.....	147
4.4.19.	Tolerability of L6 in Normal Mice	148
Chapter 5.	Ongoing and Future Directions.....	149
5.1.	Thesis Summary.....	149
5.2.	Chapter 2 and Chapter 3	150
5.2.1.	Mechanisms of p53-Independent Activity.....	150
5.2.2.	Structure Modifications and Design Strategies.....	151
5.3.	Chapter 4	155
5.3.1.	Determining the Effects of Halogenation on p53 Aggregation	156
5.3.2.	Effectiveness of L6 in Other Aggregation-Prone Mutants.....	157
5.4.	Closing Statement	158
5.5.	Experimental	158
References.....	161	

Appendix A.	Supplementary Information for Chapter 2.....	186
Appendix B.	Supplementary Information for Chapter 3.....	201
Appendix C.	Supplementary Information for Chapter 4.....	204

List of Tables

Table 2.1.	pKa values as determined by variable pH UV-vis titrations (errors are for the last digit).....	43
Table 2.2.	Stability constants (log <i>K</i>) of the Zn complexes of L1-L5 and calculated pM (pZn) values ^[a] (errors are for the last digit).	45
Table 2.3.	Selected crystallographic information for ZnL4Cl.....	46
Table 2.4.	Mean GI ₅₀ and LC ₅₀ values for L4, L5, and cisplatin from the NCI-60 screen.	49
Table 2.5.	<i>In vitro</i> cytotoxicity (IC ₅₀ values) ^[a] data for stomach cancer cell lines AGS, MKN1, and NUGC3.....	53
Table 3.1.	pKa values as determined by variable pH UV-vis titrations (errors are for the last digit).....	81
Table 3.2.	Stability constants (log <i>K</i>) of the Zn complexes of L5-P and L5-O and calculated pM values ^[a] (errors are for the last digit).....	83
Table 3.3.	Mean growth value for L5, L5-P, and L5-O from the 1-dose NCI-60 screen.	86
Table 4.1.	pKa values as determined by variable pH UV-vis titrations (errors are for the last digit).....	107
Table 4.2.	Stability constants (log <i>K</i>) of the Zn complexes of L6 and L7 and calculated pM values ^[a] (errors are for the last digit).....	108
Table 4.3.	Selected crystallographic information for ZnL6Cl and ZnL7Cl.	111
Table 4.4.	Mean GI ₅₀ and LC ₅₀ values for L6, L7, Cisplatin, and Oxaliplatin from the NCI-60 screen.	124
Table 4.5.	<i>In vitro</i> cytotoxicity (IC ₅₀ values) ^[a] data for stomach cancer cell lines NUGC3 upon indicated treatment for 48 hours.....	126
Table 4.6.	Number of organoids counted in each classification system per indicated treatment condition.....	132

List of Figures

Figure 1.1.	General cytotoxic agents commonly used in chemotherapy.	3
Figure 1.2.	FDA approved chemotherapeutics that target biological characteristics specific to cancer cells.	4
Figure 1.3.	Domain structures of p53, p63, and p73. Genes encoding the transactivation domain (TAD), proline-rich region (PR), DNA binding domain (DBD), and oligomerization domain (OD) are shown. p63 and p73 encode an additional sterile alpha motif (SAM) domain. The percent homology between p63/p73 and p53 are indicated. ⁵⁷	6
Figure 1.4.	Domain structure of full length p53, comprised of the transactivation domain (TAD, aa ~1-61), proline-rich region (PR, aa ~62-94), DNA-binding domain (DBD, aa ~98-292), a basic nuclear localization signal from aa ~293-325, oligomerization domain (OD, aa ~326-356), and the C-terminus regulatory domain (CT, aa ~363-393).The DNA binding domain is the most frequently mutated domain, highlighted by the rainbow gradient from low frequency (blue) to high frequency (red). The most frequently mutated sites, termed hotspots, and their relative frequencies are exhibited by the bars above the diagram at indicated amino acid positions. ⁵⁹ Sites of common post translational modifications including phosphorylation (P), acetylation (A), and ubiquitination (UB) are indicated.	7
Figure 1.5.	Structure of the p53 DNA binding domain. Loops L2 and L3 are stabilized by Zn ²⁺ which is bound in a tetrahedral environment as shown in the box enlargement (PDB ID: 4AGL).	9
Figure 1.6.	Regulatory network of the p53 pathway in response to cellular and metabolic stresses. p53 recruits the aid of coactivators such as p300/CBP in order to regulate a variety of genes involved in apoptosis, DNA repair, cell cycle arrest, anti-angiogenesis, and senescence. The feedback loop between p53 and MDM2 keeps p53 at basal levels in the absence of stress response.	11
Figure 1.7.	Caspase-independent and -dependent activation of apoptosis. Transcriptional upregulation of p53 target genes triggers the release of mitochondrial apoptotic factors: the release of reactive oxygen species (ROS), Endonuclease G (EndoG), and apoptosis inducing factor (AIF) result in caspase-independent apoptosis, whereas the release of cytochrome C results in binding to the apoptotic protease-activating factor-1 (Apaf1), initiating the caspase-dependent apoptotic cascade. ...	12
Figure 1.8.	A schematic representation of the phases in the cell cycle.	14
Figure 1.9.	p53C bound to DNA (yellow). Locations of amino acids 175, 220, 245, 248, 249, 273, and 282, sites of key hot spot carcinogenic mutations, are shown (PDB ID: 4AGL).	16
Figure 1.10.	Family of small molecules termed Nutlins, reported to activate WTp53 by inhibiting the p53-MDM2 complex in order to prevent MDM2-mediated degradation of p53 and allow for accumulation of functional p53.	19
Figure 1.11.	Small-molecule p53-MDM2 inhibitors that activate p53.	20

Figure 1.12.	Small molecules that restore wild-type function in mutant p53 via thiol alkylation and cysteine modification to promote protein refolding.	22
Figure 1.13.	Small molecules that restore wild-type function in mutant p53 via thermal stabilization of the mutant induced p53-Y220C cavity.	23
Figure 1.14.	Small molecules that restore wild-type function in mutant p53 by preventing and modulating aggregation or by disrupting the p53/p73 aggregated complex.....	25
Figure 1.15.	Small molecules that restore wild-type function in mutant p53 by serving as metallochaperones and restoring native zinc binding.....	27
Figure 1.16.	Small molecules used as chelators for targeted metal ion chelation and redistribution in cancer therapy.	29
Figure 1.17.	Overview of p53 function and the opportunities for therapeutic intervention (shown in red). In response to DNA damage, MDM2 allows for upregulation of p53 in order to carry out various cell death or cell repair mechanisms. However, both the loss of zinc and mutants causing unstable conformations lead to loss of protein function and provide an opportunity for aggregate formation. p53 aggregates are toxic species associated with both loss of function and gain of function and contribute to cancer development.	31
Figure 1.18.	Multifunctional ligand scaffolds presented in chapters 2-4.....	32
Figure 2.1.	Chemical structures of (a) APR-246 (PRIMA-1MET) (b) NSC319726 (ZMC1) (c) PhiKan083 and (d) iodinated phenol small molecule shown to bind the p53-Y220C mutant pocket.	35
Figure 2.2.	Structural model of p53C bound to DNA (PDB ID: 2AHI). Box enlargement shows that upon change from the larger tyrosine residue to a cysteine at position 220, a mutant-induced cavity is formed. The small molecule in Figure 2.1d is shown within the cavity and has led to restored protein function by increasing protein stability and preventing unfolding (PDB ID: 4AGL).....	37
Figure 2.3.	Chemical structures of ligands L1-L5.	38
Figure 2.4.	A low energy pose of L1-L5 (a-e) in the mutation-induced cavity for p53-Y220C (PDBID: 4AGQ) ¹⁵³ . The halogen bonding interactions (I...Leu145) are shown with a yellow line. The hydrogen bond network between the conserved water, D228, and V147 is shown in red. The Van der Waals surface of the protein is shown in gray. Atom colours: carbon is represented in gray in the protein and teal for the ligand. Oxygen is shown in red, nitrogen in blue, and sulfur in yellow. Hydrogens are omitted for clarity. (f) A low energy pose of L5 (teal) overlaid with a known p53-Y220C binding molecule (green).	41
Figure 2.5.	(a,c) Variable pH titration plots for L1 and L5. (b,d) Simulated speciation diagrams of L1 and L5. Speciation diagrams were made using HySS2009.....	43
Figure 2.6.	(a, c) Variable pH titration plots for L1 + Zn ²⁺ and L5 + Zn ²⁺ . (b, d) Simulated speciation diagrams of L1 + Zn ²⁺ and L5 + Zn ²⁺ . Speciation diagrams made using HySS2009.	44
Figure 2.7.	¹ H NMR spectra of L4 (red) and ZnL4Cl (blue) (DMSO, 400 MHz). Asterisk denotes residual CD ₂ Cl ₂ solvent peak.....	45

Figure 2.8.	ORTEP of ZnL4Cl (50% probability) using POV-Ray, excluding hydrogen atoms and solvent. Selected interatomic distances [Å]: Zn(1)-N(1-3): 2.093-2.280; Zn(1)-O(1): 1.954; Zn(1)-Cl(1): 2.286.	46
Figure 2.9.	Treatment of NUGC3 (p53-Y220C) with L4 and L5 increases intracellular Zn ²⁺ . (a) Imaging of intracellular Zn ²⁺ levels in complete serum-free media. NUGC3 cells were incubated with 1 μM FluoZin-3 ²¹⁹ for 20 minutes at 37 °C, followed by incubation with indicated treatment (ZnCl ₂ = 50 μM, L4 = L5 = 15 μM, 50 μM PYR) for 2 hours. 150 μM TPEN was added following incubation with ZnCl ₂ and L5. Cells were imaged using a Nikon ApoTome microscope and fluorescence-quantified using ImageJ. All images were taken at indicated magnification. (B) Fluorescence intensity of FluoZin-3 at 488 nm demonstrating relative Zn ²⁺ levels. The gray dots represents the fluorescence intensity in each imaged cell. Blue line indicates mean values, while black error bars demonstrate the 95% confidence interval. * indicates statistical differences from control with p < 0.0001, • indicates statistical differences from control with p < 0.01, and Δ indicates statistical difference from L5 + ZnCl ₂ with p < 0.0001. No statistical differences are observed between the control and L5 + ZnCl ₂ + TPEN.	48
Figure 2.10.	In vitro cytotoxicity (MTT) of L4 vs ZnL4Cl and L5 vs ZnL5Cl in the stomach cancer cell line AGS (WTp53) (a,b) and NUGC3 (p53-Y220C) (c,d).....	50
Figure 2.11.	Heat map showing the <i>in vitro</i> cytostatic (GI ₅₀) and cytotoxicity (LC ₅₀) of L4 and L5 in the NCI-60 screen. Blue indicates low activity (100 μM) and red indicates high activity (0.01 μM).	52
Figure 2.12.	NUGC3 cells (300 cells/well; 96 wells/plate) were grown for 4 days and then treated for 3 days at IC ₅₀ and IC ₇₅ concentrations as indicated. 3D cultures were observed by microscopy to estimate clone size (left) and cell survival was assayed using rezasurin, a fluorescent indicator of cell viability (right). * indicates statistical differences from non-treated control with p < 0.001 as established by One-Way ANOVA followed by Tukey test.	54
Figure 2.13.	AGS cells (a) and NUGC3 cells (b) were treated for 48 hours with the IC ₅₀ and IC ₇₅ concentrations of indicated compound. Total protein was extracted, and 20 μg were separated on SDS PAGE (Sodium dodecyl sulfate polyacrylamide gel electrophoresis). Cleaved caspase-3 (Caspase 3*), p53, and actin were detected by Western Blot analysis.	55
Figure 2.14.	SPR kinetic sensorgram measuring the binding of L5 to p53C-Y220C. Various concentrations of L5 ranging from 0 μM to 800 μM in running buffer (HBS-EP+ - GE Healthcare: 10 mM HEPES, 150 mM NaCl, 3 mM EDTA, 0.05% v/v Surfactant P20, pH 7.4) containing 5% DMSO was injected. The association and dissociation phase were monitored for 60 and 100 seconds respectively. (b) Solubility of L5 in SPR running buffer by measuring absorbance as a function of L5 concentration. Binding measurements of L5 to p53C-Y220C is limited by ligand insolubility beyond 400 μM and therefore higher micromolar binding affinities cannot be accurately measured.	56
Figure 2.15.	Mutant p53 levels are reduced upon treatment with increasing concentrations of L5. NUGC3 cells were treated for 2 hours with L5 at the	

	indicated concentrations. Cells were lysed, followed by total protein selection against the p53 antibody PAb240, which immunoprecipitates only mutated p53. Precipitated protein was separated on a 10% SDS page gel and incubated with the p53 antibody (DO-1), which recognizes both mutated and wild-type p53. A non-specific antibody was used as a negative control for immunoprecipitation (IgG). Actin protein levels present in the lysate are shown as a control for the quantity of protein used for immunoprecipitation.	57
Figure 2.16.	NUGC3 cells were transfected with control siRNA (siCT) or siRNA directed against p53 (sip53) and then treated for 24 hours with IC ₅₀ concentrations of indicated compounds. Top: Total protein was extracted, and 20 µg separated by SDS PAGE. p53 and actin were then detected by Western Blot. Bottom: Total RNA was extracted, and RT-qPCR performed to measure the expression of P53, P21, PUMA and NOXA. Bars represent means of triplicates with error bars. * indicates statistical differences from NT (siCT) with p<0.001, Δ indicates statistical differences from NT (siCT) with p<0.01, • indicates statistical differences from L5 (siCT) with p<0.001.	59
Figure 3.1.	Molecular surface view of the p53-Y220C mutant cavity (PDB ID: 4AGQ). The cavity can be divided into three parts: the central mutant cavity (blue), an open subsite 1 (red) that contains many solvent-exposed amino acids and a narrow subsite 2 (green). Various amino acids located around these subsites are indicated in white.	73
Figure 3.2.	Structure optimization of our lead compound from Chapter 2, L5. By modifying the spacer between the iodinated phenol and zinc chelator as well as substituting functional groups on the phenol, this chapter studies the synthesis, characterization, and biological properties of ligands L5-P and L5-O.	74
Figure 3.3.	A low energy pose of L5-P in the mutation-induced cavity for p53-Y220C (PDBID: 4AGQ) ¹⁵³ . The halogen bonding interactions (I...Leu145) are shown with a yellow line. The hydrogen bond network between the conserved water, D228, and V147 is shown in red. The Van der Waals surface of the protein is shown in gray. Atom colours: carbon is represented in gray in the protein and teal for the ligand. Oxygen is shown in red, nitrogen in blue, and sulfur in yellow. Hydrogens are omitted for clarity.	79
Figure 3.4.	A low energy pose of L5-O in the mutation-induced cavity for p53-Y220C (PDBID: 4AGQ) ¹⁵³ . The hydrogen bond network between the conserved water, D228, and V147 is shown in red. The Van der Waals surface of the protein is shown in gray. Atom colours: carbon is represented in gray in the protein and teal for the ligand. Oxygen is shown in red, nitrogen in blue, and sulfur in yellow. Hydrogens are omitted for clarity.	80
Figure 3.5.	(a,c) Variable pH titration plots for L5-P and L5-O. (b,d) Simulated speciation diagrams of L5-P and L5-O. Speciation diagrams made using HySS2009.	81
Figure 3.6.	(a, c) Variable pH titration plots for L5-P + Zn ²⁺ and L5-O + Zn ²⁺ . (b, d) Simulated speciation diagrams of L5-P + Zn ²⁺ and L5-O + Zn ²⁺ . Speciation diagrams made using HySS2009.	83

Figure 3.7.	Treatment of NUGC3 with L5-O and L5-P does not result in increased intracellular Zn ²⁺ . (a) Imaging of intracellular Zn ²⁺ levels in complete serum-free media. NUGC3 cells were incubated with 1 μM FluoZin-3 ²¹⁹ for 20 minutes at 37°C, followed by incubation with indicated treatment (ZnCl ₂ = 50 μM, L5-O = L5-P = 10 μM, 50 μM PYR) for 2 hours. Cells were imaged using a Nikon ApoTome microscope and fluorescence-quantified using ImageJ. (B) Fluorescence intensity of FluoZin-3 at 488 nm demonstrating relative Zn ²⁺ levels. Blue dots represent average fluorescence intensity of imaged cells per individual trial. Black line indicates mean values, while black error bars demonstrate the 95% confidence interval.	85
Figure 3.8.	Survival curves for NUGC3 cells (p53-Y220C) upon treatment with L5-P (a) and L5-O (b). IC ₅₀ and IC ₇₅ values are represented by the gray and teal lines respectively and are indicated on the graph.	87
Figure 3.9.	NUGC3 cells (300 cells/well; 96 wells/plate) were grown for 4 days and then treated for 3 days with 10 μM L5-P and L5-O. 3D cultures were observed by microscopy to estimate clone size (left) and cell survival was assayed using resazurin (right). * indicates statistical differences from non-treated control with p < 0.001 as established by One-Way ANOVA followed by Tukey test.	88
Figure 3.10.	AGS (a) and NUGC3 (b) cells were treated for 48 hours with indicated compounds. Total protein was extracted, and 20 μg were separated on SDS PAGE. Cleaved caspase-3 (Caspase 3*), p53, and actin were detected by Western Blot analysis.	89
Figure 3.11.	Native mass spectrometry results using recombinant p53C-Y220C (2 μM) incubated with (a) 0.2% DMSO (b) 50 μM L5-O (c) 100 μM L5-O (d) 50 μM L5-P and (e) 100 μM L5-P for 2 hours at room temperature.	91
Figure 4.1.	p53C bound to DNA shown in gold (PDB ID: 2AHI). The amyloidogenic region of p53 (residues 251-257) is shown in red. Normally buried within the protein's core, protein unfolding leads to exposure of this region and results in increased aggregation. The epitope recognized by PAb240 (yellow segment), an antibody that specifically recognizes mutant p53, is also buried within the protein's core under normal conditions and is exposed upon protein unfolding.	104
Figure 4.2.	Chemical structures of ligands L6, L7, and Thioflavin T.	105
Figure 4.3.	(a,c) Variable pH titration plots for L6 and L7. (b,d) Simulated speciation diagrams of L6 and L7. Speciation diagrams made using HySS2009.	107
Figure 4.4.	(a, c) Variable pH titration plots for L6 + Zn ²⁺ and L7 + Zn ²⁺ . (b, d) Simulated speciation diagrams of L6 + Zn ²⁺ and L7 + Zn ²⁺ . Speciation diagrams made using HySS2009.	109
Figure 4.5.	ORTEP of ZnL6Cl (50 % probability) using POV-Ray, excluding hydrogen atoms and solvent. Selected interatomic distances [Å]: Zn(1)-N(1): 2.271(3), Zn(1)-N(3): 2.090(2), Zn(1)-N(4): 2.088(3), Zn(1)-O(1): 1.954(2), Zn(1)-Cl(1): 2.2978(8).	110
Figure 4.6.	ORTEP of ZnL7Cl (50 % probability) using POV-Ray, excluding hydrogen atoms and solvent. Selected interatomic distances [Å]: Zn(1)-N(1): 2.251(5), Zn(1)-N(3): 2.067(4), Zn(1)-N(4): 2.090(5), Zn(1)-O(1): 1.964(4), Zn(1)-Cl(1): 2.341(2).	110

- Figure 4.7. Treatment of NUGC3 (p53-Y220C) with L6 and L7 increases intracellular Zn²⁺. (a) Imaging of intracellular Zn²⁺ levels in complete serum-free media. NUGC3 cells were incubated with 1 μM FluoZin-3 for 20 minutes at 37°C, followed by incubation with indicated treatment (ZnCl₂ = 50 μM, L6 = L7 = 50 μM, 50 μM PYR) for 2 hours. Cells were imaged using a Nikon ApoTome microscope and fluorescence-quantified using ImageJ. (b) Fluorescence intensity of FluoZin-3 at 488 nm demonstrating relative Zn²⁺ levels. Blue dots represent average fluorescence intensity of imaged cells per individual trial. Black line indicates mean values, while black error bars demonstrate the 95% confidence interval. Statistical differences were analyzed using One-Way ANOVA with multiple comparisons (Dunnnett test). * indicates statistical differences from control with p < 0.001..... 112
- Figure 4.8. (a) 5 μM p53C-Y220C in 30 mM Tris-HCl, 150 mM NaCl, pH 7.4 was incubated at 37 °C. Light scattering at 500 nm was monitored over time from 0 to 6 hours. Absorbance readings were recorded every 3 minutes, with 30 seconds of agitation before each reading. Addition of 5 and 10 μM of L6 shows concentration dependent inhibition of mutant p53 aggregation. (b) Addition of 5 and 10 μM of L7 results in no significant changes in mutant p53 aggregation. (c) Percent changes in light scattering of mutant p53 upon addition of 10 μM L6/L7 after 2 hours of incubation at 37 °C..... 113
- Figure 4.9. 5 μM wild-type p53 in 30 mM Tris-HCl, 150 mM NaCl, pH 7.4 was incubated at 37 °C. Light scattering at 500 nm was monitored over time from 0 to 3 hours. Absorbance readings were recorded every 3 minutes, with 30 seconds of agitation before each reading. (a) Addition of 5 and 10 μM of L6 shows inhibition of aggregation. (b) Addition of 5 and 10 μM of L7 results in no significant changes in p53 aggregation..... 114
- Figure 4.10. (a) Gel electrophoresis and Western Blot of 8 μM p53C-Y220C in 30 mM Tris, 150 mM NaCl, pH 7.4 (NT – lane 1) and two equivalents of L6 (lane 2) and L7 (lane 3) after a 2-hour incubation with constant agitation at 37 °C. Western Blot was revealed using the primary antibody PAb240, which recognizes mutant p53. (b) TEM images of 8 μM mutant p53C-Y220C under specified conditions..... 115
- Figure 4.11. NUGC3 cells were treated with 25 μM L6/L7 or 0.1% DMSO (NT) for 24 hours followed by labelling with anti-p53 (DO-1) and anti-oligomer (A11) antibodies at concentrations of 1:1000 and 1:100 respectively. Nuclei were stained with DAPI, followed by imaging using a fluorescence microscope. Columns from left to right include: DO-1 (anti-p53), A11 (anti-oligomer), and co-immunofluorescence of DO-1 and A11. The white arrows are representative of the overlap between DO-1 and A11. The scale bar represents 50 μm..... 116
- Figure 4.12. NUGC3 cells were treated with 25 μM L6, L7, or 0.1% DMSO (NT) for 24 hours followed by labelling with anti-p53 primary antibody DO-1 (1:1000) and ThT (1 mM). Nuclei were stained with DAPI, followed by imaging using a Nikon ApoTome microscope. Columns from left to right include: DO-1 (anti-p53), ThT, and co-immunofluorescence of DO-1 and ThT. The scale bar represents 50 μm..... 117

- Figure 4.13. Native mass spectrometry results using recombinant p53C-Y220C (3 μ M) incubated with (a) 0.2% DMSO (b) 30 μ M L6 (c) 75 μ M L6 (d) 30 μ M L7 and (e) 75 μ M L7 for 2 hours at room temperature. • Indicates a 564 Da mass increase representing an interaction between mutant p53 and L6, * indicates an 1128 Da mass increase representing an interaction between mutant p53 and 2 L6. [9⁺] represents the charge state of p53C-Y220C. 119
- Figure 4.14. NUGC3 cells were treated for 13 hours with L6 and L7 at the indicated concentrations. Cells were then lysed and proteins were immunoprecipitated using the p53 antibody PAb240 that immunoprecipitates only mutated p53. Precipitated proteins were separated on a 10% SDS page gel and incubated with the p53 antibody (DO-1), which recognizes both mutated and wild-type p53. An unrelated antibody was used as a negative control for immunoprecipitation (IgG). Actin protein levels present in the lysate are shown as a control for the amount of protein used in the immunoprecipitation. (a) Representative Western Blot image of lysate conditions added to the PAb240 antibody prior to immunoprecipitation (b) Representative Western Blot image of eluate samples removed post immunoprecipitation (c) Quantification of relative PAb240 antibody levels from eluates in part (b). 121
- Figure 4.15. NUGC3 cells were transfected with control siRNA (siCT) or siRNA directed against p53 (sip53) and then treated for 6 hours with 25 μ M of L6 and L7. Total RNAs were extracted and RT-qPCR performed to measure the expression of TP53 (p53), p21, PUMA, and NOXA. Bars represent means of triplicates with error bars. 123
- Figure 4.16. Heat map showing the *in vitro* cytostatic (GI₅₀) and cytotoxicity (LC₅₀) of L6 and L7 in the NCI-60 screen. Blue indicates low cytotoxicity (100 μ M) and red indicates high cytotoxicity (0.01 μ M). 125
- Figure 4.17. AGS cells (a) and NUGC3 cells (b) were treated for 48 hours with the IC₅₀ and IC₇₅ concentrations of indicated compound. Proteins were extracted, and 20 μ g were separated on SDS PAGE. Cleaved caspase-3 (Caspase 3*), p53, and actin were then detected by Western Blot. (c) NUGC3 cells were treated with 25 μ M of indicated compound for 24 hours. Proteins were extracted, and 40 μ g was separated on SDS PAGE. Cleaved caspase-3 (Caspase 3*), p53, and actin were detected by Western Blot. 128
- Figure 4.18. NUGC3 cells were treated with 5 and 25 μ M L6/L7 or 0.1% DMSO (NT) for 24 hours followed by labelling with anti-AIF antibody (1:1000). Nuclei were stained with 4',6-diamidino-2-phenylindole (DAPI), followed by imaging using a Nikon ApoTome microscope. Columns from left to right include: AIF, DAPI, and coimmunofluorescence of AIF and DAPI. The white arrows are representative of the overlap between AIF and DAPI. The scale bar represents 50 μ m. 129
- Figure 4.19. (a) NUGC3 cells were treated with 5 or 25 μ M of indicated compound for 48 hours. In the case of cotreatment, cells were incubated with L6 for 2 hours followed by a total 48-hour incubation with 25 μ M oxaliplatin. Total protein was extracted, and 40 μ g were separated on SDS PAGE. Cleaved caspase-3 (Caspase 3*) and actin were detected by Western blot. (b) Quantification of relative cleaved caspase 3 levels obtained by Western

	blot analysis upon cotreatment with L6 and oxaliplatin. Western blot image quantified using SynGene tools	130
Figure 4.20.	NUGC3 cells were treated with 10 μ M of indicated compound for 48 hours. In the case of co-treatment, cells were incubated with L6 for 2 hours followed by a total 24-hour incubation. RNAs were extracted and RT-qPCR for PUMA, BAX, and Bcl2 mRNAs quantification were performed. Graphs represent means with error bars of mRNA expression relative to the NT control (Ct). BAX and Bcl2 are represented as a ratio of their relative expression that is representative of cell death activation. .	131
Figure 4.21.	Intestinal organoids were incubated and monitored for 72 hours. F-actin (red) and nuclei (blue) were stained using Phalloidin and DAPI, respectively, at recommended concentrations and imaged using a Nikon ApoTome microscope. Organoids were then classified as normal, disorganized, dying, or dead based on cell morphology. Representative images for each classification condition are shown above. The scale bar represents 50 μ m.	132
Figure 4.22.	(a) Intestinal organoids were treated with indicated compound and monitored for 72 hours. F-actin (red) and nuclei (blue) were stained sing Phalloidin and DAPI, respectively, at recommended concentrations and imaged using a Nikon ApoTome microscope. The scale bar represents 50 μ m. (b) Characterization and quantification of organoids as either normal, disorganized, dying, or dead upon indicated treatment based on images obtained in part a. ca. 150 organoids were counted and analyzed for each condition.....	133
Figure 4.23.	Intestinal organoids were treated with indicated compound for 24 hours. F-actin (red) and nuclei (blue) were stained using Phalloidin and DAPI respectively. Apoptotic cells are stained using cleaved caspase-3 (green). Antibodies were used at recommended concentrations and imaged using a Nikon ApoTome microscope. The scale bar represents 50 μ m.....	134
Figure 4.24.	Intestinal organoids were treated with indicated compound and monitored for 23 days. Graph shows survival curves for each condition. *** indicates $p < 0.001$ established by One-Way ANOVA followed by a Dunnett post-test.	135
Figure 4.25.	C57BL/6 mice were injected intraperitoneally with increasing doses of L6 and monitored twice a week for five weeks. Mean weight of mice (three groups with $n=4$) are shown as averages \pm SD.	136
Figure 5.1.	Structures of commonly used zinc binding groups (ZBGs) in zinc-containing enzymes such as matrix metalloproteinases (MMPs) and histone deacetylases (HDACs).....	153
Figure 5.2.	Chemical structure of Pk11007 (a), and proposed structures for future modifications to the ligand scaffold (b-d). Targeting other characteristics of mutant p53 simultaneously using a multifunctional approach could provide advantages for selective activity towards mutant p53.	155

List of Schemes

Scheme 2.1.	Synthesis of L1. Yield: 56%.....	38
Scheme 2.2.	Synthesis of L2. Yield: 82%.....	39
Scheme 2.3.	Synthesis of L3. Yield: 78%.....	39
Scheme 2.4.	Synthesis of L4. Yield: 95%.....	39
Scheme 2.5.	Synthesis of L5. Yield: 64%.....	39
Scheme 3.1.	Attempted synthesis of L5-P using di-(2-picolyl)amine and 3-bromopropylamine. However, due to polymerization of 3-bromopropylamine, the reaction was unsuccessful.	75
Scheme 3.2.	Synthesis of L5-P. Yield: 27%.	75
Scheme 3.3.	Attempted synthesis of (5) using L5 and (prop-2-yn-1-yloxy)benzene (4). However, due to the strong metal-binding ability of L5, the Sonogashira coupling is inhibited and the reaction was unsuccessful.	76
Scheme 3.4.	Synthesis of desired product (6) and unwanted dialkylated side product from the Sonogashira coupling reaction. Yield (6): 18%.	77
Scheme 3.5.	Synthesis of (5). Yield: <10%.	77
Scheme 3.6.	Synthesis of L5-O. Yield: 62%.....	78
Scheme 4.1.	Synthesis of L6 and L7. Yields are 31% and 35%, respectively.....	106
Scheme 5.1.	Synthesis of chloro and bromo derivatives of L6/L7. Further purification to isolate ligands is still underway.	157

List of Acronyms

5-FU	Fluorouracil
aa	Amino Acid
ABL1	Abelson Murine Leukemia Viral Oncogene Homolog 1
AIF	Apoptosis Inducing Factor
ALS	Amyotrophic Lateral Sclerosis
Apaf1	Apoptotic Protease-activating Factor-1
BCR	Breakpoint Cluster Region Protein
BER	Base Excision Repair
BSA	Bovine Serum Albumin
Ca.	Circa
cDNA	Complementary DNA
ChIP	Chromatin Immunoprecipitation
CPPs	Cell-Penetrating Peptides
d	Doublet (NMR)
DAPI	4',6-diamidino-2-phenylindole
DBD	DNA Binding Domain
DCE	Dichloroethane
dd	Doublet of Doublets (NMR)
DIPA	N,N-Diisopropylethylamine
DMSO	Dimethyl Sulfoxide
DN	Dominant Negative
DNA	Deoxyribonucleic Acid
DpC	di-2-pyridylketone 4-cyclohexyl-4-methyl-3-thiosemicarbazone
DTC	Dithiocarbamate
DTT	Dithiothreitol
ECM	Extracellular Matrix
EDC	N-Ethyl-N'-(3-dimethylaminopropyl) carbodiimide
EDTA	Ethylenediaminetetraacetic Acid
EGFR	Epidermal Growth Factor Receptor
EGTA	Ethylene Glycol Tetraacetic Acid
EPR	Electron Paramagnetic Resonance
ESI	Electrospray Ionization

FDA	Food and Drug Administration
GGT	γ -Glutamyl Transferase
GoF	Gain of Function
HDACs	Histone Deacetylases
HEPES	(4-(2-hydroxyethyl) -1-piperazineethanesulfonic Acid
HR-MS	High-resolution Mass Spectrometry
IF	Immunofluorescence
IP	Immunoprecipitation
IPTG	Isopropyl β -D-1-thiogalactopyranoside
ITC	Isothermal Calorimetry
J	Coupling Constant (NMR)
K_d	Equilibrium Dissociation Constant
LB	Luria-Bertani Medium
LoF	Loss of Function
MDM2	Minute Double Mouse 2
mg	Milligrams
MHz	Megahertz
mL	Millilitres
mmol	Millimoles
MMPs	Matrix Metallopeptidases
MMR	Mismatch Repair
mol	Mole
MQ	Methylene Quinuclidinone
MS	Mass Spectrometry
MTD	Maximum Tolerated Dose
MTT	3-(4,5-Dimethylthiazol-2-yl) -2,5-diphenyltetrazolium bromide
NCI	National Cancer Institute
NER	Nucleotide Excision Repair
NHS	N-Hydroxysuccinimide
nM	Nanometres
NMR	Nuclear Magnetic Resonance
NT	Non-Treated Control
NTA	Nitriloacetic Acid
OD	Oligomerization Domain

OD	Optical Density
OXA	Oxaliplatin
PBS	Phosphate Buffered Saline
PCR	Polymerase Chain Reaction
PIPES	1,4-Piperazinediethanesulfonic Acid
pKa	Acid Dissociation Constant
pM	Picomolar
PMSF	Phenylmethylsulfonyl Fluoride
PPG	Photoremovable Protecting Group
ppm	Chemical Shift
PR	Proline-Rich Region
pRB	Retinoblastoma Protein
PTMs	Post Translational Modifications
PYR	Pyridithione
qPCR	Quantitative Polymerase Chain Reaction
RNA	Ribonucleic Acid
ROS	Reactive Oxygen Species
RPM	Revolutions per Minute
rtPCR	Real-time Polymerase Chain Reaction
s	Singlet (NMR)
SAM	Sterile α -Motif
SD	Standard Deviation
SDS PAGE	Sodium Dodecyl Sulfate Polyacrylamide Gel Electrophoresis
siRNA	siRNA
siRNA	Silencing RNA
SPR	Surface Plasmon Resonance
SV40	Simian Virus 40
TA	Transactivation Domain
TCEP	Tris(2-carboxyethyl) Phosphine
td	Triplet of Doublets (NMR)
TEM	Transmission Electron Microscopy
THF	Tetrahydrofuran
ThT	Thioflavin T
TNFR	Tumour Necrosis Factor Receptor

TOF	Time-of-Flight
TPEN	N,N,N',N'-Tetrakis(2-pyridylmethyl)ethylenediamine
UV-vis	Ultraviolet-Visible Spectroscopy
VEGF	Vascular Endothelial Growth Factor
ZBGs	Zinc Binding Groups

Chapter 1. Introduction

1.1. Cancer

Activation of gene-encoded processes that control the balance of cell life and death, referred to as programmed cell death or apoptosis, can rid the body of malfunctioning cells.¹ Fundamental alterations in the genetic factors that control this process results in continuous uncontrolled growth and division of cells, leading to the formation of tumours.² These changes in the deoxyribonucleic acid (DNA) sequence of cancer cell genomes are referred to as somatic mutations and include substitution of base pairs, deletion or insertion of DNA fragments, genomic amplifications, and epigenetic factors such as post translational modifications (PTMs).³⁻⁴ As such, cancer is a cumulation of over 100 diseases and is characterized by the uncontrolled proliferation of cells.¹

Studies have shown that numerous somatic mutations contribute to the development of cancer and that these mutations are highly heterogenous, with each individual presenting different mutations across various genes.⁵⁻⁷ Some of the most well-characterized genes known to carry mutations include TP53, RB1, EGFR, and KRAS and are frequently mutated across a wide range of cancer types.³ The rate of such mutations increases with exposure to endogenous factors such as tobacco carcinogens and ultraviolet radiation.⁸ Individuals can also be predisposed to cancer development via germline mutations. Located in germ cells, germline mutations can be transmitted to offspring through multiple generations, thus increasing the tendency to develop cancer. Germline mutations are present in about 5% to 10% of all cancer diagnoses.⁹ Tumours that display limited growth and motility are considered benign and generally pose minimal threat to human health. However, invasive cancer cells that secrete proteases such as matrix metalloproteinases (MMPs) and cathepsins to degrade the extracellular matrix (ECM) in their microenvironment gain motility and can penetrate the lymphatic or vascular system.¹⁰ These metastatic cells invade adjacent, healthy tissues and organs to form secondary tumours at sites beyond the location of origin and are largely responsible for the mortality of cancer.¹¹

Cancers are the second leading cause of death worldwide and are the leading cause of death in Canada. With a continually growing and aging population, it is estimated

that 1 in 2 Canadians will develop cancer throughout their lifetime, and 1 in 4 will die as a result of this disease. Although the past 50 years have brought about vast advancements for the detection and treatment of cancers, 220,000 new Canadian cancer diagnoses are projected for 2019, and the economic burden posed as a result of this disease is increasing at an alarming rate.¹² A recent study indicated that the economic burden of cancer in Canada rose from 2.9 billion in 2005 to 7.5 billion in 2012 and is projected to continually increase into the foreseeable future.¹³ Thus, the search for novel, effective anti-cancer agents elicits significant research attention.

1.2. Anti-Cancer Therapy

Early detection, surgery, radiotherapy, and chemotherapy are all vital aspects in improving cancer survival rates.¹⁴ However, once the cancer has begun to spread and metastasis occurs, chemotherapy becomes one of the most effective treatment options.¹⁵ Chemotherapy was revolutionized in the 1960s with the discovery of cisplatin (Figure 1.1), a small molecule that binds DNA and initiates cell cycle arrest. Cisplatin entered clinical trials in 1971 and was quickly granted approval from the Food and Drug Administration (FDA) for the treatment of testicular and bladder cancer by 1978.¹⁶ Cisplatin still serves as front-line treatment for cancer therapy today. However, it suffers from major clinical drawbacks such as severe toxic side effects and drug resistance.¹⁷⁻¹⁸ Since the discovery of cisplatin, the past five decades have seen vast technological advances including high-throughput screening, structure-based drug design, and the sequencing of the human genome, which has substantially improved the drug discovery process.¹⁹ While hundreds of chemotherapeutics have received FDA approval, they can be generally classified into two broad categories based on their mechanism of action: (1) general cytotoxic agents and (2) targeted agents.²⁰

1.2.1. General Cytotoxic Agents

General cytotoxic agents were among the first chemotherapies and are still a common pharmacological approach in clinics today. They are highly cytotoxic agents aimed at rapidly dividing cells during various stages of division and are often categorized based on their exhibited mechanism.²¹ The first class of cytotoxic agents are those that damage DNA directly at any stage of the cell cycle. These include alkylating agents and

commonly used platinum complexes such as the FDA approved cisplatin, oxaliplatin, and carboplatin (Figure 1.1).²² Upon displacement of their leaving groups, platinum complexes bound to DNA can form intra-strand and/or inter-strand crosslinks to disrupt cell division, thereby activating apoptotic pathways and initiating cell death.²³⁻²⁴ Oxaliplatin, however, has been known to exhibit cytotoxicity via additional mechanisms, including ribosome biogenesis stress.²⁵ A second class of cytotoxic agent includes antimetabolites, which describes a series of compounds that are similar in structure to common metabolites. The slight variations in structure, however, allows for interference with biological processes involved in metabolism. Such complexes are substituted for DNA and ribonucleic acid (RNA) base pairs during cell division and trigger cell death.²⁶ One of the most commonly used antimetabolites in chemotherapy is Fluorouracil (5-FU) (Figure 1.1).²⁷ Thirdly, antineoplastic antibiotics such as doxorubicin (Figure 1.1) block topoisomerase II activity, an enzyme involved in DNA replication, and further intercalate DNA to disrupt DNA replication and transcription to initiate cell death.²⁸ Finally, mitotic inhibitors such as paclitaxel induces cell cycle arrest by disrupting the microtubule network required for mitosis and cell growth (Figure 1.1).²⁹ Despite their widespread clinical use, general cytotoxic agents suffer from a lack of specificity towards cancer cells given that they target biological processes common to both cancer and normal cells and thus exhibit significant toxic side effects and develop drug resistance.²¹ Current research suggests that with an increasing understanding of the cancer genome and tumour biomarkers, a rational combination of both general cytotoxic agents and targeted therapies could significantly improve the efficacy of chemotherapeutics.

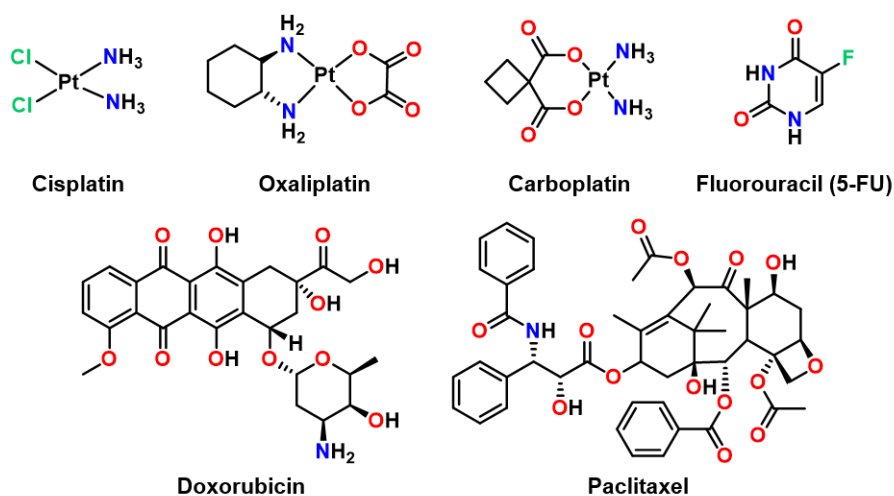


Figure 1.1. General cytotoxic agents commonly used in chemotherapy.

1.2.2. Targeted Chemotherapeutics

Targeted therapy is characterized by small molecules or monoclonal antibodies that alter or interrupt key biological processes specifically involved in tumour development.²¹ With the emergence of cancer genome sequencing projects, chemotherapy has undergone a major shift towards targeted therapy in the past decade and has expanded the possibilities of personalized medicine.³⁰ While the molecular targets involved in tumour growth and development are vastly expanding, one common approach is to target enzymes that are overexpressed in the tumour environment, specifically those involved in cell growth and survival.³¹ For example, sorafenib is a protein kinase inhibitor that acts on the epidermal growth factor receptor (EGFR) and vascular endothelial growth factor (VEGF) to interrupt tyrosine kinase signaling and induces angiogenesis in cancer cells (Figure 1.2).³² Other examples include targeting chromosomal abnormalities in cancer cells.³¹ Oftentimes in leukemia, the Abelson murine leukemia viral oncogene homolog 1 (ABL1) gene from chromosome 9 fuses with the breakpoint cluster region protein (BCR) gene on chromosome 22 to form the BCR-ABL fusion protein.³³ Imatinib (Figure 1.2) is a small molecule that specifically targets the BCR-ABL fusion protein to induce apoptosis and is highly effective in the treatment of leukemias.³⁴ Lastly, a leading approach in targeted therapeutics is to target mutated proteins that drive cancer progression.³⁵⁻³⁶ The p53 protein is mutated in over 50% of cancer diagnosis, and as a result, significant research efforts have been dedicated to both uncovering the molecular mechanisms of p53 that drive tumorigenesis and the development of chemotherapeutics that target mutant p53.³⁷ The pharmacological restoration of p53 function is the focus of this thesis and will thus be discussed in depth below.

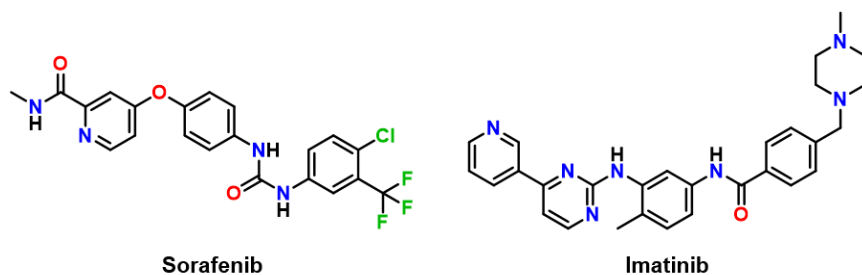


Figure 1.2. FDA approved chemotherapeutics that target biological characteristics specific to cancer cells.

1.3. p53 Structural biology

1.3.1. Discovery

The pioneering research on the discovery of the p53 protein occurred in 1979 by scientists David Lane and Lionel Crawford, and Daniel Linzer and Arnold Levine in two independent reports.³⁸⁻³⁹ While investigating the Simian Virus 40 (SV40), a DNA virus known to play a role in cancer development, they discovered a previously unknown protein bound to the viral oncoprotein of SV40, the large T antigen. The protein and its corresponding gene were named p53 and TP53 respectively because of its 53 kDa mass.⁴⁰ The notion that the large T antigen interacted with and bound to a host protein garnered significant excitement, and subsequent research determined that p53 was more prevalent in cells transformed by the virus than in normal cells. This observation of increased p53 expression in cancer cells resulted in initial reports classifying p53 as an oncogene.⁴¹⁻⁴³ However, work conducted in the 1980s demonstrated that the prevalence of cancer increased in the presence of p53 point mutations, highlighting its potential role as a regulator of cellular functions related to cell growth and control.⁴⁴⁻⁴⁶ This led to the shift in classification of p53 as tumour suppressor protein rather than an oncogene. For a gene to be unambiguously accepted as a tumour suppressor, it must meet two essential criteria: the loss of the gene should lead to an increased cancer-prone phenotype in animal models, and humans carrying germline mutations of the gene should display increased cancer susceptibility.⁴⁷ Both criteria are met by p53, beginning with mouse model studies performed in 1992 which demonstrated that p53 knock-out mice developed cancer with an increased prevalence.⁴⁸ Furthermore, it was shown that p53 mutations in germ cells are largely responsible for the hereditary Li-Fraumeni syndrome,⁴⁹ a cancer predisposition syndrome that is characterized by early onset development of classic tumours including soft tissue sarcomas, osteosarcomas, brain tumours, and leukemias.⁵⁰

Since its discovery over thirty years ago, p53 continues to revolutionize our understanding of cell division and growth. The field is becoming increasingly complex with continued advancements in technology, which are only slowly beginning to unravel the complex roles of p53 in the cell cycle.^{36, 51} By understanding the p53 pathway that leads from cellular stresses to tumour formation, we can continue to develop novel drug designs for chemotherapeutic treatment.

1.3.2. The p53 Family

Fifteen years after the discovery of p53, two functionally related proteins, p63⁵² and p73⁵³, were discovered. Together, these proteins were found to regulate the signaling network involved in cell proliferation, differentiation, and cell death. The p53, p63, and p73 genes encode proteins with very similar amino acid sequence homology in the transactivation, DNA-binding, and tetramerization domains, with the highest sequence homology observed in the DNA-binding domain (Figure 1.3). p63 and p73 both contain an additional C-terminal sterile α -motif (SAM).⁵⁴ The highly conserved homology in the DNA binding domain includes important contact residues involved in DNA binding, allowing all three proteins to activate transcription and induce cell-cycle arrest and apoptosis.⁵⁵ However, studies have shown that despite their structural similarity, these proteins are not functionally redundant; studies have demonstrated that transgenic knockout mice of each gene results in the development of individual phenotypes. For example, p53-null mice were born viable, yet die of cancer at a young age, whereas p63-null mice die immediately after birth, exhibiting a severe phenotype that lacks limbs and several important epithelial structures. p73-null mice are born with abnormalities in the nervous system and typically die within the first two months after birth.⁵⁶ Overall, the p53 family functions to regulate important cellular processes involved in division and proliferation and thus imbalances within the p53 family result in a vast array of developmental abnormalities in humans.

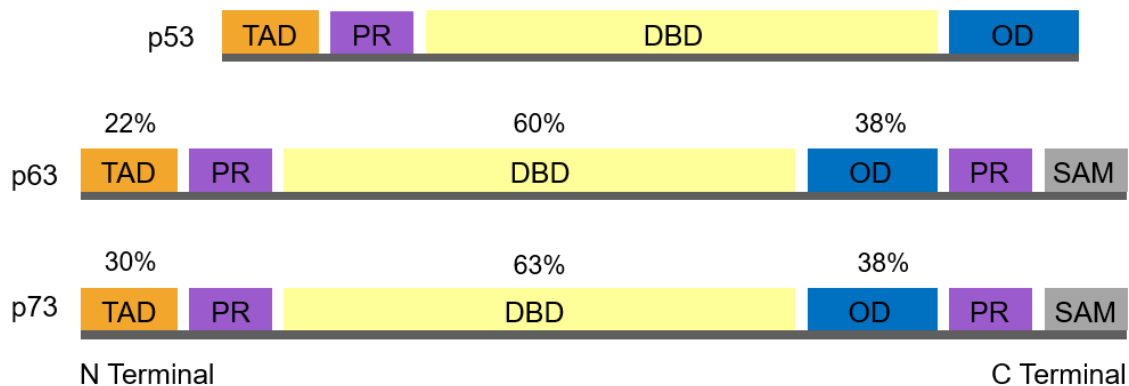


Figure 1.3. Domain structures of p53, p63, and p73. Genes encoding the transactivation domain (TAD), proline-rich region (PR), DNA binding domain (DBD), and oligomerization domain (OD) are shown. p63 and p73 encode an additional sterile alpha motif (SAM) domain. The percent homology between p63/p73 and p53 are indicated.⁵⁷

1.3.3. Structural Organization

p53 is biologically active as a homotetramer, with each monomer comprised of 393 amino acids.⁵⁸ The intrinsically disordered transactivation domain (TAD) and proline-rich region (PR) are located at the N-terminal region, while the central region is comprised of the folded DNA binding domain (DBD). Responsible for sequence-specific DNA-binding, this domain is the most frequently mutated domain in p53. The oligomerization domain (OD) follows the DNA binding domain, and the C-terminus contains a further regulatory domain.⁵⁹ Regulation of stability and activity within the individual domains is highly controlled by various posttranslational modifications (PTMs), including phosphorylation, acetylation, and ubiquitination (Figure 1.4).⁶⁰⁻⁶²

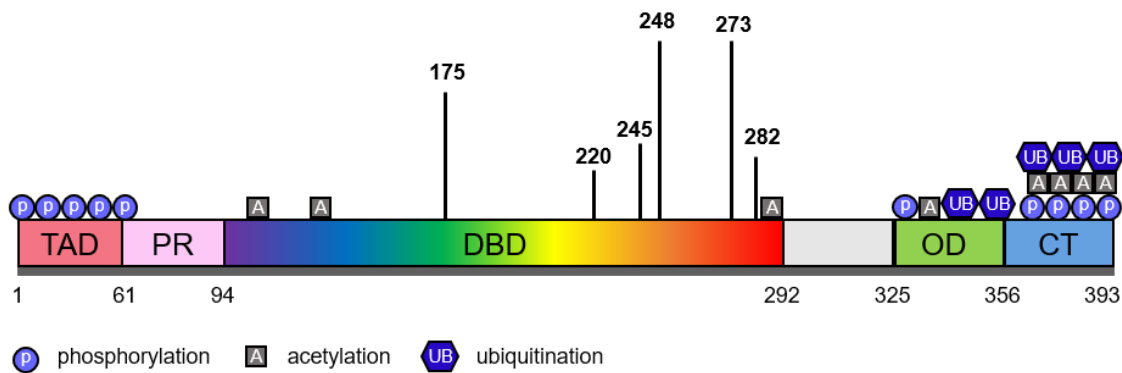


Figure 1.4. Domain structure of full length p53, comprised of the transactivation domain (TAD, aa ~1-61), proline-rich region (PR, aa ~62-94), DNA-binding domain (DBD, aa ~98-292), a basic nuclear localization signal from aa ~293-325, oligomerization domain (OD, aa ~326-356), and the C-terminus regulatory domain (CT, aa ~363-393). The DNA binding domain is the most frequently mutated domain, highlighted by the rainbow gradient from low frequency (blue) to high frequency (red). The most frequently mutated sites, termed hotspots, and their relative frequencies are exhibited by the bars above the diagram at indicated amino acid positions.⁵⁹ Sites of common post translational modifications including phosphorylation (P), acetylation (A), and ubiquitination (UB) are indicated.

The TAD can be divided into two domains, TAD1 and TAD2, both of which are crucial for p53 function by regulating transactivation of different target genes.⁶³ Mutagenesis studies in both domains revealed that inactivation of TAD1 and TAD2 abolished changes in p53-dependent gene expression.⁶⁴ In its native state, TAD is intrinsically unfolded, however, as is characteristic of natively unfolded proteins, it can fold upon interaction with target proteins.⁶⁵ The TAD domain serves as a binding site for multiple protein partners including minute double mouse 2 (MDM2),⁶⁶ a negative regulator

of p53, hRPA70,⁶⁷ a subunit of a human replication protein that is crucial for DNA replication and repair, and transcriptional coactivators such as p300/CBP⁶⁸. The activity of the transactivation domain is highly regulated by PTMs, namely phosphorylation of serine and threonine residues by protein kinases.⁶² In response to various cell stress factors, p53 phosphorylation occurs in order to shift binding affinities of different p53 binding partners to regulate p53 expression.⁵⁹ Following the TAD is the proline-rich region. Although the exact function of this region is not completely understood, its proline rich PXXP motifs (where P=proline and X=any other amino acid) mediate protein interactions involved in signal transduction, and it is thought to play a role in the proapoptotic functions of p53.^{59, 69}

The core DNA binding domain (DBD), often denoted p53C, is the most commonly mutated domain in p53.⁷⁰ This is likely owing to its thermodynamic and kinetic instability as the protein unfolds slightly above physiological temperature with a T_m of 44-45 °C.⁷¹ Several mutations causing structural perturbations within this domain result in lowering of this T_m even further, resulting in local protein unfolding. This domain functions by binding DNA promoters to initiate transcription.⁷² Its structure is comprised of a structural β -sandwich located at the surface of the domain which is responsible for site-specific interactions with DNA and can be subdivided into two groups that bind DNA at the major and minor grooves respectively.⁷³ The DNA major groove is bound by loop L1 of p53C, the C-terminal helix, and various portions of the β -strands. The second structural motif of p53C is formed by two large loops, L2 and L3.⁵⁹ Essential to the structural stability of p53C, loops 2 and 3 are stabilized by a core Zn^{2+} ion, which is tetrahedrally coordinated by a histidine (His179), and three cysteines (Cys-176, Cys-238 and Cys 242) in a tetrahedral geometry (Figure 1.5). Mutations within this site that perturb zinc binding cause structural changes in neighbouring loops, thereby causing a loss in DNA binding specificity. The loss of zinc from within the cavity substantially decreases the thermodynamic stability, causing protein unfolding and enhances aggregate formation.⁵⁹ Acetylation of the DNA binding domain, specifically at lysine120, is catalyzed by acetyltransferases and occurs in response to DNA damage.⁷⁴ This is a critical step in the induction of apoptosis, thus highlighting the role of the DNA-binding domain in preventing tumorigenesis.⁷⁵

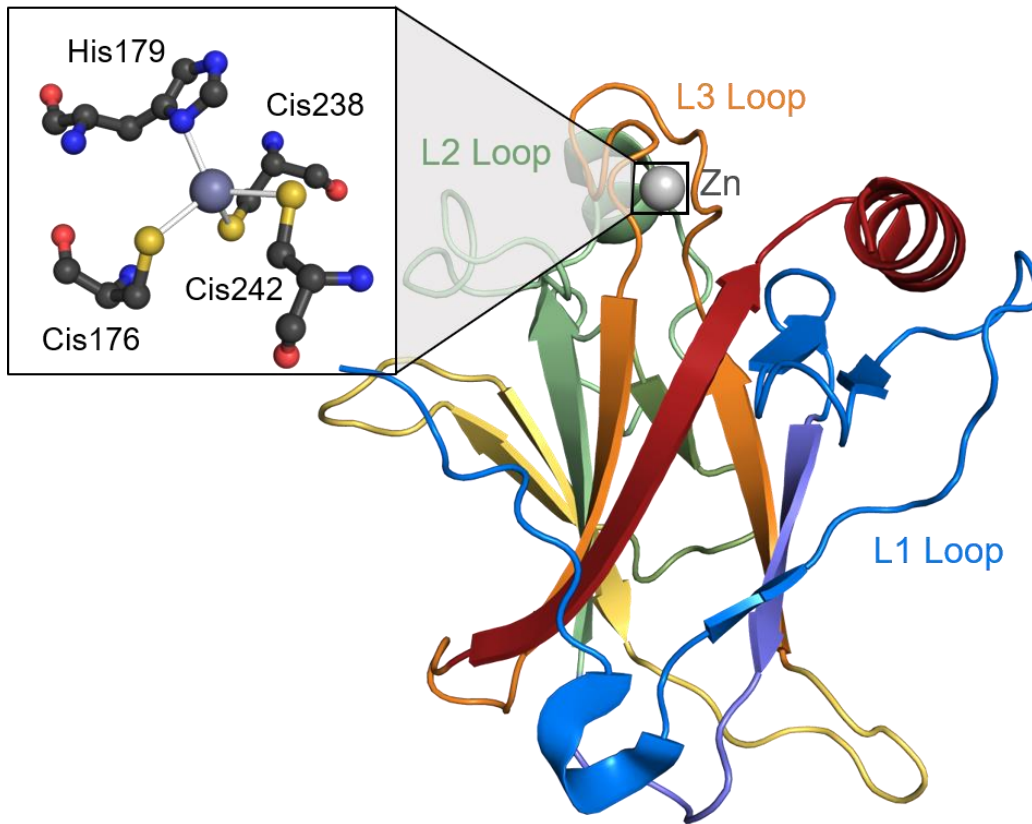


Figure 1.5. Structure of the p53 DNA binding domain. Loops L2 and L3 are stabilized by Zn²⁺ which is bound in a tetrahedral environment as shown in the box enlargement (PDB ID: 4AGL).

The oligomerization domain, also commonly referred to as the tetramerization domain, plays a key role in p53 function because it controls the quaternary structure of the protein.⁷⁶ p53 can exist in both latent and active conformations, the latter being crucial for DNA binding and interactions with other proteins. Since p53 is biologically active as a tetramer, the oligomerization domain mediates the transition between active and latent forms of p53.⁷⁷ Over 50 proteins bind to p53 within the C-terminal region of the protein, many of which specifically require tetramer formation thus highlighting the importance of this domain.⁷⁷⁻⁷⁸ The tetramer interface formed in this domain is stabilized by hydrophobic interactions, largely through two key hydrophobic residues, Leu344 and Leu348. Truncation of either of these residues results in a stabilization of the dimeric form.^{59, 79-80} PTMs play an important role in the function of the oligomerization domain, both directly and indirectly. Directly within the domain, phosphorylation for Ser392 is required for tetramer formation.⁸¹ Further, several key PTMs responsible for regulation of p53 activity within other domains are dependent on the initial formation of the tetrameric structure.⁶⁰

As a result, PTMs, and in turn, p53 function, is heavily dependent on appropriate function within the OD.

Lastly, the extreme C-terminus contains the regulatory domain, which is a basic, lysine-rich domain.⁸² This domain plays a key role in regulating protein activity and stability by undergoing extensive PTMs.⁸³ Six lysine residues within this domain are important sites for various PTMs including acetylation, ubiquitination, phosphorylation, methylation, and SUMOylation.⁶¹ For example, acetylation by p300/CBP at the C-terminus plays a role in activation of p53 transcriptional activity, while ubiquitination is essential for regulating p53 levels by controlling ubiquitin-dependent degradation of the protein.⁸⁴

1.3.4. Regulatory Mechanism

Control over cellular levels of p53 is regarded as the most important factor in regulating p53 function.⁸⁵ In order to maintain basal p53 function, cellular levels are tightly regulated in biological systems. Under normal conditions, p53 is unstable, with a half-life ranging from 5 to 30 minutes.⁸⁶⁻⁸⁷ p53 and key regulator MDM2 are linked via a negative autoregulatory feedback loop wherein p53 induces the expression of MDM2, which in turn binds to p53 to prevent transcriptional activity and promotes ubiquitin-dependent degradation.⁸⁸ This involves various PTMs to transfer ubiquitin from E3 ubiquitin ligases to p53, which signals for p53 degradation by the 26S proteasome.⁶² In the presence of cellular stress, however, degradation of p53 is suppressed in order to allow for p53 stabilization and accumulation in the nucleus. Upon accumulation, p53 tetramerization is favoured, thereby activating the protein to signal for various target genes that initiate response mechanisms.⁸⁹

1.3.5. Activation and Biological Response

In response to cellular stress factors, activation of p53 initiates various pathways involved in apoptosis, DNA repair, cell cycle arrest, anti-angiogenesis, and senescence in order to avoid propagation of damaged cells. (Figure 1.6).⁹⁰ p53 activation is largely regarded as a complicated regulatory network composed of three key steps: (1) p53 stabilization by phosphorylation, (2) DNA binding, and (3) target gene activation.⁹¹ With the aid of various PTMs, p53 binds to specific regions of its target genes and activates their transcription by recruiting coactivators.⁹²

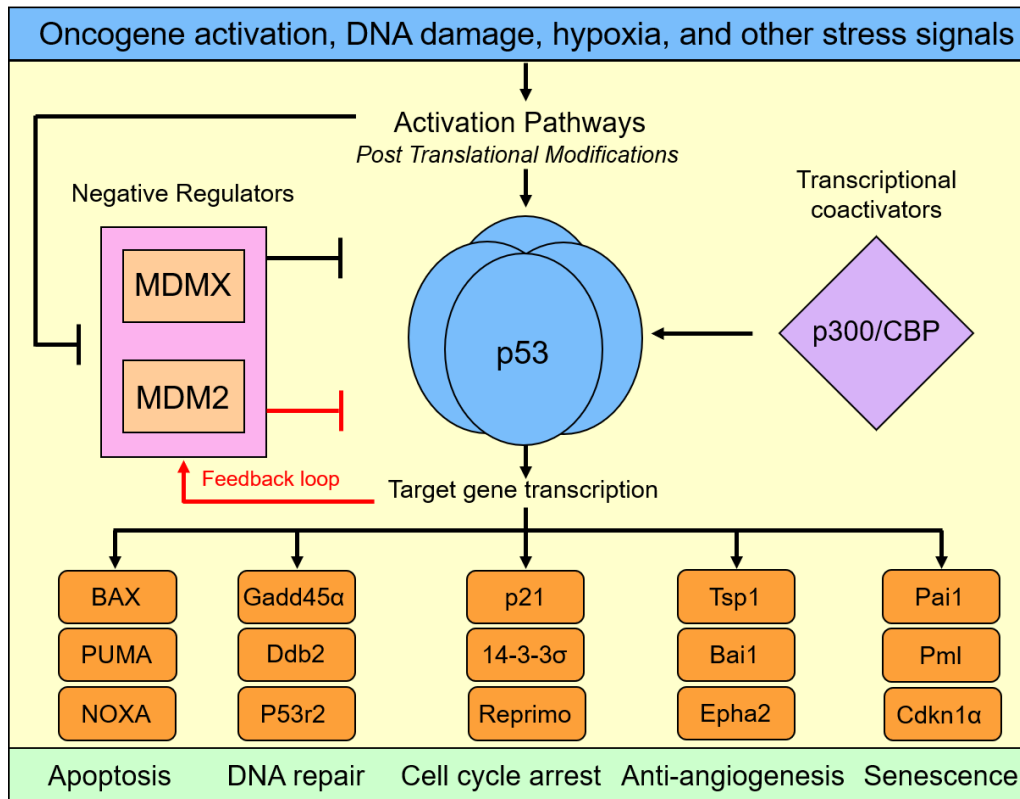


Figure 1.6. Regulatory network of the p53 pathway in response to cellular and metabolic stresses. p53 recruits the aid of coactivators such as p300/CBP in order to regulate a variety of genes involved in apoptosis, DNA repair, cell cycle arrest, anti-angiogenesis, and senescence. The feedback loop between p53 and MDM2 keeps p53 at basal levels in the absence of stress response.

The most comprehensive studies and well understood networks are the role of p53 in apoptosis and cell cycle arrest.⁹³ Several factors influence whether p53 activates apoptosis or cell cycle arrest in response to stress, including p53 expression levels, the type of stress signal, and fluctuations in the binding affinities for promoters of specific target genes.⁹⁴ Induction of apoptosis can occur via two converging pathways, referred to as the extrinsic and intrinsic apoptotic pathways.⁹⁵⁻⁹⁶ The extrinsic pathway, also called the death receptor pathway, involves p53 transcriptional activation of genes encoding the tumour necrosis factor receptor (TNFR) family.⁹⁷⁻⁹⁸ The intrinsic apoptosis pathway is the pathway activated in response to cell stress.⁹⁵ Cell stress factors initiate the activation of p53, which signals for transcriptional upregulation of target genes in the BCL-2 protein family including NOXA, PUMA, and BAX.⁹⁴ This triggers the release of mitochondrial apoptotic components, which initiate either caspase-independent or caspase-dependent apoptosis (Figure 1.7).⁹⁹

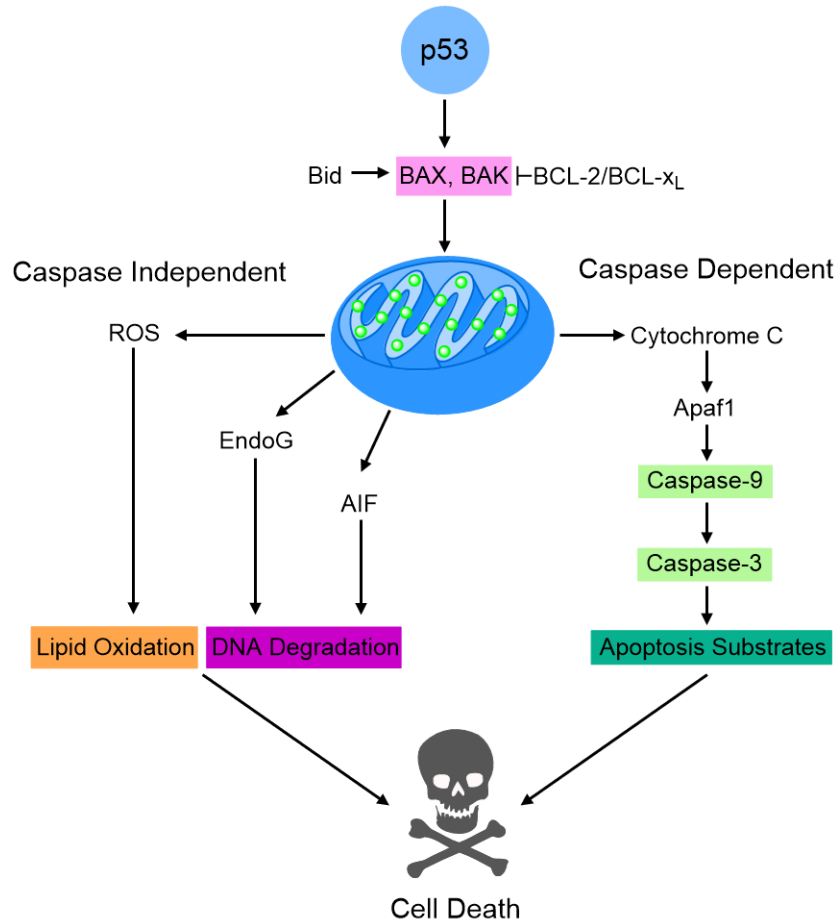


Figure 1.7. Caspase-independent and -dependent activation of apoptosis. Transcriptional upregulation of p53 target genes triggers the release of mitochondrial apoptotic factors: the release of reactive oxygen species (ROS), Endonuclease G (EndoG), and apoptosis inducing factor (AIF) result in caspase-independent apoptosis, whereas the release of cytochrome C results in binding to the apoptotic protease-activating factor-1 (Apaf1), initiating the caspase-dependent apoptotic cascade.

The release of the apoptosis inducing factor (AIF), for example, generates a caspase-independent cascade wherein it is shuttled through the outer mitochondrial membrane into the cytosol, and activates apoptosis upon translocation into the cell nucleus via chromatin condensation and DNA-fragmentation.¹⁰⁰⁻¹⁰² Alternatively, the release of cytochrome C from the mitochondria results in a caspase-dependent cascade that is initiated by a binding event between cytochrome C and the apoptotic protease-activating factor-1 (Apaf1).¹⁰³ This induces several conformational changes within Apaf1, leading to its oligomerization which is followed by recruitment and binding to the initiator caspase, caspase-9.¹⁰⁴ The complex between cytochrome C, Apaf1, and caspase-9 is often referred to as the apoptosome.¹⁰⁵⁻¹⁰⁶ Finally, the executioner caspase, caspase-3, is

activated by proteolytic cleavage, which in turn cleaves cellular substrates in order to induce apoptosis.¹⁰⁷⁻¹⁰⁹ As such, antibody detection of cleaved caspase-3 is considered a universal marker of caspase-dependent apoptosis.¹¹⁰⁻¹¹²

Activation of p53 in response to cell stress can also initiate cell cycle arrest of damaged cells.¹¹³ In the presence of low levels of DNA damage, p53 can initiate a reversible cell cycle arrest process, wherein the cell cycle is halted long enough to activate DNA repair mechanisms including nucleotide excision repair (NER), mismatch repair (MMR), and base excision repair (BER).¹¹⁴ However, if significant DNA damage is accumulated, a continued cell cycle arrest process is activated in order to remove damaged cells.¹¹⁵ Recent reports have demonstrated that p53 downregulates the expression of genes that are important for cell division, albeit in an indirect manner.¹¹⁶ Initially, activation of p53 leads to transcriptional upregulation of one of the most well-studied p53 targets, the cyclin-dependent kinase inhibitor, p21.¹¹⁷⁻¹²¹ Elevated levels of p21 promote binding to cyclin protein and cyclin-dependent protein kinase complexes cyclin E/Cdk2 and cyclin D/Cdk4, in order to cause cell cycle arrest at the G₁ phase, which is responsible for cell growth.¹²² This causes phosphorylation of proteins related to the retinoblastoma protein (pRB), p107 and p130.¹²³⁻¹²⁴ Phosphorylated p107 and p130 can then bind other proteins to form what is referred to as the DREAM complex, due to acronyms for proteins bound in this complex.¹²⁵ This complex represses genes involved in transcription in order to inhibit the progression into the S phase of the cell cycle where DNA is synthesized (Figure 1.8).¹¹⁶ Overall, various studies consider increased p21 expression to be a canonical marker of p53-mediated cell cycle arrest.¹²⁶⁻¹³⁰

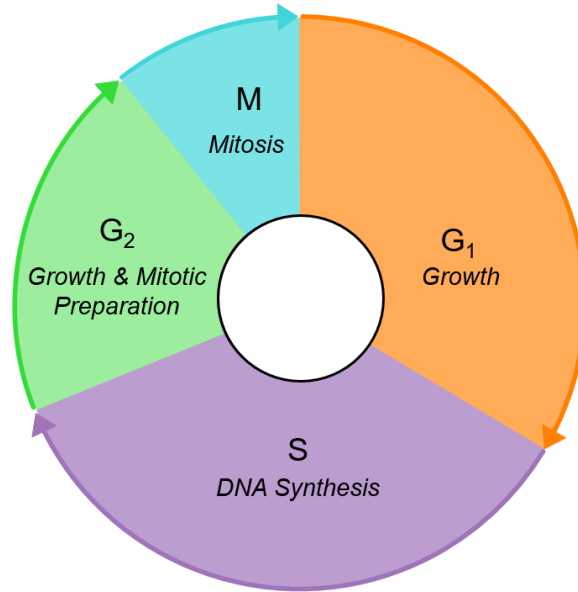


Figure 1.8. A schematic representation of the phases in the cell cycle.

Finally, p53 also plays a role in pathways such as angiogenesis and senescence, although these pathways are not as well understood.¹³¹⁻¹³³ Angiogenesis, the process in which new blood vessels are formed, is a critical process for the growth and mobility of tumours.¹³⁴ Briefly, p53 plays an important role in this process by inhibiting hypoxic regulators that normally produce blood vessels in order to increase the oxygen supply, and by transcriptionally upregulating genes that function to inhibit angiogenesis.¹³⁵⁻¹³⁶ Senescence, or cellular aging, is a process by which cells enter a permanent and irreversible state of cell cycle arrest, losing the ability to divide in response to growth factors.¹³⁷⁻¹³⁸ Induction of senescence by p53 can be triggered by many stimuli, including DNA damaging agents, oxidative stresses, and telomere shortening.¹³⁹⁻¹⁴⁰

1.4. Mutant p53 and Cancer

Commonly referred to as the “guardian of the genome”, p53 regulates a complicated cellular network, and as such, mutations resulting in its malfunction can have serious consequences.¹⁴¹ In fact, over 50% of cancer diagnoses result from point mutations directly to p53.¹⁴²⁻¹⁴³ Unlike most tumour suppressor genes, which typically exhibit deletions or truncations in cancer, p53 is frequently inactivated by a single missense mutation, wherein a single nucleotide is substituted for another, resulting in the coding of a different amino acid.¹⁴⁴ Mutations to both somatic and germline p53 genes

usually result in a loss of heterozygosity, which can inactivate the remaining wild type allele of p53 and lead to tumorigenesis.¹⁴⁵

1.4.1. Contact and Structural Mutations

More than 31,000 somatic mutations of p53 have been identified, 95% of which occur in the DNA-binding domain.¹⁴⁶ The most frequently mutated sites in p53C, termed cancer “hot spots”, are located directly near the DNA-binding site and are characterized as either contact or structural mutations.^{70, 147} Contact residues are those amino acids that bind DNA directly and mutations within these sites alter the p53-DNA interaction. The most frequently mutated contact sites are at amino acid residues 248 and 273 and include hot spot mutants R248W, R273H, and R273C (Figure 1.9). These mutants exhibit relatively little change to the overall structure and stability of the protein, but rather promote loss of function (LoF) due to weakened interactions with DNA.⁵⁹ For example, the p53 mutant R273H, where the essential DNA-contact amino acid Arg273 is replaced by histidine, exhibits a 1000-fold decreased affinity for DNA in *in vitro* experiments and thus the resulting p53-DNA interaction is too weak to activate transcriptional activity.¹⁴⁸⁻¹⁴⁹

p53 structural mutations, however, induce conformational changes within the protein that can result in loss of function for a variety of reasons. For example, structural hot spot mutations G245S and R249S (Figure 1.9) induce conformational changes within the L3 loop that stabilize inactive conformations and hinder DNA binding.⁵⁹ Further, given that p53C is relatively unstable at biological temperatures, any mutation that lowers the stability will have a substantial effect on the folded state of the protein.¹⁵⁰ Arg282 is important to the structural stability of p53C via hydrophobic interactions and hydrogen bonding networks, and the hot spot R282W (Figure 1.9) results in a loss of these important interactions, resulting in significantly decreased stability (3 kcal/mol) and enhanced protein aggregation.^{59, 72} One of the most common structural p53C mutations is R175H (Figure 1.9), which perturbs the Zn²⁺ binding site to cause a loss of Zn²⁺, thereby decreasing the thermodynamic stability of the protein, inhibiting DNA binding, and enhancing protein aggregation.¹⁵¹⁻¹⁵² Interestingly, apo p53C (zinc-free) increases the aggregation process via nucleation with zinc-bound p53C. Finally, outside of the direct DNA-binding surface, the most frequently occurring mutation is Y220C (Figure 1.9).¹⁵³ Located in the β -sandwich region of p53C, the substitution of tyrosine for cysteine in Y220C affects the structural nature of the protein by creating a solvent-accessible cavity at the surface. This reduces

protein stability by lowering the melting temperature, causing the protein to rapidly unfold and aggregate at biological temperatures.¹⁵⁴ The aggregating nature of such p53 mutations have been reported to exhibit gain of function (GoF) effects in addition to loss of function (LoF), a characteristic that has elicited significant attention in recent years.^{146,}

155-156

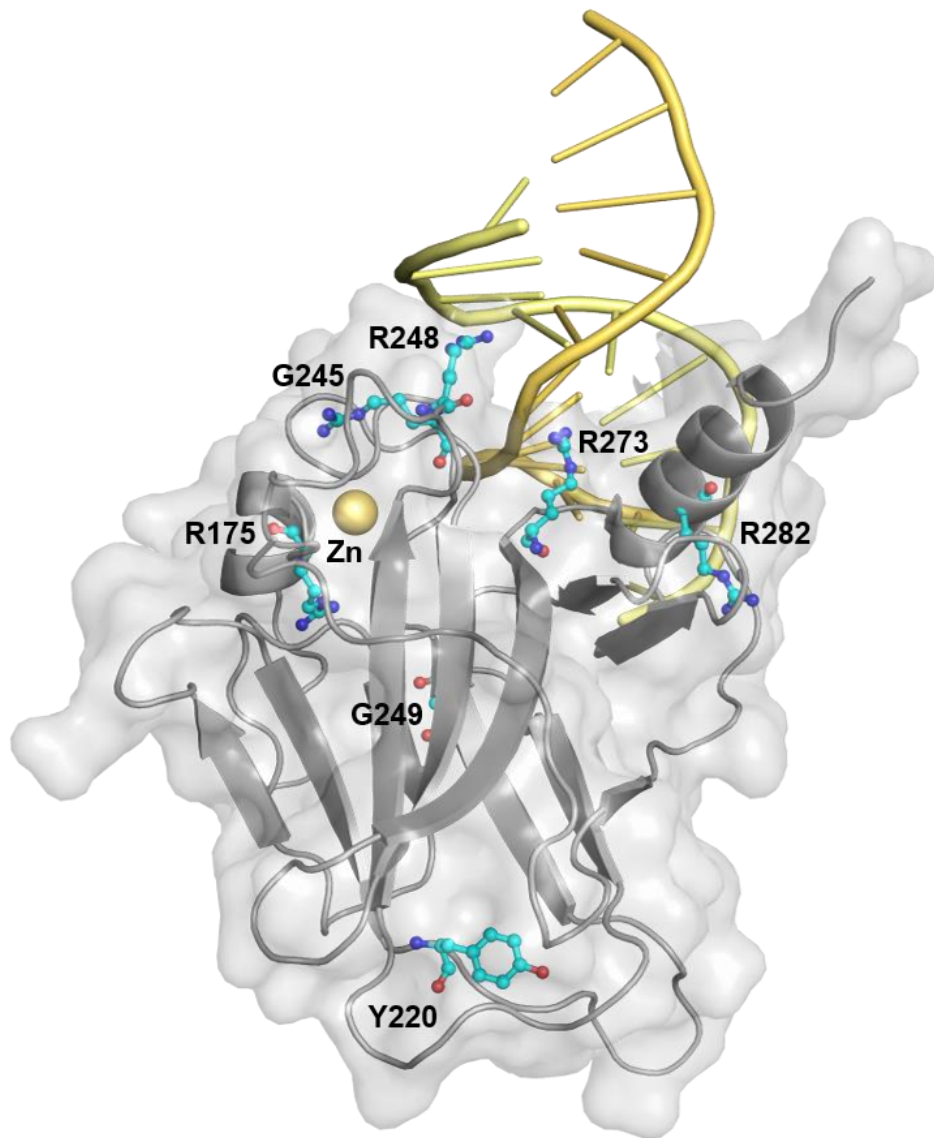


Figure 1.9. p53C bound to DNA (yellow). Locations of amino acids 175, 220, 245, 248, 249, 273, and 282, sites of key hot spot carcinogenic mutations, are shown (PDB ID: 4AGL).

1.4.2. Mutant p53 and Aggregation

Protein misfolding diseases are largely caused by peptides or proteins in pathophysiological states wherein they no longer adopt their native, folded conformation.¹⁵⁷ The most common group of protein misfolding diseases are those that undergo endogenous misfolding from a soluble, folded protein into alternative oligomeric and fibrillar structures via a partially unfolded intermediate.¹⁵⁸ Referred to as amyloids, these proteins are a hallmark characteristic of many neurodegenerative diseases.¹⁵⁹ Studies have shown that cancer also is characterized by amyloid aggregates through the misfolding and aggregation of p53, as amyloid aggregates have been identified in both tumour cell lines and patient biopsies.^{156, 160-161} p53 aggregation has been correlated with tumour growth as higher degrees of aggregation have been associated with more invasive tumours.¹⁶² Folding of p53 is driven by thermodynamic and kinetic factors and requires the assistance of molecular folding chaperones.¹⁶² Malfunctions within this process can result in the protein adopting other low energy conformations including amyloid fibrils. Current hypotheses on the contributions of mutant p53 in aggregation describe structural mutations that initially destabilize the native structure, which exposes a known aggregation-prone sequence within the DNA binding domain, termed the amyloidogenic region, that is normally buried within the protein's core. Upon exposure, this hydrophobic segment is exposed and can bind other p53 molecules and cause aggregation.¹⁶³

Mutant p53 aggregates are characterized not only by loss of function (LoF), but further exhibit dominant negative (DN) and gain of function (GoF) effects.¹⁶⁴ While their mutant status largely contributes to their LoF, aggregate formation is typically accompanied with sequestration into the cytoplasm, thereby inhibiting its nuclear activation. Mutant p53 also exerts a DN effect, both by forming a heterotetramer with wild-type p53 to inhibit its activation and by co-aggregating with wild-type p53 to inhibit its function.¹⁵⁵ Finally, p53 has also been extensively characterized to possess toxic GoF properties by self-propagating and cross-reacting with other proteins to further aggregation.¹⁶⁵ Most notably, mutant p53 aggregates can co-aggregate with homologous proteins, p63 and p73, to form amyloid oligomers and fibrils and thereby inhibit their function.¹⁶⁵ Overall, these properties have characterized p53 as an amyloid-associated disease, however, further studies to elucidate the mechanism of aggregation and GoF effects will be an important area of study moving forward.¹⁴⁶

1.5. Therapeutic Intervention of p53 Malfunction

Given that 50% of cancer diagnoses contain mutant p53 and that nearly all cancers exhibit malfunction along the p53 pathway, there is significant research that focuses on the development of p53-based chemotherapeutics.^{145, 166} While there is an extensive body of research with elegant biological methods for targeting malfunctioning p53 in tumours including gene therapy (eg. Gendicine)¹⁶⁷⁻¹⁶⁸, which delivers a functional copy of TP53 via an adenovirus, removal of mutant p53 via administration of a silencing RNA that targets p53 (sip53)¹⁶⁹, and the design of peptide vaccines (eg. p53-SLP) for p53 immunotherapy¹⁷⁰, the following survey of treatment strategies for p53 will focus specifically on small molecules that target both wild-type and mutant p53.

1.5.1. Inhibition of the p53-MDM2 Interaction

Despite the frequency with which p53 mutations occur in cancer, tumours frequently possess WTp53 but exhibit impaired p53 signaling due to mutated protein partners and other dysregulations within the p53 pathway.¹⁷¹ For example, many tumours have been characterized by increased degradation of p53 due to increased MDM2 activity, thus limiting p53 activation.¹⁷² As a result, the design of small molecules that block the p53-MDM2 complex to allow for accumulation of functional p53 is a highly sought-after strategy.¹⁷³ One of the first classes of p53-MDM2 inhibitors was discovered from a large chemical screen that identified potent cis-imidazoline small molecules termed Nutlins.¹⁷⁴ Nutlin-3, commonly referred by its most potent enantiomer¹⁷⁵, Nutlin-3a (Figure 1.10 a), selectively inhibits the p53-MDM2 interaction by imitating the p53 amino acids involved in MDM2 binding. Nutlin-3a induces significant upregulation of p21, causing cell cycle arrest at the G₁ phase and induces p53-dependent apoptosis in a number of cancer cell lines and xenograft models.¹⁷⁶ A derivative of Nutlin-3a, RG7112 (Figure 1.10 b), has been pharmacologically optimized for oral administration and has exhibited p53-dependent activity in clinical trials.¹⁷⁷ Driven by optimized stereochemical configurations within the X-ray crystal structure of MDM2, Ding *et al.* reported a modified class of MDM2-binding inhibitors adopting a *trans* geometry at the scaffold's core.¹⁷⁸ The lead compound in the study, RG7388 or Idasanutlin (Figure 1.10 c), exhibited significantly increased potency over previous inhibitors and induces p53-dependent cell cycle arrest and apoptosis. It is

currently the only p53-MDM2 inhibitor to have surpassed phase II clinical trials and is currently undergoing phase III clinical studies.¹⁷⁹

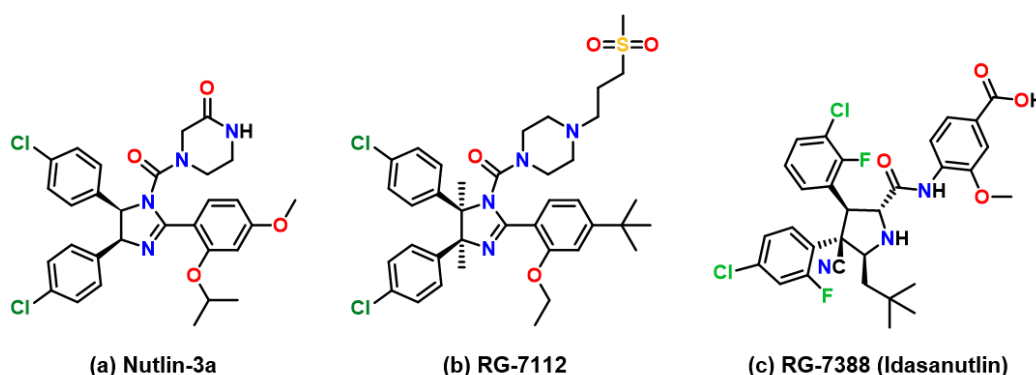


Figure 1.10. Family of small molecules termed Nutlins, reported to activate WTp53 by inhibiting the p53-MDM2 complex in order to prevent MDM2-mediated degradation of p53 and allow for accumulation of functional p53.

Other classes of p53-MDM2 inhibitors include spiro-oxindoles, which were pioneered by Wang *et al.* Upon extensive analysis into the X-ray structure of the p53-MDM2 complex, it was noted that the indole ring of Trp23 in p53 was key to the interaction of p53 within the hydrophobic cleft of MDM2.¹⁸⁰ As such, they designed a class of oxindole containing small molecules that could imitate this binding interaction. The lead compound in this study, compound 1d (Figure 1.11 a), had a nanomolar affinity for MDM2 that was 18-fold more potent than the p53 peptide used as a control. Spiro-oxindoles as MDM2 inhibitors have since undergone extensive structure modifications over the past decade and several potent analogues have undergone preclinical and clinical studies.¹⁸¹⁻¹⁸³ One of the most potent analogues to date, SAR405838 (Figure 1.11 b), exhibits sub-nanomolar binding to MDM2, allowing for activation of wild-type p53 both in cancer cell and xenograft models and is currently showing promising results in phase I clinical studies.¹⁸⁴ Finally, RITA (Figure 1.11 c) is a potent small-molecule inhibitor of the p53-MDM2 complex, however, in contrast to the previously mentioned small molecules, RITA inhibits the protein-protein interaction by binding p53, rather than MDM2. RITA activates p53 and induces apoptosis by binding p53 in the N-terminus and inducing a conformational change, thereby preventing its degradation via binding of MDM2.¹⁸⁵

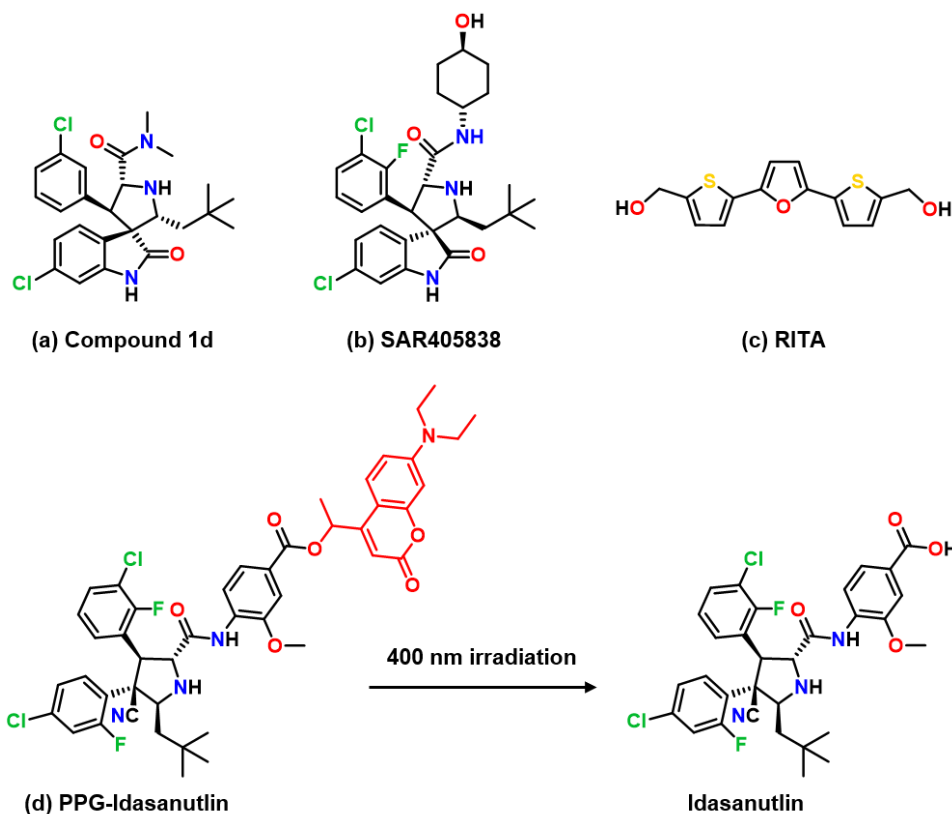


Figure 1.11. Small-molecule p53-MDM2 inhibitors that activate p53.

Overall, inhibitors of the p53-MDM2 complex hold significant promise as potent small molecules that target and activate the p53 pathway. However, a clinical drawback of p53-MDM2 inhibitors is the potential lack of selectivity over non-cancerous cells.¹⁸⁶⁻¹⁸⁷ Given that these compounds target activation of WTp53, the potential toxicities of activating p53 in normal cells must be considered.¹⁷¹ In fact, it has been demonstrated that accumulation and activation of p53 in normal cells can induce apoptosis and senescence in all cells in mice.¹⁸⁶ Interestingly, a recent study by Feringa *et al.* reported the addition of a photoswitch or photoremovable protecting group (PPG) to Idasanutlin (Figure 1.11 d) to increase the selectivity in cancerous tissues.¹⁸⁸ By appending a PPG, it allows for selective and localized activation of p53 in cancerous tissues using 400 nm light. This proof-of-concept study represents a promising avenue for overcoming the drawbacks that may occur as a result of activating p53 in normal cells. Other potential off-target effects of concern with MDM2 inhibitors are that it may interfere with its role in DNA repair and could inhibit its ability to ubiquitinate other important proteins, representing an avenue for further research and improvement moving forward.¹⁸⁷

1.5.2. Restoration of Wild-type p53 Function

p53 is the most frequently mutated protein in human cancer.¹⁴²⁻¹⁴³ Mutations are present in 96% of ovarian serous carcinomas, 85% of small cell lung cancers, and 75% of pancreatic cancers, as examples, and are also associated with worsened prognosis and patient survival.¹⁸⁹ Further, mutant p53 is a highly abundant and tumour-specific target as it is typically overexpressed in cancer, partly as a result of its inability to activate MDM2 in order to regulate its expression. As a result of its overexpression, mutant p53 also possesses toxic GoF properties that can propagate and cause malfunctions to other important proteins and pathways that regulate the cell cycle.¹⁴⁵ Considering the above factors, mutant p53 represents an important pharmacological target and the past two decades have seen considerable dedication to the development of small molecules that aim to restore wild-type function in mutant p53.^{166, 190-191} Among the small molecules developed, numerous mechanistic strategies have been developed including protein refolding via cysteine modification, protein stabilization, modulation of protein aggregation, and zinc chelation, and will be explored in detail below.

Protein Refolding via Cysteine Modification

Cysteine reactivity plays an important role in many biological functions including oxidatively controlled protein folding, and thus thiol modification is a frequent target for medicinal chemists.¹⁹²⁻¹⁹³ The first small molecule discovered to reactivate wild-type function in mutant p53 was CP-31398 (Figure 1.12 a). In their contribution to *Science*, Rastinejad *et al.* reported a small molecule that restored native p53 conformation in cells with mutant p53, allowing for activation of transcriptional activity and slowed tumour progression in xenograft models.¹⁹⁴ Later studies investigating the mechanism of action suggested that the reactive double bond could function as a Michael acceptor, implying that at least part of its mechanism involved modification of p53 cysteine residues in order to promote refolding.¹⁹⁵⁻¹⁹⁶ CP-31398 was investigated in pre-clinical studies, but it did not advance to clinical trials in part due to significant reports of p53-independent activities and multiple off-target effects.¹⁶⁶ PRIMA-1 and its more potent methylated analogue PRIMA-1^{Met} (Figure 1.12 b,c), commonly referred to as APR-246, were discovered in a screen at the National Cancer Institute and restore wild-type function in the p53 mutants R175H and R273H, and inhibit tumour growth in xenograft mice.¹⁹⁷ Reports on the mechanism of action of APR-246 indicate that upon hydrolysis, it is converted to the active Michael

acceptor methylene quinuclidinone (MQ), which covalently binds cysteine residues in p53, in particular Cys124 and Cys277, and promotes refolding into its active conformation.¹⁹⁸ APR-246 was the first p53-reactivating small molecule to enter clinical development and is currently in phase II clinical studies.¹⁹⁰ Fersht and coworkers also developed a series of cysteine-targeting small molecules that reactivate mutant p53. PK11007 (Figure 1.12 d) is part of this series of 2-sulfonylpyrimidines that alkylate the thiols of solvent-accessible cysteines Cys182 and Cys277 and promote refolding to restore function in mutant p53-Y220C.¹⁹⁹ PK11007 is currently being investigated in preclinical studies.¹⁶⁶

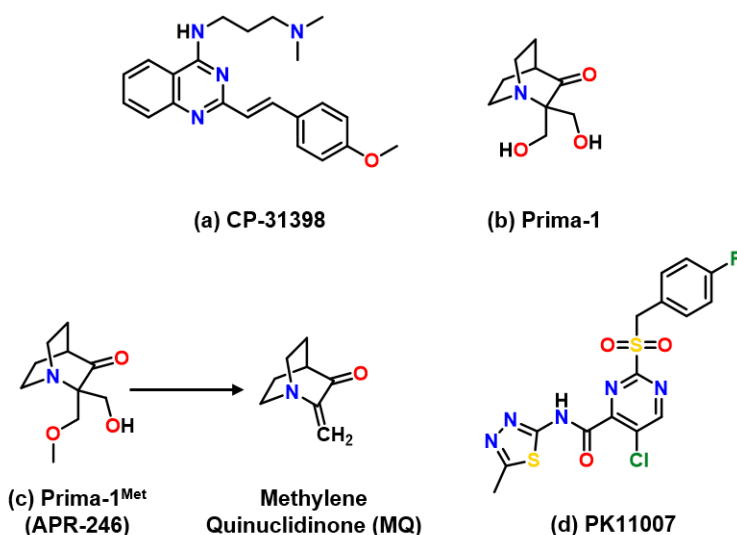


Figure 1.12. Small molecules that restore wild-type function in mutant p53 via thiol alkylation and cysteine modification to promote protein refolding.

Thermal Stabilization of Mutant p53

Structural mutations in the DNA-binding domain of p53 destabilize the local environment, causing protein unfolding and aggregation. An estimated 30% of p53 mutations are temperature sensitive, wherein they are unfolded and inactive at physiological temperatures yet exhibit a native fold to induce functional DNA-binding and transcriptional activity upon lowering to sub-physiological temperatures.²⁰⁰⁻²⁰¹ As such, researchers have proposed that small molecules that selectively bind the folded conformation over unfolded conformations should shift the equilibrium towards a folded and active wild-type protein conformation.²⁰⁰ In one of the most common thermally unstable mutants, p53-Y220C, the substitution from a large tyrosine to a smaller cysteine creates an open cavity at the surface of the protein, lowering its stability and causing ~80% unfolding.¹⁵³ Fersht and coworkers have generated a library of small molecules that target

the mutant-induced cavity of p53-Y220C in order to increase stability and restore wild-type function. Using *in silico* methods and fragment-based screening, the first of such compounds discovered was PhiKan083 (Figure 1.13 a). This compound exhibited moderate binding (150 μ M) to the p53-Y220C mutant and thermally stabilized the protein by raising its T_m by 2 $^{\circ}$ C.²⁰² PhiKan7088 (Figure 1.13 b) also exhibited modest binding within the p53-Y220C mutant cavity (140 μ M), and was shown to refold mutant p53 using conformation-specific antibodies and activated p53-dependent apoptosis and cell cycle arrest.²⁰³

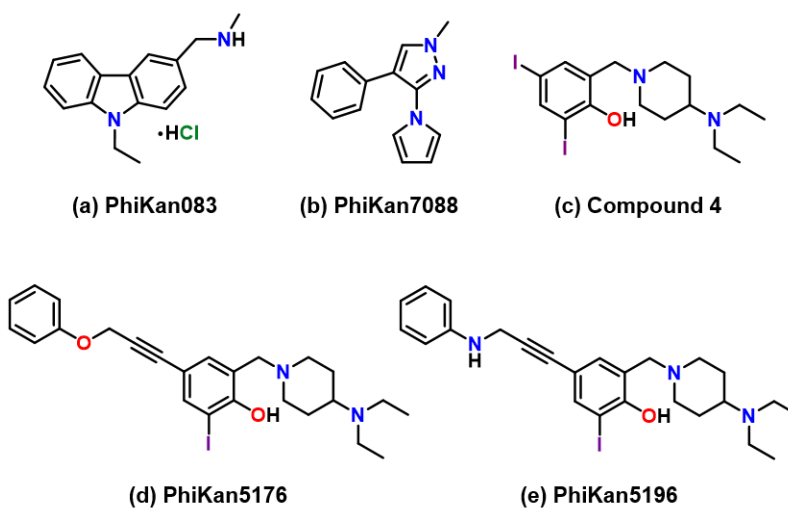


Figure 1.13. Small molecules that restore wild-type function in mutant p53 via thermal stabilization of the mutant induced p53-Y220C cavity.

Interestingly, a series of small molecules with a diiodophenol core discovered from a screening library showed improved binding to the Y220C mutant pocket (Compound 4, 105 μ M) and showed improved thermal stabilization of the mutant protein (Figure 1.13 c).¹⁵³ Based on the X-ray crystal structure, these compounds exhibit halogen bonding interactions with the carbonyl oxygen of Leu145 located within the mutant cavity. Substitution of both iodine atoms with chlorine and bromine significantly lowered the binding affinity, highlighting the importance of the halogen bonding interaction in protein binding. These compounds were structurally modified with varying acetylene linkers to extend the small molecules further into the mutant pocket, which significantly improved the binding affinity of the ligands (PhiKan5176: 21 μ M, PhiKan5196: 10 μ M) and activated mutant-specific apoptosis (Figure 1.13 d,e).

Modulating Mutant p53 Aggregation

The classification of p53 as an amyloidogenic protein is relatively recent, and important information elucidating the detailed mechanisms of p53 aggregation and GoF effects remains to be discovered.²⁰⁴ As such, it is often overlooked by cancer and amyloid researchers alike, leaving the field relatively in its infancy.¹⁴⁶ However, its involvement in cancer development has been well documented, and amyloid aggregates have been identified in patient biopsies of various cancers and are associated with more aggressive and invasive tumours.^{162, 205} This highlights the importance and need for small molecules aimed to disrupt p53 aggregation and prevent GoF effects. Although not a small molecule, a recent seminal study involving a small cell-penetrating peptide sequence, ReACp53, pioneered the concept that modulating p53 aggregation was a viable option for restoring p53 function. The peptide sequence of ReACp53 is a close mimic of the aggregation-prone sequence in p53 and could bind and prevent aggregation of p53 in cells, and caused upregulation of p63 levels, thereby alleviating its toxic GoF effects. This led to rescued function in p53 mutants R175H and R248Q via induction of apoptosis and led to decreased tumour proliferation in xenograft models.¹⁶³

Other small molecules aimed to modulate p53 aggregation have since emerged, including resveratrol and emodin. Resveratrol is a stilbenoid, a type of naturally occurring phenol in plants (Figure 1.14 a).²⁰⁶ Recent reports demonstrate that this compound slows the aggregation rate of both WTP53 and p53-R248Q *in vitro* using intrinsic tyrosine fluorescence and light scattering. Further, using immunofluorescence staining, resveratrol was able to reduce staining with an oligomeric-specific antibody (A11) in both mutant p53 cancer cell lines and tumour tissues from a xenograft model, indicating a reduction in mutant p53 aggregation. By limiting mutant p53 aggregation, resveratrol reduced the proliferative and migratory ability in the cancer cell lines.²⁰⁷ Emodin, a naturally occurring anthraquinone, was also tested for its ability to modulate p53 aggregation (Figure 1.14 b).²⁰⁸ This compound was able to reduce staining with Thioflavin S in cancer cells via immunofluorescence, although only moderately, indicating a reduction in the level of aggregated p53. Interestingly, this was coupled with activation of autophagy, which is a cellular regulatory mechanism that degrades and removes unnecessary or dysfunctional components in order to maintain homeostasis.²⁰⁹ The authors hypothesize that autophagy may be the mechanism whereby remaining p53 aggregates are removed upon restoration of p53 function with emodin treatment.

p53 aggregates have been well characterized to possess toxic GoF properties and can co-aggregate with p53 family members p63 and p73 to inhibit their function. As such, an interesting alternative strategy when targeting mutant p53 aggregation is to directly target the aggregated p53/p63 or p53/p73 complex to alleviate GoF effects and restore p63/p73 function.¹⁴⁵ Given the sequence homology of the p53 family members, restoration of p63 and p73 function can result in transcription-mediated apoptosis and cell cycle arrest.²¹⁰ RETRA, which stands for reactivation of transcriptional reporter activity, was identified using a cell-based screen that identified compounds that restored transcriptional activity in mutant p53 cell lines (Figure 1.14 c). RETRA functions by releasing and blocking p73 from the inhibitory complex with mutant p53, thereby inducing p73-mediated apoptosis and cell cycle arrest. Promisingly, RETRA is active against a variety of cell lines with mutant p53 yet does not affect normal cells.²¹¹

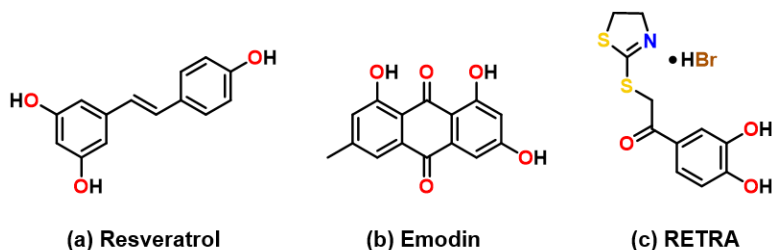


Figure 1.14. Small molecules that restore wild-type function in mutant p53 by preventing and modulating aggregation or by disrupting the p53/p73 aggregated complex.

Restoring Zinc-Binding in Mutant p53

Zinc is crucial to the structural stability of p53 and plays a major role in preserving its folded structure and facilitating DNA binding.⁵⁹ At physiological temperatures, mutants that perturb that zinc binding site and result in apo (zinc-free) p53C are primarily unfolded, prone to aggregation, and result in a loss of sequence-specific DNA binding.²¹² Interesting reports have demonstrated that manipulation of zinc concentrations within the cell can change the structure and function of p53, alluding to the reversible nature of the protein's fold.²¹³ Specifically, Milner and co-workers demonstrated that the addition of zinc chelators to cells and cell lysates to deplete p53 of zinc reduces its ability to be recognized by wild-type-specific antibodies and increases its recognition using a mutant-specific antibody.²¹⁴ This process can be reversed by supplementing the cell culture media with ZnCl₂. In fact, D'Orazi and co-workers showed that treatment with ZnCl₂ restores native p53 folding in zinc-binding mutants and restores wild-type transcriptional activity.²¹⁵ While high

concentrations of ZnCl_2 can be harmful to the cell,²¹⁶ it serves to highlight the potential clinical applications of restoring zinc-binding in mutant p53. This group has since designed a series of fluorescent zinc-curcumin complexes that restore the native conformational fold and activate function in the zinc-deficient mutants p53-R175H and p53-R273H (Figure 1.15 a).²¹⁷⁻²¹⁸ Significant research attention has now been devoted to the design of small molecules that act as metallochaperones to restore native zinc binding in mutant p53.²¹³

Loh and others have identified properties that are important when considering the design of zinc metallochaperones for mutant p53.²¹³ Given that insufficient levels of zinc result in protein misfolding and impaired DNA binding, the first criteria is that the metallochaperones must increase intracellular levels of Zn^{2+} in order to repopulate the metal-depleted mutant p53 site.²¹⁹ While the majority of intracellular zinc is bound to cytosolic Zn-binding proteins, the pool of “free Zn^{2+} ” is estimated to be in the nanomolar to picomolar range.²²⁰ However, reports have also demonstrated that excess levels of zinc induce protein misfolding via zinc binding to non-native amino acids located near the zinc binding site.²²¹ Referred to as K_{d1} , the native Zn^{2+} affinity for WTp53 is estimated to be on the order of 10^{-12} M, whereas the affinity for non-native sites, K_{d2} , is estimated to be on the order of 10^{-6} M.²²²⁻²²³ As such, the second criteria for the design of zinc metallochaperones is that they must function as a sink to prevent excess zinc accumulation. In general, they should have zinc affinities between that of K_{d1} and K_{d2} in order to buffer appropriate zinc concentrations.²²⁴ Finally, by repopulating the native zinc binding site, the third criteria is that the metallochaperones must activate wild-type p53 function.²¹⁹

A series of zinc metallochaperones that fit the criteria mentioned above were discovered using the National Cancer Institute’s anticancer drug screening data. With the aim of discovering compounds that were selectively active against cell lines harbouring p53 mutations, a series of thiosemicarbazones were identified to exhibit selective cytotoxicity against one of the most common p53 mutations, R175H.²²⁵ Initial studies focused on the identified compound NSC319726, later termed ZMC1 (Figure 1.15 b), and determined that it could restore WT structure and function in mutant p53-R175H and activate apoptosis in mutant p53 xenograft models. Given the impaired zinc-binding in p53-R175H, it was proposed that the mechanism of ZMC1 involved zinc chelation and redistribution.²²² Further investigations determined that ZMC1 had a nanomolar affinity for zinc and could form a neutral 2:1 complex with zinc wherein it could passively diffuse through the cell as a zinc ionophore.²¹⁹ Upon passage through the cell membrane, the

ligands are protonated, causing a dissociation of the complex, thereby increasing intracellular Zn^{2+} levels and restoring zinc binding in mutant p53. Recent studies have demonstrated that two other compounds identified in the study, ZMC2 (Figure 1.15 c) and ZMC3 (Figure 1.15 d), function via the same mechanism.²²⁶

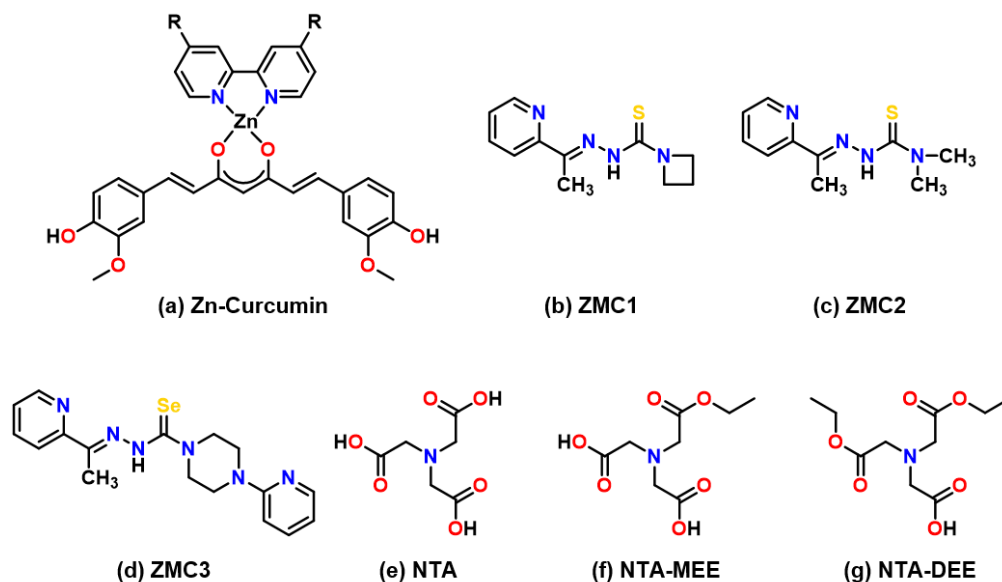


Figure 1.15. Small molecules that restore wild-type function in mutant p53 by serving as metallochaperones and restoring native zinc binding.

Interestingly, another mechanism of the ZMC1-3 compounds is the generation of reactive oxygen species (ROS). ZMC1-3 have a high affinity for other transition metals such as iron and copper, and have been shown to generate intracellular ROS through Fenton-like chemistry by chelating redox-active Fe and Cu.²²⁴ The production of ROS generates a kinase-dependent stress response that induces post-translational modifications to the now refolded p53 in order to initiate transcriptional activity.²²⁷ While the activation of PTMs is ultimately beneficial to the p53-dependent nature, generating high levels of ROS can also lead to off-target effects and general toxicity. In fact, recent studies investigating the potential synergism between ZMC1 and traditional chemotherapies found that the ROS generated by copper chelation with ZMC1 was too toxic, as synergism with traditional chemotherapies or radiation could only be observed upon treatment with ROS scavengers such as glutathione.²²⁴ The binding affinity of ZMC1 for Cu^{2+} was determined to be 10^8 -fold greater than that of Zn^{2+} , and thus they designed cell permeable derivatives of nitriloacetic acid (NTA), which exhibited significantly lowered affinity for copper and exhibited synergistic activity with chemotherapies (Figure 1.15 e-

g). As a result of this study, the authors concluded that an additional property of zinc metallochaperones for mutant p53 is that they must generate enough ROS to activate PTMs on p53 but avoid toxic side effects generated by high affinities for copper.

Overall, these studies serve to indicate the important and complicated role of zinc in p53, and how careful tuning of both the zinc affinity and the affinity for other endogenous metals is critical for on-target mutant p53 activation. This applies to biological systems in broader terms, as transition metals including copper, zinc, iron, and manganese are vital for the proper function of many cellular processes and their dysregulation is highly implicated in cancer.²²⁸⁻²²⁹ As such, the design of small molecules for targeted metal ion chelation and redistribution has been a complex yet effective ongoing anti-cancer strategy.²³⁰⁻²³²

For example, Franz and coworkers designed an elegant pro-chelator to selectively target overexpressed toxic copper ions in prostate cancer.²³³ Disulfiram is a known drug that yields dithiocarbamate (DTC) upon reduction, which is an efficient metal chelator due to the reactive thiols generated and has been studied in clinical trials as an anticancer compound.²³⁴ However, due to a lack of specificity for cancer cells, significant toxicity was observed in a Phase II clinical study. As such, the Franz group designed a pro-chelator of DTC, GGTDTC (Figure 1.16 a), that requires activation by γ -glutamyl transferase (GGT), an enzyme that is overexpressed and differentially located in many cancer types. Upon site-selective cleavage of the amide bond in GGTDTC by this overexpressed enzyme, DTC is released to chelate excess copper. The cytotoxicity of GGTDTC is both copper and GGT dependent, showing the significant promise of selective pro-chelators for copper chelation in cancer.²³³

The Richardson group has devoted extensive research efforts into the design of small-molecule metal chelators for anticancer therapy over the last two decades.²³⁵ Recent mechanistic studies provide insight into the redox activity of some of their most cytotoxic compounds, including the thiosemicarbazone di-2-pyridylketone 4-cyclohexyl-4-methyl-3-thiosemicarbazone (DpC), which entered clinical trials in 2016 (Figure 1.16 b).²³⁶ Interestingly, using fluorescent zinc complexes of DpC, they demonstrated that the zinc thiosemicarbazones complexes localized to the lysosomes, wherein lysosomal conditions induced transmetallation with copper ions. The copper complexes then provided sufficient redox activity that resulted in cytotoxicity via lysosomal membrane permeabilization. This

study provided novel details regarding the mechanistic ability of zinc thiosemicarbazone complexes to localize to the lysosomes and transmetallate with copper.²³⁷

Recent fluorescent-based studies have indicated that intracellular levels of labile iron are increased in several cancer types, prompting the design of small-molecule iron chelators as anticancer agents.²³⁸⁻²³⁹ Among others, Tomat and coworkers have designed several classes of thiosemicarbazones as effective iron chelators for cancer therapy, including a class of redox-active pro-chelators.²⁴⁰ This class of thiosemicarbazones that feature the (S,N,S) donor sets, termed the TC series, feature a disulfide bond that acts as a reduction/activation switch for a pro-chelation approach (Figure 1.16 c). Upon entry into the highly reducing tumour microenvironment, electron paramagnetic resonance (EPR) studies revealed that the disulfide bond is reduced to afford to tridentate iron chelators that form low-spin Fe(III) complexes inside the cancer cells. This resulted in activation of cell cycle arrest at the G₁/S phase and an induction of apoptosis.²⁴¹ Several derivatives of this class of iron pro-chelator have since been developed, including the addition of carbohydrate moieties to target the increased expression of glucose transporters in colorectal cancers.²⁴²

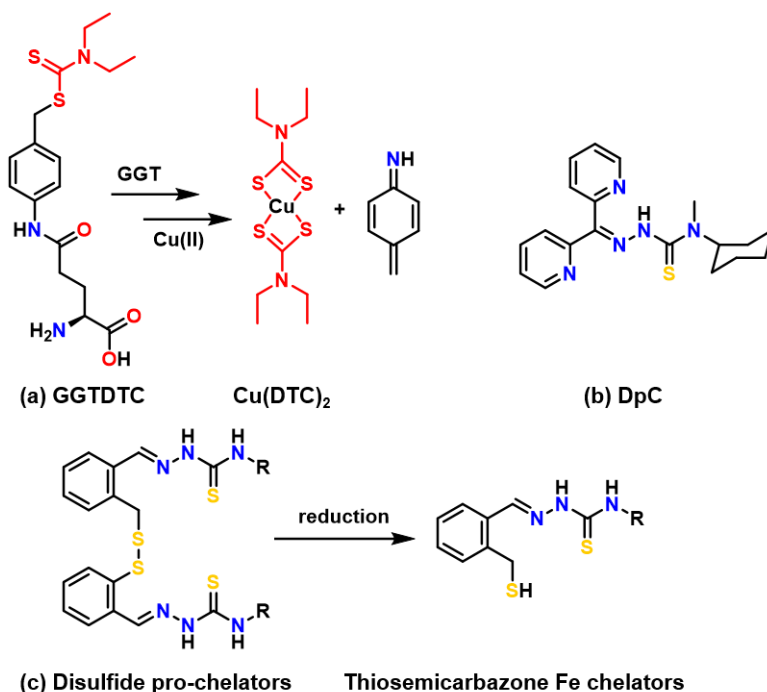


Figure 1.16. Small molecules used as chelators for targeted metal ion chelation and redistribution in cancer therapy.

Overall, the homeostasis of bio-metals is an essential yet complicated process, and dysregulation of these metals and its role in diseases, including cancer, has driven extensive research efforts into the design of small-molecule metal chelators. While these chelators hold significant promise in anticancer therapy, studies have shown that they benefit from co-administration with other anticancer drugs, and thus moving forward the design of multifunctional compounds wherein cytotoxic or targeting moieties are appended to metal chelators could significantly enhance their selectivity and overall efficacy.²³⁰

1.6. Thesis Synopsis

The frequency and aggressive nature of cancers with mutant p53 has driven a widespread effort both in academia and the pharmaceutical industry to restore functional activity in mutant p53 over the past decades. Of further interest, a large study conducted at the National Cancer Institute with 60 cancer cell lines and over 100 anticancer drugs showed significant correlation between mutant p53 and developed resistance to common chemotherapeutics.²⁴³ For example, clinically used DNA-damaging drugs such as doxorubicin and the platinum complexes depend, at least in part, on functional p53 via activation of p53-mediated cell death following generation of DNA damage.²⁴³⁻²⁴⁵ As a result, many cancers possessing mutant p53 exhibit an increased resistance to such treatments. Other studies have indicated that p53 aggregation causes platinum chemoresistance in specific cancers and indicate that inhibiting p53 aggregation could reverse the chemoresistance.²⁴⁶ This provides a further opportunity for small molecules that restore p53 function to exhibit enhanced efficacy and overcome resistance via a synergistic mechanism by co-administration with clinically approved DNA-damaging agents.²⁴³

Previous efforts to restore function in mutant p53, while of significant promise, have been monofunctional in design, targeting specific characteristics of a given p53 mutant including thermal denaturation, aggregation, or loss of zinc. However, given the multifaceted nature of p53 mutants, it is my opinion that these mutants provide a unique opportunity to design multifunctional molecules that act on different aspects of mutant p53 occurring simultaneously for increased chemotherapeutic efficacy. For example, the common hotspot mutant p53-Y220C is prone to thermal denaturation yet exhibits accelerated aggregation and is prone to loss of zinc, all of which contribute to the loss of protein function. Using p53-Y220C as a proof-of-concept mutant, the overarching goal of

this thesis is to design multifunctional small molecules that use a combination of targeting moieties to restore wild-type function in mutant p53. A general overview of p53 function and the opportunities for therapeutic intervention are shown in Figure 1.17.

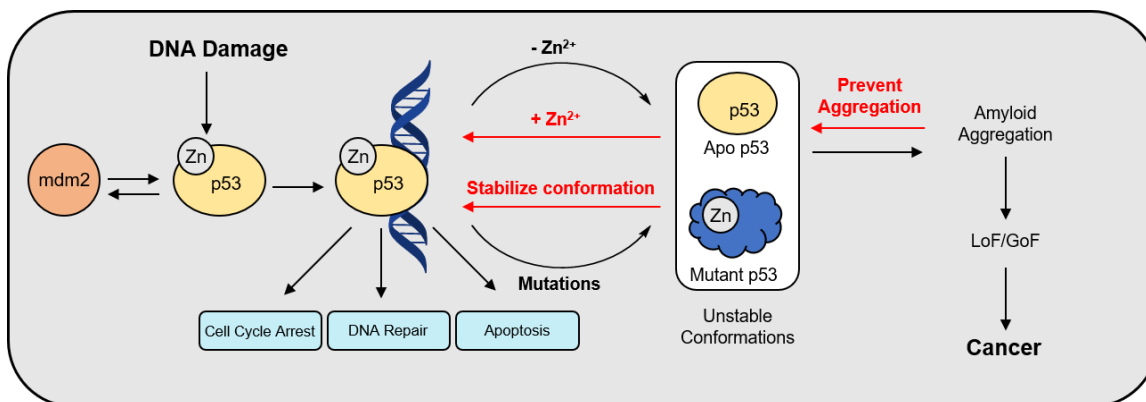


Figure 1.17. Overview of p53 function and the opportunities for therapeutic intervention (shown in red). In response to DNA damage, MDM2 allows for upregulation of p53 in order to carry out various cell death or cell repair mechanisms. However, both the loss of zinc and mutants causing unstable conformations lead to loss of protein function and provide an opportunity for aggregate formation. p53 aggregates are toxic species associated with both loss of function and gain of function and contribute to cancer development.

Chapter 2 describes a 1st generation scaffold that aims to restore wild-type p53 function by increasing mutant protein stability. The ligand design features a combination of iodinated phenols reported by Fersht *et al.* to interact with and stabilize the p53-Y220C surface cavity¹⁵³, and Zn-binding fragments for metallochaperone activity to restore stability via zinc binding. Given the importance of zinc in the human body and its involvement in many biochemical processes, the design and use of zinc chelators is ubiquitous in bioinorganic chemistry.²⁴⁷ While various structurally diverse moieties have been reported and extensively reviewed,²⁴⁸⁻²⁵² Lippard and co-workers highlight key features for effective chelation of mobile zinc: (1) chelators must exhibit a specificity for zinc over other biologically abundant metal ions such as Ca²⁺ (2) the chelator must be neutral for intracellular application and possess sufficient hydrophobicity to passively diffuse through the cell membrane (3) the pK_a of donor atoms should be below physiological pH for rapid Zn binding and (4) chelators need to bind mobile Zn with appropriate affinity while minimizing chelation from the large number of human zinc proteins.²⁵³ With these criteria in mind, the nitrogen-rich chelators 2-amino pyridine and di-(2-picolyl)amine were incorporated into the ligand design. di-(2-picolyl)amine is

reported to have high zinc affinity and has been incorporated into the structure of many fluorescent zinc probes,²⁵⁴⁻²⁵⁵ including those designed for quantification of cellular zinc, thus demonstrating its biocompatibility.²⁵⁶ A schematic representation of the ligand design in Chapters 2 and 3 is shown in Figure 1.18. The tripodal ligand structure closely mimics the active sites of many zinc containing enzymes, featuring the N/O donor set found in the coordinating amino acids in biological systems.²⁵⁷

Our novel ligand series results in a significant increase in intracellular zinc, results in restoration of transcriptional p53 activity, and induces mutant-selective apoptosis. Chapter 3 builds on the findings in Chapter 2 to further extend the ligand design into subsite cavities generated by the mutant. These ligands exhibit increased cytotoxicity compared to our lead compound from Chapter 2 in both 2D and 3D cultures and display a markedly improved ability to induce apoptosis.

Chapter 4 explores the design of a multifunctional ligand scaffold that aims to restore wild-type function in mutant p53 by simultaneously targeting zinc loss and protein aggregation. A schematic representation of the ligand design is shown in Figure 1.18. This ligand series affords an increase in intracellular zinc, and halogenation of the ligand framework led to inhibition of mutant p53 aggregation. This results in increased restoration of p53 transcriptional function and mediates both caspase-dependent and -independent cell death pathways. Tolerability in non-cancerous organoids demonstrate the cancer-cell selective potential of this multifunctional scaffold.

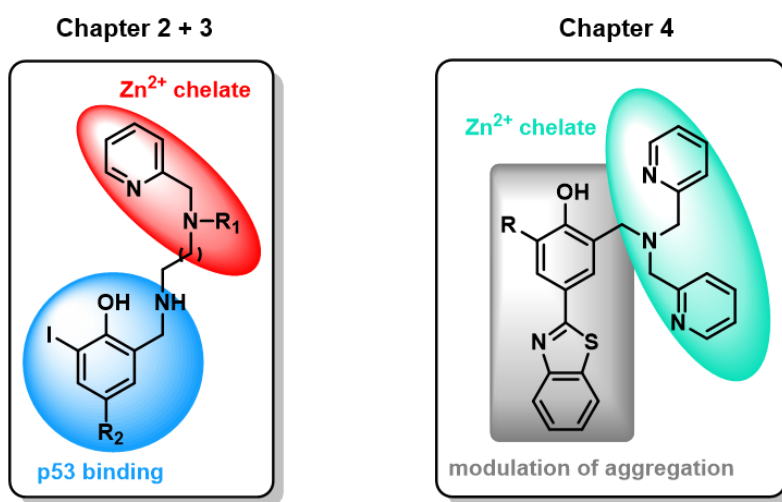


Figure 1.18. Multifunctional ligand scaffolds presented in chapters 2-4.

The ligand scaffolds contained in Chapters 2 through 4 explore the biological activity of iodinated ligand frameworks, which have the potential to interact with mutant p53 via halogen bonding. Halogenation of ligands has gained widespread attention in medicinal organic chemistry, due to the many advantages that such modifications can provide.²⁵⁸⁻²⁶⁰ During the process of hit-to-lead or lead-to-drug discoveries, insertion of halogen atoms has become common practice to increase membrane permeability, and in turn, improve oral availability.²⁶¹⁻²⁶² Furthermore, halogenation increases the ability of such compounds to cross the blood-brain barrier,²⁶³⁻²⁶⁴ leading to an estimated 20-30 percent of all pharmaceutical small-molecule drugs possessing halogen atoms.²⁶⁵ While classically halogenation of pharmaceuticals was considered mostly due to their steric parameters,²⁶¹ recent advances have highlighted their potential application in ligand-protein interactions by exploiting the advantages of halogen bonding.

Halogen bonding describes the interaction between halogens chlorine, bromine, or iodine acting as Lewis acids to form non-covalent interactions with a Lewis base.²⁶⁶ This is due to the anisotropy of the atom's charge distribution, leading to polar regions of positive electrostatic potential within the covalent R-X bond, termed the σ -hole.²⁶⁷ Halogen bonding can offer advantages over classical H-bonds, as halogen bonding to carbonyls was found to significantly improve binding of many small molecules to their protein targets.^{153, 268-270} This thesis thus explores the biological activity of halogenated ligand frameworks aimed to restore wild-type function in mutant p53.

Finally, Chapter 5 discusses both ongoing and future directions of the projects outlined in Chapters 2-4. Methods to investigate the mechanism of off-target effects and opportunities for improved selectivity are discussed. Further, studies to investigate the effects of halogenation on modulating mutant p53 as well as the effects of **L6** on other aggregation-prone mutants is described. This thesis provides significant new information on the use of multifunctional scaffolds to simultaneously target multiple characteristics of p53 mutants and provides valuable information for drug design moving forward.

Chapter 2. Multifunctional Compounds for the Activation of Mutant p53 in Cancer

Adapted from Miller, J. J.¹, Orvain, C.², Jozi, S.¹, Clarke, R. M.¹, Smith, J.¹, Blanchet, A.², Gaidon, C.², Warren, J. J.¹, and Storr, T.¹ *Chem. Eur. J.* **2018**, *24*, 17734-17742.

¹Department of Chemistry, Simon Fraser University, Burnaby, British Columbia, Canada.

²INSERM, Molecular Mechanisms of Stress Response and Pathologies, Université de Strasbourg, Strasbourg, France.

JJM performed the synthesis with assistance from SJ (L3). JJM carried out the spectroscopic titrations and zinc-binding studies. JS performed the molecular docking experiments. JJM and RMC performed the crystallography. JJM performed the cytotoxicity (2D and 3D) and caspase studies. CO carried out the zinc uptake and RT-PCR experiments. AB performed the immunoprecipitation experiment.

2.1. Introduction

The p53 protein, referred to as the “guardian of the human genome,”¹⁴¹ is a tetrameric transcription factor that regulates the expression of target genes to induce antiproliferative cellular responses.²⁷¹⁻²⁷² Among the many genes regulated by p53 are those that initiate apoptosis, DNA repair, and cell cycle arrest of damaged cells.^{58, 273} Consequently, in over 50% of cancer diagnoses, p53 does not carry out its essential function.²⁷⁴ The most common alterations to p53 are point mutations that affect tertiary structure and/or alter the protein’s ability to bind DNA.²⁷⁵⁻²⁷⁶ The net result is that cells bearing malfunctioning p53 are susceptible to enhanced proliferation and survival.¹⁴² There is significant therapeutic potential for p53 in cancer, and pharmacological restoration of function to mutant p53 is an acknowledged chemotherapeutic target that could substantially improve patient prognosis.^{145, 190, 277-279}

The majority of p53 mutations are point mutations localized to the protein’s core DNA-binding (p53C) domain,¹⁴² and a number of small molecules have been developed in an effort to reactivate mutant p53.^{37, 153, 226} One such example is APR-246 (Figure 2.1a) which has shown positive results in a Phase I/II clinical trial.²⁸⁰ APR-246 is a pro-drug and

is activated to a Michael acceptor that binds covalently to cysteine residues of mutant p53, resulting in protein reactivation.²⁸¹ Due to the non-specific nature of this process, APR-246 also binds and modifies other proteins, including modification of Thioredoxin reductase 1, which leads to increased reactive oxygen species (ROS) production, an additional cytotoxic mechanism.²⁸²

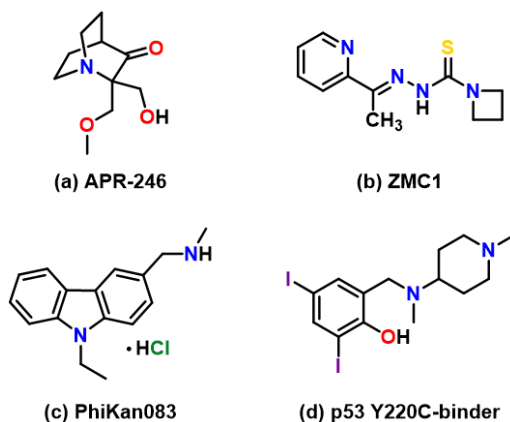


Figure 2.1. Chemical structures of (a) APR-246 (PRIMA-1MET) (b) NSC319726 (ZMC1) (c) PhiKan083 and (d) iodinated phenol small molecule shown to bind the p53-Y220C mutant pocket.

The p53C DNA-binding domain contains a single Zn^{2+} ion that is required for proper protein folding and function.¹⁵¹ Mutations to p53C can disrupt protein stability and/or cause loss of Zn .²⁸³ Consequently, the discovery of small-molecule Zn chaperones aimed to restore wild-type function in mutant p53 has generated much attention.^{226, 284} For example, the thiosemicarbazone ligand ZMC1 (Figure 2.1b) induces a conformational “wild-type-like” change in the common Zn-binding p53 mutation (R175H), and restores p53 transactivation function.²⁸⁴ Further studies indicate that subtle tuning of the Zn-binding affinity of the metallochaperones is critical for p53 reactivation,²¹⁵ as it functions by repopulating Zn-deficient p53C with Zn^{2+} .²²² More broadly, targeted metal ion chelation and redistribution has been shown to be a promising anti-cancer strategy,²⁸⁵ and a number of recent studies have highlighted both the novelty and complexity of this approach.^{226, 237,}

242, 286-288

Mutations to the p53C domain can result in structural destabilization such that the protein unfolds at or below physiological temperatures.⁵⁸ The Y220C point mutation is a common destabilizing p53 mutation and contributes to about 75,000 new cancer cases each year worldwide.¹⁵³ The Y220C mutation results in a cavity at the surface of the protein

(Figure 2.2), which decreases the melting point of the protein by ~ 2 °C, contributing to unfolding and ultimately aggregation.⁵⁸ Small molecules that bind to the Y220C cavity were developed using *in silico* and *in vitro* screening, and the carbazole-based molecule PhiKan083 (Figure 2.1c) was identified as a compound that raises the melting temperature (T_m) and slows the rate of thermal denaturation of p53-Y220C.²⁸⁹ More recently, derivatives of halogenated phenols have been reported by Boeckler and co-workers as a class of molecules that bind to the p53-Y220C cavity (Figure 2.1d).¹⁵³ It is hypothesized that halogen-bonding interactions with amino acids inside the cavity play an important role in binding. The halogenated compounds modestly increase the melting temperature of a p53-Y220C model protein and slow the rate of thermally induced protein unfolding/aggregation.¹⁵³ These results demonstrate that an iodinated-phenol core can be a starting point for envisioning new molecular designs. In addition to protein unfolding, p53-Y220C is prone to loss of Zn^{2+} in the DNA-binding domain,^{151, 283, 290-291} offering a novel target for drug design.

Multifunctional drugs, namely agents with more than one therapeutic mechanism, have gained increasing acceptance in recent years.²⁹²⁻²⁹⁶ Multifunctional drugs offer potential advantages over their monofunctional counterparts, including the potential to produce additive or synergistic effects by acting on multiple targets as well as enhancing druggable characteristics of the therapeutic molecule such as blood-brain-barrier penetration and tissue specificity.²⁹⁷ Such characteristics have been successful at enhancing drug efficacy and lowering toxic side effects, providing a new avenue in drug discovery from a “one-drug-one-target” to a “one-drug-multiple-target” strategy.^{295, 298}

In this chapter, a novel series of bifunctional ligands designed to restore wild-type activity in p53-Y220C by serving as structural stabilizers and as Zn-chaperones are reported. The compounds feature different binding groups that tune Zn^{2+} affinities and promote interactions with p53-Y220C. A full description of the ligand design and synthesis, characterization, and *in vitro* cytotoxicity testing of the bifunctional ligands is provided. We further elucidate the mechanisms of cytotoxicity and validate the therapeutic capacity of our ligands to restore function in mutant p53-Y220C.

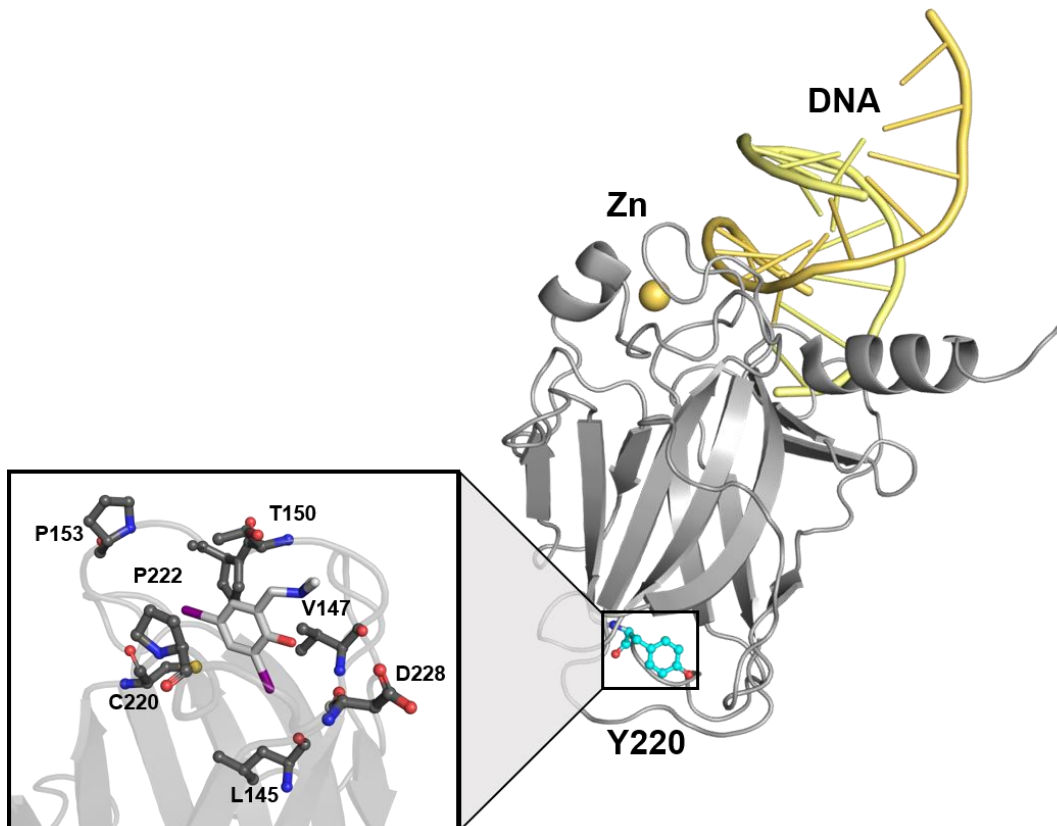


Figure 2.2. Structural model of p53C bound to DNA (PDB ID: 2AHI). Box enlargement shows that upon change from the larger tyrosine residue to a cysteine at position 220, a mutant-induced cavity is formed. The small molecule in Figure 2.1d is shown within the cavity and has led to restored protein function by increasing protein stability and preventing unfolding (PDB ID: 4AGL).

2.2. Results and Discussion

2.2.1. Ligand Design and Synthesis

A series of ligands (**L1-L5**) that are designed to restore wild-type function in p53-Y220C were synthesized and characterized (Figure 2.3). The ligand series was designed with two motifs in mind: (1) a p53-Y220C binding diiodophenol core,¹⁵³ and (2) Zn-binding groups to promote metallochaperone activity.^{219, 222, 226} Metal-binding groups were installed at the 2-position, following rationales for related p53-binding molecules.¹⁵³ Complexes of **L1** with a number of different metal ions have been investigated for their anti-cancer activity, however, the neutral metal complexes have low aqueous solubility.²⁹⁹ The carboxylic acid (**L2**) and polyethylene glycol (**L3**) groups were added to promote water

solubility and cell permeability. Pyridines and di-(2-picolyl)amine groups were appended at the 2-position as the zinc chelators based on the frequent use of these moieties in zinc chemosensors.³⁰⁰⁻³⁰³ The additional metal-binding group in **L4** and **L5** will promote 1:1 Zn²⁺ to ligand complex formation.

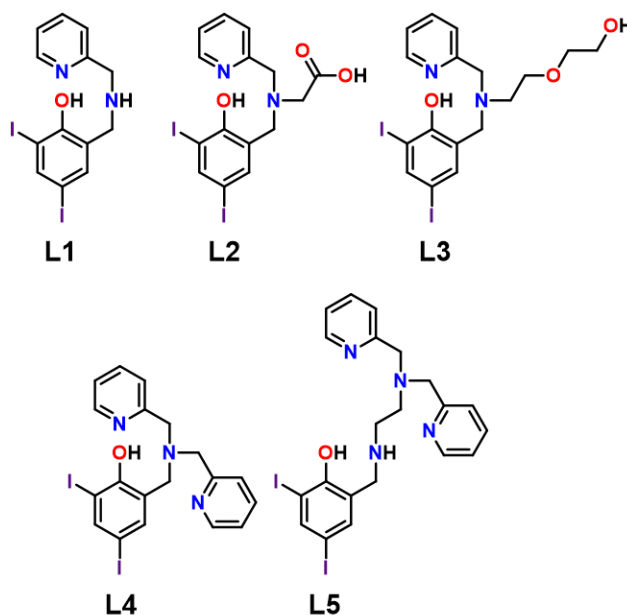
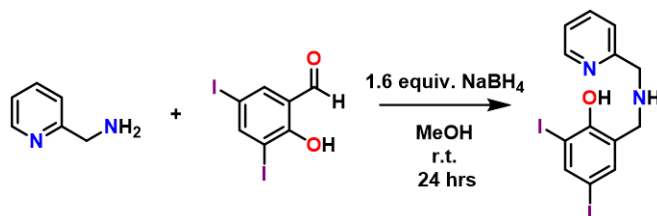
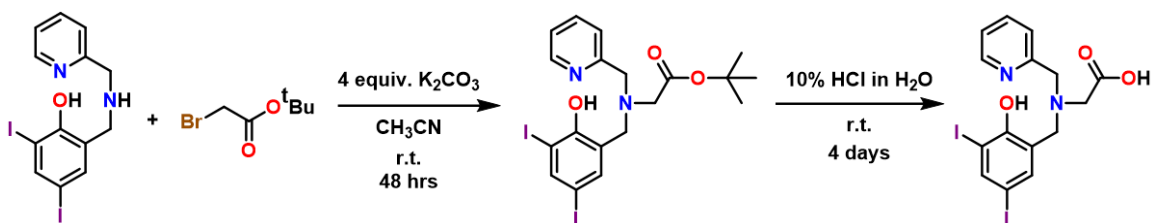


Figure 2.3. Chemical structures of ligands **L1-L5**.

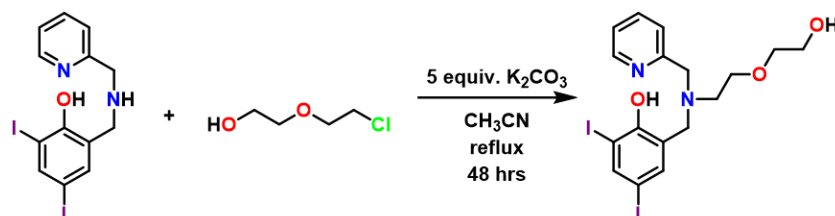
The synthetic strategies for ligands **L1-L5** are presented in Scheme 2.1-Scheme 2.5. The ligands were prepared via reductive amination of 3,5-diiodosalicylaldehyde and corresponding amines. Ligands **L2** and **L3** required subsequent functionalization of the secondary amine, while **L5** required a prior functionalization of di-(2-picolyl)amine.



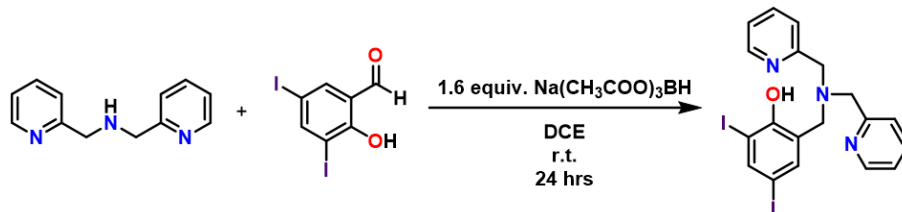
Scheme 2.1. Synthesis of **L1**. Yield: 56%.



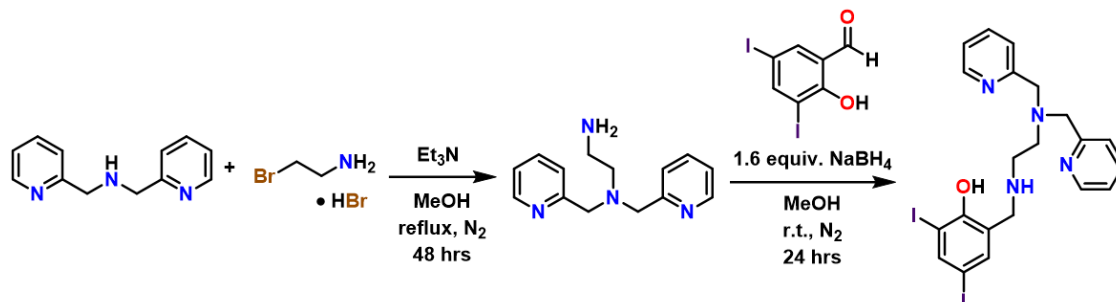
Scheme 2.2. Synthesis of **L2**. Yield: 82%.



Scheme 2.3. Synthesis of **L3**. Yield: 78%.



Scheme 2.4. Synthesis of **L4**. Yield: 95%.



Scheme 2.5. Synthesis of **L5**. Yield: 64%.

2.2.2. Molecular Docking

To investigate the potential binding mode of **L1-L5** with the mutation-induced cavity in p53-Y220C, we employed molecular docking of the ligands with available protein X-ray data.¹⁵³ Our modelling results predict that the iodinated phenol moiety in **L1-L5** orients in the p53-Y220C cavity (Figure 2.4a-e) in a similar fashion to a known p53-Y220C ligand that incorporates the same diiodophenol pharmacophore.¹⁵³ In addition, the DPA metal-binding unit in **L4** and **L5** does not significantly alter this interaction. We further

investigated the structure of **L5** by directly overlapping it with X-ray data (PDBID: 4AGQ) for a known p53-Y220C binding ligand (Figure 2.4f). The results predict similar low energy poses with both diiodophenol moieties pointing towards the mutant cavity, suggesting similar modes of binding.

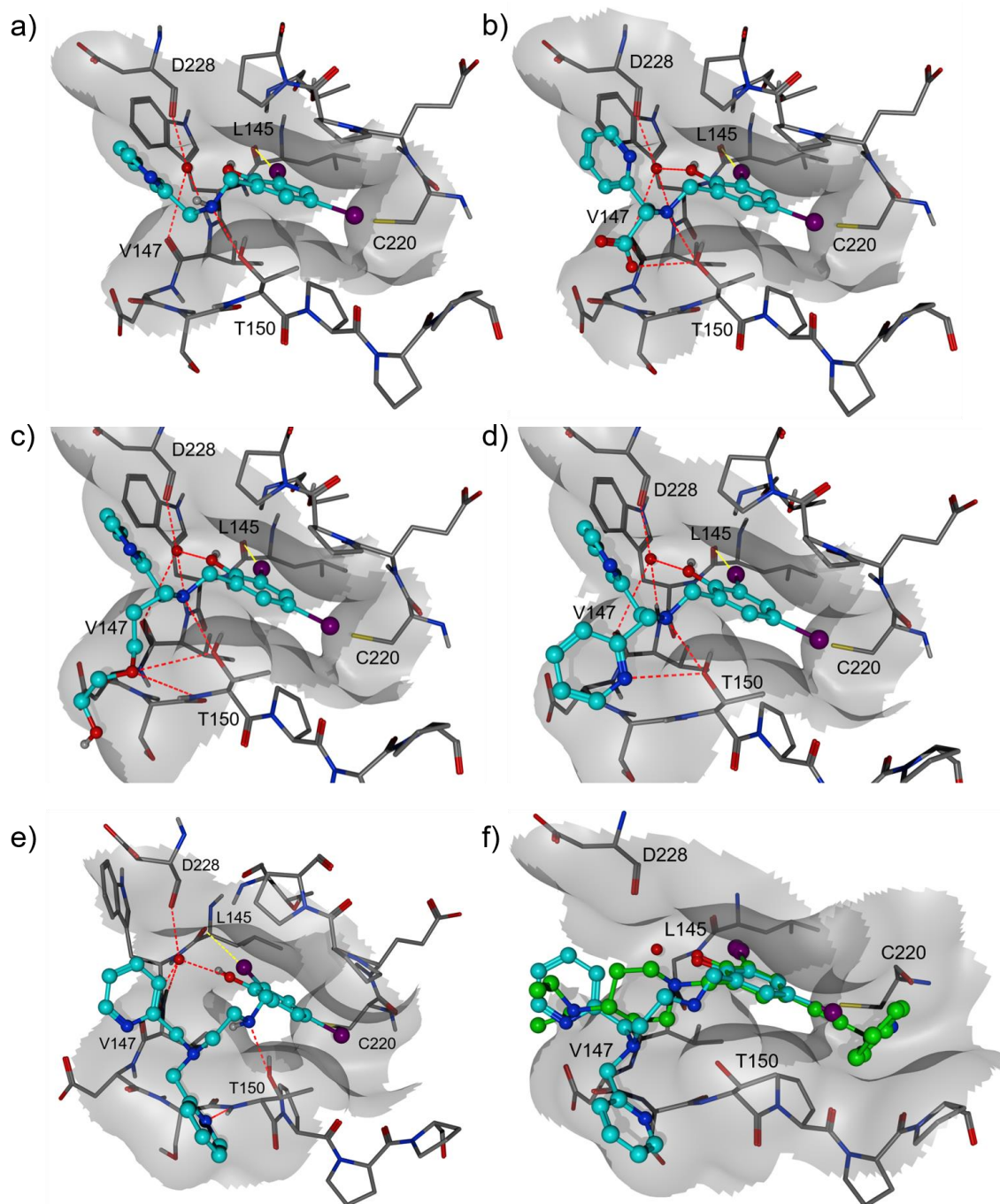


Figure 2.4. A low energy pose of **L1-L5** (a-e) in the mutation-induced cavity for p53-Y220C (PDBID: 4AGQ)¹⁵³. The halogen bonding interactions (I \cdots Leu145) are shown with a yellow line. The hydrogen bond network between the conserved water, D228, and V147 is shown in red. The Van der Waals surface of the protein is shown in gray. Atom colours: carbon is represented in gray in the protein and teal for the ligand. Oxygen is shown in red, nitrogen in blue, and sulfur in yellow. Hydrogens are omitted for clarity. (f) A low energy pose of **L5** (teal) overlaid with a known p53-Y220C binding molecule (green).

2.2.3. Zinc-Binding Affinities for L1-L5

Previously reported models for Zn-binding in p53 describe two possible ligation sites, the native binding site (K_{d1}) and the non-native (K_{d2}) sites.²¹³ The native Zn^{2+} K_{d1} for WTP53 is estimated to be on the order of 10^{-12} M.²²²⁻²²³ This value derives from the low intracellular levels of free zinc,²²²⁻²²³ and the fact that under physiological conditions, WTP53 is predominantly in the holo (zinc-bound) form.¹⁵² Metallochaperones designed to rescue Zn-binding in p53 mutants should therefore have Zn^{2+} affinities that are less than that of the native site (K_{d1}), yet higher than that of non-native sites (K_{d2}), estimated to be about 10^{-6} M for WTP53.²²⁶ The p53-Y220C mutant is prone to the loss of Zn^{2+} due to local unfolding and increased aggregation, so the exact value of K_{d1} is unknown. Assuming that the p53-Y220C mutant should have a slightly weaker Zn affinity than WTP53, we designed Zn metallochaperones for p53-Y220C wherein the Zn affinity lies between K_{d2} and K_{d1} ($10^{-9} < K_d \text{ chelator} < 10^{-12}$).

Spectrophotometric (UV-visible) pH titrations from pH 2-12 were carried out to characterize ligand speciation and Zn-affinity for **L1-L5**. The UV-visible spectrum for each ligand exhibit increases in the absorbance at 260 nm for each ligand upon addition of NaOH, and a major transition from ca. 300 nm to 310 nm indicative of the deprotonation of the phenol to give the phenolate (Figure 2.5, Appendix A, Figures 11-15). The simulated speciation diagrams are shown in Figure 2.5 and Appendix A, Figures 16-20. The best fits to the data were calculated and the pK_a values corresponding to the phenol, pyridine(s), and secondary/tertiary amines for each ligand are reported in Table 2.1. In each case, the highest pK_a s can be assigned to the phenol and ammonium group based on previously reported acidity constants,³⁰⁴⁻³⁰⁵ while the pK_a s for the pyridinium group vary depending on the ligand. For example, **L1**, which contains only one pyridinium group, has a higher pyridinium pK_a of 5.50, while pK_{a1} for ligands containing di(2-picolylamine) such as **L4** is lower (2.33).³⁰⁶⁻³⁰⁷

The metal speciation studies show that, at biological pH (7.4), both 1:1 and 2:1 ligand: Zn^{2+} complexes are present for **L1**, **L2**, and **L3** (Figure 2.6, Appendix A Figures 21-30).²⁹⁹ Verani and co-workers proposed that the 1:1 Zn:**L1** species is the biologically active form.²⁹⁹ Our speciation results are in accord with this observation, predicting that $[ZnL1]^+$ is the major constituent in solution at pH 7.4. In contrast, speciation diagrams of ligands **L4** and **L5** are described by a model with only 1:1 ligand to metal species present

(Figure 2.6). This result is consistent with the presence of an additional Zn-binding N-(2-pyridylmethyl) moiety in these ligands.²⁵⁵

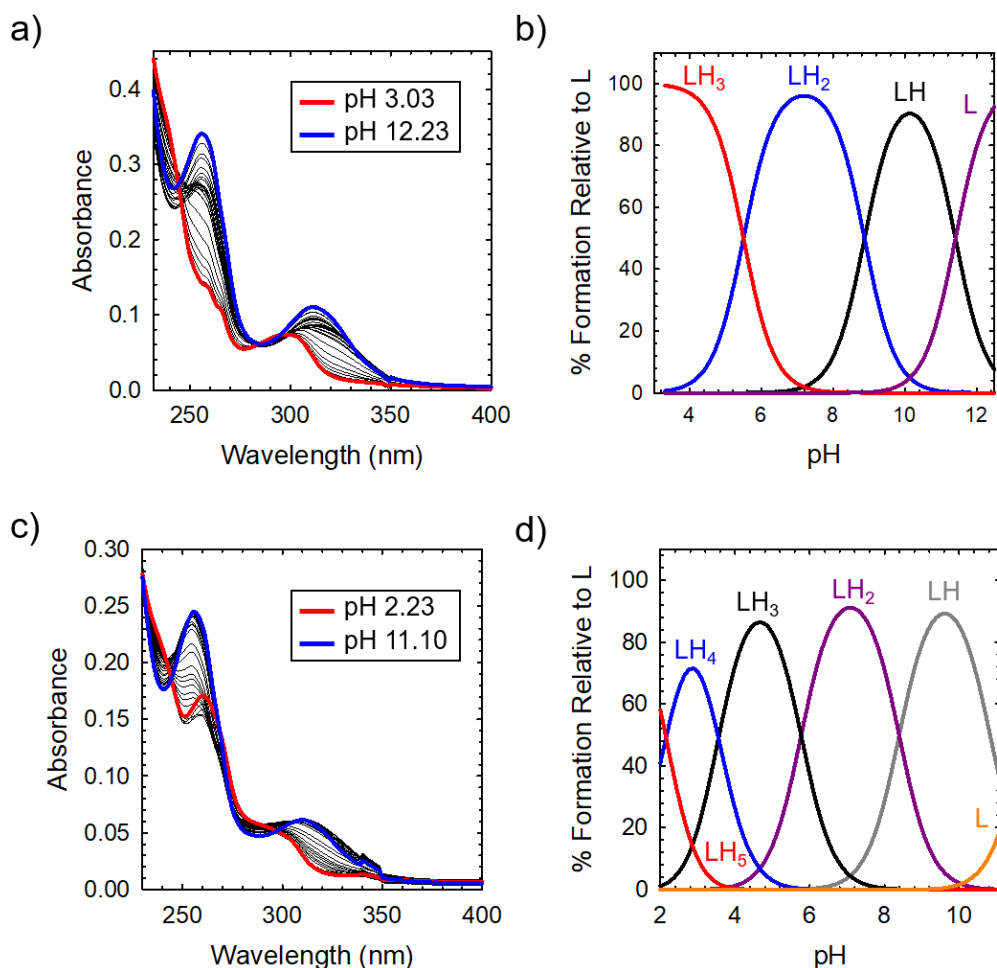


Figure 2.5. (a,c) Variable pH titration plots for **L1** and **L5**. (b,d) Simulated speciation diagrams of **L1** and **L5**. Speciation diagrams were made using HySS2009.

Table 2.1. pKa values as determined by variable pH UV-vis titrations (errors are for the last digit).

Reaction	L1	L2	L3	L4	L5
$[H_5L]^{4+} = [H_4L]^{3+} + H^+$ (pKa ₁)	-	-	-	-	2.24(2)
$[H_4L]^{3+} = [H_3L]^{2+} + H^+$ (pKa ₂)	-	3.20(2)	-	2.34(2)	3.53(2)
$[H_3L]^{2+} = [H_2L]^+ + H^+$ (pKa ₃)	5.499(9)	5.27(2)	5.10(1)	4.14(1)	5.77(2)
$[H_2L]^+ = [HL] + H^+$ (pKa ₄)	8.873(9)	9.334(9)	9.03(1)	8.14(1)	8.35(2)
$[HL] = [L]^- + H^+$ (pKa ₅)	11.413(4)	10.80(1)	9.98(1)	10.982(5)	10.79(1)

Analysis of the speciation diagrams provided the Zn²⁺ affinity of each ligand at physiological pH. The concentration of free Zn²⁺ present in solution at a given pH, referred

to as pM ($pZn = -\log[Zn_{\text{unchelated}}]$), is a direct estimate of the metal-ligand affinity when all species in solution are considered.³⁰⁸⁻³¹⁰ Calculated values for pZn are reported in Table 2.2. The calculated pM values for **L1-L3** demonstrate a high Zn^{2+} -affinity at physiological pH, however, exhibit limited biological activity (*vide infra*). The additional carboxylate binding unit of **L2** allows for potential tetradentate binding, and the phenoxyl and carboxylate moieties can serve as bridges between two central Zn atoms, forming a stable, dimerized species.³¹¹ The calculated pZn values for the 1:1 complexes **L4** and **L5** are comparable (7.9 and 8.4 respectively), and match well with reported Zn-affinities for a ligand series containing the same metal-binding fragment.²⁵⁵ These pZn values afford approximate dissociation constants (K_d) in the low nanomolar range; an affinity appropriate for functioning as a Zn metallochaperone for p53-Y220C.

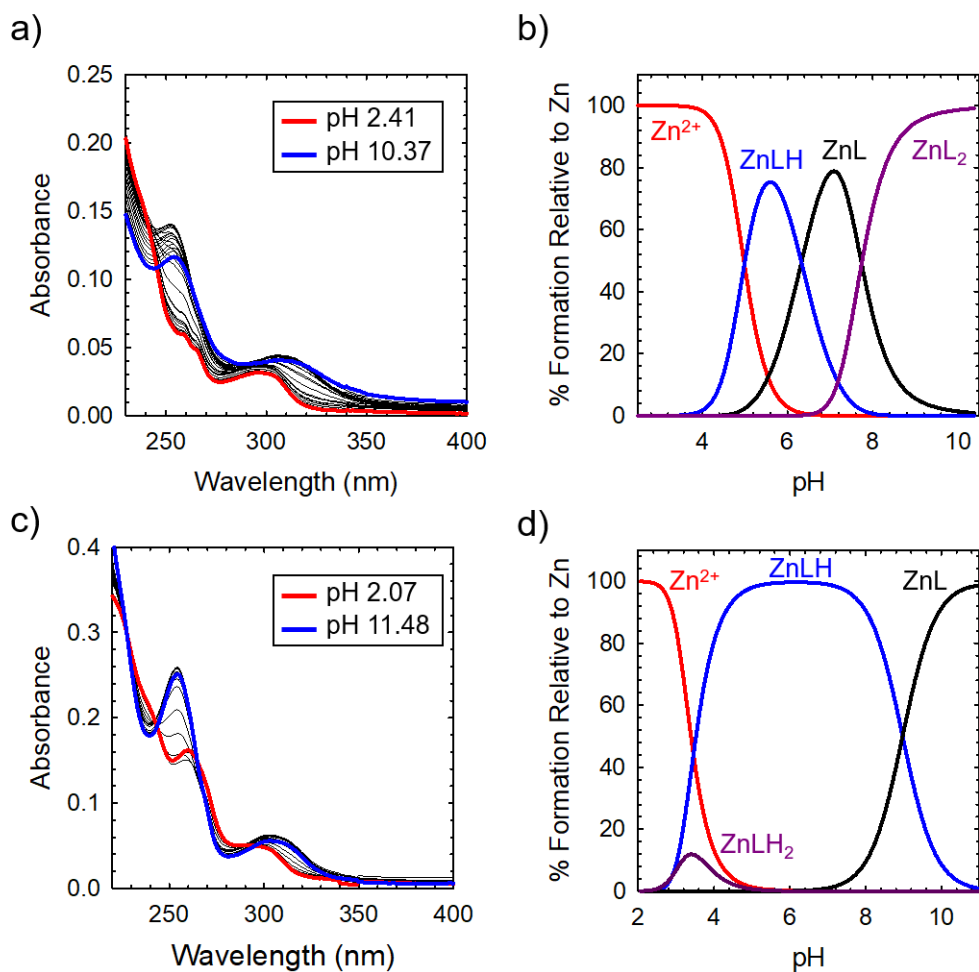


Figure 2.6. (a, c) Variable pH titration plots for **L1** + Zn^{2+} and **L5** + Zn^{2+} . (b, d) Simulated speciation diagrams of **L1** + Zn^{2+} and **L5** + Zn^{2+} . Speciation diagrams made using HySS2009.

Table 2.2. Stability constants (log K) of the Zn complexes of **L1-L5** and calculated pM (pZn) values^[a] (errors are for the last digit).

	pZn ^[a] pH 7.4	Log K			
		ZnL	ZnLH	ZnLH ₂	ZnL ₂
L1	9.2	14.63(1)	6.327(5)	-	10.34(5)
L2	10.1	15.439(6)	5.572(4)	-	10.65(4)
L3	9.4	13.59(1)	6.427(5)	-	10.04(3)
L4	7.9	14.72(1)	7.802(8)	-	-
L5	8.4	14.63(3)	8.98(2)	2.89(3)	-

^[a] pZn was calculated using $pZn = (-\log[Zn^{2+}]_{free})$, where $[Zn^{2+}]_{free}$ is determined from the Hyss model.³¹²
[L1-L3] = 6.25 μ M, **[L4-L5]** = $[Zn^{2+}]$ = 12.5 μ M, 25 °C, I = 150 mM NaCl

Zn complexes of **L4** and **L5** were also isolated and characterized using ¹H NMR and MS. Upon reaction with molar equivalents of ZnCl₂ and KOH, distinct shifts in the ¹H NMR peaks are observed. An example of the coordination of **L4** to the Zn metal center is shown in Figure 2.7. Upon metal coordination, the pyridine α -proton is shifted downfield from 8.54 (red) to 9.00 (blue) ppm. Furthermore, there is a loss in equivalence of each picolyl arm upon coordination, resulting in a change from a singlet at 3.81 ppm to an AB pattern at 4.08 ppm.

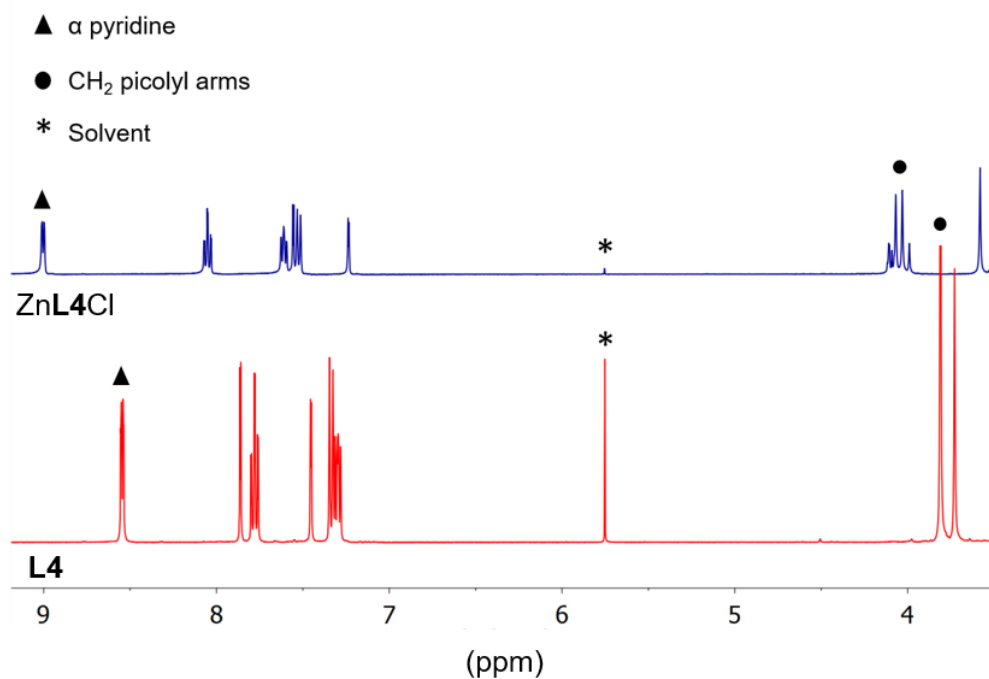


Figure 2.7. ¹H NMR spectra of **L4** (red) and Zn**L4**Cl (blue) (DMSO, 400 MHz). Asterisk denotes residual CD₂Cl₂ solvent peak.

ZnL4Cl was further characterized by X-ray crystallography (Figure 2.8). Complete crystallographic information is provided in Table 2.3. Characterization of the Zn complexes of L4 and L5 are in accord with the 1:1 binding to Zn²⁺ modelled above for variable pH titrations.

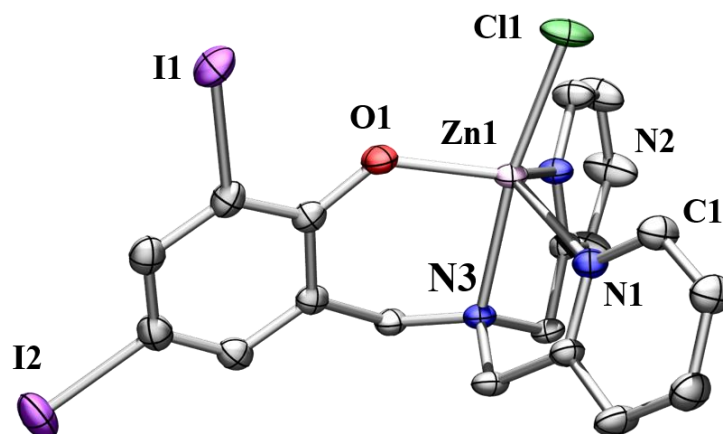


Figure 2.8. ORTEP of ZnL4Cl (50% probability) using POV-Ray, excluding hydrogen atoms and solvent. Selected interatomic distances [Å]: Zn(1)-N(1-3): 2.093-2.280; Zn(1)-O(1): 1.954; Zn(1)-Cl(1): 2.286.

Table 2.3. Selected crystallographic information for ZnL4Cl.

Crystallographic Information	ZnL4Cl
Formula	C ₃₈ H ₃₃ Cl ₃ N ₄ O ₂ Zn ₂ •CH ₂ Cl ₂
Formula weight	1356.44
Space group	P21/c
a (Å)	13.28(5)
b (Å)	15.12(5)
c (Å)	23.54(8)
α (deg)	90
β (deg)	104.5(6)
γ (deg)	90
V [Å ³]	4575(3)
Z	2
T (K)	296(2)
ρ _{calcd} (g cm ⁻³)	1.969
λ (Å)	0.71073
μ (cm ⁻¹)	3.963
R indices ^a with I > 2.0σ(I) (data)	0.0878
wR ₂	0.3195
R ₁	0.0971
Goodness-of-fit on F ₂	1.673

^aGoodness-of-fit on F.

2.2.4. Increasing Intracellular Zn²⁺ in Cancer Cells

We investigated whether **L4** and **L5** could serve as Zn metallochaperones and increase intracellular levels of Zn²⁺ in the stomach cancer cell line NUGC3 containing mutant p53-Y220C. NUGC3 cells were incubated with the fluorescent Zn²⁺ sensitive probe FluoZin-3 (1 μM),³¹³ followed by incubation with **L4** or **L5** (15 μM) and 50 μM ZnCl₂. and subsequently imaged. Pyridithione (PYR) was used as a positive control for Zn uptake. Both **L4** and **L5** increased intracellular levels of Zn²⁺ in NUGC3 cells, as indicated by intracellular fluorescence (Figure 2.9). However, due to the similar Zn K_d values of FluoZin-3 and **L4/L5** (Zn²⁺ K_d = ~ 15 nM for FluoZin-3,³¹³ 13 nM for **L4** and 4 nM for **L5**) Zn-binding to the fluorophore in this experiment is likely restricted, and thus total Zn uptake is underestimated. **L5** increased intracellular Zn²⁺ levels more than 4-fold compared to the untreated control, and a two-fold increase over untreated control is observed with **L4** (Figure 2.9). Addition of the strong membrane-permeable Zn-chelator, N-N'-N'-N'-tetrakis-(2-picolyl)-ethylenediamine (TPEN, K_d = 26 fM)³¹⁴ following treatment with **L5** results in a significant loss of fluorescence, indicating that **L5** is capable of delivering Zn²⁺ to stronger intracellular Zn chelates. These results demonstrate the ability of **L5** and to a lesser extent, **L4**, to serve as Zn metallochaperones in NUGC3 cells containing the p53-Y220C mutation.

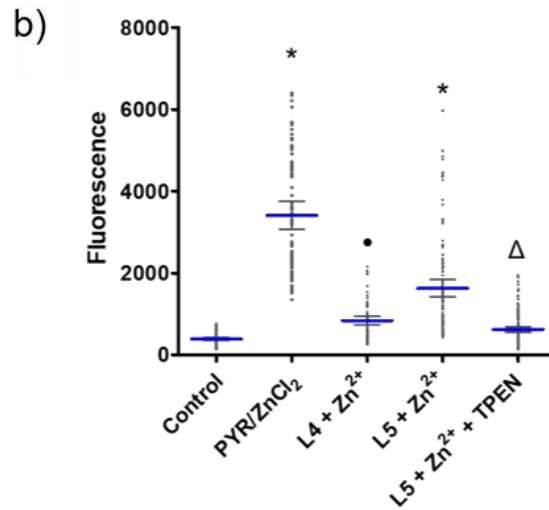
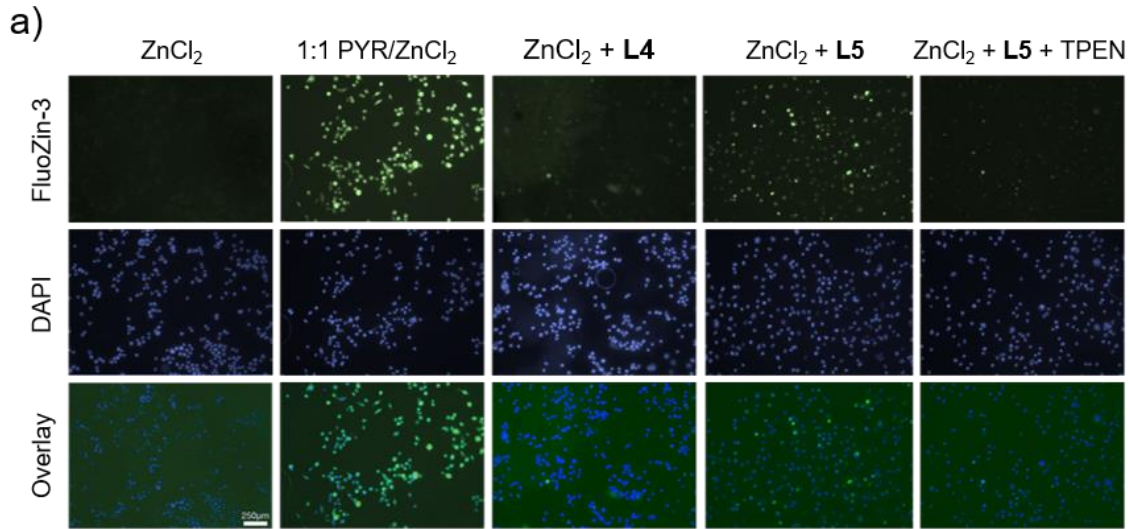


Figure 2.9. Treatment of NUGC3 (p53-Y220C) with **L4** and **L5** increases intracellular Zn²⁺. (a) Imaging of intracellular Zn²⁺ levels in complete serum-free media. NUGC3 cells were incubated with 1 μM FluoZin-3²¹⁹ for 20 minutes at 37 °C, followed by incubation with indicated treatment (ZnCl₂ = 50 μM, **L4** = **L5** = 15 μM, 50 μM PYR) for 2 hours. 150 μM TPEN was added following incubation with ZnCl₂ and **L5**. Cells were imaged using a Nikon ApoTome microscope and fluorescence-quantified using ImageJ. All images were taken at indicated magnification. (B) Fluorescence intensity of FluoZin-3 at 488 nm demonstrating relative Zn²⁺ levels. The gray dots represent the fluorescence intensity in each imaged cell. Blue line indicates mean values, while black error bars demonstrate the 95% confidence interval. * indicates statistical differences from control with p < 0.0001, • indicates statistical differences from control with p < 0.01, and Δ indicates statistical difference from L5 + ZnCl₂ with p < 0.0001. No statistical differences are observed between the control and **L5** + ZnCl₂ + TPEN.

2.2.5. *In Vitro* Cytotoxicity

L1-L5 and the corresponding zinc complexes of **L4** and **L5** (Zn**L4**Cl and Zn**L5**Cl) were submitted to the National Cancer Institute's NCI-60 program for *in vitro* screening against a panel of 60 human cancer cell lines. After initial 1-dose screening (10 μ M), **L1-L3** were rejected from further testing due to their insufficient cytotoxicity (Table 2.4). The inactivity of these 2:1 Zn²⁺-binding ligands could be due to various factors, including limited cell uptake of the ligands, and/or limited solubility of neutral complexes formed from available Zn²⁺ found in cell culture media.³¹⁴ These ligands were thus not subjected to further testing and are not discussed further. The activities of the 1:1 Zn²⁺ binding ligands, **L4** and **L5**, was significantly greater than **L1-L3** and the aggregate results from their 5-dose testing are displayed in Table 2.4. **L4** and **L5** were found to have a broad range of cytostatic (GI₅₀, 0.4 -2.2 μ M) and cytotoxic (LC₅₀, 4.6 – 93.8 μ M) activity. **L5** shows the most promising results, exhibiting high cytostatic activity in combination with a cytotoxic activity that is almost three times more potent than that of cisplatin. This combination of both cytostatic and cytotoxic activity can offer major advantages in the treatment of cancers.³¹⁵⁻³¹⁹

Table 2.4. Mean GI₅₀ and LC₅₀ values for **L4**, **L5**, and cisplatin from the NCI-60 screen.

Ligand	NSC Number ^[a]	GI ₅₀ ^[b] (μ M)	LC ₅₀ ^[b] (μ M)
L1	788643	33.1	-
L2	788644	52.1	-
L3	788645	82.6	-
L4	788646	2.2	70.3
L5	788647	1.5	15.0
ZnL4Cl	793562	30.4	-
ZnL5Cl	793563	41.7	-
Cisplatin	119875	1.5	44.0

^[a] NSC number is the compounds internal ID number at the National Cancer Institute. ^[b] GI₅₀ values correspond to the dose that inhibits 50% of cell growth compared to non-treated controls, while LC₅₀ indicates the concentration required to kill 50% of treated cells.³²⁰

Interestingly, their corresponding Zn complexes (Zn**L4**Cl) and Zn**L5**Cl) exhibited lower biological activity at the initial test concentration of 10 μ M (Table 2.4) and did not meet the necessary threshold for 5-dose testing in the NCI-60 panel. However, further investigation of the Zn complexes using stomach cancer cell lines AGS (WTP53) and NUGC3 (p53-Y220C) showed that their cytotoxicity increases at higher concentrations

(Figure 2.10), with ZnL4Cl exhibiting increased cytotoxicity in comparison to L4 at concentrations > 10 μM . Conversely, L5 is more cytotoxic than ZnL5Cl in both AGS and NUGC3 cell lines at all concentrations studied.

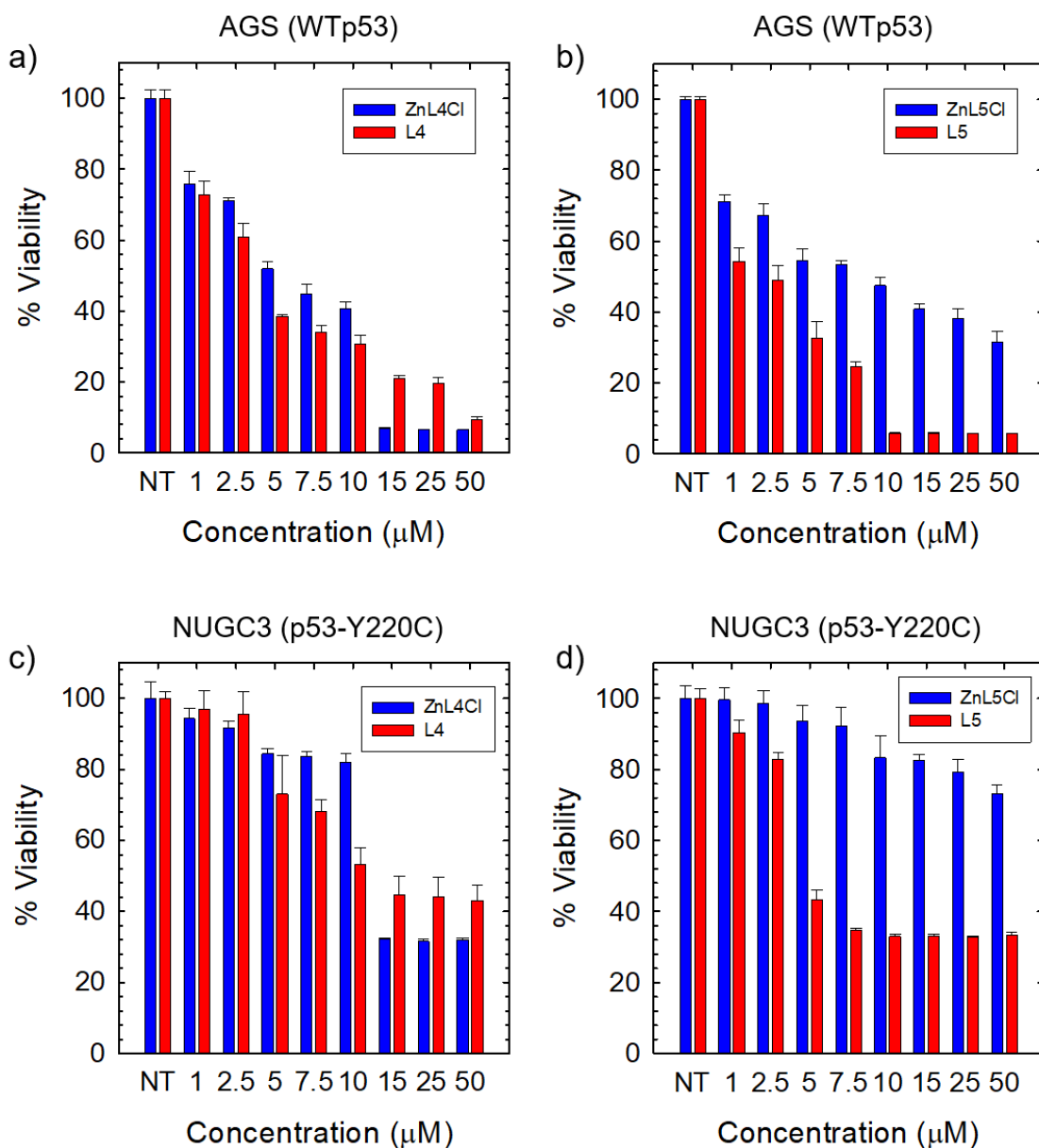


Figure 2.10. In vitro cytotoxicity (MTT) of L4 vs ZnL4Cl and L5 vs ZnL5Cl in the stomach cancer cell line AGS (WTp53) (a,b) and NUGC3 (p53-Y220C) (c,d).

A heat map of the 5-dose NCI-60 screen for L4 and L5 is shown in Figure 2.11 and summarizes the patterns of *in vitro* cytostatic (GI_{50}) and cytotoxic (LC_{50}) activities from low (blue) to high activity (red). The most striking result is the level of cytotoxicity displayed by L5 across most cell lines. However, L4 and L5 have minimal cytotoxic effect on

selected leukemia cell lines (> 100 μM in most cases). Chemoresistance in leukemia cancers is common, especially in multiple myeloma (RPMI-8226).³²¹ In contrast, **L4** and **L5** are highly cytotoxic to the melanoma cell line SK-MEL-5, with GI_{50} values of 2.6 and 1.5 μM and LC_{50} values of 13.0 and 5.2 μM , respectively. Note that the NCI-60 panel does not presently contain p53-Y220C mutant cell lines, though many other p53 mutants are included. In addition, several highly lethal cancer types are not represented in the NCI-60 screen (i.e. gastric cancer, pancreatic cancer) and is therefore not a fully comprehensive assessment of the therapeutic potential of **L4** and **L5**. For these two reasons, we further investigated the biological activity of our compounds in gastric cancer cells.

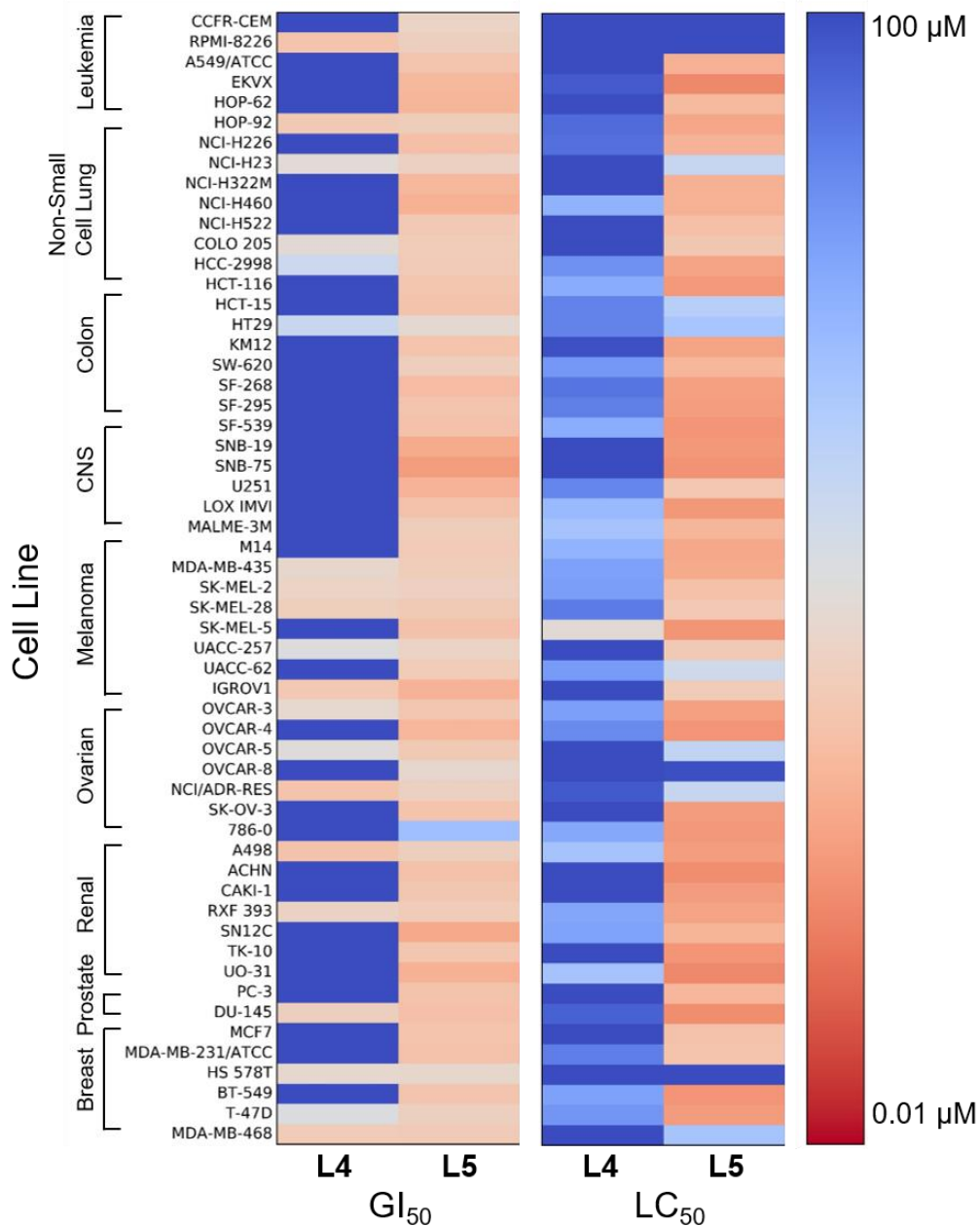


Figure 2.11. Heat map showing the *in vitro* cytostatic (GI_{50}) and cytotoxicity (LC_{50}) of **L4** and **L5** in the NCI-60 screen. Blue indicates low activity (100 μ M) and red indicates high activity (0.01 μ M).

Gastric cancer is the second leading cause of cancer-related deaths worldwide, and its lethality is particularly high as indicated by a 5-year survival rate of around 30%.³²² In addition, there are gastric cancer cell lines with different p53 status', including p53-Y220C. We tested the *in vitro* cytotoxicity of our ligand series on three human gastric cancer cell lines: AGS, which contains wild-type p53, MKN1, with the V142A point

mutation, and NUGC3, which has the p53-Y220C mutant. The data are reported in Table 2.5 as IC₅₀ values. The results are in agreement with the data obtained in the NCI-60 screen; **L1-L3** displayed minimal cytotoxic activity, whereas **L4** and **L5** were highly cytotoxic on two stomach cancer cell lines tested, AGS and NUGC3, showing a significant improvement over the IC₅₀ values of cisplatin and oxaliplatin. The compounds however, do not display higher *in vitro* cytotoxicity in NUGC3 p53-Y220C expressing cells compared to the AGS wild-type p53 cell line at the 24-hour timepoint. MKN1 is highly insensitive to **L1-L4** (IC₅₀ range of 51.6- 175 μM), however, the low IC₅₀ value for **L5** (1.2 μM) highlights its increased cytotoxicity in comparison to the other ligands in the series.

Table 2.5. *In vitro* cytotoxicity (IC₅₀ values)^[a] data for stomach cancer cell lines AGS, MKN1, and NUGC3.

Ligand	AGS (WTp53)	MKN1 (p53 ^{V143A})	NUGC3 (p53 ^{Y220C})
L1	7 ± 1	85 ± 1	7.1 ± 0.8
L2	21 ± 3	90 ± 4	36 ± 5
L3	22 ± 3	175 ± 2	26 ± 6
L4	2.7 ± 0.2	52 ± 4	2.7 ± 0.1
L5	1.6 ± 0.1	1.2 ± 0.1	1.7 ± 0.1
Cisplatin	25 ± 2	4.3 ± 0.4	20 ± 2
Oxaliplatin	7.4 ± 0.9	6.9 ± 0.1	50 ± 3

^[a] IC₅₀ is the concentration needed for 50% reduction of survival based on survival curves.³²³

To further characterize the anticancer potential of our lead cytotoxic compound **L5**, we assessed its cytotoxic activity in non-adherent 3D aggregate cultures of NUGC3 cells. The use of 3D cell cultures is becoming increasingly important in drug discovery due to their ability to more accurately represent physiological conditions, including cell signalling processes, in comparison to 2D cultures.³²⁴⁻³²⁵ Therefore, the use of 3D cell cultures can better predict promising compounds for *in vivo* testing before entering clinical trials.³²⁶⁻³²⁷ 3D spheroids of NUGC3 cells were treated with IC₇₅ concentrations obtained from 2D cultures of **L5**, and compared to treatment with oxaliplatin, one of the leading drugs for gastric cancer treatment.³²⁸⁻³³¹ Even at the markedly lower concentration of **L5** used compared to oxaliplatin (19.5 μM vs 250 μM at IC₇₅), **L5** remained more cytotoxic (Figure 2.12).

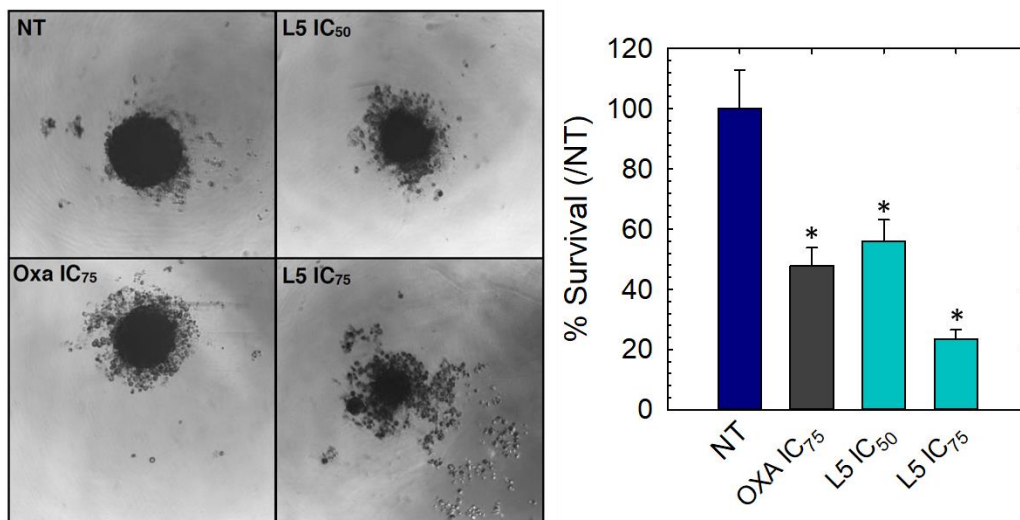


Figure 2.12. NUGC3 cells (300 cells/well; 96 wells/plate) were grown for 4 days and then treated for 3 days at IC₅₀ and IC₇₅ concentrations as indicated. 3D cultures were observed by microscopy to estimate clone size (left) and cell survival was assayed using rezasurin, a fluorescent indicator of cell viability (right). * indicates statistical differences from non-treated control with $p < 0.001$ as established by One-Way ANOVA followed by Tukey test.

2.2.6. Apoptotic Effects of L4 and L5 in Human Gastric Cancer Cell Lines

To investigate the molecular basis for the cytotoxicity of compounds **L4** and **L5** and evaluate whether this mechanism is p53-dependent, we examined whether **L4** and **L5** treatment could result in cleavage of caspase-3, an indicator of apoptosis,³³² in both AGS and NUGC3 cells. We further analysed the levels of p53 expression. AGS and NUGC3 cells were treated with the indicated compounds at both IC₅₀ and IC₇₅ concentrations for 48 hours, and then cleavage of caspase-3 and p53 protein levels were assessed by Western Blot. As expected, oxaliplatin induced an increase in p53 protein levels and low levels of cleaved caspase-3 in AGS cells (Figure 2.13).³³³⁻³³⁴ Treatment with **L5** resulted in the production of low quantities of cleaved caspase-3 at levels comparable to oxaliplatin, again highlighting its increased cytotoxicity compared to **L4**, which does not induce any changes in either caspase-3 cleavage or p53 expression levels. In contrast to oxaliplatin, however, the increase in cleaved caspase-3 for **L5** is not coupled with an induction of p53 protein level in the AGS (WTp53) cell line. In the NUGC3 cell line, oxaliplatin induces an increase in cleaved caspase-3 at both IC₅₀ and IC₇₅ concentrations. In addition, oligomeric forms of p53 are observed with molecular weights

corresponding to dimers upon treatment with IC₇₅ concentrations of oxaliplatin, which could indicate p53 activation.³³⁵⁻³³⁸ Interestingly, the level of cleaved caspase-3 upon treatment with **L5** at concentrations as low as 19.5 μM (IC₇₅ concentration) is notably increased in NUGC3 (p53-Y220C) cells in comparison to AGS (WTp53) cells under the same conditions. These results suggest that the apoptotic effect of **L5** is preferentially potentiated in the Y220C mutant cell line (*vide infra*).

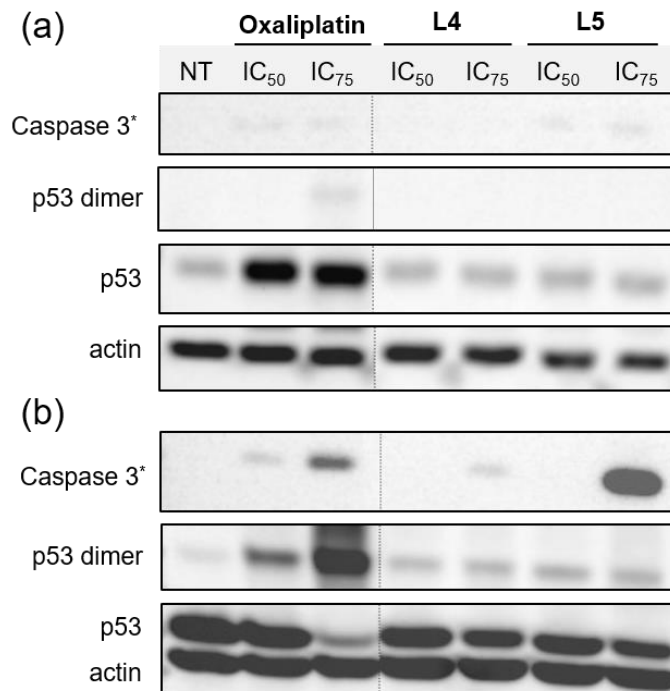


Figure 2.13. AGS cells (a) and NUGC3 cells (b) were treated for 48 hours with the IC₅₀ and IC₇₅ concentrations of indicated compound. Total protein was extracted, and 20 μg were separated on SDS PAGE (Sodium dodecyl sulfate polyacrylamide gel electrophoresis). Cleaved caspase-3 (Caspase 3*), p53, and actin were detected by Western Blot analysis.

To further explore the mechanisms by which **L5** imparts biological activity on p53-Y220C, we investigated whether **L5** could bind directly to the DNA-binding domain of mutant p53-Y220C (p53C-Y220C) using surface plasmon resonance (SPR) (Figure 2.14a). Unfortunately, binding at low micromolar concentrations was not observed, and limited solubility of **L5** beyond 400 μM prevents detection of higher micromolar affinity binding (Figure 2.14b), a range relevant to a compound with the same 3,5-diiodophenol pharmacophore ($K_d = 225 \mu\text{M}$ by isothermal calorimetry (ITC) and $184 \pm 23 \mu\text{M}$ by NMR).¹⁵³ Immunoprecipitation (IP) experiments using the conformation-specific antibody PAb240 (recognizing unfolded p53), however, indicated that treatment with **L5** leads to a

change in conformation of mutant p53 protein. Using native lysates from NUGC3 cells treated in the absence or presence of increasing concentrations of **L5**, we immunoprecipitated mutant p53 and performed a Western Blot with the DO-1 antibody, which binds p53 regardless of conformation. Treatment with **L5** for only two hours resulted in significant reduction in PAb240 staining in a concentration dependent manner (Figure 2.15), indicating that upon treatment with **L5**, p53 conformation is altered wherein the epitope recognized by PAb240 is buried within the protein's core.

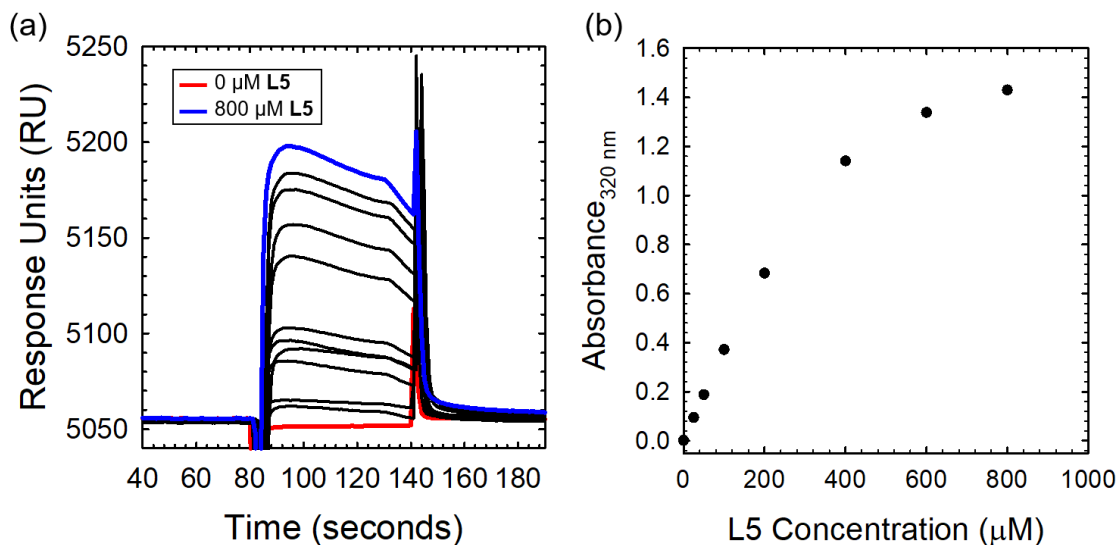


Figure 2.14. SPR kinetic sensorgram measuring the binding of **L5** to p53C-Y220C. Various concentrations of **L5** ranging from 0 μM to 800 μM in running buffer (HBS-EP+ - GE Healthcare: 10 mM HEPES, 150 mM NaCl, 3 mM EDTA, 0.05% v/v Surfactant P20, pH 7.4) containing 5% DMSO was injected. The association and dissociation phase were monitored for 60 and 100 seconds respectively. (b) Solubility of **L5** in SPR running buffer by measuring absorbance as a function of **L5** concentration. Binding measurements of **L5** to p53C-Y220C is limited by ligand insolubility beyond 400 μM and therefore higher micromolar binding affinities cannot be accurately measured.

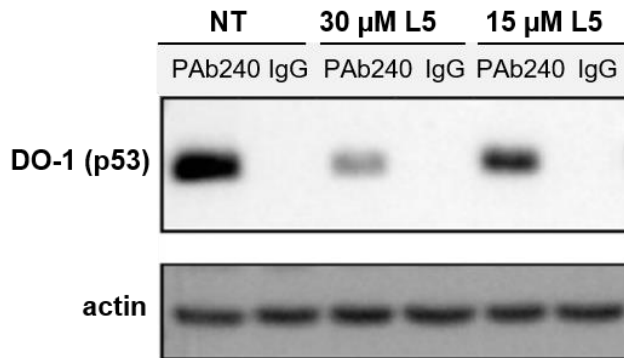


Figure 2.15. Mutant p53 levels are reduced upon treatment with increasing concentrations of **L5**. NUGC3 cells were treated for 2 hours with **L5** at the indicated concentrations. Cells were lysed, followed by total protein selection against the p53 antibody PAb240, which immunoprecipitates only mutated p53. Precipitated protein was separated on a 10% SDS page gel and incubated with the p53 antibody (DO-1), which recognizes both mutated and wild-type p53. A non-specific antibody was used as a negative control for immunoprecipitation (IgG). Actin protein levels present in the lysate are shown as a control for the quantity of protein used for immunoprecipitation.

2.2.7. Transcriptional Upregulation of p53 Targets

Based on the high *in vitro* cytotoxicity of **L5** and its increased activity in p53-Y220C expressing cells in the cleaved caspase-3 assay mentioned above, we further investigated the effect of this lead compound on the cellular activity of p53. We measured the mRNA expression levels of p53 and several p53 target genes that are involved in either cell cycle arrest (p21)⁵⁸ or apoptosis (NOXA, PUMA)^{58, 277} in p53-Y220C expressing and p53-silenced NUGC3 cells. p53 expression was silenced using the silencing RNA (siRNA) sip53 (Figure 2.16 a). NUGC3 cells were treated for 24 hours at the IC₅₀ concentration and the level of p53 target transcripts were measured by RT-qPCR (Figure 2.16 b). Upon transfection of sip53, expression levels of NOXA and p21 increased under non-treated (sip53 NT) controls compared to NT conditions with control siRNA (siCT NT). This is likely because mutant p53 can bind and inactivate p63 and p73 proteins,³³⁹⁻³⁴¹ both of which also induce cell cycle arrest and apoptosis by regulating p53 target genes such as NOXA and p21.³⁴² Therefore, silencing mutant p53 with sip53 restores function in p63 and p73, causing their expression levels to increase. In the presence of p53-Y220C (siCT), expression levels of all three target genes were significantly higher when treated with **L5** compared to non-treated controls (NT), and attained similar levels induced by oxaliplatin, despite the lower treatment concentration of **L5** (IC₅₀ **L5** = 1.7 μ M vs 50 μ M for oxaliplatin).

The increase in PUMA and NOXA transcripts is indicative of an apoptotic induction by **L5**, which correlates to the results obtained in Figure 2.15. Upon treatment with sip53, expression levels of PUMA and NOXA decrease with **L5** treatment, however, increase when treated with oxaliplatin. This is likely a result of the known ability of oxaliplatin to induce apoptosis via PUMA in a p53-independent manner.³⁴³ Strikingly, treatment of NUGC3 cells with IC₅₀ values of **L5** resulted in a 4-fold increase in p21 expression compared to the non-treated control. These changes were obtained without increasing p53 expression levels, unlike oxaliplatin, suggesting the restoration of wild-type function in existing p53-Y220C. Furthermore, the diminished expression of p53-Y220C upon treatment with siRNA significantly reduced the impact of **L5** on the mRNA level of the p53 target genes. These results indicate restoration of cellular activity to the p53-Y220C mutant, and that at least part of the biological activity of **L5** is due to restoration of wild-type p53 function.

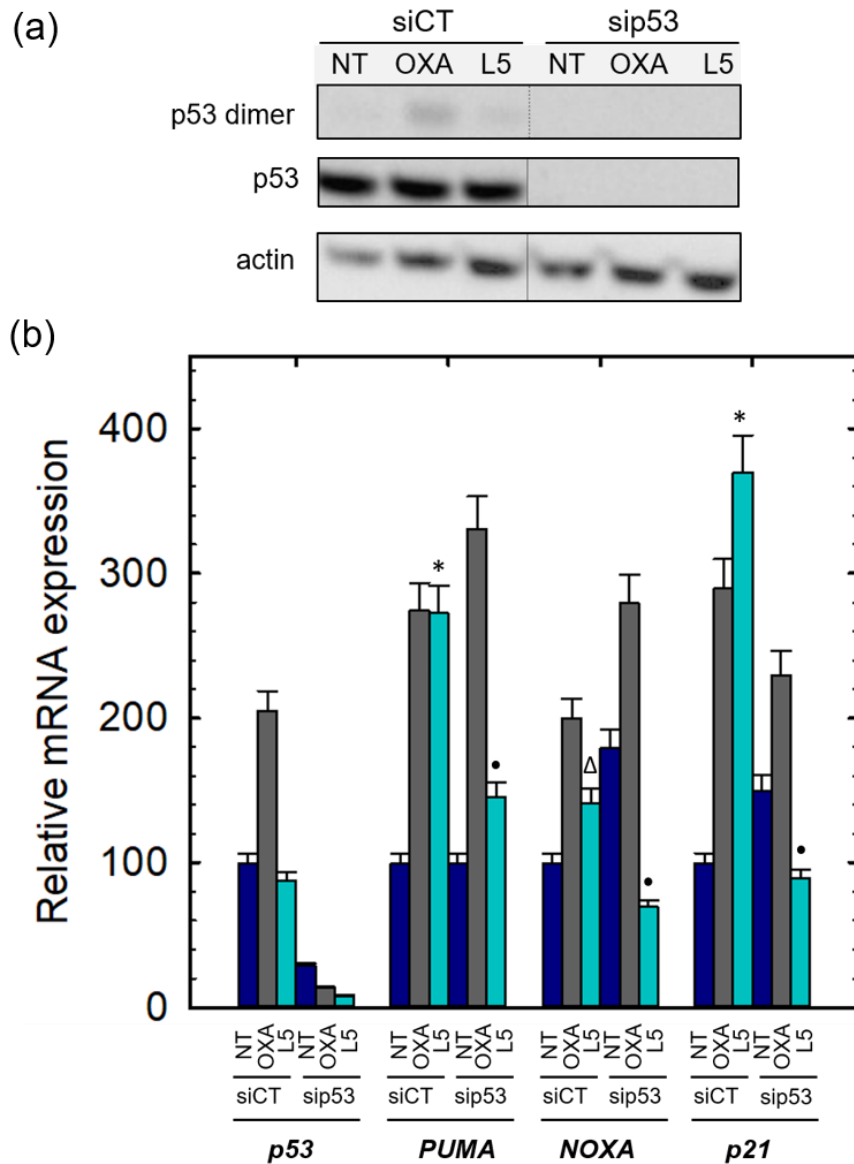


Figure 2.16. NUGC3 cells were transfected with control siRNA (siCT) or siRNA directed against p53 (sip53) and then treated for 24 hours with IC₅₀ concentrations of indicated compounds. Top: Total protein was extracted, and 20 μ g separated by SDS PAGE. p53 and actin were then detected by Western Blot. Bottom: Total RNA was extracted, and RT-qPCR performed to measure the expression of P53, P21, PUMA and NOXA. Bars represent means of triplicates with error bars. * indicates statistical differences from NT (siCT) with $p < 0.001$, Δ indicates statistical differences from NT (siCT) with $p < 0.01$, • indicates statistical differences from L5 (siCT) with $p < 0.001$.

2.3. Summary

The pharmacological reactivation of p53 is a key target in cancer research, and there is significant promise in the development of small molecules to restore wild-type function to specific p53 mutants. In this work we have designed a series of multifunctional molecules to reactivate the common p53-Y220C mutant. We show that compounds **L4** and **L5** exhibit Zn metallochaperone activity in the Y220C mutant NUGC3 cell line. Characterization of their *in vitro* cytotoxicity in the NCI-60 screen and on the stomach cancer cell lines AGS, MKN1, and NUGC3 identified lead compound **L5**, which displayed increased cytotoxicity compared to clinically validated cisplatin and oxaliplatin. Additionally, **L5** remained cytotoxic in 3D cell cultures, an important characteristic as this system more closely mimics physiological conditions. Further investigation into the mechanism of action shows that **L5** induces apoptosis in the mutant NUGC3 cell line via cleaved caspase-3, but not in wild-type AGS cells under the same conditions. This cytotoxicity is achieved at 19.5 μM **L5**, a concentration 10-fold smaller than oxaliplatin (250 μM , IC_{75}). Similar reports for Y220C-dependent induction of apoptosis using small molecules have been reported at higher concentrations, albeit on shorter time scales.^{153, 344-345} **L5** also restores p53 target gene transcription levels in the p53-Y220C mutant NUGC3 cell line. Upregulation of p53 target genes PUMA, NOXA, and p21 is significant, an effect that is decreased following knockdown of p53. These results are obtained in the absence of altered p53 expression, suggesting restoration of wild-type function.³⁴¹ Remarkably, our results for **L5** were obtained at low doses of 1.7 μM (**L5** IC_{50}), demonstrating the potent activity of this scaffold.^{199, 344} Although binding to recombinant p53C-Y220C was not observed at such low concentrations via SPR, further structural modifications can be made to increase protein affinity and ensure greater target selectivity.

Given the high levels of *in vitro* cytotoxicity of **L5** on both p53-Y220C and WTP53 cell lines, it is likely that the activity of **L5** is due to both p53-dependent and p53-independent mechanisms. Indeed, recent studies on p53 activating scaffolds show that increased ROS generation is an important component of the observed cytotoxicity, in addition to p53 activation.^{199, 226} In the case of metal-binding agents, ROS-associated toxicity could be due to the *in situ* formation of redox-active Cu complexes.^{226, 237} Overall, we have shown in this chapter that our novel series of bifunctional scaffolds have the potential to restore wild-type function in the p53-Y220C mutant and that **L5** is a promising scaffold for future

structure-activity relationship studies to increase affinity for p53-Y220C and improve selectivity. In combination with major technological advancements in gene sequencing capability and a shift towards personalized medicine, the development of small molecules capable of mutant-specific p53 reactivation holds significant promise.

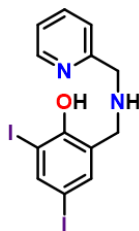
2.4. Experimental

2.4.1. Materials and Methods

All chemicals used were purchased from Sigma Aldrich and were further purified when necessary.³⁴⁶⁻³⁴⁷ (bis(2-pyridylmethyl)-amino)-ethylamine was prepared from commercially available di-(2-picolyl)amine by reported procedures.³⁴⁸ **L1** was synthesized according to published protocols.^{299, 349} All compounds were dried under vacuum for 1 week before in vitro cytotoxicity testing. ¹H and ¹³C NMR were recorded on Bruker-AV-400, 500, and 600 instruments. Mass spectra (positive ion) were obtained on an Agilent 6210 time-of-flight electrospray ionization mass spectrometer. Electronic absorption spectra were obtained on a Cary 5000 spectrophotometer. Immunofluorescence (IF) experiments were imaged using a fluorescence microscope (Axio Imager M2 Zeiss) coupled to a Hamamatsu's camera Orca Flash 4v3, using the ApoTome.2 (Zeiss) function.

2.4.2. Synthesis

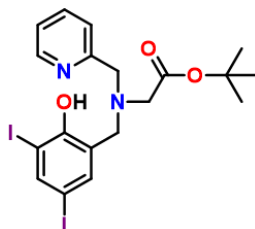
2,4-diiodo-6-(((pyridin-2-ylmethyl)amino)methyl)phenol (**L1**):



To a solution of 2-picolylamine (0.50 g, 4.62 mmol) in MeOH (5 mL) 3,5-diiodosalicylaldehyde (1.90 g, 5.09 mmol) in methanol (5 mL) was added. The solution immediately turned bright yellow upon addition of 3,5-diiodosalicylaldehyde and a yellow precipitate was formed. The reaction was stirred at room temperature for 30 minutes. NaBH₄ (0.12 g, 3.12 mmol) was added in small portions to the solution until a white precipitate formed. The white precipitate was collected and dried in vacuo. Yield: 1.85 g,

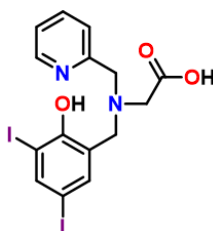
86%. ^1H NMR (500 MHz, CD_2Cl_2): δ = 8.61 (d, J = 4.8 Hz, 1H), 7.95 (d, J = 2.1 Hz, 1H), 7.73 (td, J = 7.6, 1.8 Hz, 1H), 7.33 – 7.21 (m, 3H), 3.95 (d, J = 9.5 Hz, 5H). $^{13}\text{C}\{^1\text{H}\}$ NMR (500 MHz, CDCl_3): δ = 157.8, 156.9, 149.6, 145.3, 137.2, 137.0, 124.9, 122.9, 122.8, 86.7, 80.7, 52.8, 51.4. Anal. Calcd (%) for $\text{C}_{13}\text{H}_{12}\text{I}_2\text{N}_2\text{O}$: C 33.55; H 2.60; N 6.01; found: C 32.4; H 2.64; N 5.91. Calcd for $[\text{M} + \text{H}]^+$, 466.9117; found, 466.9117.

tert-butyl N-(2-hydroxy-3,5-diiodobenzyl)-N-(pyridin-2-ylmethyl)glycinate:



To a solution of **L1** (0.30 g, 0.65 mmol) in acetonitrile (10 mL), *tert*-butyl bromoacetate (0.13 g, 0.65 mmol) and potassium carbonate (0.36 g, 2.60 mmol) were added. The resulting mixture was stirred overnight at room temperature, then filtered to remove KBr. The solvent was removed under vacuum to give a yellow residue, which was purified by silica gel column chromatography using $\text{CH}_2\text{Cl}_2/\text{MeOH}$ (95:5) as eluent to yield a yellow oil. Yield: 0.21 g, 56%. ^1H NMR (400 MHz, MeOD): δ = 8.48 (ddd, J = 5.0, 1.8, 0.9 Hz, 1H), 7.86 (d, J = 2.1 Hz, 1H), 7.77 (td, J = 7.7, 1.8 Hz, 1H), 7.34 (dt, J = 7.9, 1.1 Hz, 1H), 7.32 (d, J = 2.1 Hz, 1H), 7.28 (ddd, J = 7.6, 5.0, 1.2 Hz, 1H), 3.90 (s, 2H), 3.80 (s, 2H), 3.29 (s, 2H), 1.45 (s, 9H). $^{13}\text{C}\{^1\text{H}\}$ NMR (400 MHz, MeOD): δ = 171.7, 158.4, 157.9, 149.6, 146.9, 139.6, 138.7, 126.5, 124.9, 124.1, 87.0, 83.1, 81.4, 59.8, 57.0, 56.3, 28.4. HR-MS: Calcd for $[\text{M} + \text{H}]^+$, 580.9820; found, 580.9815.

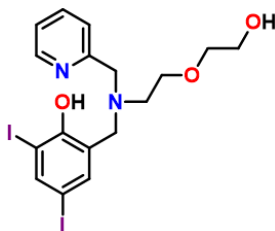
N-(2-hydroxy-3,5-diiodobenzyl)-N-(pyridin-2-ylmethyl)glycine (**L2**):



A solution of **1** (0.21 g, 0.36 mmol) in 2 mL of $\text{H}_2\text{O}/\text{HCl}$ (10:1) was stirred at room temperature for 48 hours. The solvent was removed under vacuum and the final product was purified by recrystallization with $\text{Et}_2\text{O}/\text{MeOH}$ (1:2) to afford a white solid. Yield: 0.16 g, 82%. ^1H NMR (400 MHz, CD_2Cl_2): δ = 8.59 (d, J = 3.8 Hz, 1H), 7.95 (d, J = 2.1 Hz, 1H),

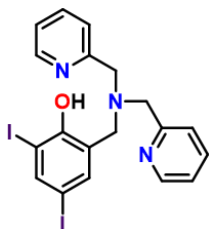
7.72 (td, $J = 7.7, 1.8$ Hz, 1H), 7.30 (dt, $J = 2.1, 0.7$ Hz, 1H), 7.27 – 7.23 (m, 2H), 4.02 (s, 2H), 3.84 (s, 2H), 3.41 (s, 2H). $^{13}\text{C}\{^1\text{H}\}$ NMR (400 MHz, CD_2Cl_2): $\delta = 171.5, 157.5, 149.2, 146.2, 139.0, 137.5, 125.5, 123.5, 123.0, 86.89, 80.5, 58.7, 55.9, 31.0$. Anal. Calcd (%) for $\text{C}_{15}\text{H}_{14}\text{I}_2\text{N}_2\text{O}_3 \cdot \text{HCl} \cdot \text{H}_2\text{O}$: C, 31.14; H, 2.96; N, 4.84; found: C, 31.04; H, 3.29; N, 4.83. HR-MS: Calcd for $[\text{M} + \text{H}]^+$, 524.9173; found, 524.9165.

2-(((2-(2-hydroxyethoxy)ethyl)(pyridine-2-ylmethyl)amino)methyl)-4,6-diiodophenol (**L3**):



To a solution of **L1** (0.46 g, 0.99 mmol) in acetonitrile (10 mL), 2-(2-chloroethoxy)ethanol (0.12 g, 0.99 mmol) and potassium carbonate (0.68 g, 4.93 mmol) was added. The solution was refluxed for 48 hours, after which the solution was cooled to room temperature and filtered. The solvent was removed under vacuum to give a yellow residue, which was purified by silica gel column chromatography using $\text{CH}_2\text{Cl}_2/\text{MeOH}$ (5:1) as eluent to yield a yellow oil. Yield: 0.43 g, 78%. ^1H NMR (400 MHz, CDCl_3): $\delta = 8.52$ (d, $J = 5.0$ Hz, 1H), 7.87 (d, $J = 2.1$ Hz, 1H), 7.68 (td, $J = 7.7, 1.8$ Hz, 1H), 7.28 (s, 1H), 7.23 (d, $J = 2.0$ Hz, 1H), 7.20 (dd, $J = 7.6, 4.9$ Hz, 1H), 3.86 (s, 2H), 3.78 (s, 2H), 3.73 (t, $J = 4.9$ Hz, 2H), 3.56 (t, $J = 5.1$ Hz, 2H), 3.50 (t, $J = 4.9$ Hz, 2H), 2.82 (t, $J = 5.0$ Hz, 2H). $^{13}\text{C}\{^1\text{H}\}$ NMR (500 MHz, CDCl_3): $\delta = 156.9, 156.5, 149.2, 145.4, 137.5, 137.2, 124.9, 123.9, 122.9, 86.7, 81.1, 72.8, 67.7, 61.8, 59.5, 57.0, 52.9$. HR-MS: Calcd for $[\text{M} + \text{Na}]^+$, 576.9461; found, 576.9457.

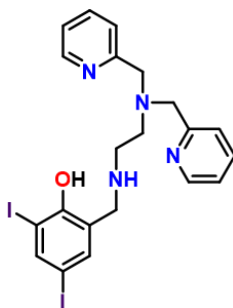
2-((bis(pyridin-2-ylmethyl)amino)methyl)-4,6-diiodophenol (**L4**):



To a solution of di-(2-picoly)amine (0.20 g, 1.00 mmol) in 1,2-dichloroethane (5 mL) 3,5-diiodosalicylaldehyde (0.40 g, 0.11 mmol) in 1,2-dichloroethane (5 mL) was added under a N_2 atmosphere. The resulting bright orange solution was stirred at room

temperature for 1 hour, at which time sodium triacetoxyborohydride (0.34 g, 1.6 mmol) was added. The mixture was stirred overnight at room temperature under N₂. Water (10 mL) was added and the mixture was stirred for 30 minutes. The organic phase was separated from the aqueous phase and dried over MgSO₄. The solvent was removed under vacuum and the final product was purified by recrystallization in cold MeOH. Yield: 0.53 g, 95%. ¹H NMR (500 MHz, CD₂Cl₂): δ = 8.60 (dd, *J* = 5.0, 1.8 Hz, 2H), 7.96 (d, *J* = 2.1 Hz, 1H), 7.96 (d, *J* = 2.1 Hz, 1H), 7.70 (td, *J* = 7.7, 1.8 Hz, 2H), 7.39 (d, *J* = 2.1 Hz, 1H), 7.32 (d, *J* = 7.8 Hz, 2H), 7.24 (dd, *J* = 7.5, 4.9 Hz, 2H). ¹³C{¹H} NMR (500 MHz, CD₂Cl₂): δ = 158.2, 157.6, 149.2, 145.9, 139.3, 137.2, 126.3, 123.5, 122.7, 87.0, 80.3, 59.0, 56.7. Anal. Calcd (%) for C₁₉H₁₇I₂N₃O•H₂O: C, 39.68; H, 3.33; N, 7.31; found: C 39.36; H 3.17; N 6.96. HR-MS: Calcd for [M + H]⁺, 557.9539; found, 557.9529.

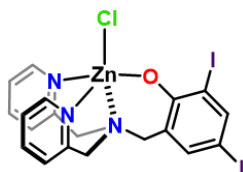
2-(bis(pyridin-2-ylmethyl)amino)ethylamino)methyl)-4,6-diiodophenol (**L5**):



To a solution of (bis(2-pyridylmethyl)-amino)-ethylamine (0.68 g, 2.84 mmol) in MeOH (17 mL) 3,5-diiodosalicylaldehyde (1.17 g, 3.13 mmol) was added under N₂ atmosphere. The resulting orange solution was stirred at room temperature for 30 minutes after which the solution was cooled in an ice bath and solid NaBH₄ (0.17 g, 4.52 mmol) was added in small portions. The mixture was then stirred overnight under N₂. Water (10 mL) was poured into the solution and stirred for 30 minutes. The organic phase was separated from the aqueous phase, dried over MgSO₄, and the solvent was removed under vacuum. The final product was purified by recrystallization with CH₂Cl₂/pentane (1:2). Yield: 1.08 g, 64%. ¹H NMR (400 MHz, MeOD): δ = 8.39 (dd, *J* = 5.0, 1.8 Hz, 2H), 7.83 (d, *J* = 2.3 Hz, 1H), 7.73 (td, *J* = 7.7, 1.8 Hz, 2H), 7.42 (dt, *J* = 7.9, 1.1 Hz, 2H), 7.29 – 7.22 (m, 3H), 3.95 (s, 2H), 3.84 (s, 4H), 3.01 (dd, *J* = 6.8, 4.6 Hz, 2H), 2.93 (dd, *J* = 6.4, 4.2 Hz, 2H). ¹³C{¹H} NMR (600 MHz, MeOD): δ = 165.1, 160.0, 149.8, 147.1, 139.2, 138.9, 125.3, 124.1, 123.9, 92.7, 74.4, 61.0, 53.1, 51.2, 45.8. Anal. Calcd (%) for

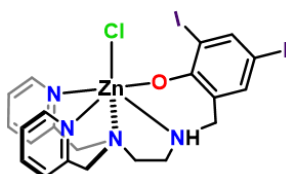
$C_{21}H_{22}I_2N_4O \cdot H_2O$: C, 40.80; H, 3.91; N, 9.06; found: C 40.71; H 4.01; N 8.96. HR-MS: Calcd for $[M + H]^+$, 600.9962; found, 600.9953.

ZnL4Cl:



To a solution of **L4** (0.10 g, 0.18 mmol) in MeOH (3 mL), KOH (0.01 g, 0.18 mmol) and $ZnCl_2$ (0.03 g, 0.18 mmol) were added. The solution was stirred at room temperature for 1 hour. The precipitated white solid was filtered and washed with cold MeOH. Yield: 0.09 g, 76%. 1H NMR (600 MHz, $(CD_3)_2SO$): δ = 9.01 (d, J = 5.0 Hz, 2H), 8.06 (td, J = 7.7, 1.7 Hz, 2H), 7.62 (dd, J = 7.5, 5.3 Hz, 2H), 7.56 (d, J = 2.3 Hz, 1H), 7.53 (d, J = 7.9 Hz, 2H), 7.24 (d, J = 2.4 Hz, 1H), 4.11 – 3.98 (m, 4H), 3.59 (s, 2H). $^{13}C\{^1H\}$ NMR (600 MHz, $(CD_3)_2SO$): δ = 165.31, 155.22, 148.36, 144.37, 140.52, 138.94, 124.91, 124.22, 124.00, 94.96, 72.36, 57.54, 57.09. HR-MS: Calcd for $[M - Cl]^+$, 618.8674; found, 618.8683. Crystals suitable for X-ray diffraction experiments were obtained by slow diffusion of a concentrated CH_2Cl_2 solution into MeOH.

ZnL5Cl:



To a solution of **L5** (0.03 g, 0.05 mmol) in MeOH (5 mL), KOH (2.8 mg, 0.05 mmol) and $ZnCl_2$ (6.8 mg, 0.05 mmol) were added and the solution was stirred at room temperature for 1 hour. The resulting white solid was collected using vacuum filtration and washed with cold MeOH. Yield: 0.028 g, 80%. 1H NMR (400 MHz, $(CD_3)_2SO$): δ 8.73 (d, J = 5.1 Hz, 1H), 8.41 (d, J = 5.2 Hz, 1H), 8.12 (td, J = 7.7, 1.7 Hz, 1H), 8.06 (td, J = 7.7, 1.7 Hz, 1H), 7.83 (d, J = 2.3 Hz, 1H), 7.63 (t, J = 6.6 Hz, 4H), 7.55 (d, J = 7.9 Hz, 1H), 7.24 (d, J = 2.4 Hz, 1H), 4.46 – 4.31 (m, 3H), 4.12 (d, J = 16.3 Hz, 1H), 3.90 (s, 1H), 3.55 (t, J = 11.6 Hz, 1H), 3.45 (d, J = 11.6 Hz, 1H), 3.04 (d, J = 13.6 Hz, 1H), 2.64 – 2.56 (m, 1H). HR-MS: Calcd for $[M - Cl]^+$ 662.9096; found, 662.9085.

2.4.3. Molecular Modeling

Default parameters were used for all computational procedures unless otherwise stated. All computational methods were performed in the Molecular Operating Environment version 2015 (MOE, Chemical Computing Group, Montreal, Canada). Images were generated in POV-ray engine v3.7.0 (www.povray.org). MOE implements a derivative of the AMBER12 force field for proteins, integrated with the Extended Hückel Theory and AM1-BCC method for handling small molecules.³⁵⁰ Ligands were drawn in MOE, and a stochastic conformational library was generated for each using default parameters. Inspection of the crystal structures 4AGL, 4AGN, 4AGO, 4AGP, 4AGQ (all containing structurally relevant iodophenol ligands), showed minimal differences in either the protein or ligand conformations, indicating a well-defined complex for docking purposes. Each crystal structure listed above contains a conserved water molecule bridging the backbone carbonyl of Asp228, the carbonyl and amide proton of Val147, and the phenol of the ligand. All solvent molecules except this one were removed from the structure used for docking (PDB:4AGQ). The protein was protonated using the Protonate3D algorithm in the Born solvation model, using the Lennard-Jones 12-6 potential, and dielectric constants of 78.6 and 4 for bulk solvent and the protein, respectively. The ligands **L1-L5** were docked into the cavity formerly occupied by the co-crystallized ligand. For each ligand, 1000 binding poses were generated, with force field-energy minimisation (RMSG=0.001) of the best 200 non-duplicate poses as ranked by the GB/VI scoring function. The pose with the lowest deviation in iodophenol atoms compared to 4AGQ were selected for each ligand.

2.4.4. X-ray Structure Determination of L4

X-ray structure determinations were performed on a Bruker APEX II Duo diffractometer with graphite monochromated Mo K α radiation. A transparent block crystal was mounted on a 150 μ m MiteGen sample holder. Data were collected at 293 K to a maximum 2θ value of $\sim 60^\circ$. Data were collected in a series of ϕ and ω in 0.50° widths with 10.0 s exposures. The crystal-to-detector distance was 50 mm. The structure was solved by intrinsic phasing³⁵¹ and refined using ShelXle.³⁵² All non-hydrogen atoms were refined anisotropically. All C-H hydrogen atoms were placed in calculated positions but were not refined. Zn**L4**Cl crystallizes with two molecules of ZnL4Cl and one molecule of CH₂Cl₂ in the asymmetric unit. CCDC number: 1828874.

2.4.5. Stability Constant Determination

Aqueous acidity constants (pK_a) for **L1-L5** were measured using variable pH titrations monitored by UV-visible spectroscopy between 200 and 600 nm as a function of pH. Solutions of all five ligands (12.5 μ M) were prepared in 0.1 M NaCl at pH 3. Due to the limited aqueous solubility of **L1**, solutions of 20% MeOH in H₂O of **L1-L5** were prepared for consistency. Small aliquots of 0.1 M NaOH were titrated into the solution to adjust the pH and at least 30 UV-vis spectra were collected in the pH 3-11 range. Spectral data were analyzed using HypSpec (Protonic Software, UK)³⁵³. Similarly, metal stability constants were obtained by titrating a solution containing 12.5 μ M ligand, 0.1 M NaCl and Zn(ClO₄)₂•6H₂O with 0.1 M NaOH to adjust the pH. For **L1-L3**, 6.25 μ M Zn(ClO₄)₂ was used, whereas 12.5 μ M Zn(ClO₄)₂ was used for **L4** and **L5**. Known metal hydrolysis constants were included in the HypSpec simulations as constant values.³⁵⁴ At least 30 UV-vis spectra were collected in the pH 3-11 range. Stability constants were calculated using the HypSpec computer program and metal speciation plots were created using the HySS2009 program (Protonic Software, UK).³⁵³

2.4.6. Increasing Intracellular Levels of Zn²⁺ in the p53-Y220C Cell Line NUGC3

NUGC3 cells (4x10⁵ cells/well) were plated on glass coverslips treated with poly-L-lysine in 12-well plates. After 48 hours, cells were washed twice with Earle's balanced salt solution (EBSS)/H (-) Ca/Mg media and incubated with 1 μ M FluoZin-3 for 20 minutes at 37°C. Cells were then washed twice with EBSS media followed by addition of the indicated treatments (ZnCl₂ = 50 μ M, **L4** = **L5** = 15 μ M) and incubated for 2 hours at 37 °C before imaging. Cells were imaged using a Nikon ApoTome microscope (Nikon, France). FluoZin-3 and Hoechst 33342 were excited at 488 nm (argon laser) and 790 nm (Chameleon Ti:sapphire laser), respectively. Imaging was performed in under ten minutes to avoid alteration of cell physiology upon imaging at room temperature. To determine the change in fluorescence, each image was processed using ImageJ Software (National Institutes of Health, Bethesda, MD) and integrated to represent the cumulative fluorescence for a single cell. Processing included adjustment of exposure and contrast to eliminate autofluorescence of the support. To exclude autofluorescence, each image was background-subtracted using the non-treated control. All images were batch processed using the same parameters. Cells were analyzed upon treatment with 50 μ M

pyrithione (PYR)/ZnCl₂ (1:1) as a positive control, and 150 μM TPEN as a negative control. Cells were also analyzed upon addition of 150 μM TPEN to cells previously treated with ZnCl₂ and **L5**. Statistical differences were analyzed using One-Way ANOVA with multiple comparisons. Bartlett's test showed unequal variance. Three replicate experiments were performed independently with 100 cells per trial.

2.4.7. *In Vitro* Cytotoxicity – NCI-60 Screening

Ligands **L1-L5** were submitted to the Developmental Therapeutics Program at the U.S National Cancer Institute for screening on a panel of 60 human tumour cell lines. Compounds are initially tested at a single high dose (10 μM) and those that satisfy pre-determined thresholds will be tested in a five-dose assay.³⁵⁵ The methodology used in the NCI-60 screen has been described elsewhere.³²⁰

2.4.8. *In Vitro* Cytotoxicity – Stomach Cancer Cell Lines

The *in vitro* cytotoxicity of **L1-L5** against stomach cancer cell lines AGS, MKN1, and NUGC3 were assayed using the 3-(4,5-dimethylthiazol-2-yl)-2,5-diphenyltetrazolium bromide (MTT) assay.³⁵⁶ In each case, cells were seeded at 10⁵ cells per well in 100 μL of RPMI media in Cellstar 96-well plates (Grenier Bio-One) and incubated at 37 °C with 5% CO₂ for 24 hours. Following incubation, the cells were exposed to drugs at increasing concentrations ranging from 0.1 to 200 μM in RPMI medium. Compounds were pre-dissolved in DMSO stocks and serial dilutions were prepared such that the final concentration of DMSO in media was below 1% (v/v). Treated cells were incubated at 37 °C with 5% CO₂ for 48 hours. Following the 48-hour incubation, the MTT test was performed as previously described.³⁵⁷ Experiments were performed in replicates of eight and repeated at least twice. Inhibition of cell viability was evaluated with reference to NT control to determine the absolute IC₅₀ value calculated from dose-response curves using nonlinear variable slope regression (Graphpad Prism 5.0 software).

2.4.9. Western Blot Analysis

NUGC3 cells were lysed with lysis buffer (125 mM Tris-HCl pH 6.7, NaCl 150 mM, NP40 0.5%, 10% glycerol). Proteins were denatured and deposited directly (75 μg total protein) onto an SDS-PAGE gel. A Western Blot was performed using the pan-specific

DO-1 primary antibody (Santa Cruz, sc-126) or cleaved caspase-3 Asp175 Antibody (Cell Signaling, 9661) at 1:1000 in phosphate buffered saline (PBS) containing 5% dry milk at 4 °C overnight. Loading was controlled with rabbit anti- β -actin (Sigma, a1978, 1:4000). Secondary antibodies (anti-rabbit, anti-mouse: GE Healthcare) were incubated at 1:1000 for three hours at room temperature.

2.4.10. Site-Directed Mutagenesis

The plasmid encoding the DNA-binding domain of human wild-type p53 (residues 94-312) was gifted by Cheryl Arrowsmith.³⁵⁸ Four mutations to the p53 gene (M133L/V203A/N239Y/N268D) were successively introduced to increase structural stability of the protein, followed by addition of the Y220C mutation.³⁵⁹ All p53 mutants were prepared by site-directed mutagenic polymerase chain reaction (PCR) according to standard protocols,¹⁵² using primers purchased from Eurofins Operon following Quikchange protocol (Agilent Technology). DNA polymerase (Q5) and DpnI enzyme were obtained from New England Biolabs. PCR products were transformed into chemically competent DH5 α *E. coli* and selected on ampicillin-supplemented agar plates. Single colonies obtained from overnight incubation at 37 °C were grown in Luria-Bertani (LB) broth for 16 hours. Plasmid DNA was purified using the plasmid spin MiniPrep kit (Qiagen, 27104) and sequenced by Eurofins Operon Sequence read service.

2.4.11. Protein Expression and Purification

Proteins were overexpressed using *E. coli* strain BL21-pLysS cells (ThermoFisher). Expression cultures containing 100 μ g/mL ampicillin were inoculated from an overnight culture and grown at 37 °C to an OD₆₀₀ of 0.7. Protein expression was induced overnight at 15 °C with 0.3 mM Isopropyl β -D-1-thiogalactopyranoside (IPTG). Cells were then harvested by centrifugation at 6500 rpm for 20 minutes. Cell pellets were resuspended in lysis buffer (50 mM Tris-HCl buffer, pH 6.5, 300 mM NaCl, 10% glycerol, 1% Triton X-100, 5 mM imidazole, 6 mM MgSO₄, 1 mM phenylmethylsulfonyl fluoride (PMSF), and 5 mM β -mercaptoethanol) and sheared using ultrasonication. Cellular debris was isolated by centrifugation at 14000 rpm for 30 minutes and incubated with Talon® beads (cobalt-nitrilotriacetic acid) at 4 °C for 30 minutes. Talon beads were transferred to a column, washed twice with 20 mL of wash buffer (50 mM Tris-HCl buffer, pH 6.5, 500 mM NaCl, 10% glycerol, 10 mM imidazole, 0.5 mM Tris(2-carboxyethyl)phosphine

(TCEP), 1 mM PMSF, and 5 mM β -mercaptoethanol), and eluted with wash buffer containing 500 mM imidazole.¹⁵² Protein concentration was determined spectrophotometrically using the reported extinction coefficient $\epsilon_{280} = 17,130 \text{ cm}^{-1}$.³⁶⁰

2.4.12. Surface Plasmon Resonance

Due to limited solubility, binding of **L1-L4** to p53C-Y220C could not be investigated. Limited protein solubility also precluded the use of isothermal calorimetry (ITC) as a complimentary binding tool. Surface plasmon resonance experiments for **L5** were performed using a Biacore X100 (GE Healthcare). Following activation with N-Hydroxysuccinimide and N-Ethyl-N'-(3-dimethylaminopropyl)carbodiimide (NHS/EDC), 100 $\mu\text{g/mL}$ of purified mutant p53C-Y220C in 10 mM sodium acetate at pH 4.5 were injected into channel two to immobilize p53C-Y220C to a final resonance value of 3,000 response units. The first channel was used as a blank control. Subsequent quenching of remaining active groups was achieved using 1 M ethanolamine. Three buffer injections were made to prime the system prior to each run. Various concentrations of **L5** ranging from 0 μM to 800 μM in running buffer (HBS-EP+ - GE Healthcare: 10 mM (4-(2-hydroxyethyl)-1-piperazineethanesulfonic acid) (HEPES), 150 mM NaCl, 3 mM EDTA, 0.05% v/v Surfactant P20, pH 7.4) containing 5% DMSO were injected. The association and dissociation phase were monitored for 60 and 100 seconds respectively. The binding responses in the steady-state region of the sensorgram (R_{eq} , 100 seconds) can be plotted against **L5** concentration to determine the equilibrium dissociation constant (K_d). Unfortunately, **L5** has limited solubility beyond 400 μM , and therefore higher micromolar binding affinities could not be accurately measured under these conditions.

2.4.13. Immunoprecipitation

NUGC3 cells were seeded at a density of 850,000 cells per petri dish and incubated at 37°C with 5% CO_2 for 48 hours, followed by treatment with 15 and 30 μM **L5** for 2 hours. Cells were lysed with NP40 lysis buffer (50 mM Tris-HCl pH 8, NaCl 150 mM, NP40 1%, Complete protease inhibitor). 1 mg of native lysates were incubated with 4 μg of p53 mutant antibody (Santa Cruz, PAb240, sc-99) and 30 μL of protein G beads (Protein G agarose, Roche) on a rotator. Samples were washed three times with lysis buffer, then 30 μL of loading buffer (50 mM Dithiothreitol (DTT), 2x Laemmli buffer (Bio-Rad)) was added and samples were boiled at 95°C for 5 min to collect the eluates. Western Blot

analysis was carried out as described above using the pan-specific DO-1 antibody (Santa Cruz, sc-126).

2.4.14. Upregulation of p53 Transcription Factors by RT-qPCR

NUGC3 cells were lysed with 1 mL of TRIzol (Invitrogen) per 10×10^6 cells and RNA was extracted according to the manufacturer's instructions. RNA samples were precipitated twice using ethanol, RNA quality was assessed, and 1 μg was used for reverse transcription (High-Capacity cDNA Reverse Transcription Kit, Applied Biosystems). qPCR was performed using 2 ng/ μL cDNA (RNA equivalent) according to the manufacturer's instructions (SYBR Green PCR Master Mix, Applied Biosystems) and with 400 μM of each primer. The relative expression was calculated using the $\Delta\Delta\text{Ct}$ method. Expression levels were normalized using G6PDH.

2.4.15. Silencing of p53 in NUGC3 Cells Using siRNA

SiRNA transfection of NUGC3 cells was performed with 30 nM of p53-targeted siRNA using lipofectamine (RNAiMAX from ThermoFisher, 13778100) as previously described.³⁶¹

Chapter 3. Ligand Modifications for Targeting Subsite Cavities in Mutant p53-Y220C

JJM performed the synthesis with assistance from Sabrina Lechnitz (**L5-P**) and Marie Sabatou (**L5-O**). JJM carried out the spectroscopic titrations and zinc-binding studies. Christophe Orvain performed the zinc uptake study. Jason Smith performed the molecular docking experiments. JJM performed the cytotoxicity (2D and 3D) studies. Anaïs Blanchet performed the cleaved caspase 3 studies. JJM and Cristina Lento performed the MS experiment.

3.1. Introduction

This chapter explores the design and synthesis of ligands aimed to restore wild-type function in mutant p53-Y220C. As previously described, the Y220C point mutation is a common p53 destabilizing mutation that results in the formation of a cavity at the surface of the protein and ultimately leads to protein unfolding and loss of function.³⁶² Research has shown that stabilization of this cavity with small molecules can prevent protein unfolding and restore wild-type function in this p53 mutant.¹⁵³ In chapter 2 we demonstrated the utility of our bifunctional scaffold in restoring wild-type function in p53-Y220C by serving as structural stabilizers and as Zn-chaperones. Our ligand series contained a p53-Y220C binding diiodophenol core¹⁵³ and di-(2-picoly)amine as the Zn-binding group to promote metallochaperone activity. Our lead compound, **L5**, induced Y220C-specific apoptosis, reduced levels of unfolded mutant p53, and recovered partial p53 transcriptional function. However, protein-binding at biologically active concentrations (low micromolar) was not observed, and high *in vitro* cytotoxicity in both p53-Y220C and WTp53 cell lines led us to hypothesize that p53-independent activities were contributing to the observed response. We therefore aimed to optimize the structure of our lead compound for improved protein-targeting and selectivity.

Previous reports on the p53-Y220C mutant have demonstrated the presence of additional subsites within the mutant cavity, and that targeting these additional subsites led to a significant increase in the binding affinity of the small molecules, thereby increasing protein stabilization.^{153, 363} As shown in Figure 3.1, in addition to the central mutant cavity (shown in blue), p53-Y220C contains additional subsites 1 (red) and 2

(green). Subsite 1 consists of a shallow cavity with neighbouring solvent-exposed residues. Subsite 2, which was previously unoccupied by **L5** according to our docking results, contains a narrow gap between Cys220 and Pro151. Previous *in silico* screening by Fersht *et al* showed that an acetylene linker was well suited to bridge the narrow gap between the central cavity and subsite 2. The addition of aromatic groups onto the alkyne led to favourable π -stacking interactions with Pro153.¹⁵³

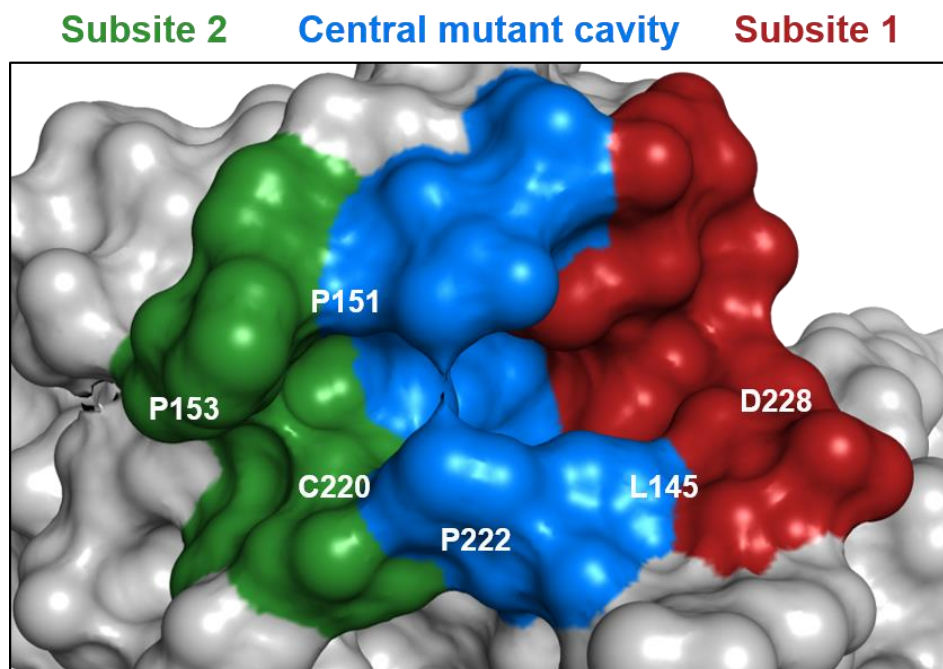


Figure 3.1. Molecular surface view of the p53-Y220C mutant cavity (PDB ID: 4AGQ). The cavity can be divided into three parts: the central mutant cavity (blue), an open subsite 1 (red) that contains many solvent-exposed amino acids and a narrow subsite 2 (green). Various amino acids located around these subsites are indicated in white.

In this chapter, we explore the design of novel ligands **L5-P** and **L5-O**, designed to occupy the additional mutant subsites in p53-Y220C and restore wild-type protein function. A full description of the ligand design and synthesis, characterization, and *in vitro* cytotoxicity testing of our new series of bifunctional ligands is provided. We further investigate the mechanism of cytotoxicity and explore the ability of our ligand series to restore apoptotic function in mutant p53-Y220C.

3.2. Results and Discussion

3.2.1. Ligand Design and Synthesis

Ligands **L5-P** and **L5-O** were designed to restore wild-type function in p53-Y220C with the aim of extending the structure beyond the central mutant cavity and occupying the additional subsites to stabilize the protein and prevent loss-of-function. These ligands build from our lead structure from Chapter 2, wherein we investigate the effects of tuning the spacer between the zinc-binding unit and phenol and modulate the iodinated phenol core (Figure 3.2). In chapter 2, we saw markedly increased biological activity in **L5** over **L4**, simply by substituting the methyl spacer between the tertiary amine and phenol for an ethyl spacer. We envision that by pushing the zinc chelating unit further into the open space in subsite 1, there is less steric crowding and a greater potential for interactions with the solvent-exposed amino acids located within the subsite. Thus, we designed **L5-P** to contain a propyl spacing unit between the tertiary amine and phenol. To probe the effects of modifying the phenol, **L5-O** contains an alkyne substituted with a phenoxy moiety with the aim of π -stacking interactions with amino acids in subsite 2.

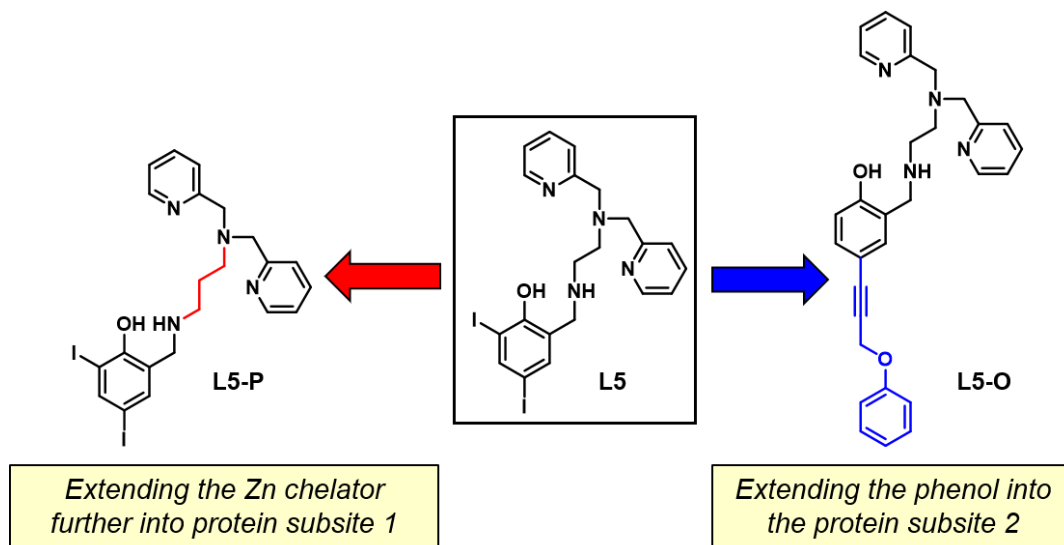
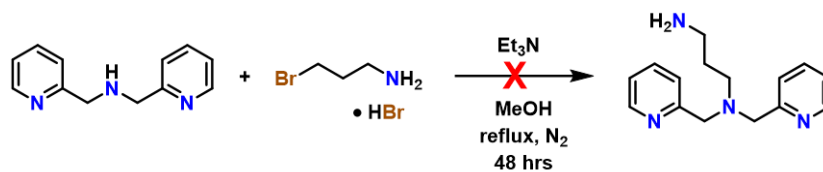


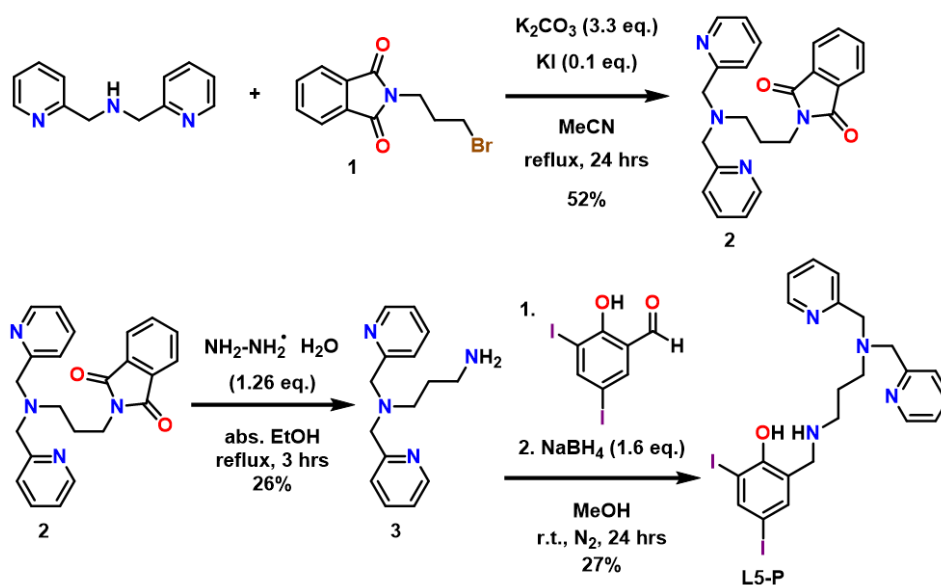
Figure 3.2. Structure optimization of our lead compound from Chapter 2, **L5**. By modifying the spacer between the iodinated phenol and zinc chelator as well as substituting functional groups on the phenol, this chapter studies the synthesis, characterization, and biological properties of ligands **L5-P** and **L5-O**.

The synthetic strategies for **L5-P** and **L5-O** are presented in Scheme 3.2 and Scheme 3.6. The ligands were prepared via reductive amination of the corresponding

aldehyde and amines. Initial attempts to synthesize **L5-P** used similar chemistry to that of **L5** (Scheme 2.5), by reacting 3-bromopropylamine and di-(2-picolyl)amine to form the extended di-(2-picolyl)amine (Scheme 3.1). However, due to the polymerization of 3-bromopropylamine, the reaction was unsuccessful. We then carried out the reaction using the N-protected 3-bromopropylamine (**1**). (**2**) was synthesized via SN₂-reaction of di-(2-picolyl)amine and (**1**), followed by a hydrazinolysis to give the precursor (**3**). In the next step, (**3**) and 3,5-diiodosalicylaldehyde afforded an intermediate imine that was reduced *in situ* to yield the secondary amine **L5-P** (Scheme 3.2).



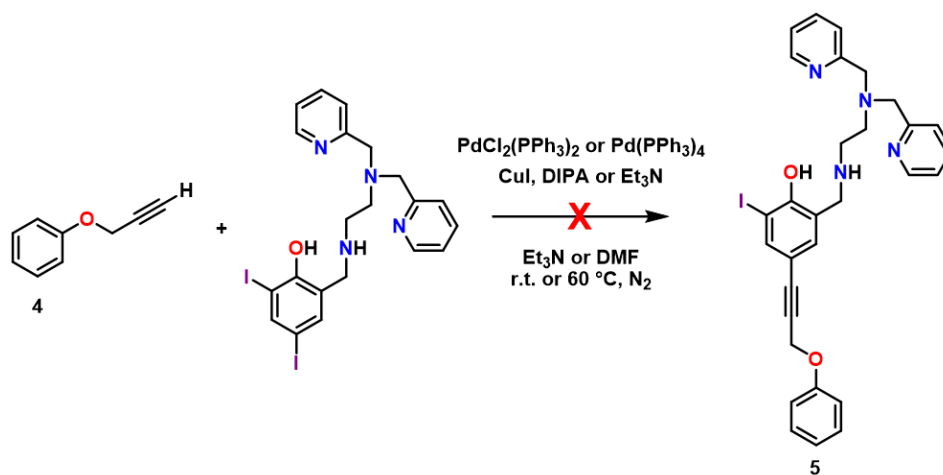
Scheme 3.1. Attempted synthesis of **L5-P** using di-(2-picolyl)amine and 3-bromopropylamine. However, due to polymerization of 3-bromopropylamine, the reaction was unsuccessful.



Scheme 3.2. Synthesis of **L5-P**. Yield: 27%.

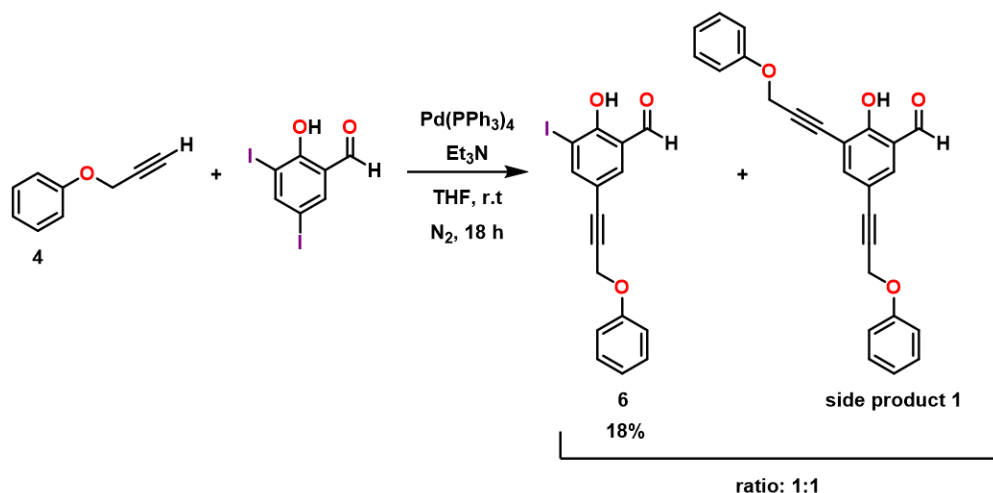
The initial design for **L5-O** contained an iodine at the 3-position with a substituted alkyne coupled onto the iodine at the 5-position. However, the Sonogashira cross-coupling reaction proved to be synthetically challenging in this case, resulting in extremely low yields and poor purification. Initial attempts involved a Sonogashira cross-coupling

between **L5** and (prop-2-yn-1-yloxy)benzene (**4**) (Scheme 3.3), however, no product formation was observed despite attempts to optimize conditions and vary the Pd(II) catalyst ($\text{PdCl}_2(\text{PPh}_3)_2$ or $\text{Pd}(\text{PPh}_3)_4$) and base (N,N-Diisopropylethylamine or triethylamine). We hypothesized that due to the strong metal-binding properties of the di-(2-picolyl)amine unit in **L5**, the Sonogashira coupling is inhibited due to chelation of Pd and/or Cu by **L5** and thus the reaction is inhibited.



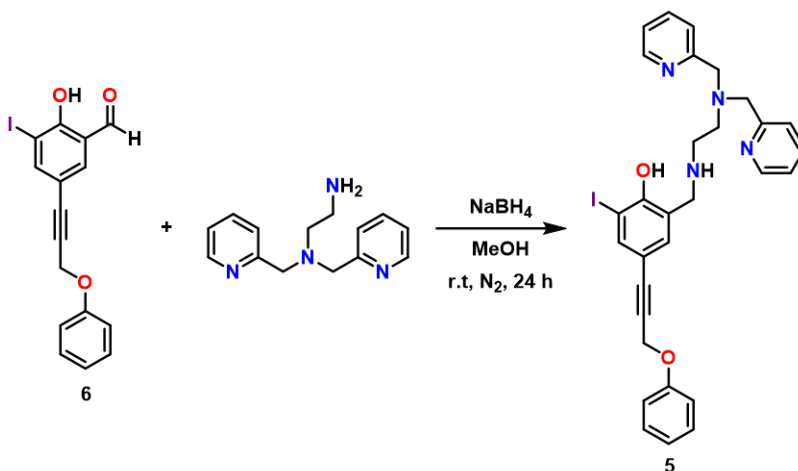
Scheme 3.3. Attempted synthesis of (**5**) using **L5** and (prop-2-yn-1-yloxy)benzene (**4**). However, due to the strong metal-binding ability of **L5**, the Sonogashira coupling is inhibited and the reaction was unsuccessful.

In order to avoid metal chelation by di-(2-picolyl)amine, the next attempt involved a Sonogashira coupling at step 1 using (prop-2-yn-1-yloxy)benzene (**4**) and 3,5-diiodosalicylaldehyde according published procedures.¹⁵³ Due to the unselective nature of the Sonogashira coupling between the iodines at position 3 and 5, dialkylation of 3,5-diiodosalicylaldehyde occurred and thus significantly lowered the yield of the desired product (**6**) (Scheme 3.4).



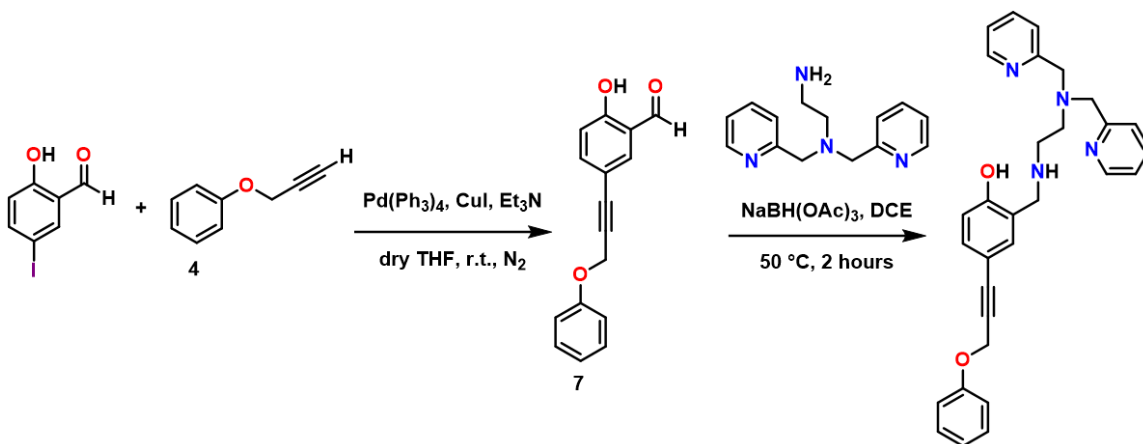
Scheme 3.4. Synthesis of desired product (**6**) and unwanted dialkylated side product from the Sonogashira coupling reaction. Yield (**6**): 18%.

The final step in the synthesis of (**5**) involved a condensation reaction between (bis(2-pyridylmethyl)-amino)-ethylamine and (**6**) (Scheme 3.5). While the crude product was detected via electrospray ionization mass spectrometry (ESI-MS) and ¹H NMR, purification using silica chromatography was very difficult due to poor separation, resulting in very low yields (<10%).



Scheme 3.5. Synthesis of (**5**). Yield: <10%.

In order to simplify the synthetic route and increase yields, we chose to forego the iodine at the 3-position and simply investigate the effects of extending the phenol into the protein subsite 2 with **L5-O**. Optimized Sonogashira coupling conditions from Scheme 3.4 afforded (**7**), followed by condensation reaction with (bis(2-pyridylmethyl)-amino)-ethylamine to afford **L5-O** in good yield (Scheme 3.6).



Scheme 3.6. Synthesis of **L5-O**. Yield: 62%.

3.2.2. Molecular Docking

Molecular docking simulations were carried out in order to visualize potential binding modes of **L5-P** and **L5-O** and determine whether their structures can extend into the desired mutant subsites. Using available protein X-ray data of mutant p53-Y220C,¹⁵³ ligands were inserted into the mutant cavity and 200 non-duplicate poses were generated to determine the lowest energy conformation. For **L5-P**, the modelling results predict that the iodinated phenol moiety orients within the central mutant cavity in a similar fashion to the results obtained for **L1-L5** in Chapter 2 and to that of a known p53-Y220C-binding ligand that incorporates the same diiodophenol pharmacophore.¹⁵³ In addition, the di-(2-picolyl)amine unit is extended out into open space of subsite 1 as desired. The pyridyl group is pointed towards Thr150 N with a distance of 3.20 Å, while the benzylamine distance to Thr150 O is 2.59 Å (Figure 3.3). The phenol participates in a hydrogen bonding network with a water molecule that forms a bridge between the backbone carbonyl of Asp228 and backbone N of Val147. For **L5-O**, the modelling results predict that the phenol orients within the central mutant cavity similar to **L5-P**, however, in the absence of the iodine, no halogen bond interactions are present. The phenoxy moiety extends significantly into the mutant subsite 2, resulting in a possible interaction with C220 at 3.16 Å away (Figure 3.4). The phenol also participates in the same hydrogen bonding network with the water mentioned previously. Overall, these molecular docking results highlight the possible interactions of **L5-P** and **L5-O** with amino acids located within additional subsites in the mutant p53-Y220C cavity.

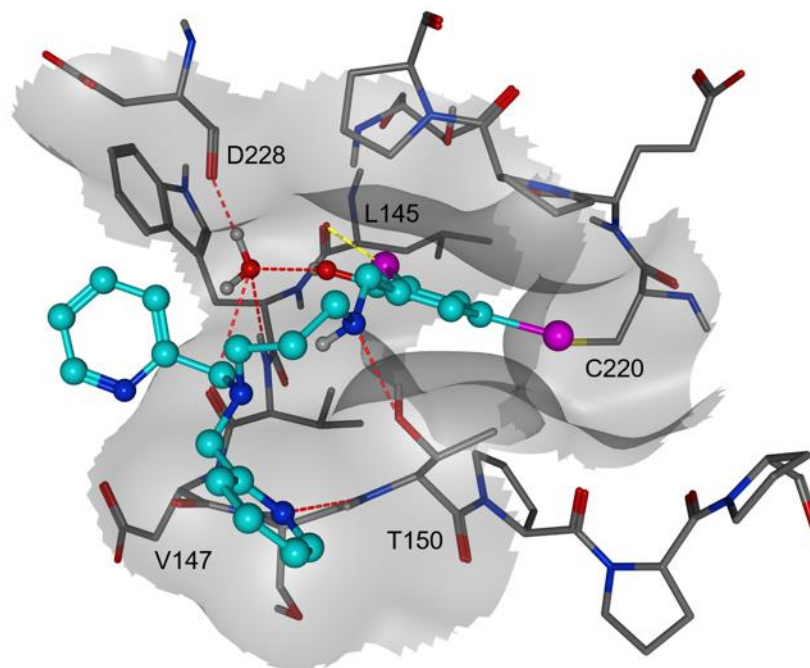


Figure 3.3. A low energy pose of **L5-P** in the mutation-induced cavity for p53-Y220C (PDBID: 4AGQ)¹⁵³. The halogen bonding interactions (I...Leu145) are shown with a yellow line. The hydrogen bond network between the conserved water, D228, and V147 is shown in red. The Van der Waals surface of the protein is shown in gray. Atom colours: carbon is represented in gray in the protein and teal for the ligand. Oxygen is shown in red, nitrogen in blue, and sulfur in yellow. Hydrogens are omitted for clarity.

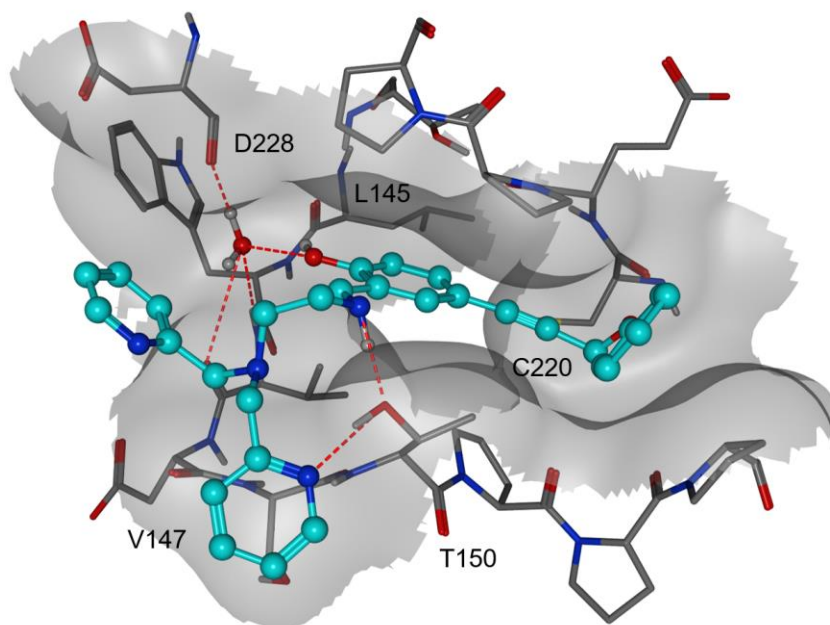


Figure 3.4. A low energy pose of **L5-O** in the mutation-induced cavity for p53-Y220C (PDBID: 4AGQ)¹⁵³. The hydrogen bond network between the conserved water, D228, and V147 is shown in red. The Van der Waals surface of the protein is shown in gray. Atom colours: carbon is represented in gray in the protein and teal for the ligand. Oxygen is shown in red, nitrogen in blue, and sulfur in yellow. Hydrogens are omitted for clarity.

3.2.3. Zinc Binding Affinities for L5-P and L5-O

As outlined in Chapter 2, reported models for Zn-binding in p53 describe two possible ligation sites, the native binding site (K_{d1}) estimated to bind on the order of 10^{-12} M, and non-native (K_{d2}) sites with an estimated affinity on the order of 10^{-6} M.^{152, 213, 222-223, 226} Metallochaperones designed to rescue zinc-binding in p53 mutants should therefore have Zn^{2+} affinities that are in between that of K_{d1} and K_{d2} . While the exact value of K_{d1} for p53-Y220C is unknown, we have shown in Chapter 2 that Zn metallochaperones with K_d values on the order of 10^{-12} M have appropriate affinities to increase intracellular levels of zinc in cells expressing this mutant.³⁶⁴ Spectrophotometric (UV-visible) pH titrations from pH 2-12 were carried out to characterize ligand speciation are shown in Figure 3.5. Upon addition of NaOH, the UV-vis spectrum for **L5-P** exhibits an increase in absorbance at 250 nm, and a major transition from 300 nm to 310 nm indicative of the deprotonation of the phenol to the phenolate. **L5-O** exhibits a red shift from 260 nm to 270 nm and a broadening in the shoulder from 270 to 310 nm upon addition of NaOH. The best fits to the data were calculated and the pK_a values corresponding to the phenol, pyridine(s), and tertiary

amines for each ligand are reported in Table 3.1. In each case, the highest pKa's can be assigned to the phenol and ammonium group based on previously reported acidity constants,³⁰⁴⁻³⁰⁵ while the lowest pKa's correspond to the pyridinium groups. The pKas are comparable due to the similarities between the protonatable groups in **L5-P** and **L5-O**.

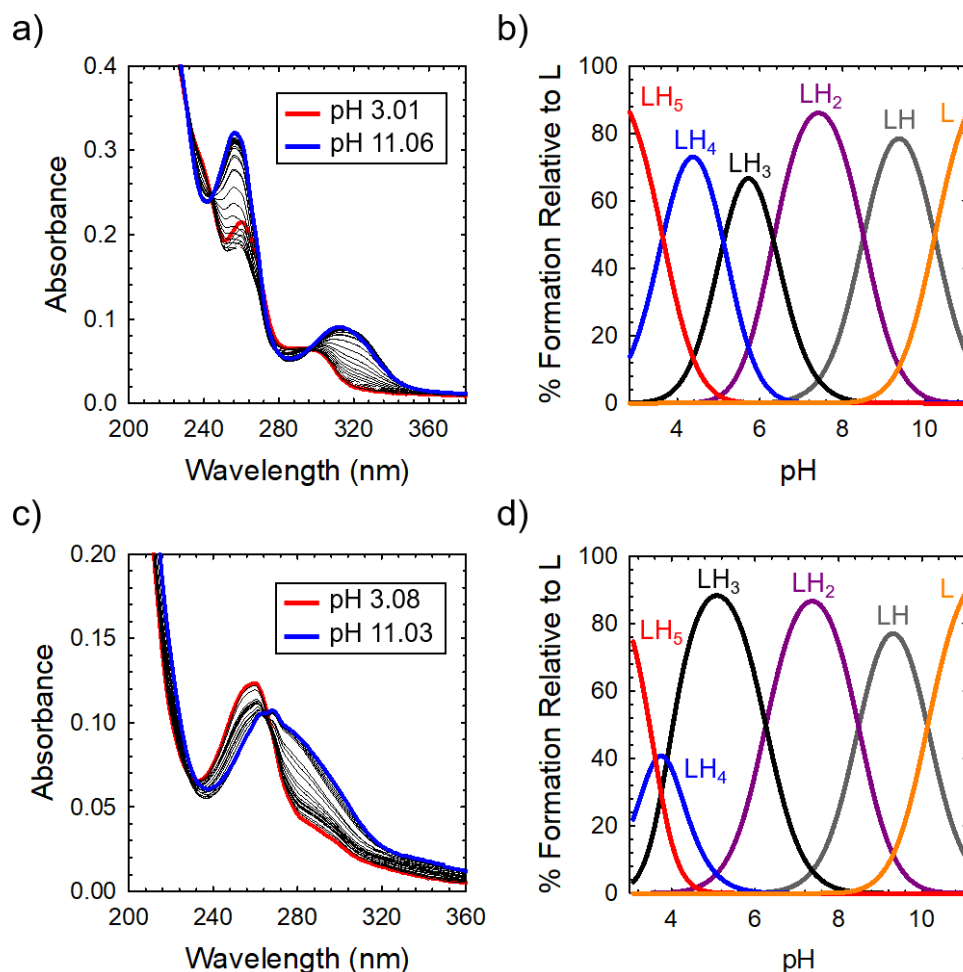


Figure 3.5. (a,c) Variable pH titration plots for **L5-P** and **L5-O**. (b,d) Simulated speciation diagrams of **L5-P** and **L5-O**. Speciation diagrams made using HySS2009.

Table 3.1. pKa values as determined by variable pH UV-vis titrations (errors are for the last digit).

Reaction	L5-P	L5-O
$[H_5L]^{4+} = [H_4L]^{3+} + H^+$ (pKa ₁)	3.77(3)	3.61(5)
$[H_4L]^{3+} = [H_3L]^{2+} + H^+$ (pKa ₂)	4.47(3)	3.89(4)
$[H_3L]^{2+} = [H_2L]^+ + H^+$ (pKa ₃)	6.17(2)	6.26(3)
$[H_2L]^+ = [HL] + H^+$ (pKa ₄)	8.31(2)	8.48(1)
$[HL] = [L]^- + H^+$ (pKa ₅)	10.53(1)	10.13(1)

Variable pH titration plots of **L5-P** and **L5-O** in the presence of $\text{Zn}(\text{ClO}_4)_2$ are shown in Figure 3.6 a,c. The concentration of free Zn^{2+} present in solution at a given pH, referred to as pM ($\text{pZn} = -\log[\text{Zn}_{\text{unchelated}}]$), is a direct estimate of the metal-ligand affinity when all species in solution are considered.³⁰⁸⁻³¹⁰ Inspection of the speciation diagrams in Figure 3.6 b,d demonstrates that at biological pH (7.4), the major species in solution is ZnLH for **L5-P**, and ZnL for **L5-O**, with very little free Zn^{2+} . By analyzing the metal speciation diagrams, the Zn affinity of each ligand at physiological pH can be determined. Calculated values for pM are reported in Table 3.2. Interestingly, despite containing a propyl spacer between the di-(2-picolyl)amine and phenol in comparison to the ethyl spacer of **L5** and **L5-O**, **L5-P** still exhibits a high Zn-binding affinity ($\text{pM} = 8.7$) that is comparable to that of **L5** (8.4) and **L5-O** (8.6). These values afford approximate dissociation constants (K_d) in the low nanomolar range, an affinity appropriate for functioning as Zn metallochaperones for p53-Y220C.

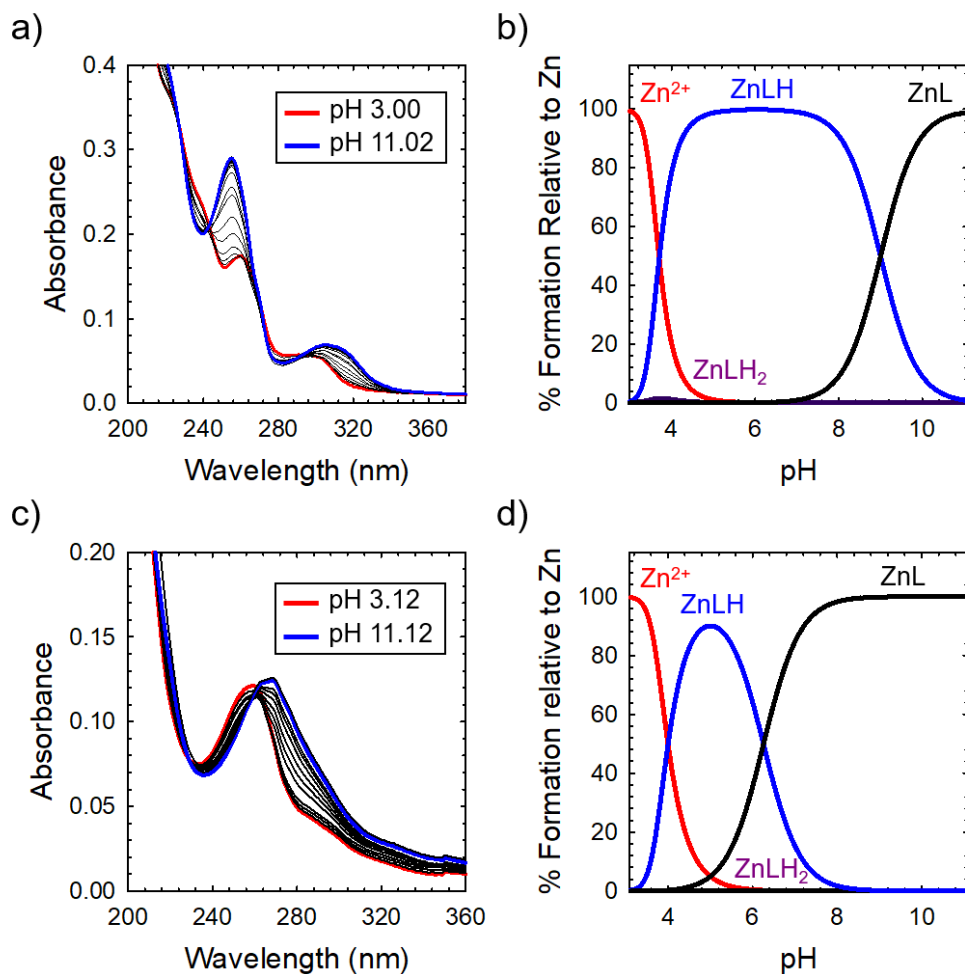


Figure 3.6. (a, c) Variable pH titration plots for **L5-P** + Zn²⁺ and **L5-O** + Zn²⁺. (b, d) Simulated speciation diagrams of **L5-P** + Zn²⁺ and **L5-O** + Zn²⁺. Speciation diagrams made using HySS2009.

Table 3.2. Stability constants (log *K*) of the Zn complexes of **L5-P** and **L5-O** and calculated pM values^[a] (errors are for the last digit).

	pZn ^[a] pH 7.4	Log <i>K</i>		
		ZnL	ZnLH	ZnLH ₂
L5-P	8.7	14.96(9)	9.00(1)	2.20(5)
L5-O	8.6	16.13(1)	6.25(1)	0.46(1)

^[a] pZn was calculated using $pZn = (-\log[Zn^{2+}]_{free})$, where $[Zn^{2+}]_{free}$ is determined from the HySS model.³¹²
[L5-P]=[L5-O] = [Zn²⁺] = 12.5 μM, 25 °C, I = 150 mM NaCl

3.2.4. Monitoring Intracellular Zn²⁺ Levels in Cancer Cells

We investigated whether **L5-O** and **L5-P** could function as Zn metallochaperones in NUGC3 cells by monitoring the change in intracellular Zn²⁺ using the fluorescent Zn²⁺ sensitive probe FluoZin-3. Following the procedures outlined in Chapter 2, NUGC3 cells were incubated with FluoZin-3, followed by incubation with **L5-O** or **L5-P** and ZnCl₂ and subsequently imaged. Pyrithione (PYR) was used as a positive control for Zn uptake. Surprisingly, neither **L5-O** or **L5-P** resulted in an increase in intracellular Zn²⁺ levels compared to ZnCl₂ only, as demonstrated in Figure 3.7. This result was unexpected given that the di-(2-picolyl)amine fragment proved effective at increasing intracellular zinc levels in Section 2.2.4, in particular for **L5**. One possible hypothesis points to the increased zinc affinity of ligands **L5-O** and **L5-P** in comparison to both **L5** and the fluorescent zinc indicator FluoZin-3. The zinc binding affinities of **L5-O** and **L5-P** are ~ 2.5 and 2.0 nM respectively, compared to 15 nM for FluoZin-3³¹³ and 4 nM for **L5**. Thus, it is likely that if ZnCl₂ were brought into the cell by **L5-O** and **L5-P**, the Zn²⁺ would be preferentially bound to the ligand over the fluorophore, and thus zinc binding to the fluorophore in this experiment is restricted. Further studies with alternate fluorescent indicators are required to determine whether this is a result of experimental design or a result of the structural modifications to the ligand. Alternatively, **L5-O** and **L5-P** exhibit a lower aqueous solubility than **L5**, and thus a possible hypothesis is that the zinc complexes formed by **L5-O** and **L5-P** exhibit a lower solubility and are unable to promote cell uptake. While further studies are required to test such hypotheses and investigate why **L5-O** and **L5-P** are not effective as Zn metallochaperones, this interesting result highlights the difficulty of designing effective metallochaperones and demonstrates how subtle changes to the ligand design can result in large biological changes.

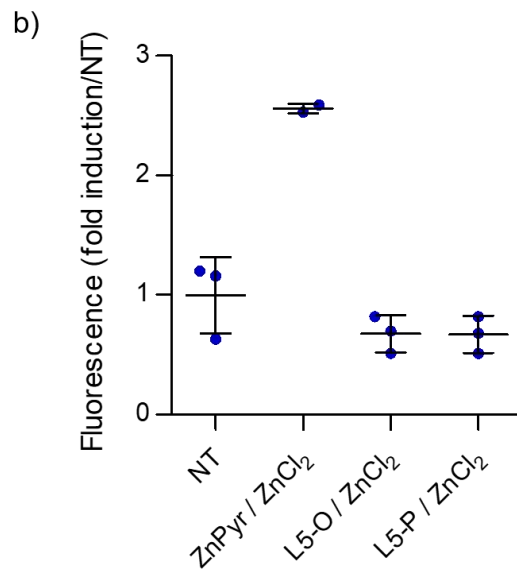
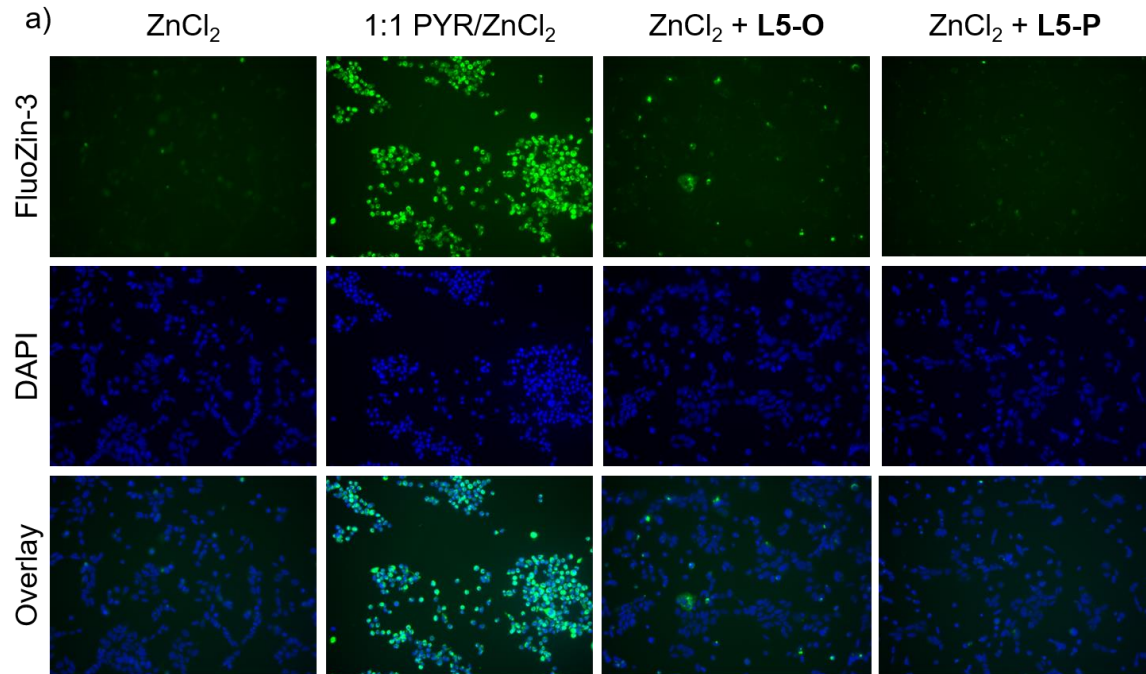


Figure 3.7. Treatment of NUGC3 with **L5-O** and **L5-P** does not result in increased intracellular Zn²⁺. (a) Imaging of intracellular Zn²⁺ levels in complete serum-free media. NUGC3 cells were incubated with 1 μM FluoZin-3²¹⁹ for 20 minutes at 37°C, followed by incubation with indicated treatment (ZnCl₂ = 50 μM, **L5-O** = **L5-P** = 10 μM, 50 μM PYR) for 2 hours. Cells were imaged using a Nikon ApoTome microscope and fluorescence-quantified using ImageJ. (B) Fluorescence intensity of FluoZin-3 at 488 nm demonstrating relative Zn²⁺ levels. Blue dots represent average fluorescence intensity of imaged cells per individual trial. Black line indicates mean values, while black error bars demonstrate the 95% confidence interval.

3.2.5. *In Vitro* Cytotoxicity

L5-P and **L5-O** were submitted to the National Cancer Institute's NCI-60 program for *in vitro* screening against a panel of 60 human cancer cell lines. In the initial 1-dose screen at 10 μM , **L5-P** and **L5-O** exhibited a broad range of cytotoxicity across all 60 cell lines. The 1-dose data is shown in Table 3.3 and is represented by the mean growth value. This value represents the mean growth inhibition or lethality across all 60 cell lines in comparison to no-drug control. The negative growth value for **L5-P** of -58 indicates an average of 58% cell death across 60 cell lines, whereas the positive value of 15 for **L5-O** indicates a mean growth inhibition of 85%. Interestingly, the growth value for lead compound **L5** in the one-dose study was -44, which represents an activity in between that of **L5-P** and **L5-O**. Given the high activity of both compounds across a wide range of cell lines, both **L5-P** and **L5-O** were chosen for further 5-dose studies, which is currently ongoing at the National Cancer Institute.

Table 3.3. Mean growth value for **L5**, **L5-P**, and **L5-O** from the 1-dose NCI-60 screen.

Ligand	NSC Number ^[a]	Growth Value ^[b]
L5	788647	-44
L5-P	820797	-58
L5-O	820798	15

^{a]} NSC number is the compounds internal ID number at the National Cancer Institute. ^[b] Growth value represents the mean growth inhibition (positive) or lethality (negative) across all 60 cell lines in comparison to no drug control

As outlined in Chapter 2, gastric cancer is one of the leading causes of cancer-related deaths worldwide and is associated with a low life expectancy upon diagnosis.³²² We tested the *in vitro* cytotoxicity of **L5-P** and **L5-O** on the gastric cancer cell line NUGC3, containing the mutant p53-Y220C. Both compounds exhibited a similar cytotoxic effect, with IC_{50} values of $3.5 \pm 0.1 \mu\text{M}$ and $3.9 \pm 0.1 \mu\text{M}$ for **L5-P** and **L5-O** respectively (Figure 3.8). This value is similar to the IC_{50} value obtained for **L5** (IC_{50} $1.7 \pm 0.1 \mu\text{M}$, Table 2.5), and exhibits significantly enhanced cytotoxicity over cisplatin ($20.0 \pm 2 \mu\text{M}$, Table 2.5) and oxaliplatin ($50.0 \pm 3 \mu\text{M}$, Table 2.5).

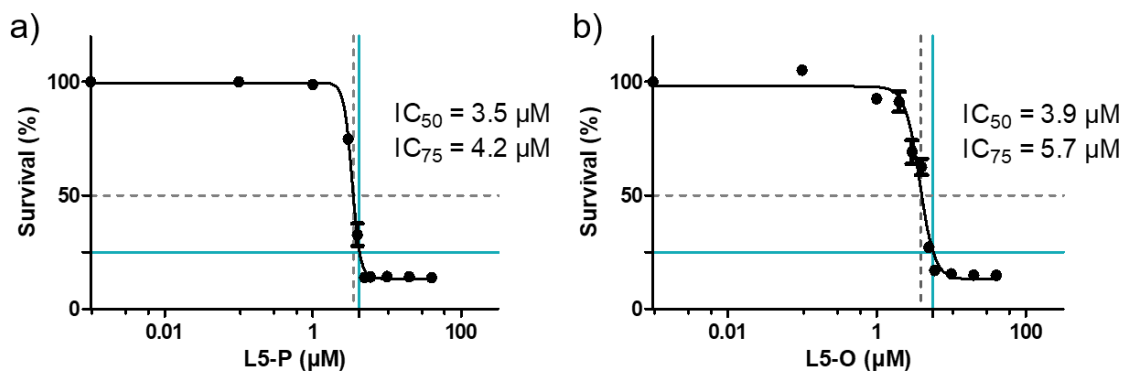


Figure 3.8. Survival curves for NUGC3 cells (p53-Y220C) upon treatment with **L5-P** (a) and **L5-O** (b). IC₅₀ and IC₇₅ values are represented by the gray and teal lines respectively and are indicated on the graph.

We further assessed the anticancer potential of **L5-P** and **L5-O** using 3D spheroids cultured from NUGC3 cells. Serving to bridge the gap between 2D cytotoxicity studies and animal experiments, 3D cultures more closely mimic the tumour microenvironment and can more accurately predict drug characteristics such as tolerance of hypoxic conditions and drug penetration and heterogeneity within the tumour.³⁶⁵ As such, the use of 3D cultures is of significant importance in drug discovery.³⁶⁶ 3D spheroids of NUGC3 cells were treated with 10 μM **L5-P** and **L5-O** and monitored in comparison to the non-treated control. Both **L5-P** and **L5-O** induced significant cell death, resulting in only 12% and 14% viability respectively in the spheroids (Figure 3.9). Even at the lower concentrations of **L5-P** and **L5-O** used, their anticancer effect in 3D spheroids is significantly greater than that of **L5** (19.5 μM, 24% viability) and oxaliplatin (250 μM, 48% viability) as reported in Chapter 2 (Figure 2.12).

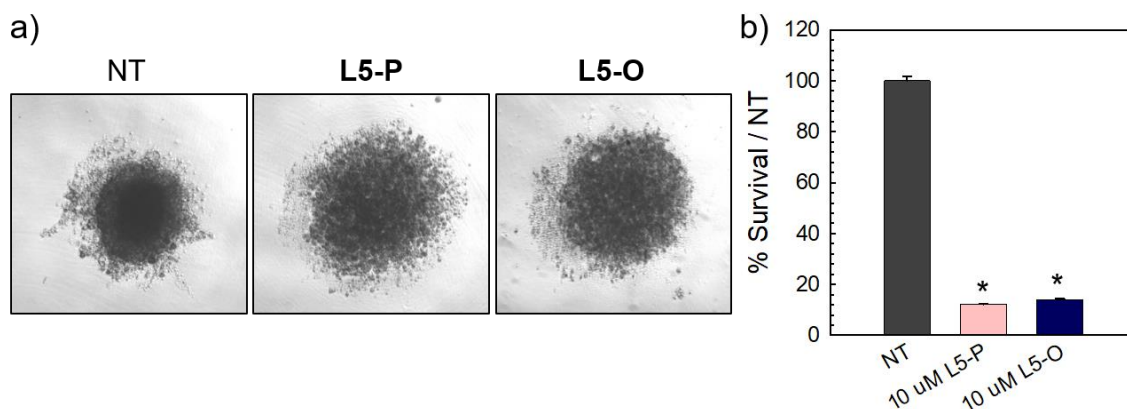


Figure 3.9. NUGC3 cells (300 cells/well; 96 wells/plate) were grown for 4 days and then treated for 3 days with 10 μ M **L5-P** and **L5-O**. 3D cultures were observed by microscopy to estimate clone size (left) and cell survival was assayed using rezasurin (right). * indicates statistical differences from non-treated control with $p < 0.001$ as established by One-Way ANOVA followed by Tukey test.

3.2.6. Apoptotic Effects of L5-P and L5-O in Human Gastric Cancer Cell Lines

To investigate both the molecular basis for the cytotoxicity of compounds **L5-O** and **L5-P** and its dependence on mutant p53, we examined whether treatment of AGS (wild-type p53) and NUGC3 (p53-Y220C) with **L5-O** and **L5-P** resulted in the production of cleaved caspase-3, an indicator of apoptotic activity. We further analysed the levels of p53 expression. AGS and NUGC3 cells were treated with oxaliplatin at indicated concentrations and 20 μ M **L5** as a control, which is the concentration that induced significant cleaved caspase-3 in NUGC3 as seen in section 2.2.6. AGS and NUGC3 cells were also treated with **L5-P** and **L5-O** at 1, 5, and 10 μ M, which represent concentrations wherein significant cytotoxicity was observed in both 2D and 3D experiments as described above. Cells were treated with the compounds for 48 hours and cleaved caspase-3 and p53 protein levels were assessed by Western Blot. As expected, treatment of AGS cells with oxaliplatin resulted in increased p53 expression and cleaved caspase-3,³³³⁻³³⁴ in agreement with the results obtained in Chapter 2 (Figure 2.13). Apart from **L5-O** at 5 μ M, low levels of cleaved caspase-3 are produced upon treatment with **L5**, **L5-O**, and **L5-P** in AGS cells (Figure 3.10), indicating minimal restoration of apoptotic activity in the wild-type p53 cell line. This does, however, suggest low levels of off-target mechanisms of cytotoxicity via p53-independent pathways. In the NUGC3 cell line, both oxaliplatin and

L5 induce relatively low quantities of cleaved caspase-3. Interestingly, despite the significantly lower concentration, a notable increase in cleaved caspase-3 levels is observed upon treatment with **L5-P** and **L5-O** compared to treatment with **L5**. These results are in agreement with both the 2D and 3D cytotoxicity studies, which reported a markedly increased cytotoxicity with **L5-O** and **L5-P** over **L5**. Further, the level of cleaved caspase-3 upon treatment with **L5-O** and **L5-P** at concentrations as low as 10 μM for **L5-O** and 5 and 10 μM for **L5-P** is notably increased in NUGC3 (p53-Y220C) cells in comparison to AGS (WTp53) cells under the same conditions. These results suggest that the apoptotic effect of **L5-O** and **L5-P** is preferentially potentiated in the Y220C mutant cell line.

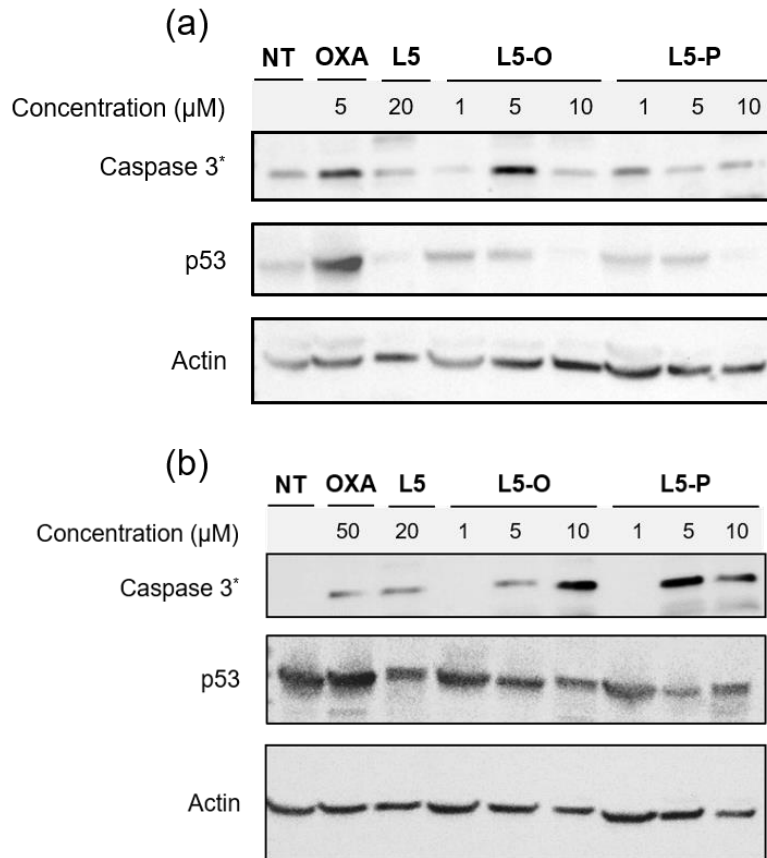


Figure 3.10. AGS (a) and NUGC3 (b) cells were treated for 48 hours with indicated compounds. Total protein was extracted, and 20 μg were separated on SDS PAGE. Cleaved caspase-3 (Caspase 3*), p53, and actin were detected by Western Blot analysis.

3.2.7. Interaction Between L5-O/L5-P and Mutant p53

To further explore the mechanisms by which **L5-O** and **L5-P** initiate biological activity on p53-Y220C, we investigated whether they could bind directly to the DNA-binding domain of mutant p53-Y220C (p53C-Y220C). **L5-P** has limited solubility beyond 100 μM , therefore we opted to use native mass spectrometry to investigate binding instead of surface plasmon resonance, as the studies in Chapter 2 revealed the need for high ligand concentrations under our experimental conditions. p53C-Y220C was incubated with concentrations of **L5-O** and **L5-P** ranging from 5 to 100 μM for two hours, and potential binding was probed using mass spectrometry. Unfortunately, binding at concentrations up to 100 μM was not observed as indicated in Figure 3.11. Upon addition of increasing concentrations of **L5-O** and **L5-P**, no spectral changes are observed in comparison to protein only, thus no complex formation is observed under the conditions of the experiment. Limited solubility of **L5-P** beyond 100 μM prevents detection of higher micromolar affinity binding, a range relevant to a compound with the same 3,5-diodophenol pharmacophore ($K_d = 225 \mu\text{M}$ by ITC).¹⁵³

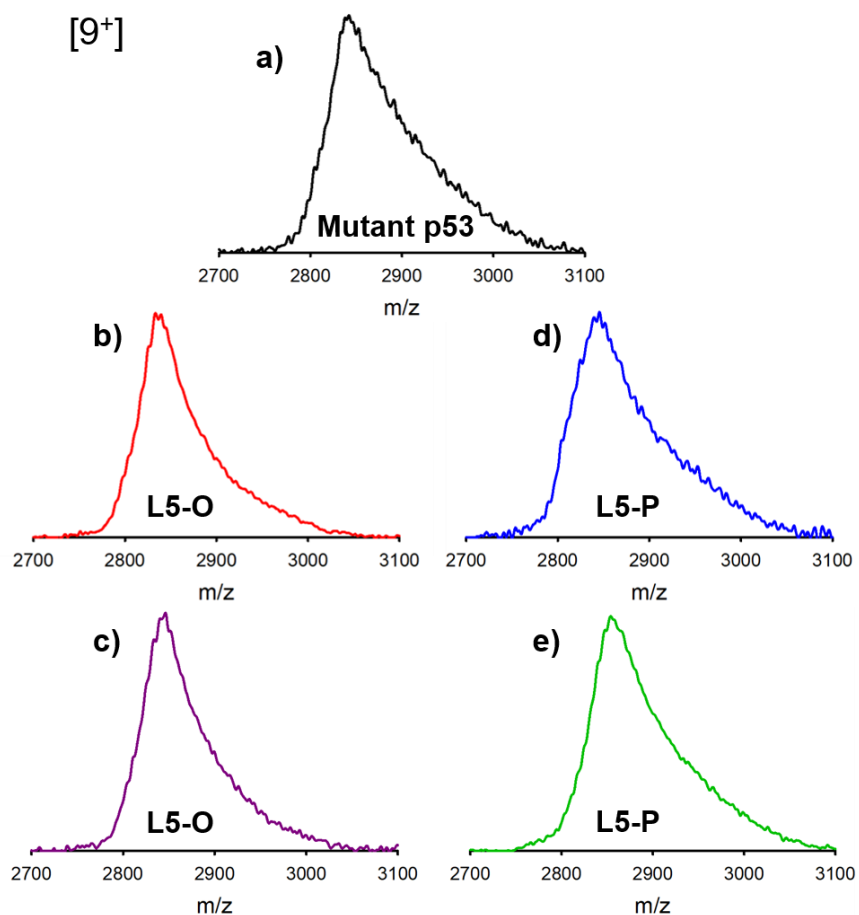


Figure 3.11. Native mass spectrometry results using recombinant p53C-Y220C (2 μ M) incubated with (a) 0.2% DMSO (b) 50 μ M **L5-O** (c) 100 μ M **L5-O** (d) 50 μ M **L5-P** and (e) 100 μ M **L5-P** for 2 hours at room temperature.

3.3. Summary

Restoration of functional activity in mutant p53 remains a highly sought-after target in cancer research. In Chapter 2, we demonstrated the utility of a bifunctional approach to restore p53 function wherein both protein stability and zinc loss were simultaneously targeted. We aimed to optimize the structure of our lead compound for improved selectivity in mutant p53-Y220C by extending the ligand design further into subsite cavities produced by the mutant. Computational docking studies suggests that the propyl spacer of **L5-P** pushed the zinc chelator further into the open space of the mutant protein subsite 1, while the alkyne substituted with a phenoxy moiety in **L5-O** is positioned in the mutant subsite 2 where π -stacking interactions with surrounding amino acids is possible. However, these structure modifications unexpectedly led to the inability of **L5-P** and **L5-O** to increase intracellular levels of Zn^{2+} in our experiments, despite possessing nanomolar zinc binding

affinities as characterized in our UV-vis studies. *In vitro* cytotoxicity studies in 3D spheroid models of NUGC3 demonstrated markedly increased cytotoxicity with **L5-P** and **L5-O** over **L5** and oxaliplatin. Further, upon investigation into the mechanism of cytotoxicity in this ligand series, cleaved caspase 3 studies demonstrated that **L5-P** and **L5-O** produced more cleaved caspase-3 in NUGC3 than **L5**. This further verified the increased biological activity of these ligands over **L5** and demonstrates their potential to restore apoptotic activity in mutant p53. Moving forward, the ability of these ligands to restore transcriptional function in mutant p53 via upregulation of target genes PUMA, NOXA, and p21 should be investigated. Further, it should also be determined whether these ligands induce conformational changes in mutant p53-Y220C via immunoprecipitation using conformation-specific antibodies.

The production of cleaved caspase-3 in AGS cells upon treatment with **L5-O** and **L5-P**, although minimal, suggests that these ligands exhibit p53-independent activity in addition to the p53-dependent mechanisms. As outlined in both the introduction and Chapter 2, studies on p53 activating scaffolds show that increased ROS generation is an important component of the observed cytotoxicity, in addition to p53 activation.^{199, 226} Specifically, metal-binding agents exhibit ROS-associated toxicity as a result of the *in situ* formation of redox-active Cu complexes.^{226, 237} As a result, comprehensive studies investigating the copper-binding affinity and ROS production with **L5-P** and **L5-O** should be investigated moving forward.

Overall, this study demonstrates the sensitivity of metallochaperone design and how subtle tuning of the ligand scaffold can impart significant changes in biological activity. We further show that by extending the ligand scaffold into mutant subsites of p53-Y220C, we increase cytotoxicity and increase apoptotic activity in mutant p53. With a shift towards targeted chemotherapeutics following the emergence of cancer genome sequencing projects, the development of small molecules capable of restoring wild-type function in mutant p53 are becoming of increasing importance.

3.4. Experimental

3.4.1. Material and Methods

All chemicals used were purchased from Sigma Aldrich and were further purified whenever necessary.³⁴⁶⁻³⁴⁷ (bis(2-pyridylmethyl)-amino)-ethylamine and N1,N1-bis(pyridin-2-ylmethyl)propane-1,3-diamine were prepared from commercially available di-(2-picolyl)amine by reported procedures.^{348, 367} (prop-2-yn-1-yloxy)benzene was prepared according to literature procedures.³⁶⁸ All compounds were dried under vacuum for 1 week before in vitro cytotoxicity testing. ¹H and ¹³C NMR were recorded on Bruker-AV-400, 500, and 600 instruments. Mass spectra (positive ion) were obtained on an Agilent 6210 time-of-flight electrospray ionization mass spectrometer. Electronic absorption spectra were obtained on a Cary 5000 spectrophotometer.

3.4.2. Synthesis

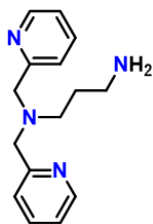
2-(3-(bis(pyridin-2-ylmethyl)amino)propyl)isoindoline-1,3-dione (**1**):



To a solution of di-(2-picolyl)amine (1.52 g, 7.61 mmol.) in acetonitrile (50 mL), anhydrous K_2CO_3 (3.47 g, 25.12 mmol), KI (0.13 g, 0.76 mmol), and bromopropylphthalimide (2.00 g, 9.14 mmol) was added. The mixture was heated at reflux for 24 hours, after which it was filtered and concentrated to yield a red oil. The resulting oil was dissolved in 30 mL of dichloromethane and washed with saturated $NaHCO_3$ solution (3 x 30 mL). The organic phase was separated from the aqueous phase and dried over $MgSO_4$. Following removal of the solvent *in vacuo*, the oil was dissolved in 2 M HCl (10 mL) and washed with dichloromethane (5 x 10 mL). Upon addition with solid sodium bicarbonate (5 g), a brown-orange solid precipitated. The product was extracted with dichloromethane (4 x 20 mL) and concentrated *in vacuo* to yield a brown solid. The product was used for the next reaction without further purification. Yield: 1.75 g, 52%. ¹H NMR (400 MHz, $CDCl_3$): δ 8.49 (d, J = 4.1 Hz, 2H), 7.83 (dd, J = 5.5, 3.1 Hz, 2H), 7.71 (dd, J = 5.5, 3.0 Hz, 2H), 7.64 (td,

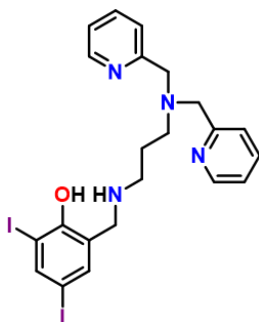
J = 7.6, 1.8 Hz, 2H), 7.55 (d, J = 7.9 Hz, 2H), 7.15 – 7.09 (m, 2H), 3.83 (s, 4H), 3.76 – 3.67 (m, 2H), 2.65 (t, J = 7.0 Hz, 2H), 1.98 – 1.90 (m, 2H).

2-(((3-(bis(pyridin-2-ylmethyl)amino)propyl)amino)methyl)-4,6-diiodophenol (**2**):



A solution of **1** (1.60 g, 4.28 mmol) in ethanol (10 mL) was added to a solution of hydrazine monohydrate (0.27 g, 5.40 mmol) in 5 mL of ethanol. The solution was heated at a reflux for 3 hours. Upon cooling, the filtrate dried in vacuo and dissolved in 13 mL of 2 M HCl followed by 640 μ L of 12 M HCl which yielded a white precipitate. The suspension was stirred for 2 hours at 50 $^{\circ}$ C, followed by 16 hours at room temperature. Then the suspension was filtered, concentrated in vacuo, and dissolved in 6.5 mL of water. This aqueous solution was basified by adding a 15% solution of aqueous NaOH which generated a red oil. The red oil was extracted from the aqueous solution with dichloromethane (3 \times 50 mL) and dried over Na₂SO₄. The residue was purified by silica gel column chromatography using CH₂Cl₂/MeOH (20:1) to remove the starting material, followed by MeOH (30%) in CH₂Cl₂ as eluent to obtain the product as an orange solid. Yield: 0.28 g, 26%. ¹H NMR (400 MHz, CDCl₃): δ 8.50 (d, J = 4.9 Hz, 2H), 7.63 (td, J = 7.6, 1.8 Hz, 2H), 7.48 (d, J = 7.8 Hz, 2H), 7.16 – 7.08 (m, 2H), 3.78 (s, 4H), 2.69 (t, J = 6.8 Hz, 2H), 2.58 (t, J = 6.9 Hz, 2H), 2.20 (s, 2H), 1.67 (p, J = 6.9 Hz, 2H).

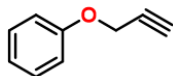
2-(bis(pyridin-2-ylmethyl)amino)ethyl)amino)methyl)-4,6-diiodophenol (**L5-P**):



To a solution of **2** (0.18 g, 0.74 mmol) in MeOH (15 mL), 3,5-diiodosalicylaldehyde (0.30 g, 0.81 mmol) was added under an N₂ atmosphere. The resulting orange solution was

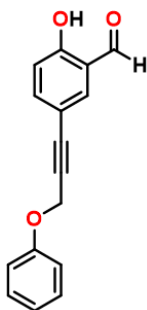
stirred at room temperature for 30 minutes, followed by cooling in an ice bath and slow addition of NaBH₄ (45.0 mg, 1.18 mmol). The mixture was then stirred overnight under N₂. Water (5 mL) was added into the solution and stirred for 30 minutes. Dichloromethane was added and the organic phase was separated from the aqueous phase and dried over Na₂SO₄. The residue was purified by silica gel column chromatography using CH₂Cl₂ to remove the starting material, followed by MeOH (30%) in CH₂Cl₂ as eluent to obtain the product as an orange solid. Yield: 0.18 mg, 27%. ¹H NMR (400 MHz, CDCl₃): δ 8.48 – 8.39 (m, 2H), 7.92 (d, J = 2.1 Hz, 1H), 7.64 (td, J = 7.7, 1.8 Hz, 1H), 7.32 (d, J = 7.7 Hz, 2H), 7.22 (d, J = 2.1 Hz, 1H), 7.20 – 7.13 (m, 2H), 3.89 (s, 2H), 3.78 (s, 4H), 2.76 – 2.63 (m, 4H), 1.81 (p, J = 5.9 Hz, 2H). ¹³C{¹H} NMR (400 MHz, CDCl₃): δ 159.36, 158.90, 149.20, 144.83, 136.60, 136.50, 124.38, 123.27, 123.13, 122.17, 77.28, 77.16, 76.96, 60.19, 52.74, 51.79, 47.31, 30.79, 25.11.

(prop-2-yn-1-yloxy)benzene (**3**):



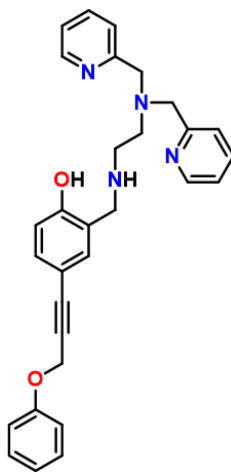
To a stirred solution of phenol (4.71 g, 50.0 mmol) in acetone (30 mL), propargyl bromide (80% solution in toluene, 5.95 g, 50.0 mmol) and potassium carbonate (6.91 g, 50.0 mmol) were added. The reaction mixture was heated at reflux for 12 hours. Upon completion of the reaction, the solvent was removed, followed by addition of water (30 mL). Subsequently, the mixture was extracted with diethyl ether (3 x 50 mL), and the organic phases were combined and dried over anhydrous Na₂SO₄. Removal of the solvent under vacuum yielded a brown oil. The residue was purified by silica gel column chromatography using hexanes/ethyl acetate (10:1) to afford a yellow oil. Yield: 4.13 g, 62%. ¹H NMR (400 MHz, CDCl₃): δ 7.32 (td, 2H), 7.01 (t, J = 8.4 Hz, 2H), 4.71 (d, J = 2.4 Hz, 2H), 2.53 (t, J = 2.4 Hz, 1H).

2-hydroxy-5-(3-phenoxyprop-1-yn-1-yl)benzaldehyde (**4**):



Dry THF (30 mL) was deoxygenated for 15 minutes by purging with N₂. 5-iodosalicylaldehyde (0.15 g, 0.60 mmol) was added, followed by addition of triethylamine (0.21 mL, 1.5 mmol). Upon stirring of the solution for 2 minutes, Pd(PPh₃)₄ (34.6 mg, 0.03 mmol) and CuI (22.8 mg, 0.12 mmol) were added under N₂ to afford a colour change from yellow to orange. Afterwards, **3** (79.3 μL, 0.60 mmol) was added dropwise to the solution and the mixture was stirred for 16 hours at room temperature under N₂. The solvent was removed under vacuum and the residue was dissolved in 40 mL ethyl acetate. The organic phase was washed with an aqueous saturated solution of NaHCO₃ (3 x 20 mL), and the aqueous phase was separated with ethyl acetate (3 x 30 mL). The organic phases were combined and washed with brine (30 mL) and dried over Na₂SO₄. The solvent was removed under vacuum and the resulting residue was purified by silica gel column chromatography using dichloromethane as the eluent to afford a yellow oil. Yield: 52.5 mg, 35%. ¹H NMR (400 MHz, CDCl₃): δ 11.13 (s, 1H), 9.87 (s, 1H), 7.69 (d, *J* = 2.2 Hz, 1H), 7.60 (dd, *J* = 8.8, 2.2 Hz, 1H), 7.35 (dd, *J* = 8.7, 7.1 Hz, 2H), 7.04 (dd, *J* = 10.2, 6.9 Hz, 3H), 6.97 (d, *J* = 8.7 Hz, 1H), 4.93 (s, 2H).

2-(((2-(bis(pyridin-2-ylmethyl)amino)ethyl)amino)methyl)-4-(3-phenoxyprop-1-yn-1-yl)phenol (**L5-O**):



To a solution of (bis(2-pyridylmethyl)-amino)-ethylamine (0.080 g, 0.31 mmol) in dichloroethane (7 mL), 2-hydroxy-5-(3-phenoxyprop-1-yn-1-yl)benzaldehyde (0.070 g, 0.29 mmol) was added. The resulting bright yellow solution was heated at 50 °C for an hour, at which time sodium triacetoxyborohydride (0.084 g, 0.40 mmol) was added. The mixture was then heated at 50 °C overnight. Then, DCE was removed and the residue was dissolved in DCM and extracted with 3 x 10 mL of water. The organic phase was separated from the aqueous phase and dried over MgSO₄. Due to difficulties in separation of impurities via silica chromatography, the product was purified by HPLC (C-18, H₂O+0.1% TFA:MeCN+0.1% TFA, 32 to 38 % MeCN gradient over 20 minutes, 2 mL.min⁻¹). HPLC retention time = 14.7 minutes (C-18, H₂O+0.1% TFA:MeCN+0.1% TFA, 32 to 38 % MeCN gradient over 20 minutes, 2 mL.min⁻¹). Lyophilisation of the fractions containing the product provided pure **L5-O** as a yellow oil. HPLC purity was determined to be 98.6%. ¹H NMR (400 MHz, MeOD): 8.52 (dd, *J* = 5.6, 1.7 Hz, 2H), 7.99 (td, *J* = 7.8, 1.7 Hz, 2H), 7.58 – 7.47 (m, 4H), 7.42 (d, *J* = 2.1 Hz, 1H), 7.37 (dd, *J* = 8.4, 2.1 Hz, 1H), 7.29 (dd, *J* = 8.7, 7.3 Hz, 2H), 7.06 – 6.99 (m, 2H), 6.98 – 6.93 (m, 1H), 6.91 (d, *J* = 8.4 Hz, 1H), 4.93 (s, 1H), 4.22 (s, 1H), 4.08 (s, 4H). ¹³C{¹H} NMR (400 MHz, MeOD): δ = 159.3, 158.1, 157.7, 147.4, 147.3, 142.2, 136.2, 135.8, 130.5, 126.2, 125.3, 122.4, 119.6, 116.7, 116.1, 115.3, 111.4, 87.0, 84.4, 59.1, 57.3, 52.5, 47.4, 46.2.

3.4.3. Molecular Modeling

Default parameters were used for all computational procedures unless otherwise stated. All computational methods were performed in the Molecular Operating Environment version 2015 (MOE, Chemical Computing Group, Montreal, Canada). Images were generated in POV-ray engine v3.7.0 (www.povray.org). MOE implements a derivative of the AMBER12 force field for proteins, integrated with the Extended Hückel Theory and AM1-BCC method for handling small molecules.³⁵⁰ Ligands were drawn in MOE, and a stochastic conformational library was generated for each using default parameters. Inspection of the crystal structures 4AGL, 4AGN, 4AGO, 4AGP, 4AGQ (all containing structurally relevant iodophenol ligands), showed minimal differences in either the protein or ligand conformations, indicating a well-defined complex for docking purposes. Each crystal structure listed above contains a conserved water molecule bridging the backbone carbonyl of Asp228, the carbonyl and amide proton of Val147, and the phenol of the ligand. All solvent molecules except this one were removed from the structure used for docking (PDB:4AGQ). The protein was protonated using the Protonate3D algorithm in the Born solvation model, using the Lennard-Jones 12-6 potential, and dielectric constants of 78.6 and 4 for bulk solvent and the protein, respectively. The ligands **L5-P** and **L5-O** were docked into the cavity formerly occupied by the co-crystallized ligand. For each ligand, 1000 binding poses were generated, with force field-energy minimisation (RMSG=0.001) of the best 200 non-duplicate poses as ranked by the GB/VI scoring function. The pose with the lowest deviation in iodophenol (**L5-P**) or phenol (**L5-O**) atoms compared to 4AGQ were selected for each ligand.

3.4.4. Stability Constant Determination

Aqueous acidity constants (pK_a) for **L5-P** and **L5-O** were measured using variable pH titrations monitored by UV-visible spectroscopy between 200 and 600 nm as a function of pH. Solutions of both ligands (12.5 μ M) were prepared in 0.1 M NaCl at pH 3. Due to the limited aqueous solubility of **L1**, solutions of 20% MeOH in H₂O of **L5-P** and **L5-O** were prepared for consistency across all ligands reported in this thesis. Small aliquots of 0.1 M NaOH were titrated into the solution to adjust the pH and at least 30 UV-vis spectra were collected in the pH 3-11 range. Spectral data were analyzed using HypSpec (Protonic Software, UK).³⁵³ Similarly, metal stability constants were obtained by titrating a solution containing 12.5 μ M ligand, 12.5 μ M Zn(ClO₄)₂•6H₂O, and 0.1 M NaCl with 0.1 M NaOH to

adjust the pH. Known metal hydrolysis constants were included in the HypSpec simulations as constant values.³⁵⁴ At least 30 UV-vis spectra were collected in the pH 3-11 range. Stability constants were calculated using the HypSpec computer program and metal speciation plots were created using the HySS2009 program (Protonic Software, UK).³⁵³

3.4.5. *In Vitro* Cytotoxicity – Stomach Cancer Cell Lines

The *in vitro* cytotoxicity of **L5-P** and **L5-O** against the stomach cancer cell line NUGC3 was assayed using the 3-(4,5-dimethylthiazol-2-yl)-2,5-diphenyltetrazolium bromide (MTT) assay.³⁵⁶ In each case, cells were seeded at 10^5 cells per well in 100 μ L of RPMI media in Cellstar 96-well plates (Grenier Bio-One) and incubated at 37 °C with 5% CO₂ for 24 hours. Following incubation, the cells were exposed to drugs at increasing concentrations ranging from 0.1 to 100 μ M in RPMI medium. Compounds were pre-dissolved in DMSO stocks and serial dilutions were prepared such that the final concentration of DMSO in media was below 1% (v/v). Treated cells were incubated at 37 °C with 5% CO₂ for 48 hours. Following the 48-hour incubation, the MTT test was performed as previously described.³⁵⁷ Experiments were performed in replicates of eight and repeated at least twice. Inhibition of cell viability was evaluated with reference to NT control to determine the absolute IC₅₀ value calculated from dose-response curves using nonlinear variable slope regression (Graphpad Prism 5.0 software).

3.4.6. Monitoring Intracellular Levels of Zn²⁺ in the p53-Y220C Cell Line NUGC3

NUGC3 cells (40,000 cells/well) were plated on glass slides treated with poly-L-lysine in 12-well plates. After 48 hours, cells were washed 2x 5 minutes in serum-free media and incubated with 1 μ M FluoZin-3³¹³ for 20 minutes at 37°C. Cells were then washed 2x 5 minutes in Earle's balanced salt solution (EBSS)/H (-) Ca/Mg containing the indicated treatments (ZnCl₂ = 50 μ M, **L5-P** = **L5-O** = 15 μ M = pyrithione = 50 μ M) and incubated for 2 hours at 37 °C before imaging. Cells were imaged using a Nikon ApoTome microscope (Nikon, France). FluoZin-3 and Hoechst 33342 were excited at 488 nm (argon laser) and 790 nm (Chameleon Ti:sapphire laser), respectively. Imaging was performed in under ten minutes to avoid alteration of cell physiology upon imaging at room temperature. To determine the change in fluorescence, each image was processed using

ImageJ Software (National Institutes of Health, Bethesda, MD) and integrated to represent the cumulative fluorescence for a single cell. Processing included adjustment of exposure and contrast to eliminate autofluorescence of the support. To avoid autofluorescence, each image was background-subtracted using the non-treated control. All images were batch processed using the same parameters. Cells were analyzed upon treatment with 50 μ M pyriothione (PYR)/ZnCl₂ (1:1) as a positive control.

3.4.7. Western Blot Analysis

NUGC3 cells were lysed with lysis buffer (125 mM Tris-HCl pH 6.7, NaCl 150 mM, NP40 0.5%, 10% glycerol). Proteins were denatured and deposited directly (75 μ g total protein) onto an SDS-PAGE gel. A Western Blot was performed using the pan-specific DO-1 primary antibody (Santa Cruz, sc-126) or cleaved caspase-3 Asp175 Antibody (Cell Signaling, 9661) at 1:1000 in PBS containing 5% dry milk at 4 °C overnight. Loading was controlled with rabbit anti- β -actin (Sigma, a1978, 1:4000). Secondary antibodies (anti-rabbit, anti-mouse: GE Healthcare) were incubated at 1:1000 for three hours at room temperature.

3.4.8. Site-Directed Mutagenesis

The plasmid encoding the DNA-binding domain of human wild-type p53 (residues 94-312) was gifted by Cheryl Arrowsmith.³⁵⁸ Four mutations to the p53 gene (M133L/V203A/N239Y/N268D) were successively introduced to increase structural stability of the protein, followed by addition of the Y220C mutation.³⁵⁹ All p53 mutants were prepared by site-directed mutagenic PCR according to standard protocols,¹⁵² using primers purchased from Eurofins Operon following Quikchange protocol (Agilent Technology). DNA polymerase (Q5) and DpnI enzyme were obtained from New England Biolabs. PCR products were transformed into chemically competent DH5 α *E. coli* and selected on ampicillin-supplemented agar plates. Single colonies obtained from overnight incubation at 37 °C were grown in Luria-Bertani (LB) broth for 16 hours. Plasmid DNA was purified using the plasmid spin MiniPrep kit (Qiagen, 27104) and sequenced by Eurofins Operon Sequence read service.

3.4.9. Protein Expression and Purification

Proteins were overexpressed using *E. coli* strain BL21-pLysS cells (ThermoFisher). Expression cultures containing 100 µg/mL ampicillin were inoculated from an overnight culture and grown at 37 °C to an OD₆₀₀ of 0.7. Protein expression was induced overnight at 15 °C with 0.3 mM IPTG. Cells were then harvested by centrifugation at 6500 rpm for 20 minutes. Cell pellets were resuspended in lysis buffer (50 mM Tris-HCl buffer, pH 6.5, 300 mM NaCl, 10% glycerol, 1% Triton X-100, 5 mM imidazole, 6 mM MgSO₄, 1 mM PMSF, and 5 mM β-mercaptoethanol) and sheared using ultrasonication. Cellular debris was isolated by centrifugation at 14000 rpm for 30 minutes and incubated with Talon® beads (cobalt-nitrilotriacetic acid) at 4 °C for 30 minutes. Talon beads were transferred to a column, washed twice with 20 mL of wash buffer (50 mM Tris-HCl buffer, pH 6.5, 500 mM NaCl, 10% glycerol, 10 mM imidazole, 0.5 mM TCEP, 1 mM PMSF, and 5 mM β-mercaptoethanol), and eluted with wash buffer containing 500 mM imidazole.¹⁵² Protein concentration was determined spectrophotometrically using the reported extinction coefficient $\epsilon_{280} = 17,130 \text{ cm}^{-1}$.³⁶⁰

3.4.10. Native Mass Spectrometry

Recombinant p53C-Y220C samples were thawed and dialysed in 200 mM ammonium acetate, and protein concentrations were measured using a Thermo Scientific NanoDrop Spectrophotometer. **L5-O** and **L5-P** were stored as DMSO stocks at 25 mM. Native MS experiments were performed on 2 µM p53C-Y220C with **L5-O** or **L5-P** ratios of 10, 25, and 50 equivalents. Each sample was incubated at room temperature for 2 hours. The final DMSO concentration in each sample is 0.2%. All MS data were acquired on a quadrupole ion mobility time-of-flight (TOF) mass spectrometer (Synapt G2S HDMS, Waters, Milford, MA, USA). Ions were produced by positive electrospray ionization (ESI) with a capillary voltage of 2 kV. The source temperature was set to 120 °C, with a sampling cone set to 150 V and the extraction cone set to 50 V. The trap cell containing argon gas was set at a pressure of 3.14×10^{-2} mbar. Trap and transfer collision energies were set to 20 V and 10 V respectively. The TOF pressure operated at 1.25×10^{-6} mbar.

Chapter 4. Bifunctional Ligand Design for Modulating Mutant p53 Aggregation in Cancer

Adapted from Miller, J. J.¹, Blanchet, A.², Orvain, C.², Nouchikian, L.³, Reviriot, Y.¹, Clarke, R. M.¹, Martelino, D.¹, Wilson, D.³, Gaiddon, C.², and Storr, T.¹ *Chem. Sci.* **2019**, *10*, 10802-10814.

¹Department of Chemistry, Simon Fraser University, Burnaby, British Columbia, Canada.

²INSERM, Molecular Mechanisms of Stress Response and Pathologies, Université de Strasbourg, Strasbourg, France.

³Chemistry Department, York University, Toronto, Ontario, Canada

JJM performed the synthesis with assistance from YR. JJM carried out the spectroscopic titrations and zinc-binding studies. JJM and RMC performed the crystallography. JJM and CO performed the zinc uptake experiments. JJM performed the light scatter experiments, TEM, immunofluorescence, cytotoxicity, cleaved caspase-3, immunoprecipitation, and RT-qPCR studies. JJM and LN carried out the native MS studies. AB performed the organoid and mouse toxicity studies.

4.1. Introduction

Amyloidogenic proteins are prone to endogenous misfolding and prion-like conversion from a soluble, folded protein into alternative oligomeric and fibrillar structures.^{158, 369-371} Proteins characterized by this feature include amyloid- β , tau, TDP-43, SOD1, and α -synuclein and contribute to a wide range of diseases including Alzheimer's disease and Amyotrophic Lateral Sclerosis (ALS).³⁷²⁻³⁷⁵ These proteins exhibit toxic gain-of-function (GoF) effects by self-propagating and acting as seeds to initiate aggregation.³⁷⁶⁻³⁷⁷ Recent studies have demonstrated that similar to neurodegenerative diseases, protein misfolding and aggregation play a role in cancer development through misfolding of the tumour suppressor protein p53.^{155-156, 204-205, 378-379} In particular, aggregation of mutant forms of p53 not only leads to loss of function (LoF), but it can exert a dominant-negative (DN) effect on WT p53. This occurs when it is converted into an aggregated species and is prevented from binding DNA, thus leading to loss of tumour

suppressor function. Further, mutant p53 possesses GoF properties wherein co-aggregation with homologous proteins, p63 and p73, can occur in a cross-seeding fashion to form amyloid oligomers and fibrils.^{156, 162, 164, 380-381} Overall, higher degrees of p53 aggregation have been associated with more invasive tumours,¹⁶⁰ and thus inhibiting its aggregation represents a promising avenue for anticancer therapy.

p53 plays a critical role in controlling the cell cycle by initiating apoptosis, DNA repair, and cell cycle arrest of damaged cells.^{58, 141, 271, 273} The core DNA-binding domain of p53 (p53C) contains a single Zn²⁺ ion that is essential for proper protein folding and function.¹⁵¹ However, in over 50% of cancer diagnoses, single point mutations render this protein inactive, the most common of which affect the protein's tertiary structure and frequently result in a loss or alteration of Zn-binding at the core site.^{274-276, 283} This can lead to protein unfolding and enhanced aggregation due to exposure of the amyloidogenic region of the protein (residues 251-257) that is normally buried within the protein's core (Figure 4.1).^{163, 283} Kinetic studies indicate that this occurs via a two-step process wherein the first involves relatively slow unfolding of p53C to expose the aggregation nucleus followed by a second, rapid aggregation step.^{291, 382} Interestingly, apo p53C (zinc-free) increases the aggregation process via nucleation with zinc-bound p53C and contributes to loss of protein function.²²³ The common hotspot mutant p53-Y220C destabilizes the protein's tertiary structure due to an exposed cavity at the surface of the protein. This can result in a loss of Zn²⁺ and causes accelerated protein aggregation.^{151, 283, 290-291} While research regarding restoration of p53 function has largely focused on stabilization of mutant p53C,^{153, 203, 364, 383-388} repopulating the metal-depleted site via metallochaperones^{213, 219, 222} and inhibiting p53 aggregation^{146, 207, 389-392} could be an effective alternative strategy.

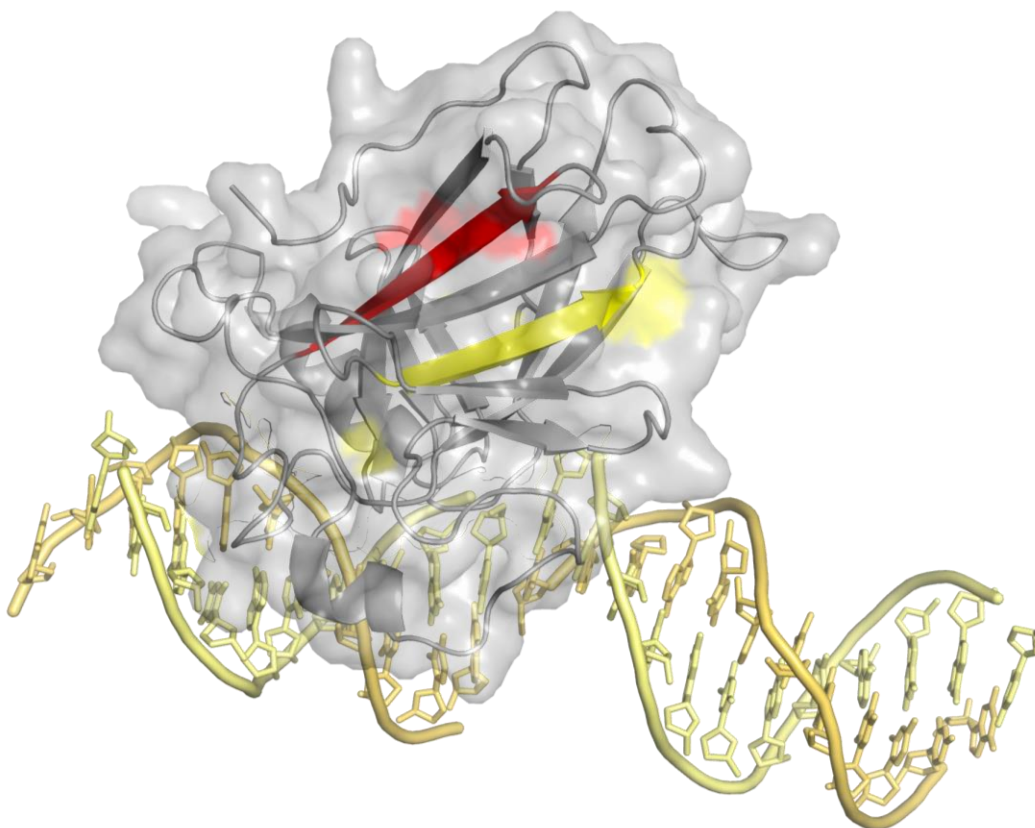


Figure 4.1. p53C bound to DNA shown in gold (PDB ID: 2AHI). The amyloidogenic region of p53 (residues 251-257) is shown in red. Normally buried within the protein's core, protein unfolding leads to exposure of this region and results in increased aggregation. The epitope recognized by PAb240 (yellow segment), an antibody that specifically recognizes mutant p53, is also buried within the protein's core under normal conditions and is exposed upon protein unfolding.

More broadly, targeted metal ion chelation and redistribution has shown utility both as an anticancer strategy^{237, 242, 285-288} and in modulating amyloidogenic protein aggregation^{255, 296, 393-394}. As such, a number of small molecule/peptide inhibitors of p53 aggregation have been developed^{146, 207, 389-392}. Specifically, Eisenberg and coworkers previously demonstrated the utility of a cell-penetrating peptide (ReACp53) targeted to interact with the amyloidogenic region of mutant p53 to inhibit its aggregation.¹⁶³ This resulted in rescued p53 function in high-grade serous ovarian carcinomas and led to decreased tumour proliferation in xenograft models. This highlights that the design of small-molecule/peptide inhibitors of p53 aggregation to rescue protein function is an important and viable chemotherapeutic strategy. Herein, we describe two novel bifunctional ligands, **L6** and **L7** (Figure 4.2), designed to reactivate p53 by inhibiting mutant p53 aggregation and restore zinc-binding using a metallochaperone approach. Given the

increased propensity for aggregation and possible zinc loss in the common mutant p53-Y220C, we used this as a model for testing compounds targeted to modulate mutant p53 aggregation. We and others have previously demonstrated the utility of zinc metallochaperones and zinc complexes for restoring function in common p53 mutants.^{213, 219, 222, 226, 364, 395-397} With reports showing that Zn-free p53 exhibits accelerated protein aggregation,^{162, 223, 283} the incorporation of a zinc metallochaperone unit to remetallate apo-p53 in combination with an aggregation-inhibiting moiety could provide advantages over reported single-target compounds. In general, multifunctional agents can be advantageous due to their ability to act on multiple targets, resulting in additive or synergistic effects, thereby increasing their therapeutic potential.²⁹⁵

In this chapter, two novel bifunctional ligands were synthesized and investigated for their ability to rescue wild-type function in mutant p53 by modulating protein aggregation and restoring zinc-binding via metallochaperone activity. We build off of our previous findings that the di-(2-picoly)amine fragment has an appropriate binding affinity to increase intracellular levels of zinc in mutant p53 and investigate the metallochaperone properties of our new ligand series. An in depth study of the importance of the iodine in our ligand framework for binding to mutant p53 and inhibiting aggregation, activating specific cell death pathways, and exhibiting cytotoxic selectivity in cancer cells over non-cancerous organoids, is highlighted in this work.

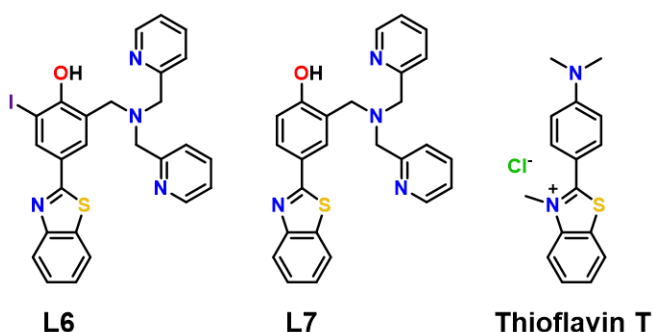


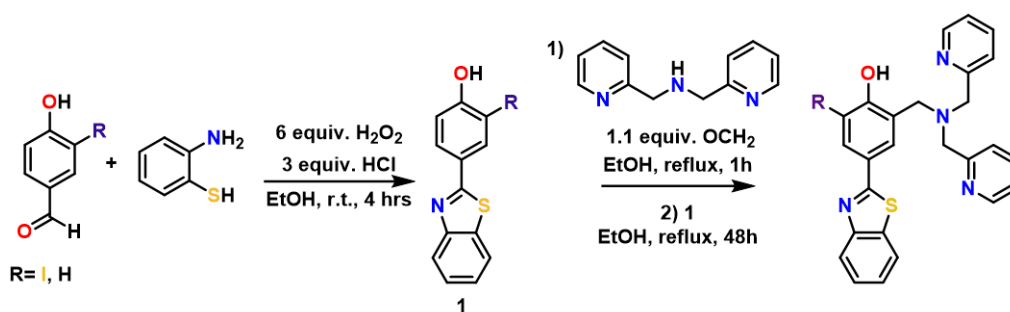
Figure 4.2. Chemical structures of ligands **L6**, **L7**, and Thioflavin T.

4.2. Results and Discussion

4.2.1. Ligand Design and Synthesis

Amyloid aggregates of the p53 protein have been identified in tumour cell lines as well as patient biopsies and are correlated with tumour growth due to loss of protein

function.^{156, 160-162} Biophysical studies have characterized p53 aggregates as largely β -sheet fibrils and demonstrate their ability to bind to the fluorescent amyloid marker Thioflavin T (ThT) (Figure 4.2).²⁰⁵ As such, we designed amyloid interacting molecules based on a structure similar to ThT. Di-(2-picoly)amine groups were appended at the 2-position as the zinc chelator based on the frequent use of this moiety in zinc chemosensors.³⁰⁰⁻³⁰³ A similar ligand scaffold was reported by Mirica and co-workers to interact with and modulate the aggregation of the amyloid- β peptide involved in Alzheimer's disease.²⁵⁵ **L6** contains an iodine substituent at the ortho position of the phenol functional group to probe the role of halogen bonding interactions and/or differing steric and electronic effects on influencing p53 aggregation (Figure 4.2). **L6** and **L7** were prepared via the Mannich reaction with 2-(4-hydroxy-3-iodo)benzothiazole (**L6**) or 2-(4-hydroxy)benzothiazole (**L7**) and di-(2-picoly)amine. **L6** required a prior iodination step of 4-hydroxybenzaldehyde with iodine monochloride. The synthetic routes are shown in Scheme 4.1.



Scheme 4.1. Synthesis of **L6** and **L7**. Yields are 31% and 35%, respectively.

4.2.2. Zinc Binding Affinities for **L6** and **L7**.

The reported models for Zn-binding in p53 were described in detail in Chapter 2. Briefly, two possible ligation sites are described, the native binding site (K_{d1} , 10^{-12} M) and the non native site (K_{d2} , 10^{-6} M). Metallochaperones designed to restore native zinc-binding should have Zn²⁺ affinities between K_{d1} and K_{d2} .^{152, 213, 222-223, 226} We demonstrate in Chapters 2 and 3 that despite the exact K_{d1} value for p53-Y220C being unknown, Zn metallochaperones on the order of 10^{-12} M have appropriate affinities to increase intracellular zinc levels of zinc in cells expressing this mutant. Spectrophotometric (UV-visible) pH titrations from pH 2-12 carried out to characterize ligand speciation are shown in Figure 4.3. The UV-vis spectra reveal a red shift from 315 to 360 nm for each ligand upon addition of NaOH. The experimental data was fit to an appropriate model and the

pKa values corresponding to the phenol, pyridine(s), and tertiary amines for each ligand are reported in Table 4.1. In each case, the highest *pKas* can be assigned to the phenol and ammonium group based on previously reported acidity constants,³⁰⁴⁻³⁰⁵ while the lowest *pKas* correspond to the pyridinium group.

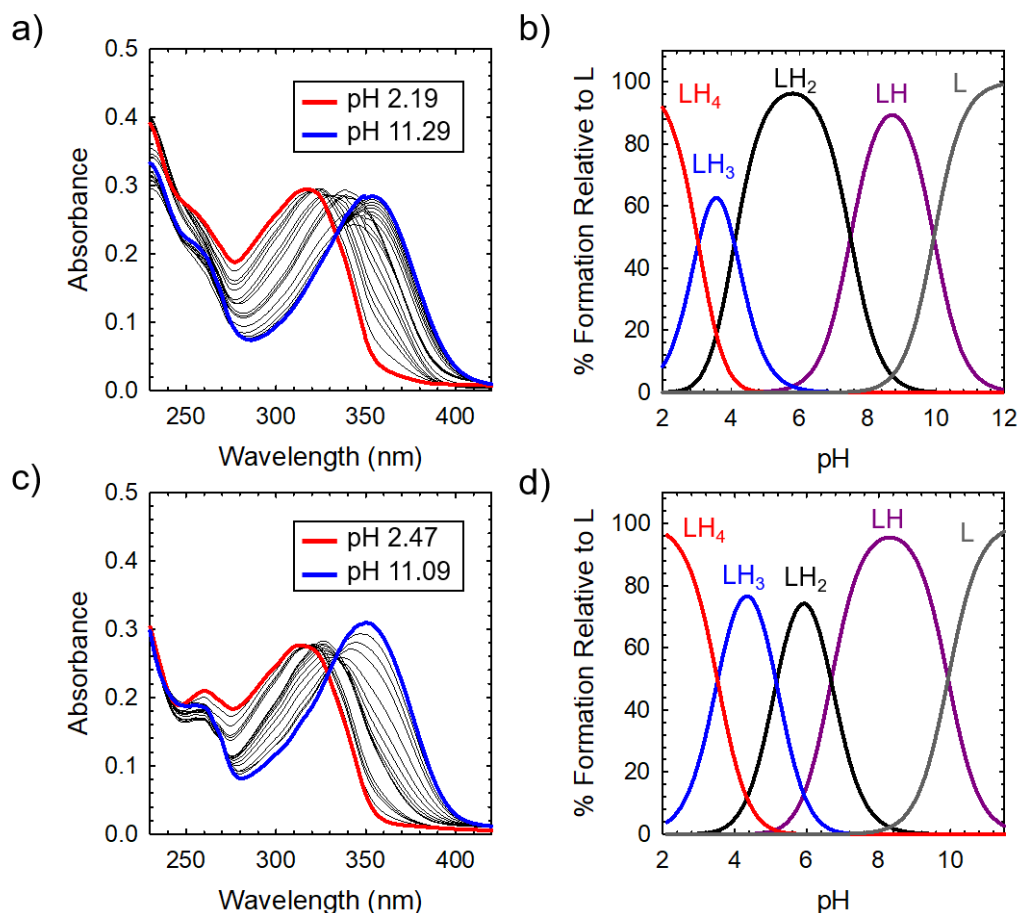


Figure 4.3. (a,c) Variable pH titration plots for **L6** and **L7**. (b,d) Simulated speciation diagrams of **L6** and **L7**. Speciation diagrams made using HySS2009.

Table 4.1. *pKa* values as determined by variable pH UV-vis titrations (errors are for the last digit).

Reaction	L6	L7
$[H_4L]^{3+} = [H_3L]^{2+} + H^+$ (<i>pKa</i> ₁)	2.98(2)	1.13(2)
$[H_3L]^{2+} = [H_2L]^+ + H^+$ (<i>pKa</i> ₂)	4.10(1)	4.78(2)
$[H_2L]^+ = [HL] + H^+$ (<i>pKa</i> ₃)	7.488(9)	7.05(2)
$[HL] = [L]^- + H^+$ (<i>pKa</i> ₄)	9.928(5)	9.937(2)

By analyzing the speciation diagrams provided in Figure 4.4, a complete model of the Zn²⁺ affinity of each ligand at physiological pH (7.4) can be obtained. The speciation diagrams for **L6** and **L7** demonstrate that the model is described with only 1:1 ligand to metal species present (Figure 4.4 b,d). The concentration of free Zn²⁺ present in solution at a given pH, referred to as pM ($pZn = -\log[Zn_{\text{unchelated}}]$), is a direct estimate of the metal-ligand affinity when all species in solution are considered.³⁰⁸⁻³¹⁰ Calculated pM (pZn) values for **L6** and **L7** (Table 4.2) are very similar (8.4 and 8.2) and are consistent with previously published reports containing similar ligands.^{255, 364} These values afford approximate dissociation constants (K_d) in the nanomolar range, an affinity appropriate for functioning as Zn metallochaperones for p53-Y220C.

Table 4.2. Stability constants (log K) of the Zn complexes of **L6** and **L7** and calculated pM values^[a] (errors are for the last digit).

	pZn ^[a] pH 7.4	Log K	
		ZnL	ZnLH
L6	8.4	14.18(2)	8.21(7)
L7	8.2	13.94(5)	5.51(6)

^[a] pZn was calculated using $pZn = -\log[Zn_{\text{unchelated}}]$, where $[Zn^{2+}]_{\text{free}}$ is determined from the HySS model.³¹² $[L6-L7] = [Zn^{2+}] = 12.5 \mu\text{M}$, 25 °C, I = 150 mM NaCl

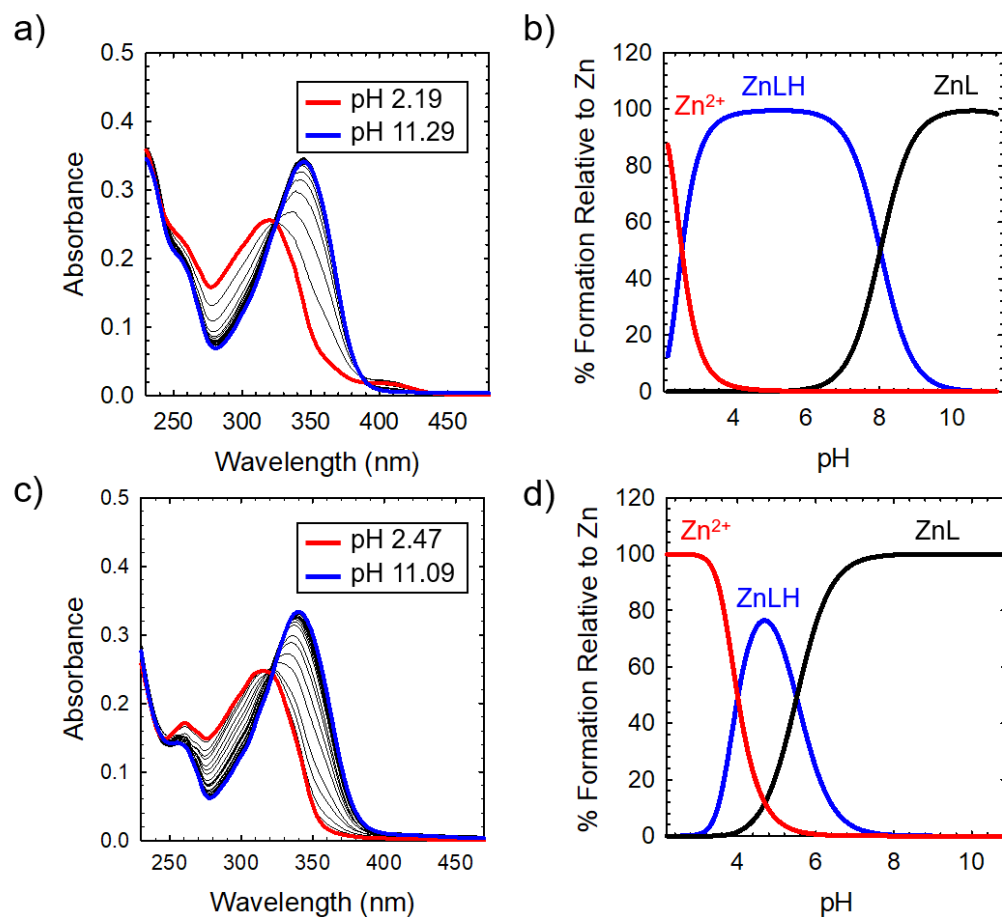


Figure 4.4. (a, c) Variable pH titration plots for **L6** + Zn^{2+} and **L7** + Zn^{2+} . (b, d) Simulated speciation diagrams of **L6** + Zn^{2+} and **L7** + Zn^{2+} . Speciation diagrams made using HySS2009.

Zn complexes of **L6** and **L7** were also isolated and characterized using NMR and X-ray crystallography (Figure 4.5 and Figure 4.6) and are in accord with the 1:1 binding of **L6** and **L7** to Zn^{2+} modelled above for variable pH titrations. Complete crystallographic information is provided in Table 4.3.

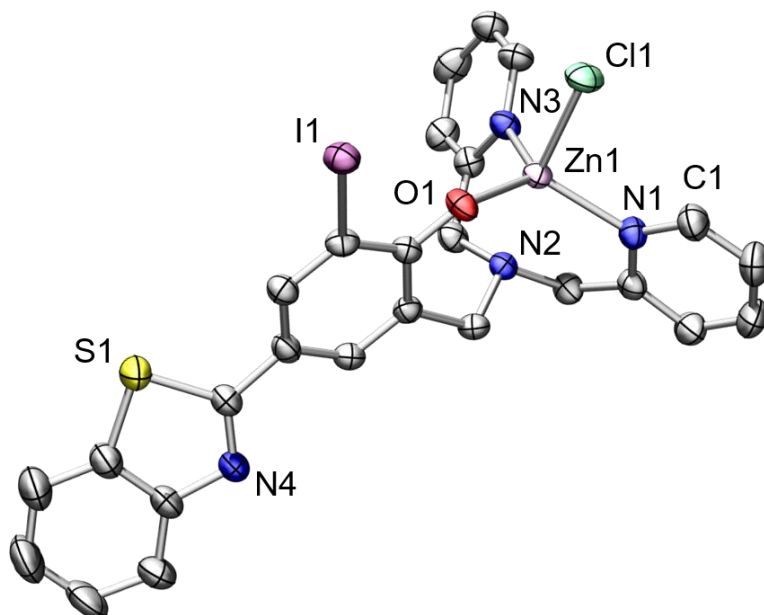


Figure 4.5. ORTEP of ZnL6Cl (50 % probability) using POV-Ray, excluding hydrogen atoms and solvent. Selected interatomic distances [Å]: Zn(1)-N(1): 2.271(3), Zn(1)-N(3): 2.090(2), Zn(1)-N(4): 2.088(3), Zn(1)-O(1): 1.954(2), Zn(1)-Cl(1): 2.2978(8).

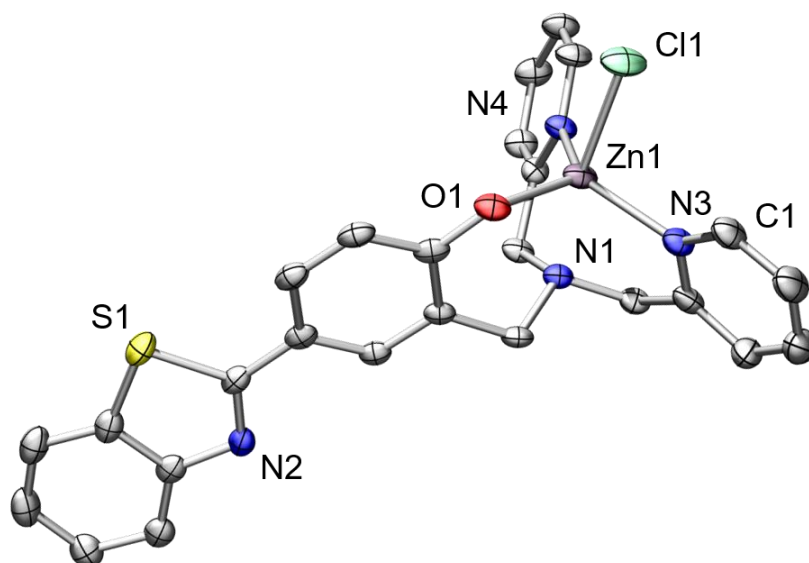


Figure 4.6. ORTEP of ZnL7Cl (50 % probability) using POV-Ray, excluding hydrogen atoms and solvent. Selected interatomic distances [Å]: Zn(1)-N(1): 2.251(5), Zn(1)-N(3): 2.067(4), Zn(1)-N(4): 2.090(5), Zn(1)-O(1): 1.964(4), Zn(1)-Cl(1): 2.341(2).

Table 4.3. Selected crystallographic information for ZnL6Cl and ZnL7Cl.

Crystallographic Information	ZnL6Cl	ZnL7Cl
Formula	C ₂₆ H ₂₀ ClIN ₄ OSZn	C ₂₆ H ₂₁ ClIN ₄ OSZn
Formula weight	664.27	538.38
Space group	P2 ₁ /c	P -1
a (Å)	15.51(2)	13.30(6)
b (Å)	13.17(2)	14.24(7)
c (Å)	14.73(2)	15.81(8)
α (deg)	90	101.7(2)
β (deg)	116.8(10)	99.1(3)
γ (deg)	90	99.5(2)
V [Å³]	2685.15	2832.98
Z	4	2
T (K)	293	150
ρ_{calcd} (g cm⁻³)	1.643	1.454
λ (Å)	1.54178	1.54178
μ (cm⁻¹)	12.148	3.163
R indices^a with I > 2.0σ(I) (data)	0.0245	0.0784
wR₂	0.0645	0.1945
R₁	0.0263	0.0819
Goodness-of-fit on F₂	1.050	1.099

^aGoodness-of-fit on F.

4.2.3. Increasing Intracellular Zn²⁺ in Cancer Cells

To determine whether **L6** and **L7** could serve as Zn metallochaperones, we analyzed the changes in levels of intracellular Zn²⁺ in the gastric cancer cell line NUGC3 expressing the p53-Y220C mutant. NUGC3 cells were incubated with the fluorescent Zn²⁺ sensitive probe FluoZin-3 (1 μM),³¹³ 50 μM of ZnCl₂, and either DMSO for non-treated (NT) controls or 50 μM of **L6** and **L7**. Pyrithione was used as a positive control for intracellular uptake of Zn²⁺.³⁹⁸ Subsequent imaging by fluorescence microscopy revealed that treatment with ZnCl₂ alone or **L6/L7** alone does not result in a significant increase in intracellular Zn²⁺ (Appendix C, Figure C7). However, addition of ZnCl₂ in combination with **L6** or **L7** significantly increased intracellular Zn²⁺ levels as indicated by increased fluorescence (Figure 4.7), thus demonstrating that both ligands and extracellular Zn²⁺ are required. However, due to the similar Zn K_d values of FluoZin-3 and **L6/L7** (Zn²⁺ K_d = ~ 15 nM for FluoZin-3,³¹³ 4 nM for **L6** and 6 nM for **L7**) Zn-binding to the fluorophore in this experiment is likely restricted, and thus total Zn uptake is underestimated. Quantification of fluorescent signals indicate that **L6** and **L7** increase intracellular Zn²⁺ by more than 3- and 2-fold, respectively, compared to the non-treated control. These results demonstrate

the potential of **L6** and **L7** to serve as Zn metallochaperones for mutant p53 by increasing intracellular Zn²⁺ concentrations.

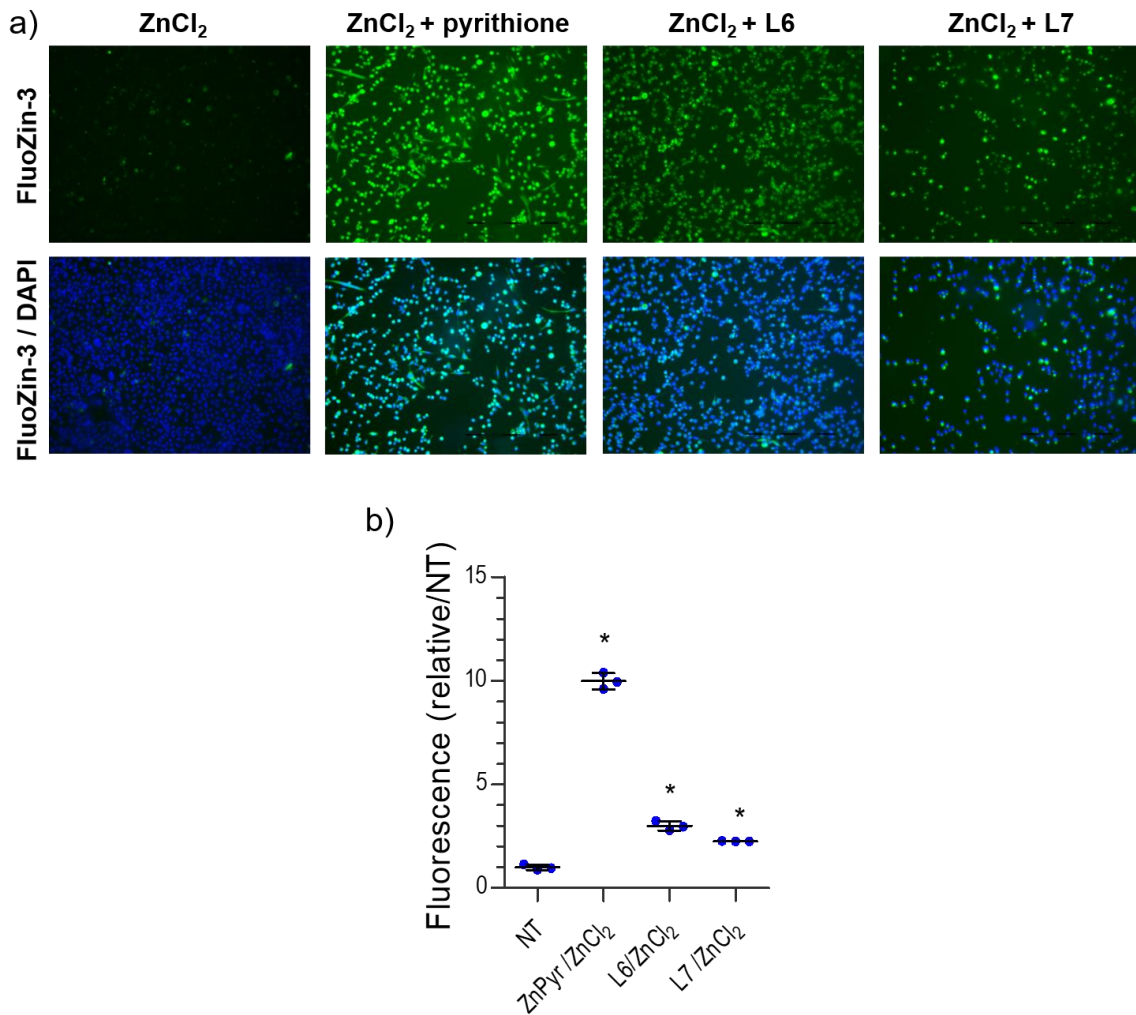


Figure 4.7. Treatment of NUGC3 (p53-Y220C) with **L6** and **L7** increases intracellular Zn²⁺. (a) Imaging of intracellular Zn²⁺ levels in complete serum-free media. NUGC3 cells were incubated with 1 μM FluoZin-3 for 20 minutes at 37°C, followed by incubation with indicated treatment (ZnCl₂ = 50 μM, **L6** = **L7** = 50 μM, 50 μM PYR) for 2 hours. Cells were imaged using a Nikon ApoTome microscope and fluorescence-quantified using ImageJ. (b) Fluorescence intensity of FluoZin-3 at 488 nm demonstrating relative Zn²⁺ levels. Blue dots represent average fluorescence intensity of imaged cells per individual trial. Black line indicates mean values, while black error bars demonstrate the 95% confidence interval. Statistical differences were analyzed using One-Way ANOVA with multiple comparisons (Dunnnett test). * indicates statistical differences from control with p < 0.001.

4.2.4. Effects of L6 and L7 on Mutant p53 Aggregation

To further explore the bifunctional nature of **L6** and **L7**, we investigated their effects on the aggregation process of mutant p53 *in vitro*. The core DNA-binding domain of mutant p53-Y220C (p53C-Y220C) was incubated at 37 °C and light scattering at 500 nm was monitored over time. Protein alone (5 μ M) demonstrated a rapid growth phase which continued to increase until two hours, where a plateau is observed, indicating a depletion of the substrate (Figure 4.8). Aggregation does not significantly increase past three hours up to six hours of monitoring (data not shown). Conversely, addition of one equivalent (5 μ M) of **L6** significantly inhibits mutant p53 aggregation, resulting in nearly 50% reduction of aggregation after only 3 hours. This effect is concentration dependent as the addition of only 10 μ M results in nearly complete inhibition of mutant p53 aggregation. Interestingly, the same result is not obtained with the addition of **L7**, as neither the addition of 5 or 10 μ M of **L7** cause inhibition of p53 aggregation. This result is unexpected given their structural similarity and hints at the importance of the iodine moiety in the **L6** structure. Increasing the **L6** or **L7** concentrations up to 25 μ M afforded similar changes in aggregation compared to results at 10 μ M (data not shown).

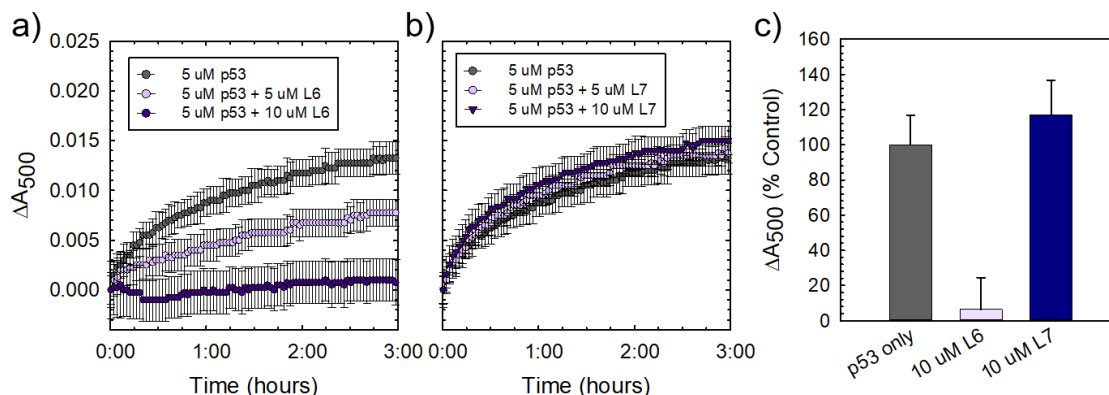


Figure 4.8. (a) 5 μ M p53C-Y220C in 30 mM Tris-HCl, 150 mM NaCl, pH 7.4 was incubated at 37 °C. Light scattering at 500 nm was monitored over time from 0 to 6 hours. Absorbance readings were recorded every 3 minutes, with 30 seconds of agitation before each reading. Addition of 5 and 10 μ M of **L6** shows concentration dependent inhibition of mutant p53 aggregation. (b) Addition of 5 and 10 μ M of **L7** results in no significant changes in mutant p53 aggregation. (c) Percent changes in light scattering of mutant p53 upon addition of 10 μ M **L6/L7** after 2 hours of incubation at 37 °C.

To investigate whether this effect was exclusive to p53-Y220C, we also tested the effect of **L6** and **L7** on the aggregation of wild-type p53 under aggregating conditions. **L6**

can also modulate the aggregation of wild-type p53, however, to a lesser extent in comparison to p53C-Y220C (Figure 4.9). **L7** had no effect on the aggregation of wild-type p53, similar to the results for p53C-Y220C. Overall, this suggests that **L6** could be used to modulate p53 aggregation beyond the specific p53-Y220C mutant.

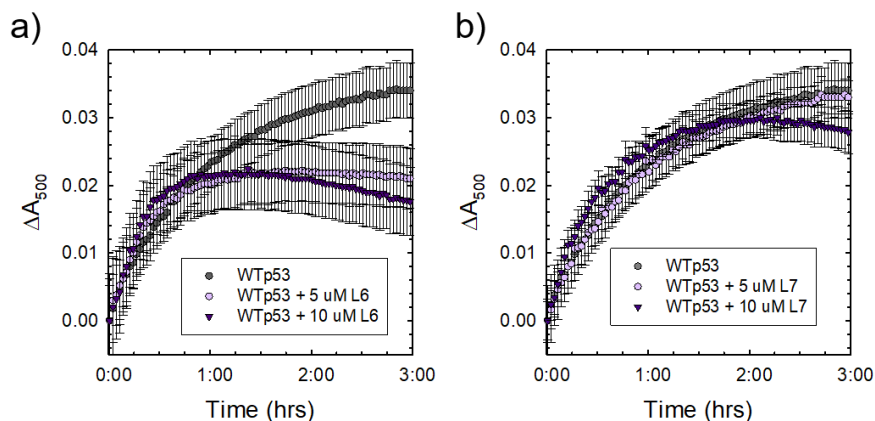


Figure 4.9. 5 μM wild-type p53 in 30 mM Tris-HCl, 150 mM NaCl, pH 7.4 was incubated at 37 $^{\circ}\text{C}$. Light scattering at 500 nm was monitored over time from 0 to 3 hours. Absorbance readings were recorded every 3 minutes, with 30 seconds of agitation before each reading. (a) Addition of 5 and 10 μM of **L6** shows inhibition of aggregation. (b) Addition of 5 and 10 μM of **L7** results in no significant changes in p53 aggregation.

Similar aggregation profiles are obtained when monitoring aggregate size distribution via gel electrophoresis, wherein incubation of mutant p53 with two equivalents of **L6** for two hours prevents aggregation and an intense band representative of monomeric species is observed (Figure 4.10 a). Conversely, protein alone and incubation with two equivalents of **L7** results in limited soluble species observable on the gel. These results were further corroborated upon investigation of aggregate morphology via transmission electron microscopy (TEM). After 30 minutes of incubation at 37 $^{\circ}\text{C}$ under constant agitation, p53 exhibits only amorphous aggregate structures by TEM, however, after 2 hours, mostly fibrillar structures are observed (Figure 4.10 b). Upon incubation of two equivalents (10 μM) of **L6**, fibrillar structures are inhibited and mostly amorphous aggregates were observed. Conversely, addition of 10 μM of **L7** resulted in the observation of mostly fibrillar structures.

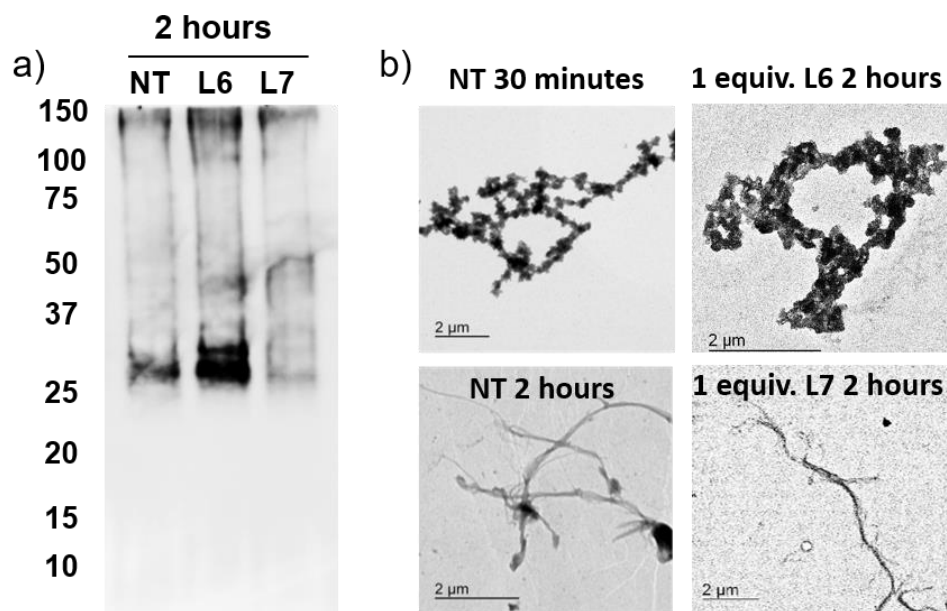


Figure 4.10. (a) Gel electrophoresis and Western Blot of 8 μ M p53C-Y220C in 30 mM Tris, 150 mM NaCl, pH 7.4 (NT – lane 1) and two equivalents of **L6** (lane 2) and **L7** (lane 3) after a 2-hour incubation with constant agitation at 37 $^{\circ}$ C. Western Blot was revealed using the primary antibody PAb240, which recognizes mutant p53. (b) TEM images of 8 μ M mutant p53C-Y220C under specified conditions.

Using recombinant protein, we demonstrated the ability of **L6** to significantly inhibit mutant p53 aggregation in contrast to **L7**, which has no observable effect. We sought to determine whether this stark contrast is still observed in cancer cell lines. It is important to study protein aggregation in the context of its complex cellular environment due to factors such as molecular chaperones and proteases, which are known to play a key role in protein folding.³⁹⁹ To this end, we used immunofluorescence to study the behaviour of p53 aggregation upon treatment with **L6/ L7** in NUGC3 cells. Further cell studies were carried out at 25 μ M (*vide infra*), as this concentration corresponds to the IC₅₀ value for **L7** (Table 4.5). Using the p53 antibody DO-1, we detected high levels of p53 expression in NUGC3 (Figure 4.11). Overexpression of p53 is commonly reported in cancer cell lines containing mutant p53 as the impaired function can often lead to changes in protein conformation and alter stability when targeted for degradation, leading to its accumulation.^{160, 400-404} We also observed high expression levels of aggregates in the NUGC3 cell line using the antibody A11, which has been used previously to label p53 aggregates.^{160-161, 405} Under non-treated conditions, NUGC3 showed widespread protein aggregation via A11 that colocalized with p53. Interestingly, 24 hours of treatment with 25 μ M **L6** significantly decreased the amount of A11-detected aggregates and resulted in decreased

colocalization observed between DO-1 (p53) and A11. This indicates that **L6** is effective at reducing p53 aggregation in the mutant p53 cell line. In agreement with results obtained in the p53 aggregation experiment above, the addition of 25 μ M **L7** did not decrease the levels of A11-detected aggregates in comparison to the control. In addition, significant colocalization between DO-1 (p53) and A11 is observed.

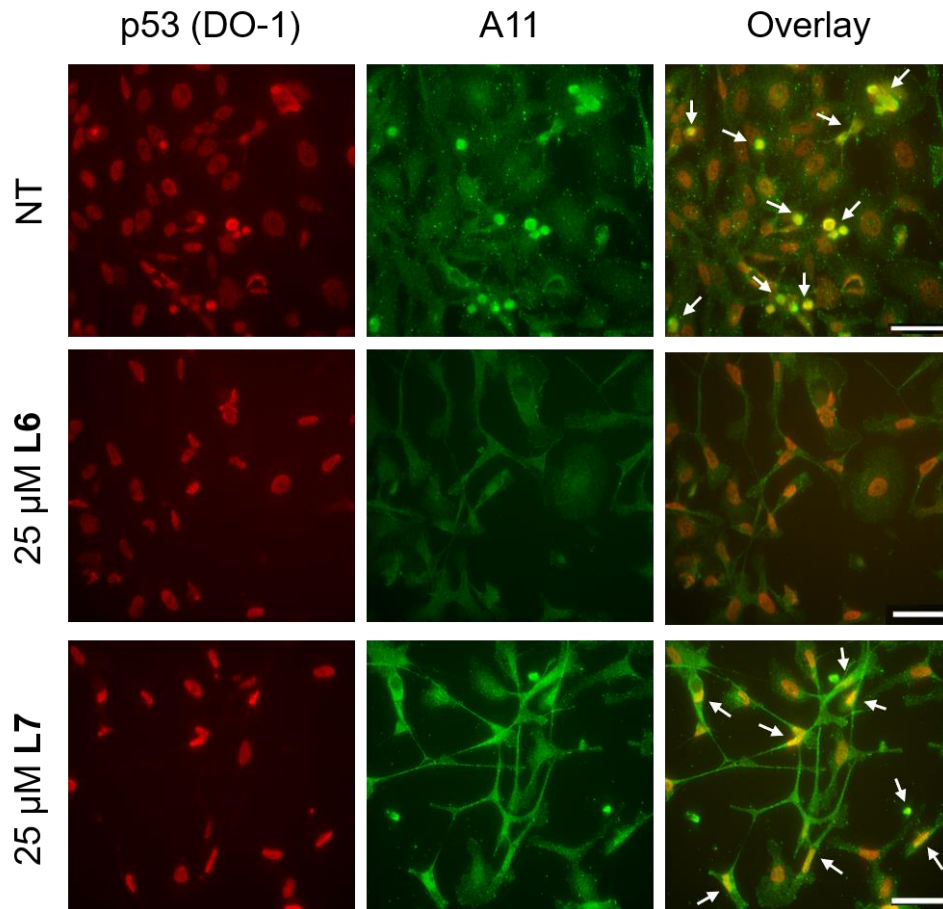


Figure 4.11. NUGC3 cells were treated with 25 μ M L6/L7 or 0.1% DMSO (NT) for 24 hours followed by labelling with anti-p53 (DO-1) and anti-oligomer (A11) antibodies at concentrations of 1:1000 and 1:100 respectively. Nuclei were stained with DAPI, followed by imaging using a fluorescence microscope. Columns from left to right include: DO-1 (anti-p53), A11 (anti-oligomer), and co-immunofluorescence of DO-1 and A11. The white arrows are representative of the overlap between DO-1 and A11. The scale bar represents 50 μ m.

We also investigated changes in p53 aggregation via co-immunofluorescence with DO-1 and ThT, a fluorescent dye that labels misfolded amyloid aggregates.⁴⁰⁶ Treatment with 25 μ M **L6** led to an observable decrease in colocalization between p53 and ThT, whereas treatment with 25 μ M **L7** exhibits high levels of colocalization similar to non-

treated controls (Figure 4.12). Taken together, these results highlight the key importance of the iodine moiety of **L6** for modulation of mutant p53 aggregation even in cellular systems.

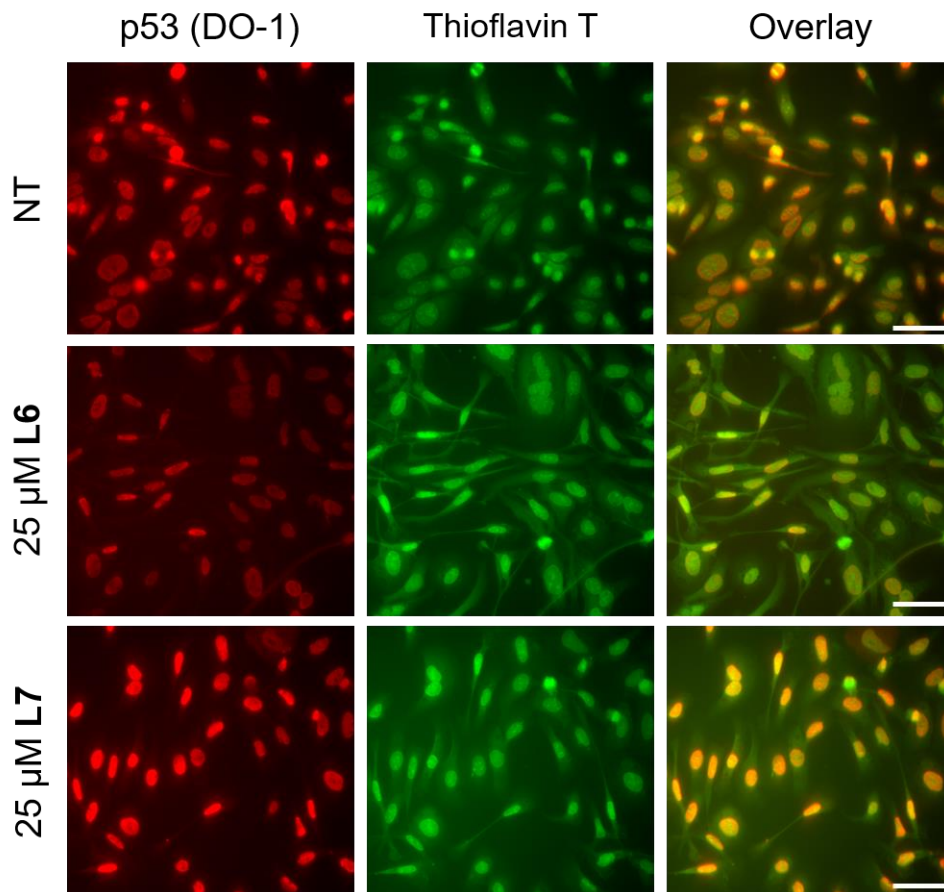


Figure 4.12. NUGC3 cells were treated with 25 μM **L6**, **L7**, or 0.1% DMSO (NT) for 24 hours followed by labelling with anti-p53 primary antibody DO-1 (1:1000) and ThT (1 mM). Nuclei were stained with DAPI, followed by imaging using a Nikon ApoTome microscope. Columns from left to right include: DO-1 (anti-p53), ThT, and co-immunofluorescence of DO-1 and ThT. The scale bar represents 50 μm .

4.2.5. Interaction Between L6/L7 and Mutant p53

The distinct differences between **L6** and **L7** in modulating mutant p53 aggregation prompted an investigation into the potential differential binding of our bifunctional ligands with mutant p53. Using native mass spectrometry, we observe that the addition of increasing concentrations of **L6** affords an additional species in the mutant p53 spectrum. This corresponds to a mass increase of 564 Da, which is indicative of one equivalent of

L6 bound to p53 (Figure 4.13). At higher equivalents of **L6**, a peak corresponding to a 1128 Da mass increase is evident, indicating the interaction of two **L6** ligands with mutant p53. In contrast, no evidence of **L7** interacting with mutant p53 was observed, even at higher concentrations. This suggests that the ability of **L6** to modulate and reduce mutant p53 aggregation is a result of direct interactions with the protein and could explain why mutant p53 aggregation is not perturbed in the presence of **L7**. While this result is both interesting and surprising due to their structural similarity, it is possible that the iodine is contributing to halogen bonding, which would result in favourable interactions with the exposed aggregation-prone, hydrophobic protein segment.⁴⁰⁷ Recent pharmaceutical advances have highlighted the advantages of halogen bonding and demonstrated significantly improved binding of many small molecules to their protein targets due to halogen bonding to carbonyl groups.^{153, 268-270} Furthermore, Eisenberg and co-workers have previously demonstrated that by binding the exposed hydrophobic segment of p53, protein aggregation was prevented and therefore contributed to restored protein function.¹⁶³

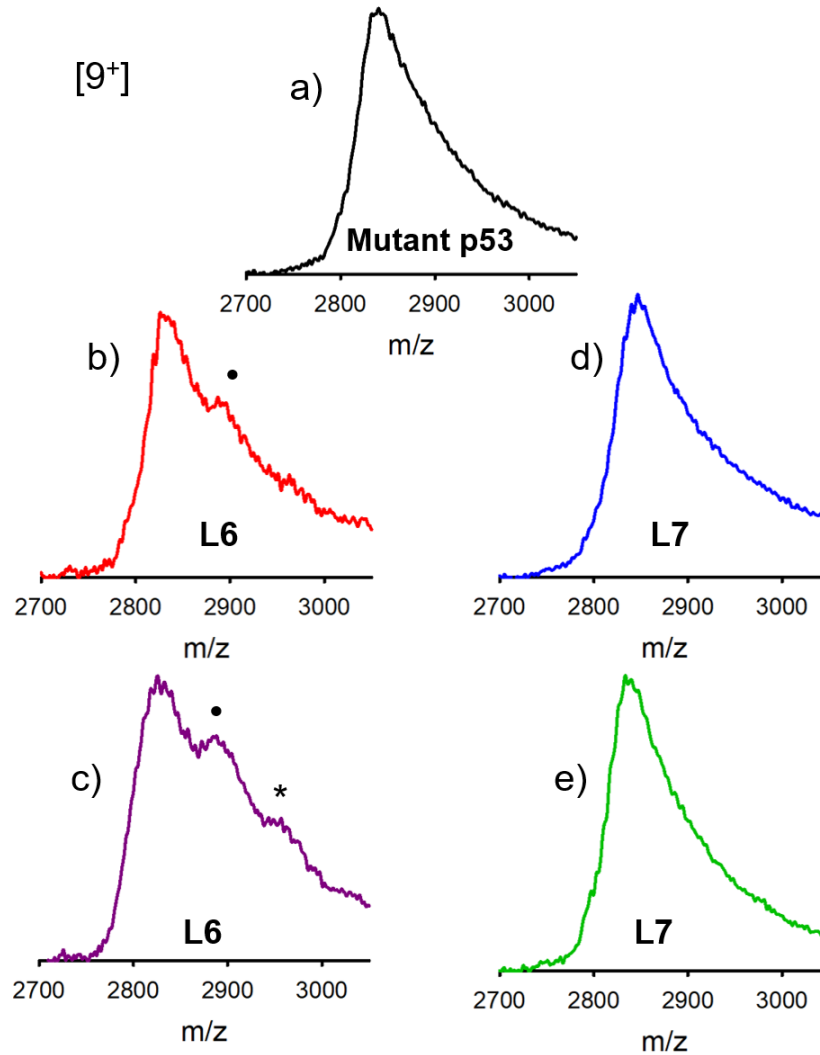


Figure 4.13. Native mass spectrometry results using recombinant p53C-Y220C (3 μ M) incubated with (a) 0.2% DMSO (b) 30 μ M **L6** (c) 75 μ M **L6** (d) 30 μ M **L7** and (e) 75 μ M **L7** for 2 hours at room temperature. • Indicates a 564 Da mass increase representing an interaction between mutant p53 and **L6**, * indicates an 1128 Da mass increase representing an interaction between mutant p53 and 2 **L6**. [9⁺] represents the charge state of p53C-Y220C.

4.2.6. Restoration of p53 Function

To determine if the ligands could restore wild-type function to mutant p53, we first investigated whether they reduced mutant p53 levels via immunoprecipitation with the PAb240 anti-p53 antibody. The PAb240 antibody recognizes a specific antigen buried within the protein core (residues 213-217), and therefore can only recognize at least partially unfolded p53.¹⁶³ Using native lysates from NUGC3 cells treated in the absence or presence of increasing concentrations of **L6** and **L7**, we immunoprecipitated mutant

p53 and performed Western Blot with DO-1, which recognizes p53 regardless of conformation. As shown in representative immunoprecipitation experiments, NUGC3 under non-treated conditions expressed an intense band for PAb240, which is expected given its p53 mutant status (Figure 4.14). Overnight treatment with **L6** and **L7** were able to reduce levels of mutant p53 by 54% and 47%, respectively. These results indicate that upon treatment with our bifunctional ligands, p53 conformation is altered wherein the antigen recognized by PAb240 is now buried within the protein's core.

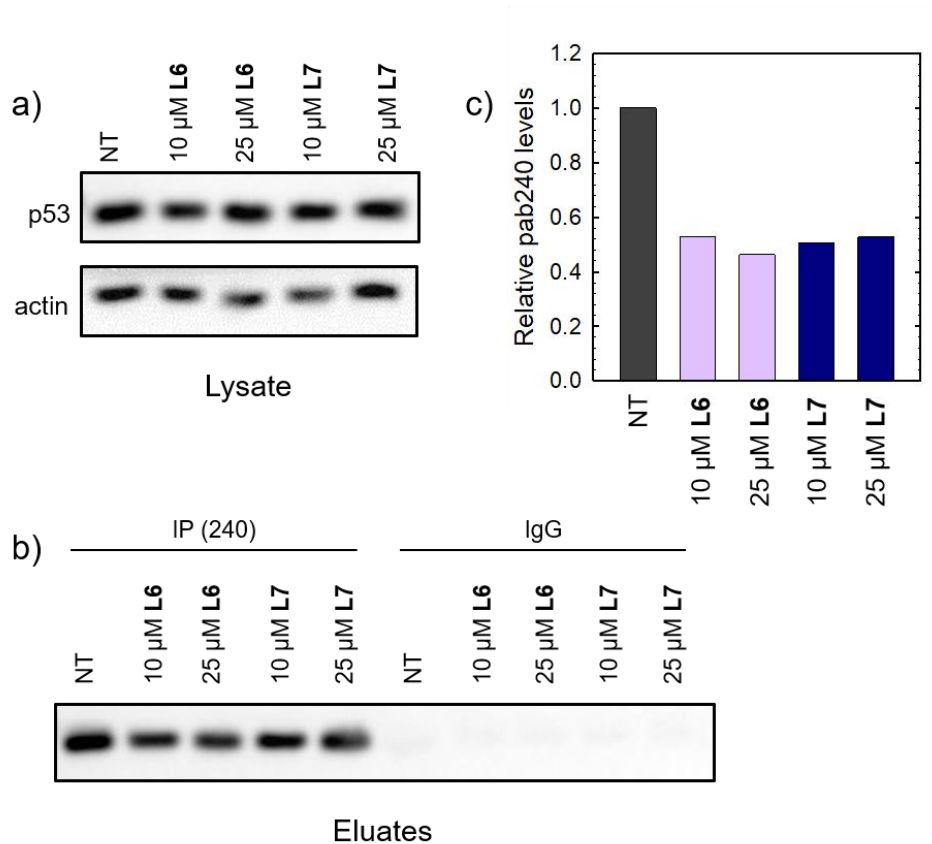


Figure 4.14. NUGC3 cells were treated for 13 hours with **L6** and **L7** at the indicated concentrations. Cells were then lysed and proteins were immunoprecipitated using the p53 antibody PAb240 that immunoprecipitates only mutated p53. Precipitated proteins were separated on a 10% SDS page gel and incubated with the p53 antibody (DO-1), which recognizes both mutated and wild-type p53. An unrelated antibody was used as a negative control for immunoprecipitation (IgG). Actin protein levels present in the lysate are shown as a control for the amount of protein used in the immunoprecipitation. (a) Representative Western Blot image of lysate conditions added to the PAb240 antibody prior to immunoprecipitation (b) Representative Western Blot image of eluate samples removed post immunoprecipitation (c) Quantification of relative PAb240 antibody levels from eluates in part (b).

Upon determination that our bifunctional ligands reduced mutant p53 levels in NUGC3 cells, we investigated whether this was coupled with an increase in the expression levels of several p53 target genes that are involved in either cell cycle arrest (p21) or apoptosis (NOXA, PUMA).^{58, 277} Expression levels were also monitored in p53-silenced NUGC3 cells using the p53 silencing RNA (sip53) to probe the extent of p53 dependence in this experiment. NUGC3 cells were treated for 6 hours with 25 μ M of **L6** or **L7** and the expression level of p53 and three of its representative target transcripts (p21, NOXA,

PUMA) were measured by RT-qPCR. Strikingly, treatment of NUGC3 with **L6** and **L7** in the presence of a non-targeting siRNA used as a control, SiCT, resulted in a 4.3- and 3.9-fold increase in p21, a common indicator of p53 function (Figure 4.15).¹²⁶⁻¹²⁷ A 2.0- and 1.5-fold increase in NOXA was also observed upon treatment with **L6** and **L7**, respectively. No changes in PUMA expression are observed upon treatment with **L6** or **L7** during the 6-hour treatment time of this experiment. The changes in p21 and NOXA were obtained without increasing p53 expression levels, suggesting restored p53 function in mutant p53 wherein cell cycle arrest and apoptotic pathways are now activated. Silencing of p53 with sip53 resulted in a significant decrease in p21 levels in the presence of **L6**. Notably, p21 expression was not completely abolished. This may be a result of several causes: one possibility is the lack of complete silencing of the p53 protein, however, another likely explanation is related to the ability of mutant p53 to bind and inactivate p63 and p73, both of which regulate target genes p21 and NOXA.³³⁹⁻³⁴² Thus, knock-out of mutant p53 might result in increased activity of p63 and p73, causing an increase in p21/NOXA expression levels. Interestingly, the addition of sip53 to **L7** treatment resulted in no significant difference in p21 and NOXA expression levels from SiCt conditions. These results can be rationalized when considering the aggregation experiments above, as **L6** interacts directly with mutant p53 and reduces aggregation whereas **L7** has no observable effect. This suggests that in contrast to **L6**, **L7** may act largely through a p53-independent mechanism.

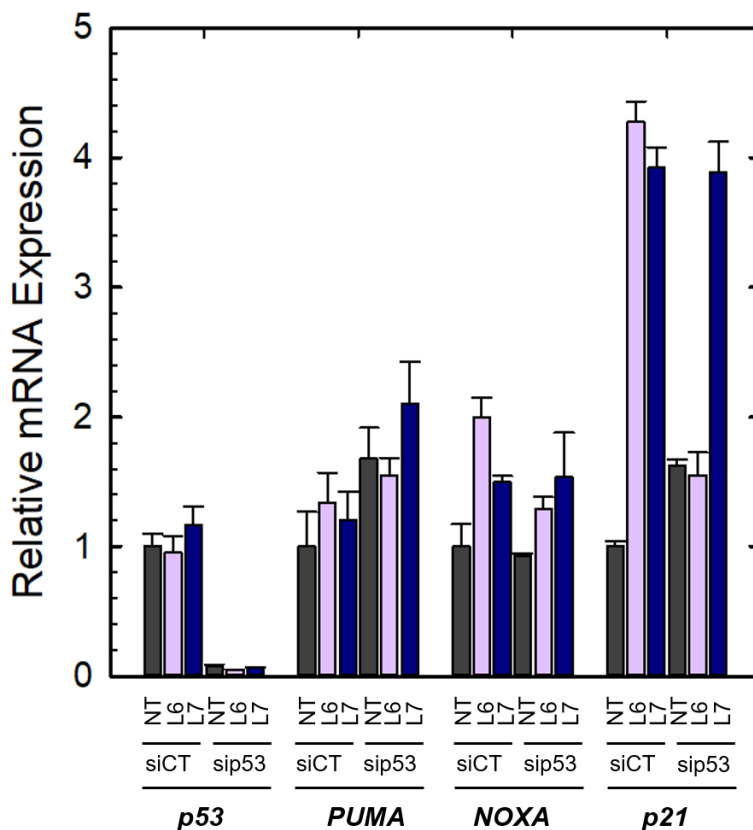


Figure 4.15. NUGC3 cells were transfected with control siRNA (siCT) or siRNA directed against p53 (sip53) and then treated for 6 hours with 25 μ M of **L6** and **L7**. Total RNAs were extracted and RT-qPCR performed to measure the expression of TP53 (p53), p21, PUMA, and NOXA. Bars represent means of triplicates with error bars.

4.2.7. *In Vitro* Cytotoxicity

The cytostatic (GI_{50}) and cytotoxic (LC_{50}) activities of **L6** and **L7** were evaluated against a panel of 60 cancer cell lines (NCI-60 screening program) containing a wide range of cancer types. Both ligands passed the minimum cytotoxic threshold in the 1-dose assay to advance to 5-dose testing and showed high activity across all 60 cell lines as demonstrated by their average growth inhibitory (GI_{50}) concentrations (Table 4.4). **L6** exhibited a 3-fold increase in average GI_{50} compared to both **L7** and cisplatin and a 6-fold decrease in average GI_{50} compared to oxaliplatin. The corresponding zinc complexes Zn**L6**Cl and Zn**L7**Cl were also tested but exhibited lower biological activity at the initial test concentration of 10 μ M and were not subjected to further studies. A heat map summarizing the patterns of *in vitro* cytostatic and cytotoxic activities from low activity (blue) to high activity (red) is shown in Figure 4.16.

Table 4.4. Mean GI₅₀ and LC₅₀ values for **L6**, **L7**, Cisplatin, and Oxaliplatin from the NCI-60 screen.

Ligand	NSC Number ^[a]	GI ₅₀ (μM) ^[b]	LC ₅₀ (μM) ^[b]
L6	788648	0.44	93.8
L7	788649	1.58	79.2
Cisplatin ⁴⁰⁸	119875	1.5	44.0
Oxaliplatin ⁴⁰⁸	226046	2.8	> 90

[a] NSC number is the compounds internal ID number at the National Cancer Institute. [b] GI₅₀ values correspond to the dose that inhibits 50% of cell growth compared to non-treated controls, while LC₅₀ indicates the concentration required to kill 50% of treated cells.³²⁰

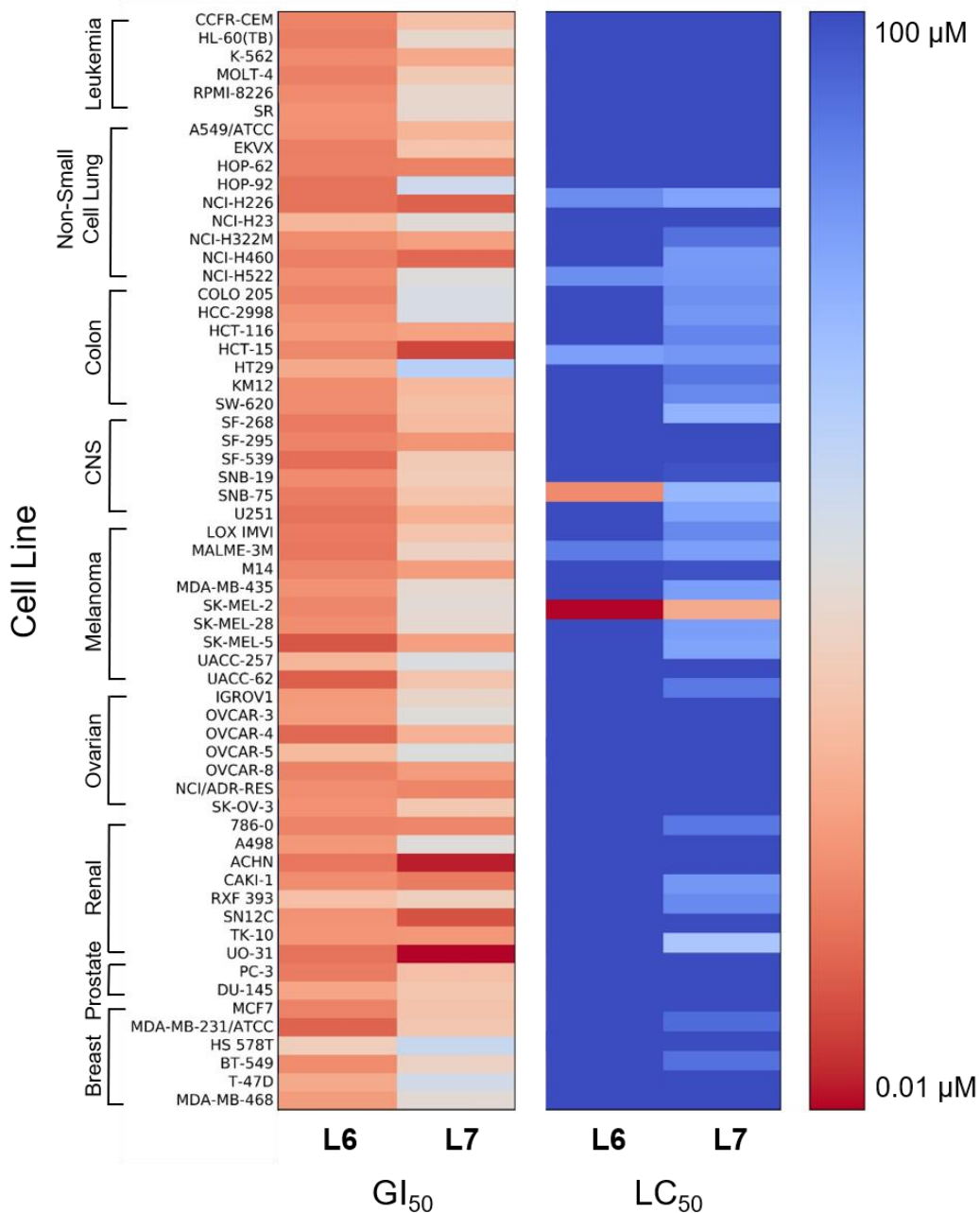


Figure 4.16. Heat map showing the *in vitro* cytostatic (GI_{50}) and cytotoxicity (LC_{50}) of **L6** and **L7** in the NCI-60 screen. Blue indicates low cytotoxicity (100 μ M) and red indicates high cytotoxicity (0.01 μ M).

The *in vitro* cytotoxicity of ligands **L6** and **L7** was also tested in the gastric cancer cell line NUGC3. Gastric cancer is the second leading cause of cancer-related deaths worldwide and contains a wide range of p53 mutations that are present in up to 77% of gastric carcinomas.⁴⁰⁹ Using standard MTT protocols,³⁵⁶ we determined that **L6** exhibited

a significant 11-fold increase in cytotoxicity compared to oxaliplatin and a 5-fold increase in cytotoxicity over **L7** (Table 4.5).

Table 4.5. *In vitro* cytotoxicity (IC₅₀ values)^[a] data for stomach cancer cell lines NUGC3 upon indicated treatment for 48 hours.

Ligand	NUGC3 (p53 ^{Y220C}) IC ₅₀ ^[a] (μM)
L6	5 ± 1
L7	25 ± 3
Cisplatin ⁴⁰⁸	20 ± 2
Oxaliplatin ⁴⁰⁸	50 ± 3

^[a] IC₅₀ is the concentration needed for 50% reduction of survival based on survival curves.³²³

4.2.8. Apoptotic Effects of L6 and L7 in Human Gastric Cancer Cell Lines

To investigate the molecular basis for the observed cytotoxicity, we examined whether **L6** and **L7** could induce apoptosis in gastric cancer cell lines containing wild-type (AGS) and mutant p53 (NUGC3). AGS and NUGC3 cells were treated with IC₅₀ and IC₇₅ concentrations of ligands **L6** and **L7** and oxaliplatin for 48 hours and then cleavage of caspase-3 and p53 protein levels were assessed via Western Blot. In the wild-type p53 cell line, oxaliplatin exhibits a significant increase in p53 levels, however, very little cleavage of caspase-3 is observed at selected concentrations (Figure 4.17 a). Neither **L6** nor **L7** induced any changes in either p53 expression levels or cleavage of caspase-3, even at the IC₇₅ concentration. In the NUGC3 cell line, cleavage of caspase-3 is observed with oxaliplatin and **L6**, whereas no caspase-3 cleavage is observed with **L7** (Figure 4.17 b). NUGC3 cells were also treated with 25 μM of oxaliplatin, **L6**, or **L7** as this concentration of **L6** resulted in reduction of mutant p53 aggregation in NUGC3 cells, and therefore we investigated whether this was coupled with an induction of apoptosis. Upon treatment of NUGC3 cells with 25 μM of indicated compound for 48 hours, the Western Blot revealed that **L6** did in fact result in a strong presence of cleaved-caspase-3 as indicated by the intense band in Figure 4.17 c. Treatment with **L7** also resulted in cleavage of caspase-3, however to a significantly lesser extent than treatment with **L6**. Oxaliplatin did not induce caspase-dependent apoptosis in NUGC3 cells at 25 μM. Interestingly, this induction of apoptosis by **L6** and **L7** in NUGC3 cells was not abolished by treatment with sip53, but rather an increase in cleaved caspase-3 is observed. While this could be an indication of off-target effects, the p53-dependent increase in apoptosis is suggestive of a removal of

toxic gain-of-function effects from mutant p53 aggregates.⁴¹⁰ Furthermore, although faint, the presence of cleaved caspase-3 under sip53 NT conditions additionally suggests removal of toxic gain-of-function effects rather than off-target mechanisms. Gain-of-function effects for mutant p53 have been well characterized, and structurally destabilized mutants have been documented to co-aggregate with the homologous protein p73, thereby inactivating its function.^{339, 411-415} Thus, removal of mutant p53 in this case could result in p73-mediated apoptosis. Although this hypothesis is attractive and highly plausible, it is likely that additional mechanisms are also involved.

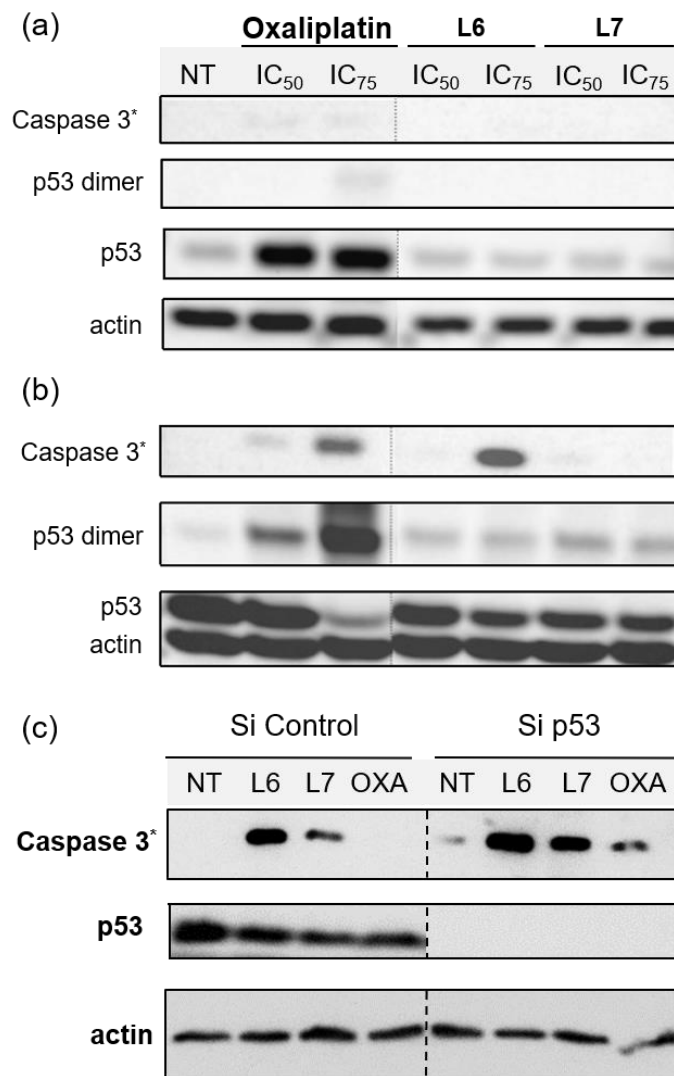


Figure 4.17. AGS cells (a) and NUGC3 cells (b) were treated for 48 hours with the IC₅₀ and IC₇₅ concentrations of indicated compound. Proteins were extracted, and 20 μ g were separated on SDS PAGE. Cleaved caspase-3 (Caspase 3*), p53, and actin were then detected by Western Blot. (c) NUGC3 cells were treated with 25 μ M of indicated compound for 24 hours. Proteins were extracted, and 40 μ g was separated on SDS PAGE. Cleaved caspase-3 (Caspase 3*), p53, and actin were detected by Western Blot.

To further explore possible cell death pathways activated by our ligands, we investigated whether **L6** and **L7** were involved in caspase-independent cell death. Specifically, we investigated whether they participated in translocation of the apoptosis inducing factor (AIF). During apoptosis, AIF moves through the outer mitochondrial membrane into the cytosol and participates in chromatin condensation and DNA-fragmentation upon translocation into the cell nucleus.^{100, 112, 416} Using immunofluorescence and confocal microscopy, we monitored AIF localization upon

treatment of **L6** and **L7** in NUGC3 cells. In NT conditions, AIF punctate staining is observed that spares the nucleus, exhibiting mitochondrial localization (Figure 4.18). Upon treatment with 5 μ M **L6** for 24 hours, AIF expression is largely upregulated, and nuclear localization is partially observed. Increasing concentrations of **L6** (25 μ M) lead to almost completely diffuse and nuclear staining, indicative of apoptotic cells. In contrast, very little change in AIF expression levels or localization is observed upon treatment with **L7**, again highlighting the increased apoptosis-inducing activity of **L6** in mutant p53 cell lines. Importantly, studies have shown that in mutant p53 cell lines, caspase-independent cell death is compromised, and that functional p53 could regulate AIF expression and result in activation of cell death.⁴¹⁷⁻⁴¹⁸ This provides further indication that by reducing mutant p53 aggregation, **L6** can restore protein function and activate otherwise compromised cell death pathways.

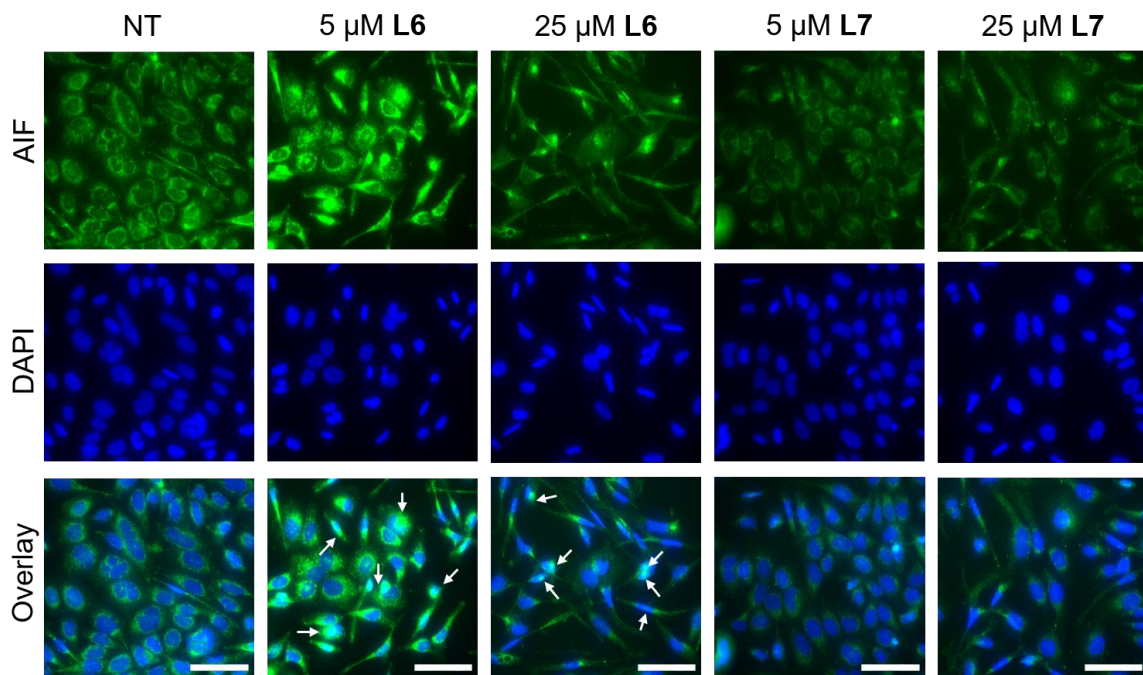


Figure 4.18. NUGC3 cells were treated with 5 and 25 μ M **L6/L7** or 0.1% DMSO (NT) for 24 hours followed by labelling with anti-AIF antibody (1:1000). Nuclei were stained with 4',6-diamidino-2-phenylindole (DAPI), followed by imaging using a Nikon ApoTome microscope. Columns from left to right include: AIF, DAPI, and coimmunofluorescence of AIF and DAPI. The white arrows are representative of the overlap between AIF and DAPI. The scale bar represents 50 μ m.

Platinum-based chemotherapy is among the first line standard of care for gastric cancer patients, however, cancers with p53 mutations often exhibit decreased sensitivity

and increased resistance to platinum agents.²⁴³⁻²⁴⁵ This is due to the fact that the mechanism of these agents includes induction of DNA damage, which leads to downstream activation of the p53 pathway, providing that functional p53 is present.^{18, 163} With up to 77% of gastric cancers harbouring p53 mutations,⁴⁰⁹ co-administration of agents that first restore p53 function and exhibit a synergism with platinum agents are highly desirable. To this end, we tested whether pre-incubation of NUGC3 cells with **L6** could result in an activation of apoptosis with oxaliplatin. Incubation of NUGC3 cells for 48 hours with 25 μ M oxaliplatin or 5 μ M **L6** separately results in no to very little cleavage of caspase-3 (Figure 4.19). However, pre-incubation with 5 μ M **L6** for two hours followed by subsequent incubation with oxaliplatin for 48 hours results in a significant increase in cleaved caspase-3.

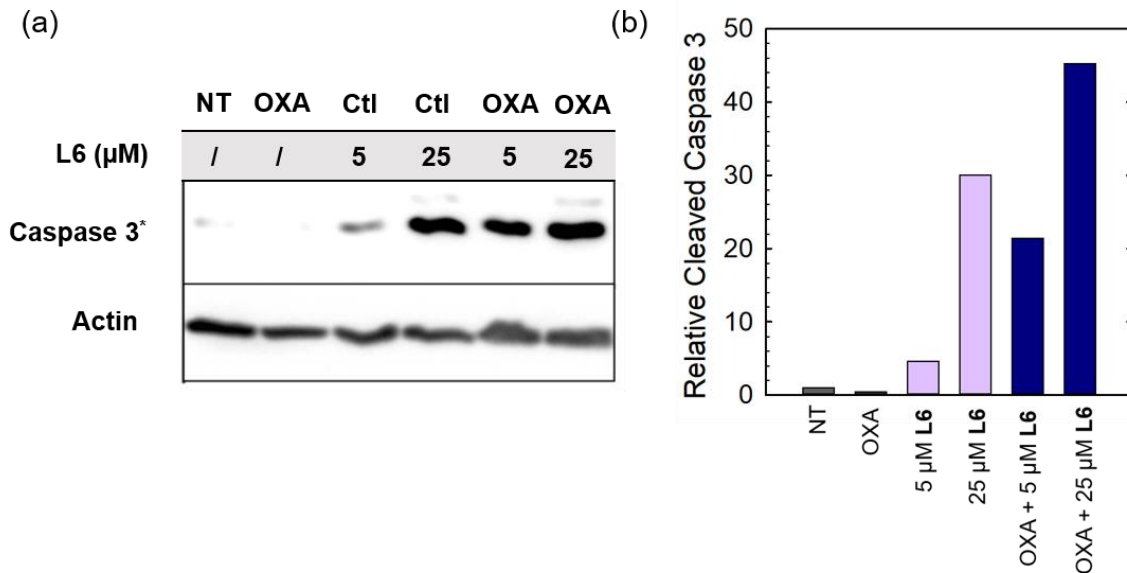


Figure 4.19. (a) NUGC3 cells were treated with 5 or 25 μ M of indicated compound for 48 hours. In the case of cotreatment, cells were incubated with **L6** for 2 hours followed by a total 48-hour incubation with 25 μ M oxaliplatin. Total protein was extracted, and 40 μ g were separated on SDS PAGE. Cleaved caspase-3 (Caspase 3*) and actin were detected by Western blot. (b) Quantification of relative cleaved caspase 3 levels obtained by Western blot analysis upon cotreatment with **L6** and oxaliplatin. Western blot image quantified using SynGene tools

Similarly, pre-incubation with **L6** followed by additional incubation with oxaliplatin for 24 hours further induced *PUMA* expression and the ratio of *BAX* (proapoptotic) and *Bcl2* (antiapoptotic) expression compared to individual treatments. (Figure 4.20). The ratio of *BAX/Bcl2* has been described as an indicator of apoptosis sensitivity as an increased

ratio results in a higher response to apoptotic signals.⁴¹⁹⁻⁴²⁰ The result for cleaved caspase-3 and *BAX/Bcl2* highlight a possible synergistic mechanism between **L6** and oxaliplatin and provides a potential application for **L6** in co-administration with platinum agents for tumours harbouring malfunctioning p53.

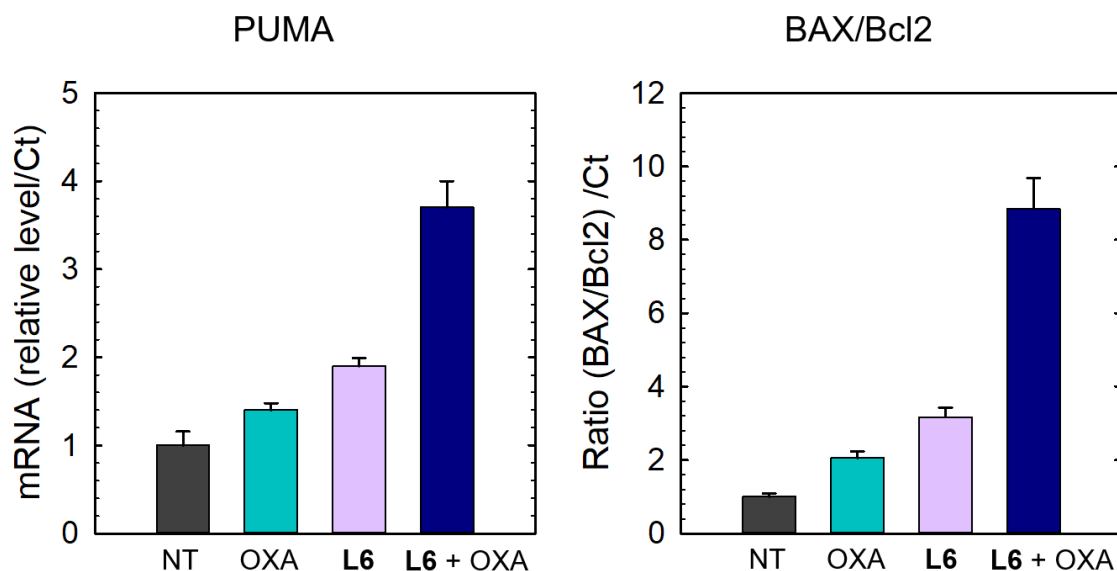


Figure 4.20. NUGC3 cells were treated with 10 μ M of indicated compound for 48 hours. In the case of co-treatment, cells were incubated with **L6** for 2 hours followed by a total 24-hour incubation. RNAs were extracted and RT-qPCR for PUMA, BAX, and Bcl2 mRNAs quantification were performed. Graphs represent means with error bars of mRNA expression relative to the NT control (Ct). BAX and Bcl2 are represented as a ratio of their relative expression that is representative of cell death activation.

4.2.9. Cytotoxicity in Non-Cancerous Intestinal Organoids

Despite new anti-cancer drugs representing one of the largest areas in pharmaceutical development, the onset of adverse side effects from chemotherapeutics still presents a major clinical hurdle.⁴²¹⁻⁴²² Promisingly, pharmacological restoration of p53 function has been associated with increased protection of normal cells from cytotoxicity due to their selective nature of targeting mutant p53-bearing tumours.⁴²³⁻⁴²⁴ To this extent, we tested the cytotoxicity of **L6** and **L7** in non-cancerous cells using mouse small intestine organoids. Intestinal organoids are three-dimensional multicellular structures that comprise of crypts and villi to reproduce an intestinal organization. They are an important aspect in drug discovery due to their increased similarities to physiological models over two-dimensional cell lines. The three-dimensional organization with budding is an

indication of a healthy and viable organoid.⁴²⁵⁻⁴²⁶ To analyse the cytotoxicity of our compounds on normal organoids, we performed a long-term survival assay by monitoring organoid viability over a 23-day period. To further elucidate the impact of treatment on the organoid organization, we performed an immunofluorescence assay and monitored organoid shape upon treatment with **L6** and **L7**. Organoids were classified as normal, disorganized, dying, or dead based on the images obtained (see Figure 4.21 and Table 4.6 for description and quantification of each classification system).

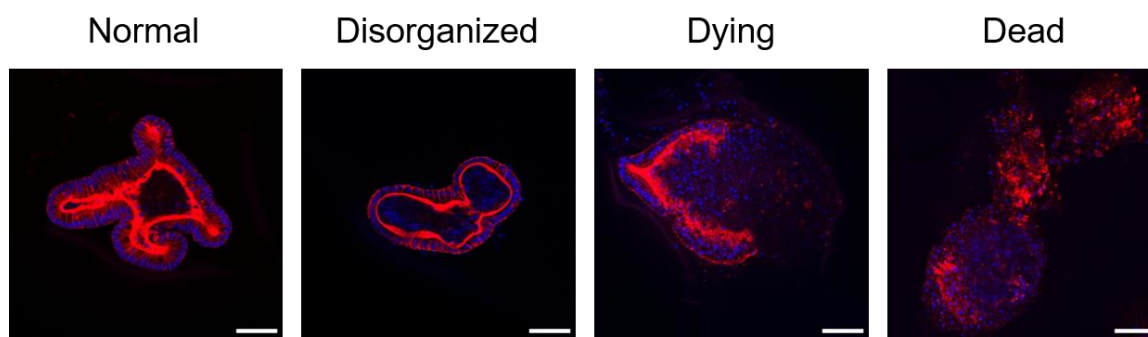


Figure 4.21. Intestinal organoids were incubated and monitored for 72 hours. F-actin (red) and nuclei (blue) were stained using Phalloidin and DAPI, respectively, at recommended concentrations and imaged using a Nikon ApoTome microscope. Organoids were then classified as normal, disorganized, dying, or dead based on cell morphology. Representative images for each classification condition are shown above. The scale bar represents 50 μ m.

Table 4.6. Number of organoids counted in each classification system per indicated treatment condition.

Treatment	Normal	Disorganized	Dying	Dead	Total
NT	84	35	20	6	145
25 μ M OXA	0	87	42	36	165
2.5 μ M L6	64	45	11	10	130
5 μ M L6	77	70	27	16	190
10 μ M L6	41	76	33	11	161
2.5 μ M L7	41	63	30	27	161
5 μ M L7	0	27	45	64	136
10 μ M L7	0	0	0	166	166

Interestingly, treatment with **L6** retained mostly viable organoids after a 72-hour period resembling normal and disorganized structures similar to the NT control (Figure 4.22). In contrast, treatment with oxaliplatin resulted in about 50% of organoids classified

as either dying or dead, and strikingly, after 72 hours all organoids treated with **L7** were dead.

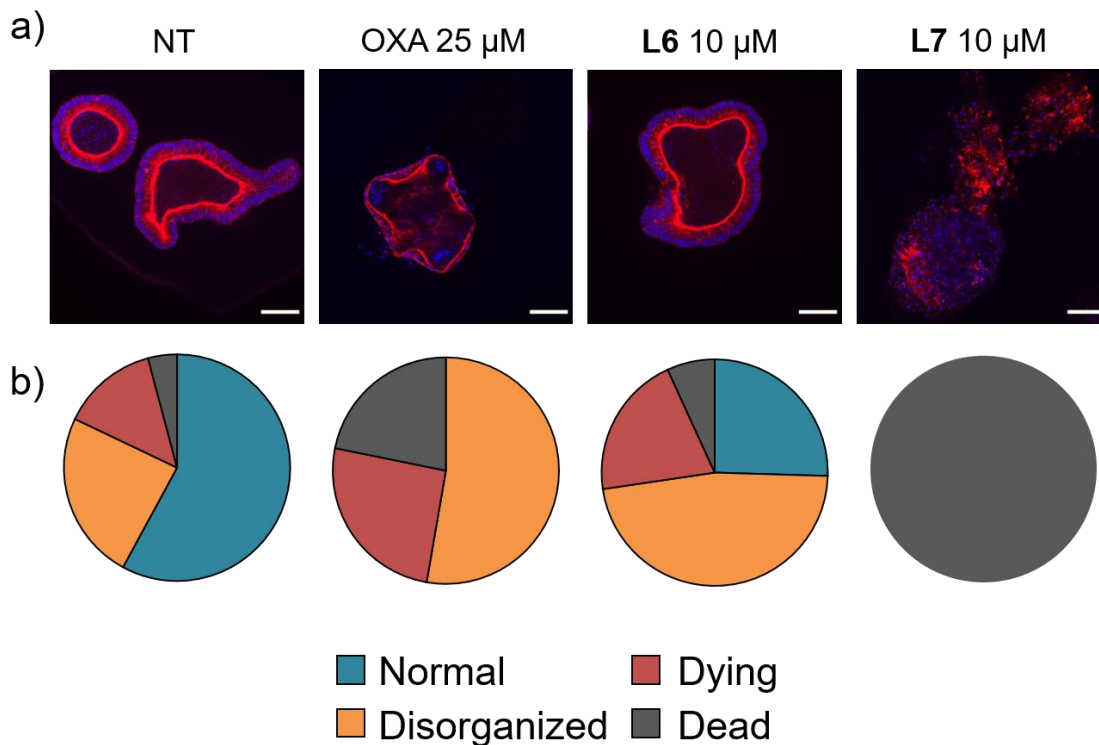


Figure 4.22. (a) Intestinal organoids were treated with indicated compound and monitored for 72 hours. F-actin (red) and nuclei (blue) were stained using Phalloidin and DAPI, respectively, at recommended concentrations and imaged using a Nikon ApoTome microscope. The scale bar represents 50 μ m. (b) Characterization and quantification of organoids as either normal, disorganized, dying, or dead upon indicated treatment based on images obtained in part a. *ca.* 150 organoids were counted and analyzed for each condition.

To further probe their differing cytotoxicity in our non-cancerous organoid model and investigate the mechanism by which **L6** imparts cytotoxicity, we incubated cells treated with oxaliplatin, **L6**, and **L7** with an antibody recognizing cleaved caspase-3. In agreement with the results obtained above, treatment with **L6** resembled that of non-treated conditions with no significant cleaved caspase-3 detected (Figure 4.23). In contrast, significant cleavage of caspase-3 was detected upon treatment with oxaliplatin and **L7**, indicating that both treatments induce apoptosis in non-cancerous organoids.

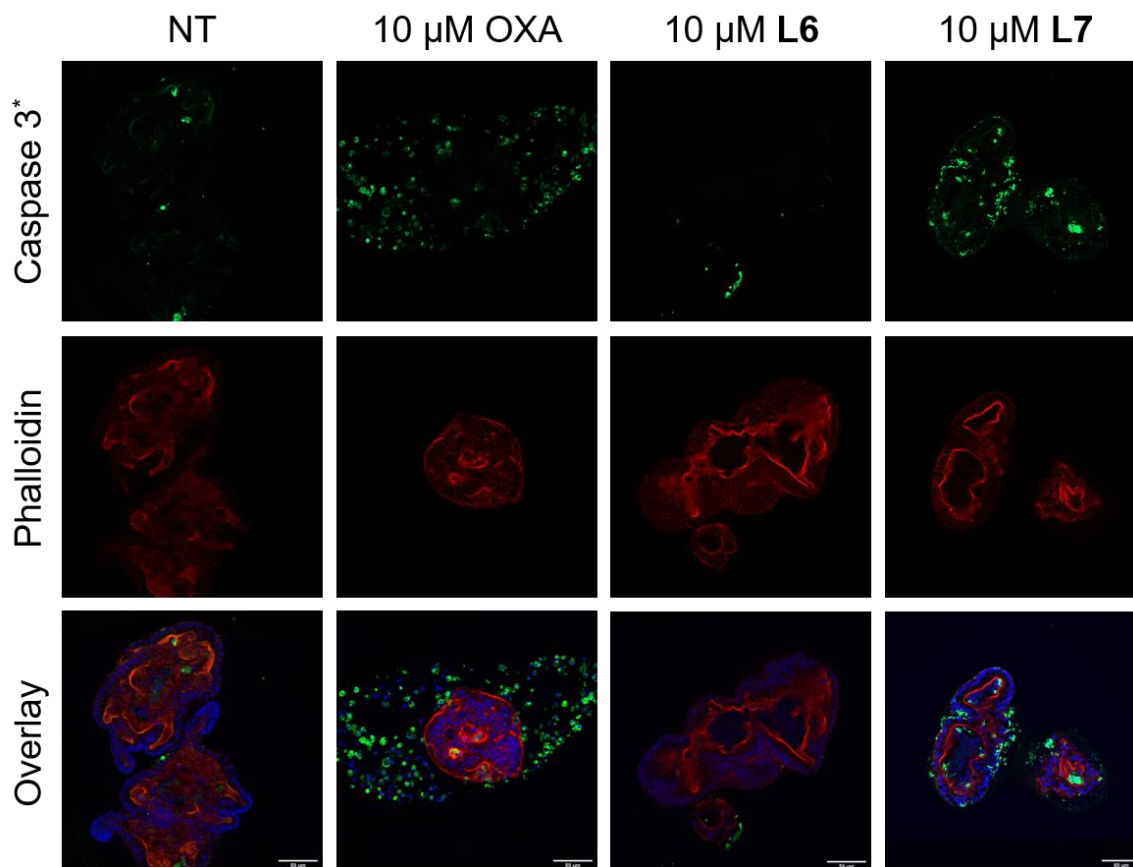


Figure 4.23. Intestinal organoids were treated with indicated compound for 24 hours. F-actin (red) and nuclei (blue) were stained using Phalloidin and DAPI respectively. Apoptotic cells are stained using cleaved caspase-3 (green). Antibodies were used at recommended concentrations and imaged using a Nikon ApoTome microscope. The scale bar represents 50 μ m.

Importantly, even over a period of 23 days, organoid treatment with **L6** (2.5 and 5 μ M) has a similar survival profile to NT organoids, resulting in substantial viability after 23 days (Figure 4.24). In contrast, treatment with **L7** resulted in complete cell death after 5 days (5 μ M). Treatment with **L6** also results in organoids with more budding than those treated with **L7**.

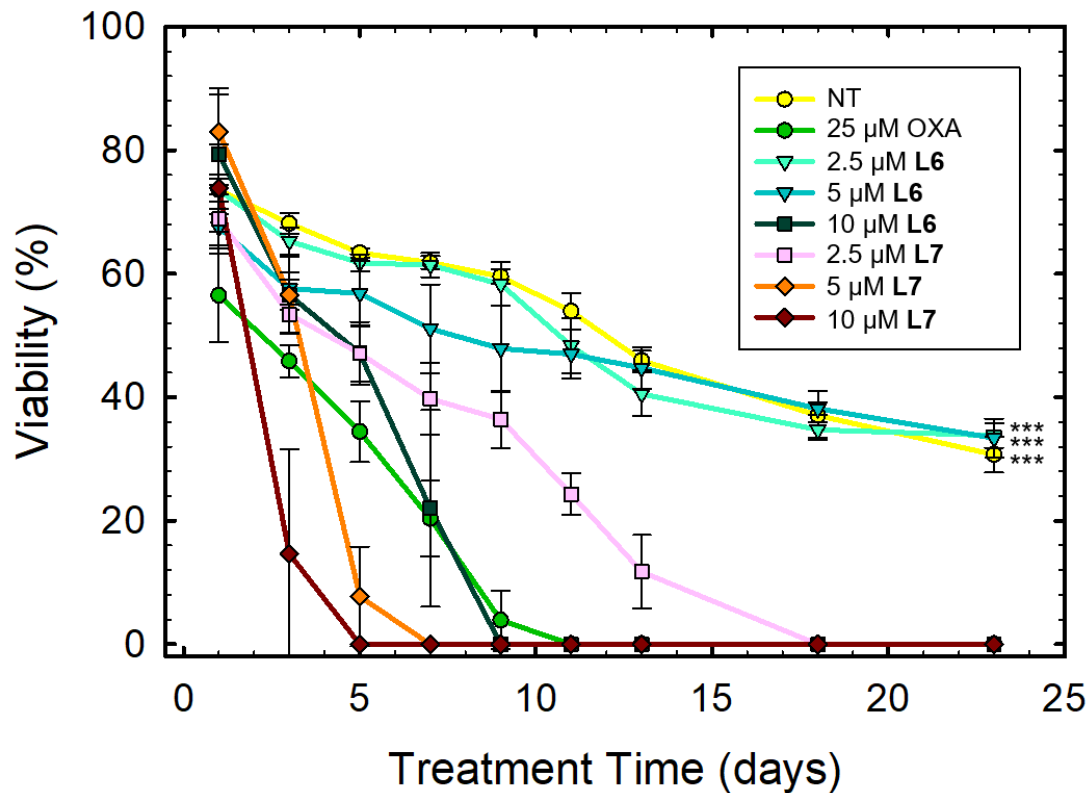


Figure 4.24. Intestinal organoids were treated with indicated compound and monitored for 23 days. Graph shows survival curves for each condition. *** indicates $p < 0.001$ established by One-Way ANOVA followed by a Dunnett post-test.

Finally, given that chemotherapeutic regimens involve treating patients at the maximum tolerated dose (MTD), we sought to determine the maximum dose of **L6** tolerated in normal C57BL/6 mice. Promisingly, no decrease in weight is observed up to 13 mg/kg **L6** treatment (Figure 4.25), which corresponds to the solubility limit of **L6**. Overall, these results highlight that by iodination of our bifunctional scaffold, we have increased cytotoxicity in cancerous cells lines yet have significantly decreased cytotoxicity in a non-cancerous organoid model. Taken together, these results highlight **L6** as a suitable candidate for *in vivo* testing in xenograft models.

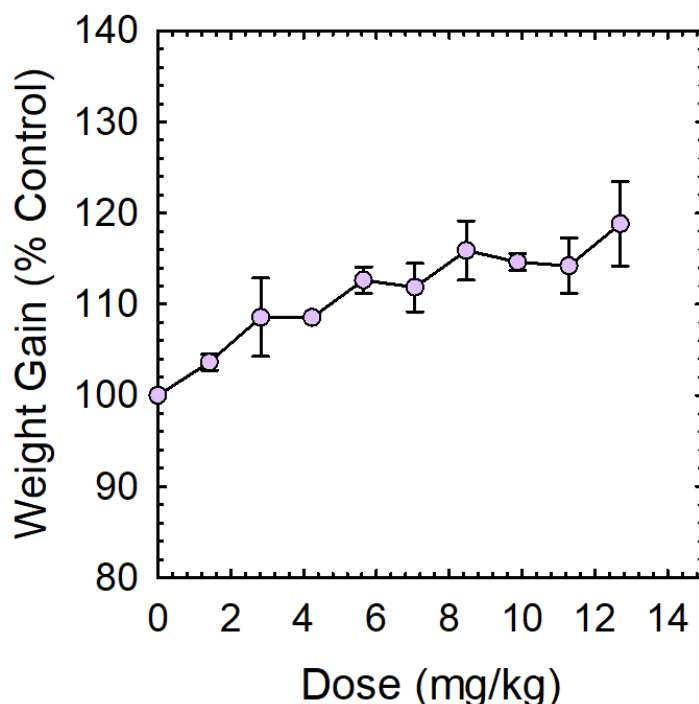


Figure 4.25. C57BL/6 mice were injected intraperitoneally with increasing doses of **L6** and monitored twice a week for five weeks. Mean weight of mice (three groups with $n=4$) are shown as averages \pm SD.

4.3. Summary

Restoration of p53 function holds significant promise in the search for effective chemotherapeutics as over 50% of cancer diagnoses are attributed to mutant p53. Given that a large proportion of these mutations result in accelerated protein aggregation and contribute to loss of function, molecules aimed to inhibit protein aggregation are of particular interest. Importantly, the loss of zinc within the protein's DNA-binding core further increases the aggregation process via nucleation with zinc-bound p53C. In this work, we have designed bifunctional ligands (**L6** and **L7**) aimed to restore p53 function by modulating mutant p53 aggregation and incorporating zinc-binding fragments for metallochaperone activity. After extensive characterization of the zinc-binding capability of **L6** and **L7**, we show that our bifunctional ligands significantly increase intracellular levels of zinc in cells, thus demonstrating their potential for metallochaperone function. Interestingly, upon investigation into their ability to modulate mutant p53 aggregation, we demonstrated that only the iodinated framework **L6** was effective at inhibiting aggregation. This was demonstrated in recombinant systems via light scattering, TEM, gel

electrophoresis, and in cellular systems using immunofluorescence. These results prompted an investigation into the binding capabilities of these ligands with mutant p53. Using native MS, we showed that only **L6** interacted with mutant p53. This result can explain the differing abilities of **L6** and **L7** to modulate mutant p53 aggregation and leads us to hypothesize that the iodine in **L6** is contributing to favourable interactions with protein via the hydrophobic, aggregation-prone segment; further investigations into whether this interaction is a result of halogen bonding needs to be pursued. We further demonstrate the increased cytotoxicity of **L6** in cancer cells compared to **L7** and demonstrate that by restoring protein function, it contributes to activation of apoptotic pathways. **L6** is well tolerated in non-cancerous organoids, whereas in contrast, **L7** was highly toxic.

Overall, we have demonstrated in this chapter that by iodination of our bifunctional framework, we have substantially changed the biological properties of our molecules. **L6** can modulate mutant p53 aggregation, activate otherwise inaccessible apoptotic pathways, and is well tolerated in non-cancerous 3D models. The utility of **L6** in restoring p53-dependent pathways presents an interesting opportunity for co-administration with clinically approved platinum agents. Cancers with mutant p53 status have been associated with increased resistance, and thus restoring p53 function to increase the effectiveness of platinum agents is an interesting opportunity that we plan to investigate in the future.

4.4. Experimental

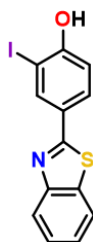
4.4.1. Materials and Methods

All chemicals used were purchased from Sigma Aldrich at the highest grade available and were further purified whenever necessary.³⁴⁶⁻³⁴⁷ All compounds were dried under vacuum for 1 week before in vitro cytotoxicity testing. ¹H and ¹³C NMR were recorded on Bruker-AV-400, 500, and 600 instruments. Elemental analyses (C, H, N) were performed by Mr. Paul Mulyk at Simon Fraser University on a Carlo Erba EA 1110 CHN elemental analyzer. Mass spectra (negative ion) were obtained on an Agilent 6210 time-of-flight electrospray ionization mass spectrometer. Electronic absorption spectra were obtained on a Cary 5000 spectrophotometer. Scatter experiments were carried out on a Synergy 4 MultiDetection microplate reader (BioTek). TEM images were obtained on a STEM 1 – FEI Tecnai Osiris transmission electron microscope. Immunofluorescence

experiments were imaged using a fluorescence microscope (Axio Imager M2 Zeiss) coupled to a Hamamatsu's camera Orca Flash 4v3, using the ApoTome.2 (Zeiss) function.

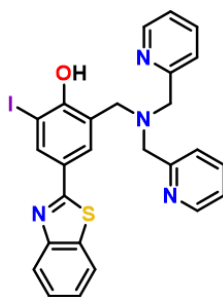
4.4.2. Synthesis

4-(benzo[d]thiazol-2-yl)-2-iodophenol (**1**):



To a solution of 4-hydroxy-3-iodobenzaldehyde (0.59 g, 2.39 mmol) in EtOH (13 mL) 2-aminothiophenol (0.30 g, 2.39 mmol) was added. Aqueous hydrogen peroxide (1.5 mL, 30%, 6 molar equivalents) and 37% aqueous HCl (1.9 eq) were added. Upon stirring for 2 hours, a green precipitate formed. The precipitate was filtered, washed with cold ethanol, and dried in vacuo. Yield: 0.80 g, 95%. ^1H NMR (400 MHz, MeOD): δ = 8.47 (d, J = 2.2 Hz, 1H), 8.01 - 7.97 (m, 2H), 7.94 (dd, J = 8.5 Hz and 2.2 Hz, 1H), 7.54 (td, J = 8.4 and 1.2 Hz, 1H), 7.44 (td, J = 8.3 and 1.2 Hz, 1H), 6.98 (d, J = 8.5 Hz, 1H). ^{13}C $\{^1\text{H}\}$ NMR (400 MHz, MeOD) δ = 166.9, 159.8, 153.6, 138.0, 134.4, 128.7, 126.2, 125.0, 122.0, 121.4, 114.50, 83.8. Anal. Calcd (%) for $\text{C}_{13}\text{H}_8\text{INOS}$: C, 44.21; H, 2.28; N, 3.97; found: C, 44.43; H, 2.23; N, 4.01. Calcd for M, 352.9371; found, 352.9372.

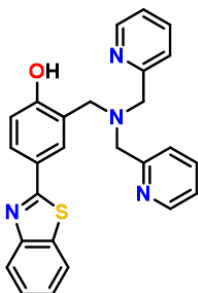
4-(benzo[d]thiazol-2-yl)-2-((bis(pyridin-2-ylmethyl)amino)methyl)-6-iodophenol (**L6**):



Paraformaldehyde (0.107 g, 3.57 mmol) was added to a solution of di-(2-picolyl)amine (0.339 g, 1.70 mmol) in THF (14 mL) and refluxed for 1 hour. 2-(4-hydroxy-3-iodo)benzothiazole (0.60 g, 1.70 mmol) in 12 mL of THF was added, and the solution was refluxed for an additional 72 hours. The THF was removed in vacuo and the resulting solid

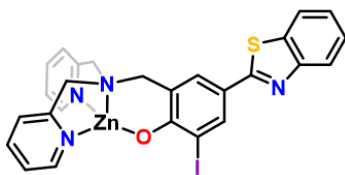
was recrystallized in hot methanol to afford a white precipitate. The precipitate was removed using vacuum filtration and washed with cold methanol. Yield: 0.29 g, 31%. ^1H NMR (500 MHz, CD_2Cl_2): δ = 8.63 (dd, J = 4.9, 1.8 Hz, 2H), 8.44 (d, J = 2.2 Hz, 1H), 8.03 – 7.99 (m, 1H), 7.96 – 7.93 (m, 1H), 7.88 (d, J = 2.2 Hz, 1H), 7.72 (td, J = 7.7, 1.8 Hz, 2H), 7.51 (dd, J = 8.3, 7.2 Hz, 1H), 7.40 (dd, J = 8.2, 7.3 Hz, 1H), 7.36 (d, J = 7.8 Hz, 2H), 7.25 (dd, J = 7.5, 4.9 Hz, 2H), 3.97 (s, 4H), 3.94 (s, 2H). $^{13}\text{C}\{^1\text{H}\}$ NMR (400 MHz, CD_2Cl_2): δ = 166.2, 159.9, 157.9, 154.2, 148.8, 137.6, 136.8, 134.9, 129.8, 126.2, 126.1, 124.8, 123.9, 123.1, 122.6, 122.3, 121.5, 85.8, 58.8, 56.8. Anal. Calcd (%) for $\text{C}_{26}\text{H}_{21}\text{N}_4\text{OS}$: C, 55.33; H, 3.75; N, 9.93; found: C, 55.40; H, 3.71; N, 9.98. HR-MS: Calcd for $[\text{M} + \text{H}]^+$, 565.0559; found, 565.0520.

4-(benzo[d]thiazol-2-yl)-2-((bis(pyridin-2-ylmethyl)amino)methyl)phenol (**L7**):



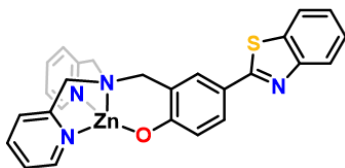
Paraformaldehyde (0.31 g, 10.9 mmol) was added to a solution of di-(2-picolyl)amine (1.04 g, 5.45 mmol) in EtOH (40 mL) and refluxed for 1 hour. 2-(4-hydroxy)benzothiazole (1.19 g, 5.45 mmol) in 35 mL of EtOH was added, and the resulting solution was heated at a reflux for an additional 48 hours. The solvent was removed to give a dark gray residue that was purified by silica gel column chromatography using EtOAc/iPrOH/ NH_4OH (75:20:5) as eluent to yield a brown solid. Yield: 0.84 g, 35%. ^1H NMR (400 MHz, CD_2Cl_2): δ = 8.56 (dd, J = 4.9, 1.8 Hz, 2H), 7.96 (dd, J = 8.2, 1.2 Hz, 1H), 7.91 – 7.87 (m, 3H), 7.65 (td, J = 7.7, 1.8 Hz, 2H), 7.45 (dd, J = 8.3, 7.2 Hz, 1H), 7.36 – 7.31 (m, 3H), 7.19 (dd, J = 7.5, 4.9 Hz, 2H), 6.99 – 6.96 (m, 1H), 3.92 (s, 4H), 3.89 (s, 2H). $^{13}\text{C}\{^1\text{H}\}$ NMR (500 MHz, CD_2Cl_2): δ = 168.5, 161.4, 158.6, 154.7, 149.1, 137.2, 135.2, 130.1, 129.1, 126.5, 124.9, 124.8, 124.4, 123.5, 122.8, 122.6, 121.9, 117.5, 59.2, 57.0. Anal. Calcd (%) for $\text{C}_{26}\text{H}_{22}\text{N}_4\text{OS}\cdot\text{H}_2\text{O}$: C, 68.40; H, 5.30; N, 12.27; found: C, 68.73; H, 5.17; N, 12.47. HR-MS: Calcd for $[\text{M} + \text{H}]^+$, 439.1593; found, 439.1567.

4-(benzo[d]thiazol-2-yl)-2-((bis(pyridin-2-ylmethyl)amino)methyl)-6-iodophenol zinc (II) (**ZnL6Cl**):



Into a solution of **L6** (0.02 g, 0.04 mmol) in MeOH (5 mL), KOH (2 mg, 0.04 mmol) and ZnCl₂ (5 mg, 0.04 mmol) were added and the solution was stirred for 1 hour. The solution was filtered through Celite to remove precipitated KCl and the complex was precipitated from cold diethyl ether. The resulting white solid was collected using vacuum filtration and washed with cold MeOH. Yield: 0.019 g, 73%. ¹H NMR (400 MHz, (CD₃)₂SO): δ = 9.01 (d, *J* = 5.1 Hz, 2H), 8.09 (d, *J* = 2.4 Hz, 1H), 8.06 – 7.99 (m, 3H), 7.90 – 7.87 (m, 1H), 7.74 (d, *J* = 2.4 Hz, 1H), 7.63 – 7.58 (m, 2H), 7.51 (d, *J* = 7.8 Hz, 2H), 7.46 (dd, *J* = 8.3, 7.2, 1H), 7.34 (dd, *J* = 8.2, 7.2 Hz, 1H), 4.12 (d, *J* = 3.2 Hz, 4H), 3.76 (s, 2H). Crystals suitable for X-ray diffraction experiments were obtained by slow diffusion of a concentrated CH₂Cl₂ solution into hexanes.

4-(benzo[d]thiazol-2-yl)-2-((bis(pyridin-2-ylmethyl)amino)methyl)phenol zinc (II) (Zn**L7**Cl):



Into a solution of **L7** (0.05 g, 0.11 mmol) in MeOH (5 mL), KOH (6.4 mg, 0.11 mmol) and ZnCl₂ (15.5 mg, 0.11 mmol) were added and the solution stirred for 1 hour. The solution was filtered through Celite to remove precipitated KCl and the complex was precipitated from cold diethyl ether. The resulting white solid was collected using vacuum filtration and washed with cold MeOH. Yield: 0.042 g, 71%. ¹H NMR (400 MHz, (CD₃)₂SO): δ = 9.07 (d, *J* = 5.4 Hz, 1H), 7.99 (d, *J* = 7.9 Hz, 1H), 7.86 (d, *J* = 8.1 Hz, 1H), 7.76 (d, *J* = 2.5 Hz, 1H), 7.65 (t, *J* = 6.4 Hz, 2H), 7.60 (t, *J* = 7.1 Hz, 2H), 7.44 (t, *J* = 7.6 Hz, 1H), 7.31 (t, *J* = 7.6 Hz, 1H), 6.49 (d, *J* = 8.6 Hz, 1H), 4.08 (s, 4H), 3.76 (s, 2H). Crystals suitable for X-ray diffraction experiments were obtained by slow diffusion of a concentrated CH₂Cl₂ solution into hexanes.

4.4.3. X-ray Structure Determination of L6 and L7

X-ray structure determinations were performed on a Bruker APEX II Duo diffractometer with graphite monochromated Mo K α radiation. A transparent block crystal

was mounted on a 150 μm MiteGen sample holder. Data were collected at 293 K to a maximum 2θ value of $\sim 60^\circ$. Data were collected in a series of ϕ and ω in 0.50° widths with 10.0 s exposures. The crystal-to-detector distance was 50 mm. The structure was solved by intrinsic phasing³⁵¹ and refined using ShelXle.³⁵² All non-hydrogen atoms were refined anisotropically. All C-H hydrogen atoms were placed in calculated positions but were not refined. ZnL6Cl crystallizes with only one molecule in the asymmetric unit, while ZnL7Cl crystallizes with two molecules in the asymmetric unit. CCDC numbers: 1947980 (ZnL6Cl), 1947981 (ZnL7Cl).

4.4.4. Stability Constant Determination

Aqueous acidity constants ($\text{p}K_a$) for L6 and L7 were measured using variable pH titrations monitored by UV-visible spectroscopy between 200 and 600 nm as a function of pH. Solutions of both ligands (12.5 μM) were prepared in 0.1 M NaCl pH 3. Due to the limited aqueous solubility, solutions of 20% MeOH in H_2O were prepared. Small aliquots of 0.1 M NaOH were titrated into the solution to adjust the pH and at least 30 UV-vis spectra were collected in the pH 3-11 range. Spectral data were analyzed using HypSpec (Protonic Software, UK).³⁵³ Similarly, metal stability constants were obtained by titrating a solution containing 12.5 μM ligand, 12.5 μM $\text{Zn}(\text{ClO}_4)_2 \cdot 6\text{H}_2\text{O}$, 0.1 M NaCl and 0.1 M NaOH to adjust the pH. At least 30 UV-vis spectra were collected in the pH 3-11 range. Known metal hydrolysis constants were included in the HypSpec simulations as constant values.³⁵⁴ Stability constants were calculated using the HypSpec computer program and metal speciation plots were created using the HySS2009 program (Protonic Software, UK).³⁵³

4.4.5. Increasing Intracellular Levels of Zn^{2+} in the p53-Y220C Cell Line NUGC3

NUGC3 cells (40,000 cells/well) were plated on glass slides treated with poly-L-lysine in 12-well plates. After 48 hours, cells were washed 2x 5 minutes in serum-free media and incubated with 1 μM FluoZin-3³¹³ for 20 minutes at 37°C . Cells were then washed 2x 5 minutes in Earle's balanced salt solution (EBSS)/H (-) Ca/Mg containing the indicated treatments ($\text{ZnCl}_2 = 50 \mu\text{M}$, L6 = L7 = pyrithione = 50 μM) and incubated for 2 hours at 37°C before imaging. Cells were imaged using a Nikon ApoTome microscope (Nikon, France). FluoZin-3 and Hoechst 33342 were excited at 488 nm (argon laser) and

790 nm (Chameleon Ti:sapphire laser), respectively. Imaging was performed in under ten minutes to avoid alteration of cell physiology upon imaging at room temperature. To determine the change in fluorescence, each image was processed using ImageJ Software (National Institutes of Health, Bethesda, MD) and integrated to represent the cumulative fluorescence for a single cell. Processing included adjustment of exposure and contrast to eliminate autofluorescence of the support. To avoid autofluorescence, each image was background-subtracted using the non-treated control. All images were batch processed using the same parameters. Cells were analyzed upon treatment with 50 μ M pyriothione (PYR)/ZnCl₂ (1:1) as a positive control. Statistical differences were analyzed using One-Way ANOVA with multiple comparisons. Bartlett's test showed unequal variance. Three replicate experiments were performed independently with 100 cells per trial.

4.4.6. Site-Directed Mutagenesis

The plasmid encoding the DNA-binding domain of human wild-type p53 (residues 94-312) was gifted by Cheryl Arrowsmith.³⁵⁸ Four mutations to the p53 gene (M133L/V203A/N239Y/N268D) were successively introduced to increase structural stability of the protein, followed by addition of the Y220C mutation.³⁵⁹ All p53 mutants were prepared by site-directed mutagenic PCR according to standard protocols,¹⁵² using primers purchased from Eurofins Operon following Quikchange protocol (Agilent Technology). DNA polymerase (Q5) and DpnI enzyme were obtained from New England Biolabs. PCR products were transformed into chemically competent DH5 α *E. coli* and selected on ampicillin-supplemented agar plates. Single colonies obtained from overnight incubation at 37 °C were grown in Luria-Bertani (LB) broth for 16 hours. Plasmid DNA was purified using the plasmid spin MiniPrep kit (Qiagen, 27104) and sequenced by Eurofins Operon Sequence read service.

4.4.7. Protein Expression and Purification

Proteins were overexpressed using *E. coli* strain BL21-pLysS cells (ThermoFisher). Expression cultures containing 100 μ g/mL ampicillin were inoculated from an overnight culture and grown at 37 °C to an OD₆₀₀ of 0.7. Protein expression was induced overnight at 15 °C with 0.3 mM IPTG. Cells were then harvested by centrifugation at 6500 rpm for 20 minutes. Cell pellets were resuspended in lysis buffer (50 mM Tris-HCl buffer, pH 6.5, 300 mM NaCl, 10% glycerol, 1% Triton X-100, 5 mM imidazole, 6 mM

MgSO₄, 1 mM PMSF, and 5 mM β-mercaptoethanol) and sheared using ultrasonication. Cellular debris was isolated by centrifugation at 14000 rpm for 30 minutes and incubated with Talon® beads (cobalt-nitrilotriacetic acid) at 4 °C for 30 minutes. Talon beads were transferred to a column, washed twice with 20 mL of wash buffer (50 mM Tris-HCl buffer, pH 6.5, 500 mM NaCl, 10% glycerol, 10 mM imidazole, 0.5 mM TCEP, 1 mM PMSF, and 5 mM β-mercaptoethanol), and eluted with wash buffer containing 500 mM imidazole.¹⁵² Protein concentration was determined spectrophotometrically using the reported extinction coefficient $\epsilon_{280} = 17,130 \text{ cm}^{-1}$.³⁶⁰

4.4.8. Light Scattering

To monitor the effect of **L6** and **L7** on the aggregation of p53-Y220C, we measured light scattering by monitoring the changes in absorbance at 500 nm using a Synergy 4 MultiDetection microplate reader (BioTek). Experiments were carried out at 37 °C, with 30 seconds of agitation before each read. Spectra were taken in five-minute intervals. Protein concentration was 5 μM in 30 mM tris, 150 mM NaCl at pH 7.4. 5% DMSO was used in the buffer to pre-dissolve **L6** and **L7** at final concentrations of 5 and 10 μM. Each experiment contained 8 replicates per condition, and values are represented as mean ± SD.

4.4.9. Transmission Electron Microscopy

p53C-Y220C (μM) was incubated at 37 °C with agitation at 100 rpm for indicated time points in the absence (NT) or presence of 5 μM **L6** or **L7**. The protein and ligands were dissolved in a buffer containing 30 mM Tris, 150 mM NaCl, pH 7.4 with 5% DMSO. Samples of 10 μL were adsorbed onto freshly glow-discharged formvar coated copper grids, rinsed with deionized water to remove NaCl crystals, and stained with 1% uranyl acetate. Images were taken on a STEM 1 – FEI Tecnai Osiris transmission electron microscope.

4.4.10. Immunofluorescence (A11, ThT, and AIF)

Cells were plated at a density of 600,000 cells per well in 6-well plates and treated with **L6**, **L7**, or an equivalent volume of DMSO for 24 hours. The cell culture medium was removed and 2 mL of fixation buffer (3.7% paraformaldehyde in PBS) was added to each

well and incubated for 10 minutes at room temperature. Fixation buffer was removed, and wells were washed twice with PBS followed by incubation with 2 mL of permeabilization buffer (0.2% Triton X-100 in PBS) for 5 minutes. Wells were washed 2x10 min with PBS and blocking solution (10% normal goat serum in PBS) was added for 2 hours. The cells were simultaneously labelled with mouse monoclonal anti-human p53 DO-1 primary antibody (Santa Cruz, sc-126, 1:1000) and an oligomer-specific primary antibody, A11 (StressMarq Biosciences, SPC-506, 1:1000) for the aggregation studies overnight in the dark at 4 °C. For apoptosis detection, cells were labelled with the primary antibody AIF (Invitrogen, PA5-19960, 1:100,). Cells were washed 3x with PBS followed by labelling with AlexaFluor 568- conjugated goat anti-mouse (abcam, ab175473) and AlexaFluor 647- conjugated goat anti-rabbit (abcam, ab150079) secondary antibodies (1:2,000) for 1.5 hours at room temperature in the dark. In the case of Thioflavin T labelling, a 1 mM solution of ThT was added to the wells following labelling with secondary antibodies, washed with 2 mL of 70% ethanol to remove excess ThT, followed by washing with water. The cells were washed three times with PBS, followed by subsequent nuclei staining using DAPI (Sigma). The cover slips were mounted using Fluorsave (Fisher Scientific) and allowed to dry overnight, followed by analysis using confocal microscopy.

4.4.11. Native Mass Spectrometry

Recombinant p53C-Y220C samples were thawed and dialysed in 200 mM ammonium acetate, and protein concentrations were measured using a Thermo Scientific NanoDrop Spectrophotometer. **L6** and **L7** were stored as DMSO stocks at 50 mM. Native MS experiments were performed on 3 µM p53C-Y220C with **L6** or **L7** ratios of 2, 5, 10 and 25 equivalents. Each sample was incubated at room temperature for 2 hours. The final DMSO concentration in each sample is 0.2%. All MS data were acquired on a quadrupole ion mobility time-of-flight (TOF) mass spectrometer (Synapt G2S HDMS, Waters, Milford, MA, USA). Ions were produced by positive electrospray ionization (ESI) with a capillary voltage of 2 kV. The source temperature was set to 120 °C, with a sampling cone set to 150 V and the extraction cone set to 50 V. The trap cell containing argon gas was set at a pressure of 3.14×10^{-2} mbar. Trap and transfer collision energies were set to 20 V and 10 V respectively. The TOF pressure operated at 1.25×10^{-6} mbar.

4.4.12. Immunoprecipitation

NUGC3 cells were seeded at a density of 850,000 cells per petri dish and incubated at 37°C with 5% CO₂ for 48 hours, followed by treatment with 10 and 25 µM **L6** and **L7** for 13 hours. Cells were lysed with NP40 lysis buffer (50 mM Tris-HCl pH 8, NaCl 150 mM, NP40 1%, Complete protease inhibitor). 1 mg of native lysates were incubated with 4 µg of p53 mutant antibody (Santa Cruz, Pab240, sc-99) and 30 µL of protein G beads (Protein G agarose, Roche) on a rotator. Samples were washed three times with lysis buffer, then 30µL of loading buffer (50 mM DTT, 2x Laemmli buffer (Bio-Rad)) was added and samples were boiled at 95°C for 5 min to collect the eluates.

4.4.13. Western Blot Analysis

For molecular weight distribution analysis, a solution of mutant p53C-Y220C was prepared at a concentration of 8 µM in 30 mM Tris, 150 mM NaCl at pH 7.4. Solutions in the presence of two equivalents of **L6** and **L7** were prepared and all samples were incubated for 2 hours at 37 °C with constant agitation at 180 rpm. Electrophoresis to separate protein aggregates was employed using 10- 20% Mini-PROTEAN® Tris-Tricine Precast Gels (Bio-Rad) at 100 V for 100 min. Using a nitrocellulose membrane, the membrane was transferred for 1 hour at 100 V (4 °C) followed by blocking in 3% bovine serum albumin (BSA) solution in TBS for 1 hour and then overnight incubation (4 °C) with the primary PAb240 antibody (Santa Cruz, sc-99, 1:1000). After three washes of ten minutes with TBS buffer, the membrane was incubated in a solution containing the secondary antibody (Horseradish peroxidase, Caymen Chemicals) for 3 hours. Thermo Scientific SuperSignal® West Pico Chemiluminescent Substrate kit was used to visualize the mutant p53 protein using a FUJIFILM Luminescent Image Analyzer (LAS-4000). For caspase-3 assays, NUGC3 cells were seeded at a density of 600,000 cells/well and incubated at 37°C with 5% CO₂ for 24 hours, followed by treatment with 25 µM **L6** and **L7** for 24 hours. SiRNA transfection was performed using 30 nM of siRNA with RNAiMAX (ThermoFisher, 13778100) as previously described.³⁶¹ In the case of co-treatment, cells were incubated with **L6** for 2 hours followed by a total 48-hour incubation with oxaliplatin. Cells were lysed with lysis buffer (50 mM Tris-HCl pH 8, NaCl 150 mM, NP40 1%). Proteins were denatured and deposited directly (40 µg of protein) onto an SDS-PAGE gel. For immunoprecipitation, 20µL of the eluates were deposited onto an SDS-PAGE gel. Western blotting was performed using the pan-specific DO-1 primary antibody (Santa

Cruz, sc-126) or cleaved caspase-3 Asp175 Antibody (Cell Signaling, 9661) at 1:1000 in PBS containing 5% dry milk at 4 °C overnight. Secondary antibodies (anti-rabbit, anti-mouse: GE Healthcare) were incubated at 1:1000 for three hours at room temperature. Loading was controlled with rabbit anti- β -actin (Sigma, a1978, 1:4000). Signals have been quantified with Genetools software (Syngene) and normalized to actin.

4.4.14. RNA Extraction and RT-qPCR

RNA was isolated from NUGC3 cells with 1mL of TRI Reagent (MRC) and RNA was extracted according to the manufacturer's protocol. RNA samples were precipitated with 500 μ L isopropanol followed by washes with 70% cold ethanol. RNA quality was assessed and 1 μ g was used for reverse transcription (High-Capacity cDNA Reverse Transcription Kit, Applied Biosystems). qPCR was performed with performed using a 1:10 dilution of cDNA according to the manufacturer's instructions (LightCycler 480 SYBR Green I Master, Roche), with 500 nM of each primer. The relative expression was calculated using the $\Delta\Delta$ Ct method. Expression levels were normalized using RPLPO.

4.4.15. *In Vitro* Cytotoxicity – NCI-60 Screening

Ligands **L6** and **L7** were submitted to the Developmental Therapeutics Program at the U.S National Cancer Institute for screening on a panel of 60 human tumour cell lines. Compounds are initially tested at a single high dose (10 μ M) and those that satisfy pre-determined thresholds will be tested in a five-dose assay.³⁵⁵ The methodology used in the NCI-60 screen has been described elsewhere.³²⁰

4.4.16. *In Vitro* Cytotoxicity – Stomach Cancer Cell Lines

The *in vitro* cytotoxicity of **L6** and **L7** against NUGC3 was assayed using the 3-(4,5-dimethylthiazol-2-yl)-2,5-diphenyltetrazolium bromide (MTT) assay.³⁵⁶ NUGC3 cells were seeded at 10,000 cells per well (100 μ L) in Cellstar 96-well plates (Grenier Bio-One) and incubated at 37 °C with 5% CO₂ for 24 hours. Following incubation, the cells were exposed to drugs at increasing concentrations ranging from 0.1 to 200 μ M in RPMI medium. Compounds were pre-dissolved in DMSO stocks and serial dilutions were prepared such that the final concentration of DMSO in media was below 1% (v/v). Treated cells were incubated at 37 °C with 5% CO₂ for 48 hours. Following 48-hour incubation, the

MTT test was performed as previously described. Experiments were performed in replicates of eight and repeated at least two times. Inhibition of cell viability was evaluated with reference to determine the absolute IC₅₀ value calculated from dose-response curves using nonlinear variable slope regression (Prism™ software).

4.4.17. Organoid Culture and Immunofluorescence

Small intestinal organoids were obtained from intestinal crypts isolated from a 2-month old female C57BL/6 mouse. They are cultured in a drop of 20 µL/well Matrigel (Corning) in 48-well plates (Greiner Bio-One) with 250 µL mouse IntestiCult™ Organoid Growth Medium (StemCell) at 37°C with 5% CO₂. After 3 days, organoids were treated with 2.5 µM, 5 µM and 10 µM of **L6** and **L7**, and 25µM of oxaliplatin. The medium was replaced every 48 hours. For the immunofluorescence experiment, organoids were cultured on 8-well Lab-Tek®II Chamber Slide™ (D. Dutscher). After 24h, 48h and 72h of treatment, organoids were fixed with fixation buffer (4% Paraformaldehyde, 60 mM 1,4-Piperazinediethanesulfonic acid (PIPES), 25 mM HEPES, 10 mM ethylene glycol tetraacetic acid (EGTA), 2 mM magnesium acetate) for 30 minutes followed by 45-minute quenching (50 mM NH₄Cl mM). The organoids were permeabilized for 30 minutes with 0.5% PBS-Triton and blocked with 5% PBS-BSA for 30 minutes. The organoids were incubated for 2 hours at 37°C with Phalloidin-TRITC (Sigma-Aldrich), followed by 10 minutes at 37°C with DAPI (Sigma-Aldrich). Phalloidin is used to reveal actin networks and cellular contours, and DAPI is used to stain DNA. ca. 150 organoids were counted and analyzed for each condition. Both observations were done using a fluorescence microscope (Axio Imager M2 Zeiss) coupled to a Hamamatsu's camera Orca Flash 4v3, using the ApoTome.2 (Zeiss) function. Images were analyzed using ImageJ software.

4.4.18. Organoid Survival Assay

For the survival assay experiment, organoids were cultured in 48-well plates (Greiner Bio-one) and treated with **L6** and **L7** at indicated concentrations. Images of each well were taken every day using a AXIO Zoom.V16 (Zeiss) microscope and analyzed using ImageJ software. Cell Counter plugin was used to distinguish “alive/dead” organoids with or without buddings. Four replicates of each condition were used and 250 organoids per condition were analyzed.

4.4.19. Tolerability of L6 in Normal Mice

The tolerability of **L6** has been investigated in C57BL/6 mice treated chronically by intraperitoneal injection twice a week for 5 weeks. Three groups (n = 3) have been used to test in parallel three doses of the compound. The dose in each group was increased after 2 weeks of monitoring without any observable secondary effects.

Chapter 5. Ongoing and Future Directions

5.1. Thesis Summary

p53 is the most frequently mutated protein in human cancer and accounts for over 50% of cancer diagnoses.²⁷⁴ This thesis explores small-molecule design strategies to restore wild-type function in mutant p53 for anticancer therapy. Considering the multifaceted nature of p53 mutants, a multifunctional approach was employed to simultaneously target various characteristics including zinc loss, thermal denaturation, and aggregation. A combination of fragments targeting zinc loss and thermal denaturation was effective at restoring p53 activity in the common mutant p53-Y220C, wherein wild-type function is lost due to an exposed cavity at the surface of the protein that promotes protein unfolding. This ligand scaffold increased intracellular zinc levels, exhibited low micromolar cytotoxicity in cancer cells across a wide range of cancer types, and maintained cytotoxicity in a 3D spheroid model in cells containing the p53-Y220C mutant. This led to restoration of apoptotic function, induced a conformational change wherein levels of unfolded p53 was decreased, and recovered p53 transcriptional activity. Modifications made to this ligand scaffold to extend the structures into subsite cavities formed by this mutant increased the cytotoxicity of the ligands and restored apoptotic activity, however, resulted in a loss in their ability to serve as zinc metallochaperones. This study demonstrated the sensitivity of metallochaperone design and how subtle tuning of the ligand scaffold can impart significant changes in biological activity. Lastly, a combination of fragments targeting zinc loss and protein aggregation found success in restoring wild-type function in mutant p53. These studies highlighted the possible advantages of halogenation in modulating mutant p53 aggregation, as an iodinated scaffold limited mutant p53 aggregation in both recombinant and cellular systems and restored wild-type activity in mutant p53.

Through these studies, the potential for multifunctional ligand scaffolds to restore wild-type function in mutant p53 was established. Previous efforts in the field to restore function in mutant p53 have been monofunctional in design; this work represents a foundation to simultaneously target the multiple characteristics of p53 mutants and provides important information for drug design moving forward. Outlined below are

ongoing and future directions that build from the results obtained and discussed in previous chapters.

5.2. Chapter 2 and Chapter 3

Chapter 2 describes the design, synthesis, and biological testing of a series of first-generation small molecules aimed at stabilizing the p53-Y220C mutant. Chapter 3 builds from the lead scaffold to expand the ligand design into mutant subsite cavities and explores the biological impact of such structure modifications. Despite using a range of techniques including mass spectrometry and surface plasmon resonance to probe potential binding interactions between our ligands and mutant p53, no binding was observed at biologically relevant concentrations. Future binding studies should use robust NMR techniques such as $^1\text{H}/^{15}\text{N}$ -HSQC NMR spectroscopy or saturation transfer difference (STD) NMR spectroscopy, which are commonly used methods to detect binding of small molecules to macromolecular structures such as proteins. Further, despite the selectivity for mutant p53 in the apoptosis studies, significant *in vitro* cytotoxicity is also observed in wild-type p53 cell lines, indicating potential off-target activity. Future work on these ligand constructs should investigate the potential mechanisms for off-target activity in order to improve the ligand design and optimize properties for increased selectivity. In particular, the copper binding affinity of the ligand series should be determined and their ability to generate ROS should be investigated.

5.2.1. Mechanisms of p53-Independent Activity

There is a significant body of literature demonstrating the impact of copper-mediated ROS production in cancer cell death with metal chelating agents.^{231, 237, 427-430} While ROS generation can be beneficial when considering general cytotoxic agents, it is a common contributor to off-target cytotoxicity with target-specific chemotherapeutics. In fact, recent studies on p53 activating scaffolds show that increased ROS generation is a major component of the observed cytotoxicity, in addition to p53 activation.²²⁶ For example, Carpizo and co-workers determined that the toxicity generated by copper-mediated ROS prevented their zinc metallochaperones from exhibiting synergistic activity with common chemotherapeutics. As a result, they conclude that both copper and zinc affinities must be considered into the design strategy and describe a revised model

wherein metallochaperones should exhibit nanomolar zinc affinity in addition to a copper affinity that is weaker than 10 pM in order to significantly decrease the ROS signal.²²⁴

Studies on similar ligand scaffolds containing both 2-picolylamine and di-(2-picolyl)amine as metal chelators have shown significant copper affinity ranging from nanomolar to picomolar, and thus copper-mediated ROS is a likely mechanism of off-target cytotoxicity in our ligand scaffold.²⁵⁵ Initial UV-vis studies as described in sections 2.2.3 and 3.2.3 should be carried out using lead compounds **L5**, **L5-O**, and **L5-P** and $\text{Cu}(\text{ClO}_4)_2 \cdot 6\text{H}_2\text{O}$ to generate speciation diagrams and determine the copper binding affinity. Next, the ability of **L5**, **L5-O**, and **L5-P** to generate ROS in cells should be investigated using the mutant NUGC3 cell line. While several methods and probes exist to measure ROS generation in cells, the CellROX reagents have been extensively used in the literature to detect ROS generation in p53 compromised cell lines.^{199, 431-432} The CellROX dyes exhibit minimal fluorescence in a reduced state and generate a fluorescent signal upon oxidation by reactive oxygen species. Thus, an experiment using NUGC3 cells and increasing concentrations of **L5**, **L5-O**, and **L5-P** should be performed to measure ROS generation compared to non-treated controls. Interestingly, CellROX green is only fluorescent upon subsequent binding to DNA and thus selectively measures ROS generation in the nucleus. Alternatively, CellROX Deep Red does not require DNA binding and is localized to the cytoplasm. Given that mutant p53 is frequently localized in the cytoplasm,⁴³³ simultaneous incubation of NUGC3 cells with CellROX green and red in the presence and absence of our compounds could not only indicate ROS generation but could also provide information regarding the effect of p53 activation and nuclear localization. For example, if treatment with our compounds led to restored p53 function and facilitated nuclear localization, the increase in fluorescent signal upon ROS generation should be greater with the CellROX green as opposed to the CellROX red. Overall, determining the copper-binding affinity of our ligand series and their ability to generate ROS would provide important information for future structure optimizations to minimize ROS and increase selectivity moving forward.

5.2.2. Structure Modifications and Design Strategies

A number of structure modifications and design strategies can be applied to the ligand scaffold in order to improve target selectivity. Initial studies should involve modulating the zinc binding unit in order to optimize both zinc and copper chelation to

prevent off-target toxicity via ROS. Zinc binding groups (ZBGs) have been of significant interest in medicinal chemistry, specifically with regards to the design of enzyme inhibitors for matrix metalloproteinases (MMPs) and histone deacetylases (HDACs).²⁴⁸⁻²⁵² Extensive reviews, including those by Cohen and Wiest, have identified libraries of zinc binding fragments, some of which are shown in Figure 5.1.⁴³⁴⁻⁴³⁵ Hydroxamic acids (**1**) are frequently used as ZBGs in medicinal chemistry due to their high affinity for zinc, but also provide advantages via the potential to form hydrogen bonds with surrounding amino acids in the protein or enzyme target site.⁴³⁶ Other examples include hydrazides (**2-3**), *N*-hydroxyureas (**4**), a carbamoyl phosphonate (**5**), and several nitrogen (**6-12**) and heterocycle-based (**13-21**) ZBGs. Hydrazides offer bidentate chelation with the potential for derivatization to incorporate protein targeting moieties,⁴³⁷ while *N*-hydroxyureas offer similar advantages as hydroxamic acids, however, have improved bioavailability.⁴³⁸ The electron donating ability of the amide group in the carbamoylphosphonate can contribute to a strong zinc binding affinity while also providing the possibility of protein interactions through hydrogen bonding.⁴³⁹ Nitrogen-containing ZBGs have a high affinity for zinc, and it is hypothesized that they exhibit selectivity towards Zn²⁺-dependent enzymes.²⁴⁸ In particular, pyrimidine-2,4,6-trione groups have been extensively studied and are known groups in many FDA approved drugs.⁴⁴⁰ Finally, heterocyclic ZBGs are also of interest due to their biostability and ligand rigidity which contributes to tighter Zn²⁺ binding.^{249, 435}

These fragments should be explored for both their zinc and copper binding affinities, and thus their ability to serve as Zn metallochaperones for mutant p53. Initial experiments should involve competition experiments using chelators with a known copper binding affinity for a more high-throughput approach, in order to eliminate those with greater than picomolar affinity for copper. Next, high throughput experiments using mutant p53 NUGC3 cells in multi-well plates with the fluorescent zinc indicator FluoZin-3 should screen the ZBGs for their ability to increase intracellular fluorescence. Lead binding fragments should be incorporated into the iodinated phenol core of the ligand scaffold and tested for its biological activity in cancer cells and selectivity towards p53 mutants with compromised zinc binding.

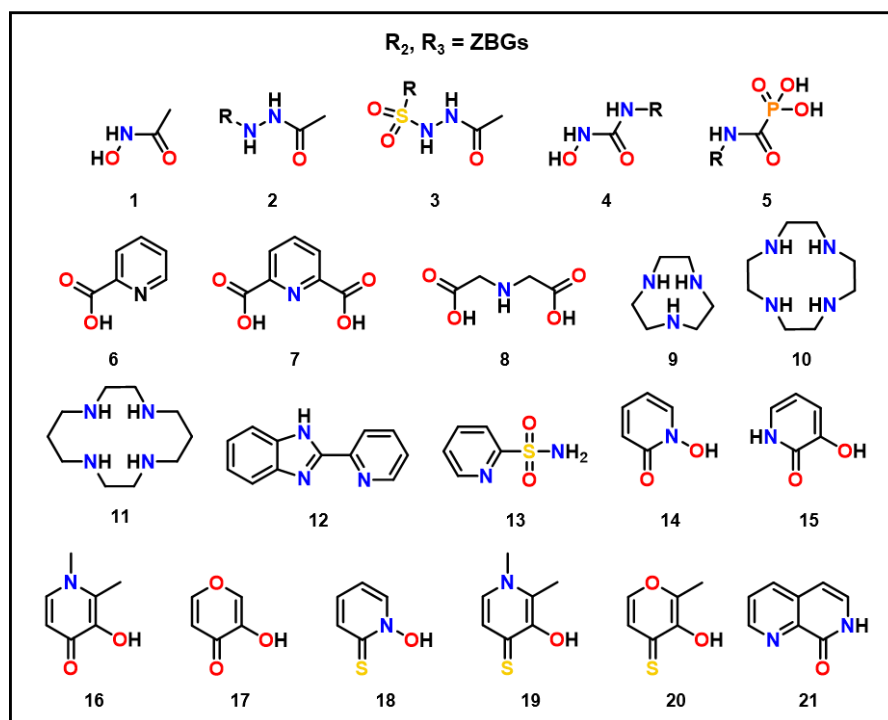
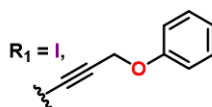
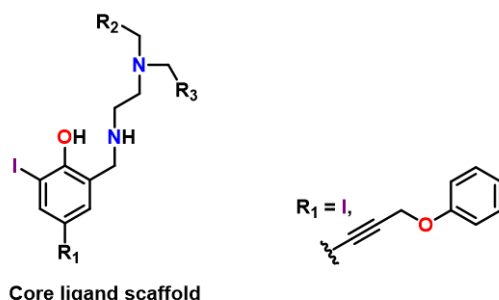


Figure 5.1. Structures of commonly used zinc binding groups (ZBGs) in zinc-containing enzymes such as matrix metalloproteinases (MMPs) and histone deacetylases (HDACs).

Other structure modifications to the ligand scaffold to improve target selectivity could involve the use of a delivery system such as cell-penetrating peptides (CPPs). A significant obstacle faced by many novel drugs designed as anticancer agents is inefficient delivery to the target site.⁴⁴¹ Oftentimes, this is due to the compound's inability to cross the semi-permeable hydrophobic plasma membrane.⁴⁴² As such, the past decade has seen significant advancements in the development of delivery systems including CPPs and nanoparticles, which enhance cellular internalization. CPPs are among the most exploited systems for intracellular delivery as over 1700 CPPs have been reported and experimentally validated for *in vitro* or *in vivo* delivery of cargo ranging from small molecules to large proteins.⁴⁴³ Such systems are comprised of short amino acid

sequences (approximately 5-30 residues) covalently attached to the target molecule. Polyarginine CPPs are the most commonly used as the guanidine groups can form bidentate hydrogen bonds with negatively charged groups of protein cell membranes, which leads to efficient cellular internalization under physiological conditions.⁴⁴⁴ CPPs can be designed for cancer-cell specific delivery, either via incorporation of targeting peptides into the CPP sequence, or via attachment to the cargo using a target-specific cleavable linker.⁴⁴⁵ While research surrounding the application of CPPs in cancer therapy is still relatively in its infancy, CPPs have shown promise due to their low cytotoxicity, rapid renal clearance, and efficient tumour delivery.⁴⁴⁶ In fact, studies have shown that conjugation of CPPs to common anticancer drugs such as Paclitaxel and Doxorubicin has increased the membrane permeability and thus drug delivery, and selectively increased the accumulation in cancer cells.⁴⁴⁴ As such, exploring the possibility for covalent attachment of tumour-specific CPPs to lead compounds **L5**, **L5-O**, and **L5-P** could significantly enhance target specificity and thus reduce unwanted toxic side effects.

Finally, moving forward, other characteristics of mutant p53 could be targeted simultaneously using our multifunctional approach. For example, several small molecules targeting cysteine modification have found success in refolding mutant p53 in order to restore wild-type function. PK11007 (Figure 5.2 a) in particular was shown to alkylate the thiols of solvent-accessible cysteines Cys182 and Cys277 and promote refolding to restore function in mutant p53-Y220C. However, significant p53-independent cell death was observed, providing an opportunity to improve the structural scaffold.¹⁹⁹ Incorporation of the iodinated phenol core from **L1-L5** with the 2-sulfonylpyrimidine group from PK11007 could allow for simultaneous stabilization of the p53-Y220C core in addition to cysteine modification (Figure 5.2 b). Further, recent reports from Lim and co-workers demonstrate the advantages of small molecules with biologically-accessible redox-properties in modulating protein aggregation.⁴⁴⁷ Incorporation of the 2-sulfonylpyrimidine group from PK11007 with the core scaffold from **L6** could provide advantages for modulating mutant p53 aggregation via the addition of redox activity (Figure 5.2 c). Specifically, PK11007 is hypothesized to generate ROS via the depletion of glutathione (GSH), an antioxidant and major redox buffer in cells.¹⁹⁹ GSH is highly abundant in cells and has a freely accessible thiol group, which is prone to adduct formation with thiol alkylators such as PK11007. Lastly, it would be of interest to investigate the effects of targeting both cysteine modification and restoring zinc binding in mutant p53. Combining the di-(2-picolyl)amine

zinc binding unit with the 2-sulfonylpyrimidine group would allow for investigation of the possible advantages of targeting loss of zinc binding in addition to cysteine alkylation in mutant p53-Y220C (Figure 5.2 d).

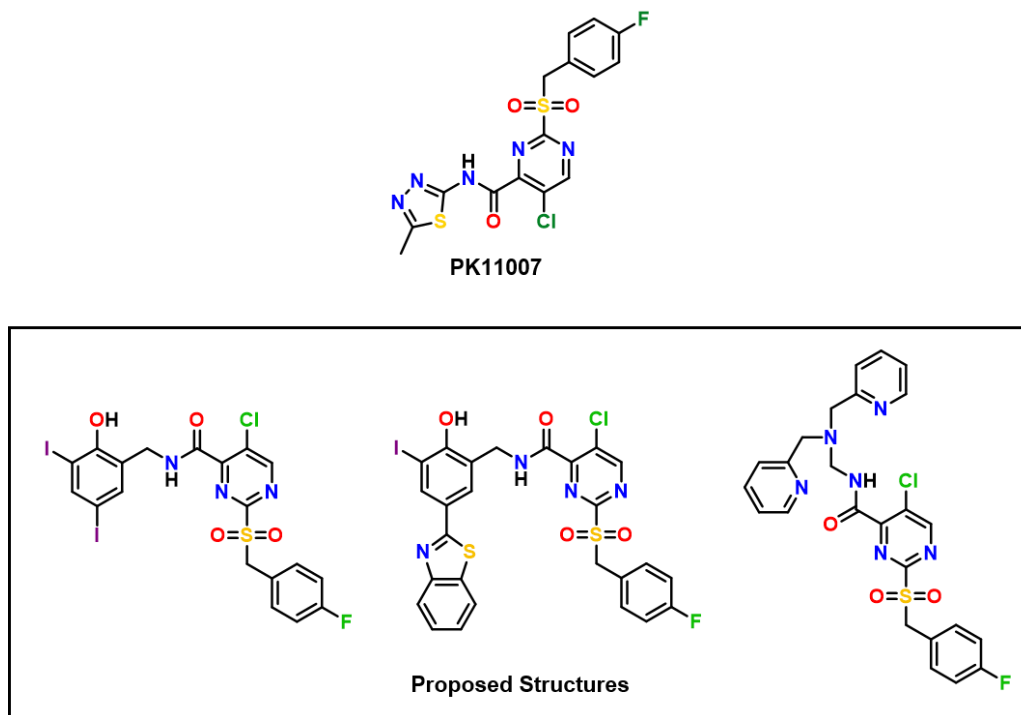


Figure 5.2. Chemical structure of Pk11007 (a), and proposed structures for future modifications to the ligand scaffold (b-d). Targeting other characteristics of mutant p53 simultaneously using a multifunctional approach could provide advantages for selective activity towards mutant p53.

5.3. Chapter 4

Chapter 4 describes the design, synthesis, and biological testing of bifunctional ligands **L6** and **L7**, designed to restore wild-type function in mutant p53 by simultaneously targeting zinc loss and protein aggregation. Our results demonstrate that despite the structural similarity between these two ligands, only **L6**, which contains an iodinated phenol, binds to the protein and limits protein aggregation in both recombinant protein models and NUGC3 cells. Future work on these ligand constructs should investigate whether the influence on p53 aggregation is a result of halogen bonding interactions and/or differing steric and electronic effects from the iodine. Further, whether **L6** can be widely applicable to other aggregation-prone mutants of p53 should be explored.

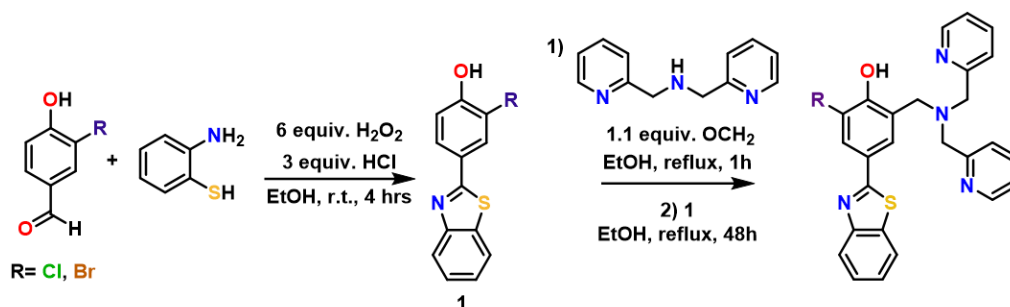
The studies outlined in Chapter 4 demonstrate that **L6** limits mutant p53 aggregation, and that apoptotic and transcriptional activity are restored. To link the two and ensure that this is a direct result of p53 activation, future studies using chromatin immunoprecipitation coupled with massively parallel DNA sequencing, commonly referred to as ChIP-seq, should be employed. ChIP-seq is a commonly used technique to study binding between proteins and transcription factors with DNA and could provide important information on whether treatment with **L6** activates p53 function and DNA binding is restored.⁴⁴⁸ Further information on whether target genes such as p21, NOXA, and BAX are upregulated directly due to p53 activation can be obtained by identifying p53 bound to the promoter of these genes.⁴⁴⁹

5.3.1. Determining the Effects of Halogenation on p53 Aggregation

Based on the differing biological impact of **L6** and **L7** on mutant p53, further investigations into the effects of halogenation on modulating p53 aggregation should be considered. Halogen bonding has been reported to alter aromatic interactions that mediate self-assembly processes,⁴⁵⁰⁻⁴⁵¹ and in particular, the self-assembly of cross β -sheet structures formed by the amyloid-beta protein has elicited significant interest.⁴⁵²⁻⁴⁵⁴ In particular, the potential for halogenated small molecules to modulate the aggregation of amyloid beta and reduce associated neurotoxicity has been recently investigated.⁴⁵⁵⁻⁴⁵⁶ As such, it would be of significant interest to further probe the binding mode of **L6** for possible halogen bonds using X-ray crystallography. X-ray quality crystals of p53-Y220C should be grown following published protocols¹⁵³ and then soaked in varying concentrations of an **L6** solution. Analysis of the crystal structure should provide further information on the detailed binding mode of **L6** to mutant p53 and reveal whether halogen bonding plays a role in this interaction.

To provide further information regarding the effects of halogen atoms on modulating mutant p53 aggregation, the iodine in **L6** should be replaced with lighter halogen atoms that are predicted to form weaker halogen bonds.¹⁵³ In particular, the chlorine and bromine derivatives should be tested for their ability to modulate mutant p53 aggregation to explore whether the size and/or electronegativity of the halogen atom influences its ability to modulate p53 aggregation. Following synthetic procedures outlined in Scheme 4.1, attempts to synthesize the -chloro and -bromo derivatives have been successful, however, purification of these ligands requires further optimization (Scheme

5.1). Following purification, the ability of these ligands to modulate mutant p53 aggregation should be explored. Initial studies using recombinant protein models should explore changes in light scattering at 500 nm, transmission electron microscopy to investigate the morphology of the protein aggregates, and gel electrophoresis to examine changes in size distribution with treatment. If these derivatives prove capable of modulating mutant p53 aggregation in recombinant models, immunofluorescence experiments using NUGC3 cells and A11 and p53 antibodies should be employed. Taken together, investigations into the detailed binding mode of **L6** and studies on the effects of the size of the halogen atom on modulating protein aggregation would provide important information for drug design moving forward.



Scheme 5.1. Synthesis of chloro and bromo derivatives of **L6/L7**. Further purification to isolate ligands is still underway.

5.3.2. Effectiveness of **L6** in Other Aggregation-Prone Mutants

Given the frequency with which p53 mutants aggregate and the aggressive nature of the resulting tumours, it would be highly advantageous if the utility of **L6** extended beyond p53-Y220C. Specifically, if the target of **L6** is the aggregation-prone sequence that is exposed in a large number of p53 mutants rather than the specific mutant cavity in p53-Y220C, then it could be, in principle, effective in all tumours wherein p53 inactivation occurs via partial unfolding and aggregation.¹⁶³ As such, the ability of **L6** to inhibit aggregation in mutants other than p53-Y220C should be explored. Of immediate interest are mutants R248Q and R282W. R248 is a common hotspot mutation in p53, accounting for approximately 4% of all cancer diagnoses.¹⁴³ Mutants at this position have been widely considered as contact mutants due to the interaction between R248 and the minor groove of DNA, however, recent reports have shown that mutations at this site can also induce

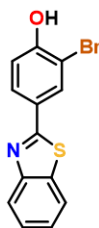
conformational changes. The R248Q mutant exhibits a decreased stability, and recent molecular dynamics studies have detected a more solvent-exposed conformation of this mutant, likely accounting for its tendency to partially unfold and aggregate.⁴⁵⁷ Of particular interest to the work, this study demonstrated that the zinc ion dissociates more readily in R248Q, promoting protein aggregation. Alternatively, the R282W mutant is a common conformational mutant that undergoes partial unfolding and aggregation due to loss of key hydrophobic interactions and hydrogen bonding networks. Cytoplasmic aggregates of p53 have been well characterized in patient tumour samples containing R282W and would thus be of interest to determine if **L6** can modulate aggregation in this commonly occurring mutant.¹⁵⁶

5.4. Closing Statement

This thesis outlined small molecule design strategies to restore wild-type function in mutant p53 for anticancer therapy using a multifunctional approach to simultaneously target various mutant characteristics including zinc loss, thermal denaturation, and aggregation. Future directions should focus on the potential for ROS generation as a contributing factor to off-target activity and expand the concept and utility of our ligands in a wide number of p53 mutants.

5.5. Experimental

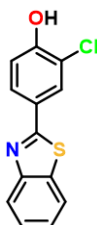
4-(benzo[d]thiazol-2-yl)-2-bromophenol (1)



To a solution of 3-bromo-4-hydroxybenzaldehyde (0.30 g, 1.49 mmol) in EtOH (7 mL) 2-aminothiophenol (0.19 g, 1.49 mmol) was added. Aqueous hydrogen peroxide (0.91 mL, 30%, 6 molar equivalents) and 37% aqueous HCl (1.9 eq) were added. Upon stirring for 2 hours, a green precipitate formed. The precipitate was filtered, washed with cold ethanol, and dried in vacuo. Yield: 70%. ¹H NMR (400 MHz, MeOD): δ = 11.19 (s, 1H), 8.20 (d, J = 2.2 Hz, 1H), 8.12 (dd, J = 8.2, 1.1 Hz, 1H), 8.01 (dd, J = 7.9, 0.9 Hz, 1H), 7.93 (d, J =

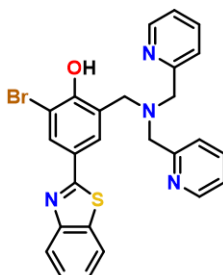
2.2 Hz, 1H), 7.91 (d, $J = 2.2$ Hz, 1H), 7.53 (ddd, $J = 8.3, 7.2, 1.3$ Hz, 1H), 7.44 (ddd, $J = 8.2, 7.2, 1.2$ Hz, 1H), 7.16 (d, $J = 8.4$ Hz, 1H). ^{13}C { ^1H } NMR (400 MHz, MeOD) $\delta = 166.3, 157.5, 154.0, 140.6, 134.7, 131.8, 128.7, 127.0, 125.9, 125.7, 123.0, 122.7, 117.4, 110.6$.

4-(benzo[d]thiazol-2-yl)-2-chlorophenol (**2**)



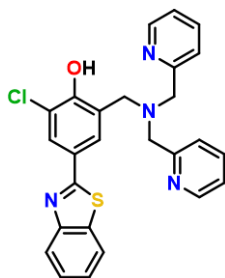
To a solution of 3-chloro-4-hydroxybenzaldehyde (0.30, 1.91 mmol) in EtOH (7 mL) 2-aminothiophenol (0.24 g, 1.91 mmol) was added. Aqueous hydrogen peroxide (1.17 mL, 30%, 6 molar equivalents) and 37% aqueous HCl (1.9 eq) were added. Upon stirring for 2 hours, a green precipitate formed. The precipitate was filtered, washed with cold ethanol, and dried in vacuo. Yield: 44%. ^1H NMR (400 MHz, MeOD): $\delta = 11.15$ (s, 1H), 8.11 (ddd, $J = 8.0, 1.3, 0.6$ Hz, 1H), 8.05 (d, $J = 2.2$ Hz, 1H), 8.01 (ddd, $J = 8.1, 1.2, 0.6$ Hz, 1H), 7.88 (dd, $J = 8.5, 2.2$ Hz, 1H), 7.53 (ddd, $J = 8.3, 7.2, 1.3$ Hz, 1H), 7.43 (ddd, $J = 8.3, 7.2, 1.2$ Hz, 1H), 7.20 (d, $J = 8.5$ Hz, 1H). ^{13}C { ^1H } NMR (400 MHz, MeOD) $\delta = 166.5, 156.5, 154.0, 134.7, 128.8, 128.0, 127.0, 125.7, 125.5, 123.0, 122.7, 121.1, 117.7$.

4-(benzo[d]thiazol-2-yl)-2-((bis(pyridin-2-ylmethyl)amino)methyl)-6-bromophenol



Paraformaldehyde (0.062 g, 2.06 mmol) was added to a solution of di-(2-picolyl)amine (0.20 g, 0.98 mmol) in THF (14 mL) and refluxed for 1 hour. 2-(4-hydroxy-3-bromo)benzothiazole (0.30 g, 0.98 mmol) in 12 mL of THF was added, and the solution was refluxed for an additional 72 hours. The product was identified via mass spectrometry (Calcd for $[\text{M} + \text{H}]^+$, 517.0698, found, 517.0696), however, isolation and purification require further optimization.

4-(benzo[d]thiazol-2-yl)-2-((bis(pyridin-2-ylmethyl)amino)methyl)-6-chlorophenol



Paraformaldehyde (0.048 g, 1.60 mmol) was added to a solution of di-(2-picolyl)amine (0.15 g, 0.76 mmol) in THF (12 mL) and refluxed for 1 hour. 2-(4-hydroxy-3-chloro)benzothiazole (0.20 g, 0.76 mmol) in 10 mL of THF was added, and the solution was refluxed for an additional 72 hours. The product was identified via mass spectrometry (Calcd for $[M + H]^+$, 473.1203, found, 473.1204) however, isolation and purification require further optimization.

References

1. Stratton, M. R.; Campbell, P. J.; Futreal, P. A., *Nature* 2009, **458**, 719-724.
2. Vermeulen, K.; Van Bockstaele, D. R.; Berneman, Z. N., *Cell Prolif.* 2003, **36**, 131-149.
3. Chakravarthi, B. V. S. K.; Nepal, S.; Varambally, S., *Am. J. Pathol.* 2016, **186**, 1724-1735.
4. Pleasance, E. D.; Cheetham, R. K.; Stephens, P. J.; McBride, D. J.; Humphray, S. J.; Greenman, C. D.; Varella, I.; Lin, M.-L.; Ordóñez, G. R.; Bignell, G. R.; Ye, K.; Alipaz, J.; Bauer, M. J.; Beare, D.; Butler, A.; Carter, R. J.; Chen, L.; Cox, A. J.; Edkins, S.; Kokko-Gonzales, P. I.; Gormley, N. A.; Grocock, R. J.; Haudenschild, C. D.; Hims, M. M.; James, T.; Jia, M.; Kingsbury, Z.; Leroy, C.; Marshall, J.; Menzies, A.; Mudie, L. J.; Ning, Z.; Royce, T.; Schulz-Trieglaff, O. B.; Spiridou, A.; Stebbings, L. A.; Szajkowski, L.; Teague, J.; Williamson, D.; Chin, L.; Ross, M. T.; Campbell, P. J.; Bentley, D. R.; Futreal, P. A.; Stratton, M. R., *Nature* 2010, **463**, 191-196.
5. Przytycki, P. F.; Singh, M., *Genome Med.* 2017, **9**, 79-90.
6. Vogelstein, B.; Papadopoulos, N.; Velculescu, V. E.; Zhou, S.; Diaz, L. A.; Kinzler, K. W., *Science* 2013, **339**, 1546.
7. Garraway, Levi A.; Lander, Eric S., *Cell* 2013, **153**, 17-37.
8. Anand, P.; Kunnumakara, A. B.; Sundaram, C.; Harikumar, K. B.; Tharakan, S. T.; Lai, O. S.; Sung, B.; Aggarwal, B. B., *Pharm. Res.* 2008, **25**, 2097-2116.
9. Ngeow, J.; Eng, C., *NPJ Genom. Med.* 2016, **1**, 15006-15009.
10. DeClerck, Y. A.; Mercurio, A. M.; Stack, M. S.; Chapman, H. A.; Zutter, M. M.; Muschel, R. J.; Raz, A.; Matrisian, L. M.; Sloane, B. F.; Noel, A.; Hendrix, M. J.; Coussens, L.; Padarathsingh, M., *Am. J. Pathol.* 2004, **164**, 1131-1139.
11. Seyfried, T. N.; Huysentruyt, L. C., *Crit. Rev. Oncog.* 2013, **18**, 43-73.
12. Canadian Cancer Statistics Advisory Committee. Canadian Cancer Statistics 2019. cancer.ca/Canadian-Cancer-Statistics-2019-EN (accessed October 29th).
13. de Oliveira, C.; Weir, S.; Rangrej, J.; Krahn, M. D.; Mittmann, N.; Hoch, J. S.; Chan, K. K. W.; Peacock, S., *CMAJ Open* 2018, **6**, E1-E10.
14. Baskar, R.; Lee, K. A.; Yeo, R.; Yeoh, K.-W., *Int. J. Med. Sci.* 2012, **9**, 193-199.
15. Alderden, R. A.; Hall, M. D.; Hambley, T. W., *J. Chem. Educ.* 2006, **83**, 728-734.
16. Dasari, S.; Tchounwou, P. B., *Eur. J. Pharmacol.* 2014, **740**, 364-378.

17. Galluzzi, L.; Senovilla, L.; Vitale, I.; Michels, J.; Martins, I.; Kepp, O.; Castedo, M.; Kroemer, G., *Oncogene* 2012, **31**, 1869-1883.
18. Siddik, Z. H., *Oncogene* 2003, **22**, 7265-7279.
19. Paul, S. M.; Mytelka, D. S.; Dunwiddie, C. T.; Persinger, C. C.; Munos, B. H.; Lindborg, S. R.; Schacht, A. L., *Nature Rev. Drug. Disc.* 2010, **9**, 203-214.
20. Sun, J.; Wei, Q.; Zhou, Y.; Wang, J.; Liu, Q.; Xu, H., *BMC Syst. Biol.* 2017, **11**, 87-87.
21. Masui, K.; Gini, B.; Wykosky, J.; Zanca, C.; Mischel, P. S.; Furnari, F. B.; Cavenee, W. K., *Carcinogenesis* 2013, **34**, 725-738.
22. Chatterjee, N.; Walker, G. C., *Environ. Mol. Mutagen.* 2017, **58**, 235-263.
23. Johnstone, T. C.; Park, G. Y.; Lippard, S. J., *Anticancer Res.* 2014, **34**, 471-476.
24. Hato, S. V.; Khong, A.; de Vries, I. J. M.; Lesterhuis, W. J., *Clinical Cancer Res.* 2014, **20**, 2831-2837.
25. Bruno, P. M.; Liu, Y.; Park, G. Y.; Murai, J.; Koch, C. E.; Eisen, T. J.; Pritchard, J. R.; Pommier, Y.; Lippard, S. J.; Hemann, M. T., *Nat. Med.* 2017, **23**, 461-471.
26. Parker, W. B., *Chem. Rev.* 2009, **109**, 2880-2893.
27. Longley, D. B.; Harkin, D. P.; Johnston, P. G., *Nat. Rev. Cancer* 2003, **3**, 330-338.
28. Minotti, G.; Menna, P.; Salvatorelli, E.; Cairo, G.; Gianni, L., *Pharmacol. Rev.* 2004, **56**, 185-229.
29. Weaver, B. A., *Mol. Biol. Cell* 2014, **25**, 2677-2681.
30. Chin, L.; Andersen, J. N.; Futreal, P. A., *Nat. Med.* 2011, **17**, 297-303.
31. Gerber, D., *Am. Fam. Physician* 2008, **77**, 311-319.
32. Wilhelm, S. M.; Adnane, L.; Newell, P.; Villanueva, A.; Llovet, J. M.; Lynch, M., *Mol. Cancer Ther.* 2008, **7**, 3129-3140.
33. Cilloni, D.; Saglio, G., *Clinical Cancer Res.* 2012, **18**, 930-937.
34. Marcucci, G.; Perrotti, D.; Caligiuri, M. A., *Clin. Cancer Res.* 2003, **9**, 1248-1252.
35. Jin, J.; Wu, X.; Yin, J.; Li, M.; Shen, J.; Li, J.; Zhao, Y.; Zhao, Q.; Wu, J.; Wen, Q.; Cho, C. H.; Yi, T.; Xiao, Z.; Qu, L., *Front. Oncol.* 2019, **9**, 1-7.
36. Hofseth, L. J.; Hussain, S. P.; Harris, C. C., *Trends Pharmacol. Sci.* 2004, **25**, 177-181.
37. Bykov, V. J. N.; Eriksson, S. E.; Bianchi, J.; Wiman, K. G., *Nat. Rev. Cancer* 2017, 89-102.

38. Lane, D. P.; Crawford, L. V., *Nature* 1979, **278**, 261-263.
39. Linzer, D. I. H.; Levine, A. J., *Cell* 1979, **17**, 43-52.
40. Lane, D.; Levine, A., *Cold Spring Harb. Perspect. Biol.* 2010, **2**, a000893-a000903.
41. Eliyahu, D.; Michalovitz, D.; Oren, M., *Nature* 1985, **316**, 158-160.
42. Parada, L. F.; Land, H.; Weinberg, R. A.; Wolf, D.; Rotter, V., *Nature* 1984, **312**, 649-651.
43. Eliyahu, D.; Raz, A.; Gruss, P.; Givol, D.; Oren, M., *Nature* 1984, **312**, 646-649.
44. Baker, S. J.; Fearon, E. R.; Nigro, J. M.; Hamilton, S. R.; Preisinger, A. C.; Jessup, J. M.; VanTuinen, P.; Ledbetter, D. H.; Barker, D. F.; Nakamura, Y.; White, R.; Vogelstein, B., *Science* 1989, **244**, 217-221.
45. Wolf, D.; Rotter, V., *Proc. Natl. Acad. Sci. U. S. A.* 1985, **82**, 790-794.
46. Wolf, D.; Rotter, V., *Mol. Cell. Biol.* 1984, **4**, 1402-1410.
47. Levine, A. J.; Oren, M., *Nat. Rev. Cancer* 2009, **9**, 749-758.
48. Donehower, L. A.; Harvey, M.; Slagle, B. L.; McArthur, M. J.; Montgomery, C. A.; Butel, J. S.; Bradley, A., *Nature* 1992, **356**, 215-221.
49. Malkin, D.; Li, F. P.; Strong, L. C.; Fraumeni, J. F.; Nelson, C. E.; Kim, D. H.; Kassel, J.; Gryka, M. A.; Bischoff, F. Z.; Tainsky, M. A.; et, a., *Science* 1990, **250**, 1233-1238.
50. Malkin, D., *Genes Cancer* 2011, **2**, 475-484.
51. Joerger, A. C.; Fersht, A. R., *Cold Spring Harb. Perspect. Biol.* 2010, **2**, 1-20.
52. Yang, A.; Kaghad, M.; Wang, Y.; Gillett, E.; Fleming, M. D.; Dötsch, V.; Andrews, N. C.; Caput, D.; McKeon, F., *Mol. Cell* 1998, **2**, 305-316.
53. Jost, C. A.; Marin, M. C.; Jr, W. G. K., *Nature* 1997, **389**, 191-194.
54. Thanos, C. D.; Bowie, J. U., *Protein Sci.* 1999, **8**, 1708-1710.
55. DeYoung, M. P.; Ellisen, L. W., *Oncogene* 2007, **26**, 5169-5183.
56. Collavin, L.; Lunardi, A.; Del Sal, G., *Cell Death Differ.* 2010, **17**, 901-911.
57. Dötsch, V.; Bernassola, F.; Coutandin, D.; Candi, E.; Melino, G., *Cold Spring Harb. Perspect. Biol.* 2010, **2**, a004887-a004901.
58. Joerger, A. C.; Fersht, A. R., *Annu. Rev. Biochem.* 2016, **85**, 375-404.
59. Joerger, A. C.; Fersht, A. R., *Annu. Rev. Biochem.* 2008, **77**, 557-582.

60. Jimenez, G. S.; Khan, S. H.; Stommel, J. M.; Wahl, G. M., *Oncogene* 1999, **18**, 7656-7665.
61. Meek, D. W.; Anderson, C. W., *Cold Spring Harb. Perspect. Biol.* 2009, **1**, a000950-a000966.
62. Bode, A. M.; Dong, Z., *Nat. Rev. Cancer* 2004, **4**, 793-805.
63. Candau, R.; Scolnick, D. M.; Darpino, P.; Ying, C. Y.; Halazonetis, T. D.; Berger, S. L., *Oncogene* 1997, **15**, 807-816.
64. Brady, Colleen A.; Jiang, D.; Mello, Stephano S.; Johnson, Thomas M.; Jarvis, Lesley A.; Kozak, Margaret M.; Broz, Daniela K.; Basak, S.; Park, Eunice J.; McLaughlin, Margaret E.; Karnezis, Anthony N.; Attardi, Laura D., *Cell* 2011, **145**, 571-583.
65. Bell, S.; Klein, C.; Müller, L.; Hansen, S.; Buchner, J., *J. Mol. Biol.* 2002, **322**, 917-927.
66. Kussie, P. H.; Gorina, S.; Marechal, V.; Elenbaas, B.; Moreau, J.; Levine, A. J.; Pavletich, N. P., *Science* 1996, **274**, 948-953.
67. Harms, K. L.; Chen, X., *Cell Death Differ.* 2006, **13**, 890-897.
68. Teufel, D. P.; Freund, S. M.; Bycroft, M.; Fersht, A. R., *Proc. Natl. Acad. Sci. U. S. A.* 2007, **104**, 7009-7014.
69. Walker, K. K.; Levine, A. J., *Proc. Natl. Acad. Sci. U. S. A.* 1996, **93**, 15335-15340.
70. Baugh, E. H.; Ke, H.; Levine, A. J.; Bonneau, R. A.; Chan, C. S., *Cell Death Differ.* 2018, **25**, 154-160.
71. Natan, E.; Baloglu, C.; Pagel, K.; Freund, S. M. V.; Morgner, N.; Robinson, C. V.; Fersht, A. R.; Joerger, A. C., *J. Mol. Biol.* 2011, **409**, 358-368.
72. Cho, Y.; Gorina, S.; Jeffrey, P.; Pavletich, N., *Science* 1994, **265**, 346-355.
73. Pradhan, M. R.; Siau, J. W.; Kannan, S.; Nguyen, M. N.; Ouaray, Z.; Kwoh, C. K.; Lane, D. P.; Ghadessy, F.; Verma, C. S., *Nucleic Acids Res.* 2019, **47**, 1637-1652.
74. Sykes, S. M.; Mellert, H. S.; Holbert, M. A.; Li, K.; Marmorstein, R.; Lane, W. S.; McMahon, S. B., *Mol. Cell* 2006, **24**, 841-851.
75. Sykes, S. M.; Stanek, T. J.; Frank, A.; Murphy, M. E.; McMahon, S. B., *J. Biol. Chem.* 2009, **284**, 20197-20205.
76. Tidow, H.; Melero, R.; Mylonas, E.; Freund, S. M. V.; Grossmann, J. G.; Carazo, J. M.; Svergun, D. I.; Valle, M.; Fersht, A. R., *Proc. Natl. Acad. Sci. U. S. A.* 2007, **104**, 12324-12329.
77. Chène, P., *Oncogene* 2001, **20**, 2611-2617.

78. Lomax, M. E.; Barnes, D. M.; Hupp, T. R.; Picksley, S. M.; Camplejohn, R. S., *Oncogene* 1998, **17**, 643-649.
79. Mateu, M. G.; Fersht, A. R., *Proc. Natl. Acad. Sci. U. S. A.* 1999, **96**, 3595-3599.
80. Mateu, M. G.; Fersht, A. R., *EMBO J.* 1998, **17**, 2748-2758.
81. Kamada, R.; Nomura, T.; Anderson, C. W.; Sakaguchi, K., *J. Biol. Chem.* 2011, **286**, 252-258.
82. Hamard, P.-J.; Lukin, D. J.; Manfredi, J. J., *J. Biol. Chem.* 2012, **287**, 22397-22407.
83. Weinberg, R. L.; Freund, S. M. V.; Veprintsev, D. B.; Bycroft, M.; Fersht, A. R., *J. Mol. Biol.* 2004, **342**, 801-811.
84. Feng, L.; Lin, T.; Uranishi, H.; Gu, W.; Xu, Y., *Mol. Cell. Biol.* 2005, **25**, 5389-5395.
85. Moll, U. M.; Petrenko, O., *Mol. Cancer Res.* 2003, **1**, 1001-1008.
86. Wu, L.; Levine, A. J., *Mol Med* 1997, **3**, 441-451.
87. Levine, A. J., *Cell* 1997, **88**, 323-331.
88. Nag, S.; Qin, J.; Srivenugopal, K. S.; Wang, M.; Zhang, R., *J. Biomed. Res.* 2013, **27**, 254-271.
89. Friedman, P. N.; Chen, X.; Bargonetti, J.; Prives, C., *Proc. Natl. Acad. Sci. U. S. A.* 1993, **90**, 3319-3323.
90. Brooks, C. L.; Gu, W., *Cell Res.* 2010, **20**, 614-621.
91. Kruse, J.-P.; Gu, W., *Cell* 2009, **137**, 609-622.
92. Beckerman, R.; Prives, C., *Cold Spring Harb. Perspect. Biol.* 2010, **2**, 1-18.
93. Kasthuber, E. R.; Lowe, S. W., *Cell* 2017, **170**, 1062-1078.
94. Haupt, S.; Berger, M.; Goldberg, Z.; Haupt, Y., *J. Cell Sci.* 2003, **116**, 4077-4085.
95. Aubrey, B. J.; Kelly, G. L.; Janic, A.; Herold, M. J.; Strasser, A., *Cell Death Differ.* 2018, **25**, 104-113.
96. Igney, F. H.; Krammer, P. H., *Nat. Rev. Cancer* 2002, **2**, 277-288.
97. Ashkenazi, A., *Nat. Rev. Cancer* 2002, **2**, 420-430.
98. Ashkenazi, A., *Cytokine Growth Factor Rev.* 2008, **19**, 325-331.
99. Jin, C.; Reed, J. C., *Nat. Rev. Mol. Cell Biol.* 2002, **3**, 453-459.
100. Sevrioukova, I. F., *Antioxid. Redox Signal.* 2011, **14**, 2545-2579.

101. Cheung, E. C. C.; Melanson-Drapeau, L.; Cregan, S. P.; Vanderluit, J. L.; Ferguson, K. L.; McIntosh, W. C.; Park, D. S.; Bennett, S. A. L.; Slack, R. S., *J. Neurosci.* 2005, **25**, 1324-1334.
102. Candé, C.; Cecconi, F.; Dessen, P.; Kroemer, G., *J. Cell Sci.* 2002, **115**, 4727-4734.
103. Li, P.; Nijhawan, D.; Budihardjo, I.; Srinivasula, S. M.; Ahmad, M.; Alnemri, E. S.; Wang, X., *Cell* 1997, **91**, 479-489.
104. McIlwain, D. R.; Berger, T.; Mak, T. W., *Cold Spring Harb. Perspect. Biol.* 2013, **5**, a008656-a008684.
105. Green, D. R., *Cell* 2005, **121**, 671-674.
106. Cain, K.; Bratton, S. B.; Cohen, G. M., *Biochimie* 2002, **84**, 203-214.
107. Thornberry, N. A.; Lazebnik, Y., *Science* 1998, **281**, 1312-1316.
108. Porter, A. G.; Jänicke, R. U., *Cell Death Differ.* 1999, **6**, 99-104.
109. Cryns, V.; Yuan, J., *Genes Dev.* 1998, **12**, 1551-1570.
110. Crowley, L. C.; Waterhouse, N. J., *Cold Spring Harb. Protoc.* 2016, **2016**, 958-962.
111. Chang, H. Y.; Yang, X., *Microbiol. Mol. Biol. Rev.* 2000, **64**, 821-846.
112. Elmore, S., *Toxicol. Pathol.* 2007, **35**, 495-516.
113. Chen, J., *Cold Spring Harb. Perspect. Med.* 2016, **6**, a026104-a026119.
114. Helton, E. S.; Chen, X., *J. Cell. Biochem.* 2007, **100**, 883-896.
115. Lukin, D. J.; Carvajal, L. A.; Liu, W.-j.; Resnick-Silverman, L.; Manfredi, J. J., *Mol. Cancer Res.* 2015, **13**, 16-28.
116. Engeland, K., *Cell Death Differ.* 2018, **25**, 114-132.
117. El-Deiry, W. S.; Tokino, T.; Velculescu, V. E.; Levy, D. B.; Parsons, R.; Trent, J. M.; Lin, D.; Mercer, W. E.; Kinzler, K. W.; Vogelstein, B., *Cell* 1993, **75**, 817-825.
118. Abbas, T.; Dutta, A., *Nat. Rev. Cancer* 2009, **9**, 400-414.
119. Karimian, A.; Ahmadi, Y.; Yousefi, B., *DNA Repair* 2016, **42**, 63-71.
120. Georgakilas, A. G.; Martin, O. A.; Bonner, W. M., *Trends Mol. Med.* 2017, **23**, 310-319.
121. El-Deiry, W. S., *Cancer Res.* 2016, **76**, 5189-5191.
122. Wade Harper, J.; Adami, G. R.; Wei, N.; Keyomarsi, K.; Elledge, S. J., *Cell* 1993, **75**, 805-816.

123. Henley, S. A.; Dick, F. A., *Cell Div.* 2012, **7**, 10-10.
124. Farkas, T.; Hansen, K.; Holm, K.; Lukas, J.; Bartek, J., *J. Biol. Chem.* 2002, **277**, 26741-26752.
125. Uxa, S.; Bernhart, S. H.; Mages, C. F. S.; Fischer, M.; Kohler, R.; Hoffmann, S.; Stadler, P. F.; Engeland, K.; Müller, G. A., *Nucleic Acids Res.* 2019, **47**, 9087-9103.
126. Macleod, K. F.; Sherry, N.; Hannon, G.; Beach, D.; Tokino, T.; Kinzler, K.; Vogelstein, B.; Jacks, T., *Genes Dev.* 1995, **9**, 935-944.
127. Benson, E. K.; Mungamuri, S. K.; Attie, O.; Kracikova, M.; Sachidanandam, R.; Manfredi, J. J.; Aaronson, S. A., *Oncogene* 2014, **33**, 3959-3969.
128. Waldman, T.; Kinzler, K. W.; Vogelstein, B., *Cancer Res.* 1995, **55**, 5187-5190.
129. Fischer, M., *Oncogene* 2017, **36**, 3943-3956.
130. Kim, E. M.; Jung, C.-H.; Kim, J.; Hwang, S.-G.; Park, J. K.; Um, H.-D., *Cancer Res.* 2017, **77**, 3092-3100.
131. Yoon, M.-H.; Kang, S.-m.; Lee, S.-J.; Woo, T.-G.; Oh, A.-Y.; Park, S.; Ha, N.-C.; Park, B.-J., *Cell Death Dis.* 2019, **10**, 107-125.
132. Demidenko, Z. N.; Korotchkina, L. G.; Gudkov, A. V.; Blagosklonny, M. V., *Proc. Natl. Acad. Sci. U. S. A.* 2010, **107**, 9660-9664.
133. Assadian, S.; El-Assaad, W.; Wang, X. Q. D.; Gannon, P. O.; Barrès, V.; Latour, M.; Mes-Masson, A.-M.; Saad, F.; Sado, Y.; Dostie, J.; Teodoro, J. G., *Cancer Res.* 2012, **72**, 1270-1279.
134. Carmeliet, P.; Jain, R. K., *Nature* 2000, **407**, 249-257.
135. Teodoro, J. G.; Evans, S. K.; Green, M. R., *J. Mol. Med.* 2007, **85**, 1175-1186.
136. Ravi, R.; Mookerjee, B.; Bhujwalla, Z. M.; Sutter, C. H.; Artemov, D.; Zeng, Q.; Dillehay, L. E.; Madan, A.; Semenza, G. L.; Bedi, A., *Genes Dev.* 2000, **14**, 34-44.
137. Kuilman, T.; Michaloglou, C.; Mooi, W. J.; Peeper, D. S., *Genes Dev.* 2010, **24**, 2463-2479.
138. Gire, V.; Dulić, V., *Cell Cycle* 2015, **14**, 297-304.
139. Campisi, J., *Annu. Rev. Physiol.* 2013, **75**, 685-705.
140. Rufini, A.; Tucci, P.; Celardo, I.; Melino, G., *Oncogene* 2013, **32**, 5129-5143.
141. Lane, D. P., *Nature* 1992, **358**, 15-16.
142. Olivier, M.; Hollstein, M.; Hainaut, P., *Cold Spring Harb. Perspect. Biol.* 2010, **2**, 1-17.

143. Petitjean, A.; Mathe, E.; Kato, S.; Ishioka, C.; Tavtigian, S. V.; Hainaut, P.; Olivier, M., *Hum. Mutat.* 2007, **28**, 622-629.
144. Rivlin, N.; Brosh, R.; Oren, M.; Rotter, V., *Genes Cancer* 2011, **2**, 466-474.
145. Bo, H.; Heuvel, A. P. J. v. d.; Varun, V. P.; Shengliang, Z.; Wafik, S. E.-D., *Curr. Drug Targets* 2014, **15**, 80-89.
146. Silva, J. L.; Cino, E. A.; Soares, I. N.; Ferreira, V. F.; A. P. de Oliveira, G., *Acc. Chem. Res.* 2018, **51**, 181-190.
147. Freed-Pastor, W. A.; Prives, C., *Genes Dev.* 2012, **26**, 1268-1286.
148. Ang, H. C.; Joerger, A. C.; Mayer, S.; Fersht, A. R., *J. Biol. Chem.* 2006, **281**, 21934-21941.
149. Kato, S.; Han, S.-Y.; Liu, W.; Otsuka, K.; Shibata, H.; Kanamaru, R.; Ishioka, C., *Proc. Natl. Acad. Sci. U. S. A.* 2003, **100**, 8424-8429.
150. Joerger, A. C.; Fersht, A. R., *Oncogene* 2007, **26**, 2226-2242.
151. Loh, S. N., *Metallomics* 2010, **2**, 442-449.
152. Bullock, A. N.; Henckel, J.; DeDecker, B. S.; Johnson, C. M.; Nikolova, P. V.; Proctor, M. R.; Lane, D. P.; Fersht, A. R., *Proc. Natl. Acad. Sci. U. S. A.* 1997, **94**, 14338-14342.
153. Wilcken, R.; Liu, X.; Zimmermann, M. O.; Rutherford, T. J.; Fersht, A. R.; Joerger, A. C.; Boeckler, F. M., *J. Am. Chem. Soc.* 2012, **134**, 6810-6818.
154. Joerger, A. C.; Ang, H. C.; Fersht, A. R., *Proc. Natl. Acad. Sci. U. S. A.* 2006, **103**, 15056-15061.
155. Navalkar, A.; Ghosh, S.; Pandey, S.; Paul, A.; Datta, D.; Maji, S. K., *Biochemistry* 2019, 146-155.
156. Xu, J.; Reumers, J.; Couceiro, J. R.; De Smet, F.; Gallardo, R.; Rudyak, S.; Cornelis, A.; Rozenski, J.; Zwolinska, A.; Marine, J.-C.; Lambrechts, D.; Suh, Y.-A.; Rousseau, F.; Schymkowitz, J., *Nat. Chem. Biol.* 2011, **7**, 285-295.
157. Chiti, F.; Dobson, C. M., *Annu. Rev. Biochem.* 2006, **75**, 333-366.
158. Eisenberg, D. S.; Sawaya, M. R., *Annu. Rev. Biochem.* 2017, **86**, 69-95.
159. Muchowski, P. J., *Neuron* 2002, **35**, 9-12.
160. Levy, C. B.; Stumbo, A. C.; Ano Bom, A. P. D.; Portari, E. A.; Carneiro, Y.; Silva, J. L.; De Moura-Gallo, C. V., *Int. J. Biochem. Cell Biol.* 2011, **43**, 60-64.
161. Ghosh, S.; Salot, S.; Sengupta, S.; Navalkar, A.; Ghosh, D.; Jacob, R.; Das, S.; Kumar, R.; Jha, N. N.; Sahay, S.; Mehra, S.; Mohite, G. M.; Ghosh, S. K.; Kombrabail,

- M.; Krishnamoorthy, G.; Chaudhari, P.; Maji, S. K., *Cell Death Differ.* 2017, **24**, 1784-1798.
162. Silva, J. L.; Gallo, C. V. D. M.; Costa, D. C. F.; Rangel, L. P., *Trends Biochem. Sci.* 2014, **39**, 260-267.
163. Soragni, A.; Janzen, D. M.; Johnson, L. M.; Lindgren, A. G.; Thai-Quynh Nguyen, A.; Tiourin, E.; Soriaga, A. B.; Lu, J.; Jiang, L.; Faull, K. F.; Pellegrini, M.; Memarzadeh, S.; Eisenberg, D. S., *Cancer Cell* 2016, **29**, 90-103.
164. Costa, D. C. F.; de Oliveira, G. A. P.; Cino, E. A.; Soares, I. N.; Rangel, L. P.; Silva, J. L., *Cold Spring Harb. Perspect. Biol.* 2016, **8**, 1-21.
165. Wang, G.; Fersht, A. R., *Proc. Natl. Acad. Sci. U. S. A.* 2015, **112**, 2443-2448.
166. Bykov, V. J. N.; Eriksson, S. E.; Bianchi, J.; Wiman, K. G., *Nat. Rev. Cancer* 2018, **18**, 89-102.
167. Roth, J. A.; Nguyen, D.; Lawrence, D. D.; Kemp, B. L.; Carrasco, C. H.; Ferson, D. Z.; Hong, W. K.; Komaki, R.; Lee, J. J.; Nesbitt, J. C.; Pisters, K. M. W.; Putnam, J. B.; Schea, R.; Shin, D. M.; Walsh, G. L.; Dolormente, M. M.; Han, C. I.; Martin, F. D.; Yen, N.; Xu, K.; Stephens, L. C.; McDonnell, T. J.; Mukhopadhyay, T.; Cai, D., *Nat. Med.* 1996, **2**, 985-991.
168. Olivier, M.; Petitjean, A.; Marcel, V.; Pétré, A.; Mounawar, M.; Plymoth, A.; de Fromentel, C. C.; Hainaut, P., *Cancer Gene Ther.* 2009, **16**, 1-12.
169. Ubbly, I.; Krueger, C.; Rosato, R.; Qian, W.; Chang, J.; Sabapathy, K., *Oncogene* 2019, **38**, 3415-3427.
170. Speetjens, F. M.; Kuppen, P. J. K.; Welters, M. J. P.; Essahsah, F.; Voet van den Brink, A. M. E. G.; Lantrua, M. G. K.; Valentijn, A. R. P. M.; Oostendorp, J.; Fathers, L. M.; Nijman, H. W.; Drijfhout, J. W.; van de Velde, C. J. H.; Melief, C. J. M.; van der Burg, S. H., *Clinical Cancer Res.* 2009, **15**, 1086-1095.
171. Yu, X.; Narayanan, S.; Vazquez, A.; Carpizo, D. R., *Apoptosis* 2014, **19**.
172. Momand, J.; Jung, D.; Wilczynski, S.; Niland, J., *Nucleic Acids Res.* 1998, **26**, 3453-3459.
173. Zhao, Y.; Aguilar, A.; Bernard, D.; Wang, S., *J. Med. Chem.* 2015, **58**, 1038-1052.
174. Vassilev, L. T.; Vu, B. T.; Graves, B.; Carvajal, D.; Podlaski, F.; Filipovic, Z.; Kong, N.; Kammlott, U.; Lukacs, C.; Klein, C.; Fotouhi, N.; Liu, E. A., *Science* 2004, **303**, 844-848.
175. ElSawy, K. M.; Verma, C. S.; Lane, D. P.; Caves, L. S. D., *Cell Cycle* 2013, **12**, 3727-3735.

176. Tovar, C.; Rosinski, J.; Filipovic, Z.; Higgins, B.; Kolinsky, K.; Hilton, H.; Zhao, X.; Vu, B. T.; Qing, W.; Packman, K.; Myklebost, O.; Heimbrook, D. C.; Vassilev, L. T., *Proc. Natl. Acad. Sci. U. S. A.* 2006, **103**, 1888-1893.
177. Vu, B.; Wovkulich, P.; Pizzolato, G.; Lovey, A.; Ding, Q.; Jiang, N.; Liu, J.-J.; Zhao, C.; Glenn, K.; Wen, Y.; Tovar, C.; Packman, K.; Vassilev, L.; Graves, B., *Acs Med. Chem. Lett.* 2013, **4**, 466-469.
178. Ding, Q.; Zhang, Z.; Liu, J.-J.; Jiang, N.; Zhang, J.; Ross, T. M.; Chu, X.-J.; Bartkovitz, D.; Podlaski, F.; Janson, C.; Tovar, C.; Filipovic, Z. M.; Higgins, B.; Glenn, K.; Packman, K.; Vassilev, L. T.; Graves, B., *J. Med. Chem.* 2013, **56**, 5979-5983.
179. Skalniak, L.; Kocik, J.; Polak, J.; Skalniak, A.; Rak, M.; Wolnicka-Glubisz, A.; Holak, T. A., *Cancers* 2018, **10**, 396-413.
180. Ding, K.; Lu, Y.; Nikolovska-Coleska, Z.; Qiu, S.; Ding, Y.; Gao, W.; Stuckey, J.; Krajewski, K.; Roller, P. P.; Tomita, Y.; Parrish, D. A.; Deschamps, J. R.; Wang, S., *J. Am. Chem. Soc.* 2005, **127**, 10130-10131.
181. Gupta, A. K.; Bharadwaj, M.; Kumar, A.; Mehrotra, R., *Top. Curr. Chem.* 2016, **375**, 1-25.
182. Ding, K.; Lu, Y.; Nikolovska-Coleska, Z.; Wang, G.; Qiu, S.; Shangary, S.; Gao, W.; Qin, D.; Stuckey, J.; Krajewski, K.; Roller, P. P.; Wang, S., *J. Med. Chem.* 2006, **49**, 3432-3435.
183. Gollner, A.; Rudolph, D.; Arnhof, H.; Bauer, M.; Blake, S. M.; Boehmelt, G.; Cockroft, X.-L.; Dahmann, G.; Ettmayer, P.; Gerstberger, T.; Karolyi-Oezguer, J.; Kessler, D.; Kofink, C.; Ramharter, J.; Rinnenthal, J.; Savchenko, A.; Schnitzer, R.; Weinstabl, H.; Weyer-Czernilofsky, U.; Wunberg, T.; McConnell, D. B., *J. Med. Chem.* 2016, **59**, 10147-10162.
184. Wang, S.; Sun, W.; Zhao, Y.; McEachern, D.; Meaux, I.; Barrière, C.; Stuckey, J. A.; Meagher, J. L.; Bai, L.; Liu, L.; Hoffman-Luca, C. G.; Lu, J.; Shangary, S.; Yu, S.; Bernard, D.; Aguilar, A.; Dos-Santos, O.; Besret, L.; Guerif, S.; Pannier, P.; Gorge-Bernat, D.; Debussche, L., *Cancer Res.* 2014, **74**, 5855-5865.
185. Issaeva, N.; Bozko, P.; Enge, M.; Protopopova, M.; Verhoef, L. G. G. C.; Masucci, M.; Pramanik, A.; Selivanova, G., *Nat. Med.* 2004, **10**, 1321-1328.
186. Krenning, L.; Feringa, Femke M.; Shaltiel, Indra A.; van den Berg, J.; Medema, René H., *Mol. Cell* 2014, **55**, 59-72.
187. Burgess, A.; Chia, K. M.; Haupt, S.; Thomas, D.; Haupt, Y.; Lim, E., *Front. Oncol.* 2016, **6**, 1-7.
188. Hansen, M. J.; Feringa, F. M.; Kobauri, P.; Szymanski, W.; Medema, R. H.; Feringa, B. L., *J. Am. Chem. Soc.* 2018, **140**, 13136-13141.
189. Blandino, G.; Di Agostino, S., *J. Exp. Clin. Canc. Res.* 2018, **37**, 1-13.

190. Zawacka-Pankau, J.; Selivanova, G., *J. Intern. Med.* 2015, **277**, 248-259.
191. Parrales, A.; Iwakuma, T., *Front Oncol* 2015, **5**, 1-13.
192. Fra, A.; Yoboue, E. D.; Sitia, R., *Front. Mol. Neurosci.* 2017, **10**, 167-167.
193. Hallenbeck, K. K.; Turner, D. M.; Renslo, A. R.; Arkin, M. R., *Curr. Top. Med. Chem.* 2017, **17**, 4-15.
194. Foster, B. A.; Coffey, H. A.; Morin, M. J.; Rastinejad, F., *Science* 1999, **286**, 2507-2510.
195. Zache, N.; Lambert, J. M. R.; Rökaeus, N.; Shen, J.; Hainaut, P.; Bergman, J.; Wiman, K. G.; Bykov, V. J. N., *Mol. Oncol.* 2008, **2**, 70-80.
196. Bykov, V. J. N.; Lambert, J. M. R.; Hainaut, P.; Wiman, K. G., *Cell Cycle* 2009, **8**, 2509-2517.
197. Bykov, V. J. N.; Issaeva, N.; Shilov, A.; Hultcrantz, M.; Pugacheva, E.; Chumakov, P.; Bergman, J.; Wiman, K. G.; Selivanova, G., *Nat. Med.* 2002, **8**, 282-288.
198. Zhang, Q.; Bykov, V. J. N.; Wiman, K. G.; Zawacka-Pankau, J., *Cell Death Dis.* 2018, **9**, 439.
199. Bauer, M. R.; Joerger, A. C.; Fersht, A. R., *Proc. Natl. Acad. Sci. U. S. A.* 2016, **113**, e5271-e5280.
200. Bauer, M. R.; Jones, R. N.; Tareque, R. K.; Springett, B.; Dingler, F. A.; Verduci, L.; Patel, K. J.; Fersht, A. R.; Joerger, A. C.; Spencer, J., *Future Med. Chem.* 2019, **11**, 2491-2504.
201. Como, C. J. D.; Prives, C., *Oncogene* 1998, **16**, 2527-2539.
202. Boeckler, F. M.; Joerger, A. C.; Jaggi, G.; Rutherford, T. J.; Veprintsev, D. B.; Fersht, A. R., *Proc. Natl. Acad. Sci. U. S. A.* 2008, **105**, 10360-10365.
203. Joerger, A. C.; Chuckowree, I. S.; Amin, J.; Spencer, J.; Wilcken, R.; Liu, X.; Fersht, A. R., *Nucleic Acids Res.* 2013, **41**, 6034-6044.
204. Rangel, L. P.; Costa, D. C. F.; Vieira, T. C. R. G.; Silva, J. L., *Prion* 2014, **8**, 75-84.
205. Ano Bom, A. P. D.; Rangel, L. P.; Costa, D. C. F.; de Oliveira, G. A. P.; Sanches, D.; Braga, C. A.; Gava, L. M.; Ramos, C. H. I.; Cepeda, A. O. T.; Stumbo, A. C.; De Moura Gallo, C. V.; Cordeiro, Y.; Silva, J. L., *J. Biol. Chem.* 2012, **287**, 28152-28162.
206. Berman, A. Y.; Motechin, R. A.; Wiesenfeld, M. Y.; Holz, M. K., *NPJ Precis. Oncol.* 2017, **1**, 35-44.
207. Ferraz da Costa, D. C.; Campos, N. P. C.; Santos, R. A.; Guedes-da-Silva, F. H.; Martins-Dinis, M. M. D. C.; Zanzhporlin, L.; Ramos, C.; Rangel, L. P.; Silva, J. L., *Oncotarget* 2018, **9**, 29112-29122.

208. Haque, E.; Kamil, M.; Irfan, S.; Sheikh, S.; Hasan, A.; Nazir, A.; Mir, S. S., *Int. J. Biochem. Cell Biol.* 2018, **96**, 90-95.
209. Rabinowitz, J. D.; White, E., *Science* 2010, **330**, 1344-1348.
210. Melino, G.; Bernassola, F.; Ranalli, M.; Yee, K.; Zong, W. X.; Corazzari, M.; Knight, R. A.; Green, D. R.; Thompson, C.; Vousden, K. H., *J. Biol. Chem.* 2004, **279**, 8076-8083.
211. Kravchenko, J. E.; Ilyinskaya, G. V.; Komarov, P. G.; Agapova, L. S.; Kochetkov, D. V.; Strom, E.; Frolova, E. I.; Kovriga, I.; Gudkov, A. V.; Feinstein, E.; Chumakov, P. M., *Proc. Natl. Acad. Sci. U. S. A.* 2008, **105**, 6302-6307.
212. Butler, J. S.; Loh, S. N., *Protein Sci.* 2006, **15**, 2457-2465.
213. Blanden, A. R.; Yu, X.; Loh, S. N.; Levine, A. J.; Carpizo, D. R., *Drug Discov. Today* 2015, **20**, 1391-1397.
214. Hainaut, P.; Milner, J., *Cancer Res.* 1993, **53**, 1739-1742.
215. Puca, R.; Nardinocchi, L.; Porru, M.; Simon, A. J.; Rechavi, G.; Leonetti, C.; Givol, D.; D'Orazi, G., *Cell Cycle* 2011, **10**, 1679-1689.
216. Jayaraman, A. K.; Jayaraman, S., *J. Nutr. Biochem.* 2011, **22**, 79-88.
217. Pucci, D.; Crispini, A.; Mendiguchía, B. S.; Pirillo, S.; Ghedini, M.; Morelli, S.; De Bartolo, L., *Dalton Trans.* 2013, **42**, 9679-9687.
218. Garufi, A.; Trisciuglio, D.; Porru, M.; Leonetti, C.; Stoppacciaro, A.; D'Orazi, V.; Avantaggiati, M. L.; Crispini, A.; Pucci, D.; D'Orazi, G., *J. Exp. Clin. Canc. Res.* 2013, **32**, 72-82.
219. Blanden, A. R.; Yu, X.; Wolfe, A. J.; Gilleran, J. A.; Augeri, D. J.; O'Dell, R. S.; Olson, E. C.; Kimball, S. D.; Emge, T. J.; Movileanu, L.; Carpizo, D. R.; Loh, S. N., *Mol. Pharmacol.* 2015, **87**, 825-831.
220. Maret, W., *Int. J. Mol. Sci.* 2017, **18**, 2285.
221. Loh, S. N., *Metallomics* 2010, **2**, 442-449.
222. Yu, X.; Blanden, A. R.; Narayanan, S.; Jayakumar, L.; Lubin, D.; Augeri, D.; Kimball, S. D.; Loh, S. N.; Carpizo, D. R., *Oncotarget* 2014, **5**, 8879-8892.
223. Butler, J. S.; Loh, S. N., *Biochemistry* 2003, **42**, 2396-2403.
224. Zaman, S.; Yu, X.; Bencivenga, A. F.; Blanden, A. R.; Liu, Y.; Withers, T.; Na, B.; Blayney, A. J.; Gilleran, J.; Boothman, D. A.; Loh, S. N.; Kimball, S. D.; Carpizo, D. R., *Mol. Cancer Ther.* 2019, molcanther.1080.2018.
225. Yu, X.; Vazquez, A.; Levine, Arnold J.; Carpizo, Darren R., *Cancer Cell* 2012, **21**, 614-625.

226. Yu, X.; Blanden, A.; Tsang, A. T.; Zaman, S.; Liu, Y.; Gilleran, J.; Bencivenga, A. F.; Kimball, S. D.; Loh, S. N.; Carpizo, D. R., *Mol. Pharmacol.* 2017, **91**, 567-575.
227. Kogan, S.; Carpizo, D., *Transl. Cancer Res.* 2016, **5**, 698-706.
228. Kalinowski, D. S.; Stefani, C.; Toyokuni, S.; Ganz, T.; Anderson, G. J.; Subramaniam, N. V.; Trinder, D.; Olynyk, J. K.; Chua, A.; Jansson, P. J.; Sahni, S.; Lane, D. J. R.; Merlot, A. M.; Kovacevic, Z.; Huang, M. L. H.; Lee, C. S.; Richardson, D. R., *Biochim. Biophys. Acta* 2016, **1863**, 727-748.
229. Gaur, K.; Vázquez-Salgado, A. M.; Duran-Camacho, G.; Dominguez-Martinez, I.; Benjamín-Rivera, J. A.; Fernández-Vega, L.; Carmona Sarabia, L.; Cruz García, A.; Pérez-Deliz, F.; Méndez Román, J. A.; Vega-Cartagena, M.; Loza-Rosas, S. A.; Rodriguez Acevedo, X.; Tinoco, A. D., *Inorganics* 2018, **6**, 126-164.
230. Utterback, R. D.; Tomat, E., Developing Ligands to Target Transition Metals in Cancer. In *EIBC*, pp 1-19.
231. Denoyer, D.; Masaldan, S.; La Fontaine, S.; Cater, M. A., *Metallomics* 2015, **7**, 1459-1476.
232. Kalinowski, D. S.; Richardson, D. R., *Chem. Res. Toxicol.* 2007, **20**, 715-720.
233. Bakthavatsalam, S.; Sleeper, M. L.; Dharani, A.; George, D. J.; Zhang, T.; Franz, K. J., *Angew. Chem. Int. Ed.* 2018, **57**, 12780-12784.
234. Iljin, K.; Ketola, K.; Vainio, P.; Halonen, P.; Kohonen, P.; Fey, V.; Grafström, R. C.; Perälä, M.; Kallioniemi, O., *Clinical Cancer Res.* 2009, **15**, 6070-6078.
235. Angelica, M. M.; Danuta, S. K.; Zaklina, K.; Patric, J. J.; Sumit, S.; Michael, L. H. H.; Darius, J. R. L.; Hiu, L.; Des, R. R., *Curr. Med. Chem.* 2019, **26**, 302-322.
236. Guo, Z.-L.; Richardson, D. R.; Kalinowski, D. S.; Kovacevic, Z.; Tan-Un, K. C.; Chan, G. C.-F., *J. Hematol. Oncol.* 2016, **9**, 98-98.
237. Stacy, A. E.; Palanimuthu, D.; Bernhardt, P. V.; Kalinowski, D. S.; Jansson, P. J.; Richardson, D. R., *J. Med. Chem.* 2016, **59**, 4965-4984.
238. Spangler, B.; Morgan, C. W.; Fontaine, S. D.; Vander Wal, M. N.; Chang, C. J.; Wells, J. A.; Renslo, A. R., *Nat. Chem. Biol.* 2016, **12**, 680-685.
239. Aron, A. T.; Loehr, M. O.; Bogena, J.; Chang, C. J., *J. Am. Chem. Soc.* 2016, **138**, 14338-14346.
240. Akam, E. A.; Utterback, R. D.; Marcero, J. R.; Dailey, H. A.; Tomat, E., *J. Inorg. Biochem.* 2018, **180**, 186-193.
241. Chang, T. M.; Tomat, E., *Dalton Trans.* 2013, **42**, 7846-7849.
242. Akam, E. A.; Tomat, E., *Bioconjugate Chem.* 2016, **27**, 1807-1812.
243. Hientz, K.; Mohr, A.; Bhakta-Guha, D.; Efferth, T., *Oncotarget* 2017, **8**, 8921-8946.

244. Zhou, X.; Hao, Q.; Lu, H., *J. Mol. Cell Biol.* 2019, **11**, 293-305.
245. Blandino, G.; Levine, A. J.; Oren, M., *Oncogene* 1999, **18**, 477-485.
246. Yang-Hartwich, Y.; Soteras, M. G.; Lin, Z. P.; Holmberg, J.; Sumi, N.; Craveiro, V.; Liang, M.; Romanoff, E.; Bingham, J.; Garofalo, F.; Alvero, A.; Mor, G., *Oncogene* 2015, **34**, 3605-3616.
247. Vahrenkamp, H., *Dalton Trans.* 2007, 4751-4759.
248. Jacobsen, F. E.; Lewis, J. A.; Cohen, S. M., *J. Am. Chem. Soc.* 2006, **128**, 3156-3157.
249. Puerta, D. T.; Lewis, J. A.; Cohen, S. M., *J. Am. Chem. Soc.* 2004, **126**, 8388-8389.
250. Zhang, L.; Zhang, J.; Jiang, Q.; Zhang, L.; Song, W., *J. Enzyme Inhib.* 2018, **33**, 714-721.
251. Li, Y.; Woster, P. M., *MedChemComm* 2015, **6**, 613-618.
252. Madsen, A. S.; Kristensen, H. M. E.; Lanz, G.; Olsen, C. A., *ChemMedChem* 2014, **9**, 614-626.
253. Radford, R. J.; Lippard, S. J., *Curr. Opin. Chem. Biol.* 2013, **17**, 129-136.
254. Wong, B. A.; Friedle, S.; Lippard, S. J., *Inorg. Chem.* 2009, **48**, 7009-7011.
255. Sharma, A. K.; Pavlova, S. T.; Kim, J.; Finkelstein, D.; Hawco, N. J.; Rath, N. P.; Kim, J.; Mirica, L. M., *J. Am. Chem. Soc.* 2012, **134**, 6625-6636.
256. Alker, W.; Schwerdtle, T.; Schomburg, L.; Haase, H., *Int. J. Mol. Sci.* 2019, **20**, 4006-4019.
257. Parkin, G., *Chem. Comm.* 2000, 1971-1985.
258. Wilcken, R.; Zimmermann, M. O.; Lange, A.; Joerger, A. C.; Boeckler, F. M., *J. Med. Chem.* 2013, **56**, 1363-1388.
259. Fraley, A. E.; Sherman, D. H., *Bioorg. Med. Chem. Lett.* 2018, **28**, 1992-1999.
260. Mendez, L.; Henriquez, G.; Sirimulla, S.; Narayan, M., *Molecules* 2017, **22**, 1397-1412.
261. Marcelo Zaldini, H.; Suellen Melo, T. C.; Diogo Rodrigo, M. M.; Walter Filgueira de Azevedo, J.; Ana Cristina Lima, L., *Curr. Drug Targets* 2010, **11**, 303-314.
262. Gerebtzoff, G.; Li-Blatter, X.; Fischer, H.; Frentzel, A.; Seelig, A., *ChemBioChem* 2004, **5**, 676-684.
263. Gentry, C. L.; Egleton, R. D.; Gillespie, T.; Abbruscato, T. J.; Bechowski, H. B.; Hruby, V. J.; Davis, T. P., *Peptides* 1999, **20**, 1229-1238.

264. Banks, W. A., *Nature Rev. Drug. Disc.* 2016, **15**, 275-292.
265. Xu, Z.; Yang, Z.; Liu, Y.; Lu, Y.; Chen, K.; Zhu, W., *J. Chem. Inf. Model.* 2014, **54**, 69-78.
266. Cavallo, G.; Metrangolo, P.; Milani, R.; Pilati, T.; Priimagi, A.; Resnati, G.; Terraneo, G., *Chem. Rev.* 2016, **116**, 2478-2601.
267. Politzer, P.; Murray, J. S.; Clark, T., *Phys. Chem. Chem. Phys.* 2013, **15**, 11178-11189.
268. Auffinger, P.; Hays, F. A.; Westhof, E.; Ho, P. S., *Proc. Natl. Acad. Sci. U. S. A.* 2004, **101**, 16789-16794.
269. Shah, M. B.; Liu, J.; Zhang, Q.; Stout, C. D.; Halpert, J. R., *ACS Chem. Biol.* 2017, **12**, 1204-1210.
270. Erdélyi, M., *Biochemistry* 2017, **56**, 2759-2761.
271. Riley, T.; Sontag, E.; Chen, P.; Levine, A., *Nat. Rev. Mol. Cell Biol.* 2008, **9**, 402-412.
272. Zilfou, J. T.; Lowe, S. W., *Cold Spring Harb. Perspect. Biol.* 2009, **1**, a001883.
273. Lazo, P. A., *Cell. Signal.* 2017, **33**, 49-58.
274. Vogelstein, B.; Lane, D.; Levine, A. J., *Nature* 2000, **408**, 307-310.
275. Muller, P. A. J.; Vousden, K. H., *Nat. Cell Biol.* 2013, **15**, 2-8.
276. Hollstein, M.; Sidransky, D.; Vogelstein, B.; Harris, C., *Science* 1991, **253**, 49-53.
277. Hoe, K. K.; Verma, C. S.; Lane, D. P., *Nat. Rev. Drug. Discov.* 2014, **13**, 217-236.
278. Paek, A.; Liu, J.; Loewer, A.; Forrester, W.; Lahav, G., *Cell* 2016, **165**, 631-642.
279. Selivanova, G.; Wiman, K. G., *Oncogene* 2007, **26**, 2243-2254.
280. Lehmann, S.; Bykov, V. J. N.; Ali, D.; Andrén, O.; Cherif, H.; Tiddefelt, U.; Uggla, B.; Yachnin, J.; Juliusson, G.; Moshfegh, A.; Paul, C.; Wiman, K. G.; Andersson, P.-O., *J. Clin. Oncol.* 2012, **30**, 3633-3639.
281. Mohell, N.; Alfredsson, J.; Fransson, A.; Uustalu, M.; Bystrom, S.; Gullbo, J.; Hallberg, A.; Bykov, V. J. N.; Bjorklund, U.; Wiman, K. G., *Cell Death Dis.* 2015, **6**, e1794-e1804.
282. Peng, X.; Zhang, M. Q. Z.; Conserva, F.; Hosny, G.; Selivanova, G.; Bykov, V. J. N.; Arner, E. S. J.; Wiman, K. G., *Cell Death Dis.* 2013, **4**, e881-e887.
283. Wang, G.; Fersht, A. R., *Proc. Natl. Acad. Sci. U. S. A.* 2012, **109**, 13590-13595.
284. Yu, X.; Vazquez, A.; Levine, A. J.; Carpizo, D. R., *Cancer Cell* 2012, **21**, 614-625.

285. Weekley, C. M.; He, C., *Curr. Opin. Chem. Biol.* 2017, **37**, 26-32.
286. Mertens, C.; Akam, E. A.; Rehwald, C.; Brüne, B.; Tomat, E.; Jung, M., *PLOS ONE* 2016, **11**, 1-19.
287. Park, K. C.; Fouani, L.; Jansson, P. J.; Wooi, D.; Sahni, S.; Lane, D. J. R.; Palanimuthu, D.; Lok, H. C.; Kovacevic, Z.; Huang, M. L. H.; Kalinowski, D. S.; Richardson, D. R., *Metallomics* 2016, **8**, 874-886.
288. King, A. P.; Gellineau, H. A.; Ahn, J.-E.; MacMillan, S. N.; Wilson, J. J., *Inorg. Chem.* 2017, **56**, 6609-6623.
289. Boeckler, F. M.; Joerger, A. C.; Jaggi, G.; Rutherford, T. J.; Veprintsev, D. B.; Fersht, A. R., *Proc. Natl. Acad. Sci. U. S. A.* 2008, **105**, 10360-10365.
290. D'Orazi, G.; Givol, D., *Cell Cycle* 2012, **11**, 2581-2582.
291. Wilcken, R.; Wang, G.; Boeckler, F. M.; Fersht, A. R., *Proc. Natl. Acad. Sci. U. S. A.* 2012, **109**, 13584-13589.
292. Fernandes, A. R.; Jesus, J.; Martins, P.; Figueiredo, S.; Rosa, D.; Martins, L. M. R. D. R. S.; Corvo, M. L.; Carvalheiro, M. C.; Costa, P. M.; Baptista, P. V., *J. Controlled Release* 2017, **245**, 52-61.
293. Silver, H.; Chertkow, Y.; Weinreb, O.; Danovich, L.; Youdim, M., *Neurotherapeutics* 2009, **6**, 86-93.
294. Geldenhuys, W. J.; Youdim, M. B. H.; Carroll, R. T.; Van der Schyf, C. J., *Prog. Neurobiol.* 2011, **94**, 347-359.
295. Morphy, R.; Rankovic, Z., *J. Med. Chem.* 2005, **48**, 6523-6543.
296. Jones, M. R.; Mathieu, E.; Dyrager, C.; Faissner, S.; Vaillancourt, Z.; Korshavn, K. J.; Lim, M. H.; Ramamoorthy, A.; Wee Yong, V.; Tsutsui, S.; Stys, P. K.; Storr, T., *Chem. Sci.* 2017, **8**, 5636-5643.
297. Van der Schyf, C. J.; Youdim, M. B. H., *Neurotherapeutics* 2009, **6**, 1-3.
298. Fang, J.; Jiang, F.; Li, J.; Zhu, Y., *Neural Regen. Res.* 2012, **7**, 313-318.
299. Frezza, M.; Hindo, S. S.; Tomco, D.; Allard, M.; Cui, Q. C.; Heeg, M. J.; Chen, D.; Dou, Q. P.; Verani, C. N., *Inorg. Chem.* 2009, **48**, 5928-5937.
300. Burdette, S. C.; Walkup, G. K.; Spingler, B.; Tsien, R. Y.; Lippard, S. J., *J. Am. Chem. Soc.* 2001, **123**, 7831-7841.
301. Nolan, E. M.; Lippard, S. J., *Acc. Chem. Res.* 2009, **42**, 193-203.
302. Chang, C. J.; Nolan, E. M.; Jaworski, J.; Burdette, S. C.; Sheng, M.; Lippard, S. J., *Chem. Biol.* 2004, **11**, 203-210.
303. Xu, Z.; Yoon, J.; Spring, D. R., *Chem. Soc. Rev.* 2010, **39**, 1996-2006.

304. Perrin, D. D.; Dempsey, B.; Serjeant, E. P., *pK_a Prediction for Organic Acids and Bases*. Springer: Netherlands, 1981.
305. Storr, T.; Merkel, M.; Song-Zhao, G. X.; Scott, L. E.; Green, D. E.; Bowen, M. L.; Thompson, K. H.; Patrick, B. O.; Schugar, H. J.; Orvig, C., *J. Am. Chem. Soc.* 2007, **129**, 7453-7463.
306. Wong, B. A.; Friedle, S.; Lippard, S. J., *J. Am. Chem. Soc.* 2009, **131**, 7142-7152.
307. Martell, A. E.; Smith, R. M., *Critical Stability Constants*. Springer: New York, US, 1982; Vol. 5.
308. Martell, A. E.; Hancock, R. D., *Metal Complexes in Aqueous Solutions*. Springer: New York, US, 1996.
309. Choi, J.-S.; Braymer, J. J.; Nanga, R. P. R.; Ramamoorthy, A.; Lim, M. H., *Proc. Natl. Acad. Sci. U. S. A.* 2010, **107**, 21990-21995.
310. Harris, W. R.; Carrano, C. J.; Cooper, S. R.; Sofen, S. R.; Avdeef, A. E.; McArdle, J. V.; Raymond, K. N., *J. Am. Chem. Soc.* 1979, **101**, 6097-6104.
311. Mitra, M.; Singh, R.; Pyrkosz-Bulska, M.; Haukka, M.; Gumienna-Kontecka, E.; Nordlander, E., *Z. Anorg. Allg. Chem.* 2013, **639**, 1534-1542.
312. Alderighi, L.; Gans, P.; Ienco, A.; Peters, D.; Sabatini, A.; Vacca, A., *Coord. Chem. Rev.* 1999, **184**, 311-318.
313. Gee, K. R.; Zhou, Z. L.; Ton-That, D.; Sensi, S. L.; Weiss, J. H., *Cell Calcium* 2002, **31**, 245-251.
314. Golovine, K.; Uzzo, R. G.; Makhov, P.; Crispen, P. L.; Kunkle, D.; Kolenko, V. M., *The Prostate* 2008, **68**, 1443-1449.
315. Hearn, J. M.; Romero-Canelón, I.; Qamar, B.; Liu, Z.; Hands-Portman, I.; Sadler, P. J., *ACS Chem. Biol.* 2013, **8**, 1335-1343.
316. Gaiddon, C.; Jeannequin, P.; Bischoff, P.; Pfeffer, M.; Sirlin, C.; Loeffler, J. P., *J. Pharmacol. Exp. Ther.* 2005, **315**, 1403-1411.
317. Lim, P.; Mahammed, A.; Okun, Z.; Saltsman, I.; Gross, Z.; Gray, H. B.; Termini, J., *Chem. Res. Toxicol.* 2012, **25**, 400-409.
318. Verheul, H. M. W.; Qian, D. Z.; Carducci, M. A.; Pili, R., *Cancer Chemother. Pharmacol.* 2007, **60**, 329-339.
319. Rixe, O.; Fojo, T., *Clinical Cancer Res.* 2007, **13**, 7280-7287.
320. Shoemaker, R. H., *Nat. Rev. Cancer* 2006, **6**, 813-823.
321. Abdi, J.; Chen, G.; Chang, H., *Oncotarget* 2013, **4**, 2186-2207.
322. Zhang, D.; Fan, D., *Expert Rev. Anticancer Ther.* 2007, **7**, 1369-1378.

323. Sebaugh, J. L., *Pharm. Stat.* 2011, **10**, 128-134.
324. Breslin, S.; O'Driscoll, L., *Drug Discov. Today* 2013, **18**, 240-249.
325. Zanoni, M.; Piccinini, F.; Arienti, C.; Zamagni, A.; Santi, S.; Polico, R.; Bevilacqua, A.; Tesei, A., *Sci. Rep.* 2016, **6**, 19103.
326. Yamada, K. M.; Cukierman, E., *Cell* 2007, **130**, 601-610.
327. Fang, Y.; Eglen, R. M., *SLAS Discov.* 2017, **22**, 1-17.
328. Bilici, A., *World J. Gastroenterol.* 2014, **20**, 3905-3915.
329. Di Lauro, L.; Vici, P.; Belli, F.; Tomao, S.; Fattoruso, S. I.; Arena, M. G.; Pizzuti, L.; Giannarelli, D.; Paoletti, G.; Barba, M.; Sergi, D.; Maugeri-Saccà, M., *Gastric Cancer* 2014, **17**, 718-724.
330. Chan, B.; Jang, R.; Wong, R.; Swallow, C.; Darling, G.; Elimova, E., *Oncology (Williston Park)* 2016, **30**, 635-647.
331. Inadomi, K.; Kusaba, H.; Matsushita, Y.; Tanaka, R.; Mitsugi, K.; Arimizu, K.; Hirano, G.; Makiyama, A.; Ohmura, H.; Uchino, K.; Hanamura, F.; Shibata, Y.; Kuwayama, M.; Esaki, T.; Takayoshi, K.; Arita, S.; Ariyama, H.; Akashi, K.; Baba, E., *Anticancer Res.* 2017, **37**, 2663-2671.
332. Hengartner, M. O., *Nature* 2000, **407**, 770-776.
333. Chen, H.-Y.; Cheng, H.-L.; Lee, Y.-H.; Yuan, T.-M.; Chen, S.-W.; Lin, Y.-Y.; Chueh, P. J., *Oncotarget* 2017, **8**, 15338-15348.
334. Arango, D.; Wilson, A. J.; Shi, Q.; Corner, G. A.; Aranes, M. J.; Nicholas, C.; Lesser, M.; Mariadason, J. M.; Augenlicht, L. H., *Br. J. Cancer* 2004, **91**, 1931-1946.
335. Gaglia, G.; Guan, Y.; Shah, J. V.; Lahav, G., *Proc. Natl. Acad. Sci. U. S. A.* 2013, **110**, 15497-15501.
336. Nicholls, C. D.; McLure, K. G.; Shields, M. A.; Lee, P. W. K., *J. Biol. Chem.* 2002, **277**, 12937-12945.
337. Chong, L. T.; Snow, C. D.; Rhee, Y. M.; Pande, V. S., *J. Mol. Biol.* 2005, **345**, 869-878.
338. Schlereth, K.; Beinoraviciute-Kellner, R.; Zeitlinger, M. K.; Bretz, A. C.; Sauer, M.; Charles, J. P.; Vogiatzi, F.; Leich, E.; Samans, B.; Eilers, M.; Kisker, C.; Rosenwald, A.; Stiewe, T., *Mol. Cell* 2010, **38**, 356-368.
339. Gaiddon, C.; Lokshin, M.; Ahn, J.; Zhang, T.; Prives, C., *Mol. Cell. Biol.* 2001, **21**, 1874-1887.
340. Li, Y.; Prives, C., *Oncogene* 2007, **26**, 2220-2225.
341. Muller, P.; Vousden, K., *Cancer Cell* 2014, **25**, 304-317.

342. Pietsch, E. C.; Sykes, S. M.; McMahon, S. B.; Murphy, M. E., *Oncogene* 2008, **27**, 6507-6521.
343. Wang, X.; Li, M.; Wang, J.; Yeung, C.-M.; Zhang, H.; Kung, H.-f.; Jiang, B.; Chia-mi Lin, M., *Biochem. Pharmacol.* 2006, **71**, 1540-1550.
344. Liu, X.; Wilcken, R.; Joerger, A. C.; Chuckowree, I. S.; Amin, J.; Spencer, J.; Fersht, A. R., *Nucleic Acids Res.* 2013, **41**, 6034-6044.
345. Similar reports by Fersht and co-workers show p53 Y220C-dependent induction of caspase-3 at 200 μ M for PK7088, however, at an earlier time point of 6 hours (see reference 44a). Boeckler and co-worker also report NUGC3-dependent induction of apoptosis after 6 hours, at concentrations of 50 and 100 μ M for PhiKan5196 and PhiKan5974 respectively (reference 8b).
346. Kieboom, A. P. G., *Recueil des Travaux Chimiques des Pays-Bas* 1988, **107**, 685.
347. Perrin, D. D.; Armarego, W. L. F., *Purification of Laboratory Chemicals*. 1st ed. ed.; Pergamo Press: New York, 1988.
348. Horner, O.; Anxolabéhère-Mallart, E.; Charlot, M.-F.; Tchertanov, L.; Guilhem, J.; Mattioli, T. A.; Boussac, A.; Girerd, J.-J., *Inorg. Chem.* 1999, **38**, 1222-1232.
349. Imbert, C.; Hratchian, H. P.; Lanznaster, M.; Heeg, M. J.; Hryhorczuk, L. M.; McGarvey, B. R.; Schlegel, H. B.; Verani, C. N., *Inorg. Chem.* 2005, **44**, 7414-7422.
350. Araz, J.; B., J. D.; I., B. C., *J. Comput. Chem.* 2002, **23**, 1623-1641.
351. Sheldrick, G. M., *SHELXT v2014*; , Bruker AXS Inc: Madison, WI.
352. Hübschle, C. B.; Sheldrick, G. M.; Dittrich, B., *J. Appl. Crystallogr.* 2011, **44**, 1281-1284.
353. Gans, P.; Sabatini, A.; Vacca, A., *Ann. Chim.* 1999, **89**, 45-49.
354. Baes, C. F. J.; Mesmer, R. E., *The Hydrolysis of Cations*. R. E. Krieger Publishing Co: Malabar, FL, 1986.
355. Paull, K. D.; Shoemaker, R. H.; Hodes, L.; Monks, A.; Scudiero, D. A.; Rubinstein, L.; Plowman, J.; Boyd, M. R., *J. Natl. Cancer Inst.* 1989, **81**, 1088-1092.
356. Mosmann, T., *J. Immunol. Methods* 1983, **65**, 55-63.
357. Benosman, S.; Gross, I.; Clarke, N.; Jochemsen, A. G.; Okamoto, K.; Loeffler, J. P.; Gaidon, C., *Cell Death Differ.* 2007, **14**, 2047-2057.
358. Ayed, A.; Mulder, F. A. A.; Yi, G.-S.; Lu, Y.; Kay, L. E.; Arrowsmith, C. H., *Nat. Struct. Mol. Biol.* 2001, **8**, 756-760.
359. Nikolova, P. V.; Henckel, J.; Lane, D. P.; Fersht, A. R., *Proc. Natl. Acad. Sci. U. S. A.* 1998, **95**, 14675-14680.

360. Gill, S. C.; von Hippel, P. H., *Anal. Biochem.* 1989, **182**, 319-326.
361. von Grabowiecki, Y.; Abreu, P.; Blanchard, O.; Palamiuc, L.; Benosman, S.; Mériaux, S.; Devignot, V.; Gross, I.; Mellitzer, G.; Gonzalez de Aguilar, J. L.; Gaiddon, C., *eLife* 2016, **5**, e10528-e10548.
362. Basse, N.; Kaar, J. L.; Settanni, G.; Joerger, A. C.; Rutherford, T. J.; Fersht, A. R., *Chem. Biol.* 2010, **17**, 46-56.
363. Baud, M. G. J.; Bauer, M. R.; Verduci, L.; Dingler, F. A.; Patel, K. J.; Horil Roy, D.; Joerger, A. C.; Fersht, A. R., *Eur. J. Med. Chem.* 2018, **152**, 101-114.
364. Miller, J. J.; Orvain, C.; Jozi, S.; Clarke, R. M.; Smith, J. R.; Blanchet, A.; Gaiddon, C.; Warren, J. J.; Storr, T., *Chem. Eur. J.* 2018, **24**, 17734-17742.
365. Melissaridou, S.; Wiechec, E.; Magan, M.; Jain, M. V.; Chung, M. K.; Farnebo, L.; Roberg, K., *Cancer Cell Int.* 2019, **19**, 16-26.
366. Hoffmann, O. I.; Ilmberger, C.; Magosch, S.; Joka, M.; Jauch, K.-W.; Mayer, B., *J. Biotechnol.* 2015, **205**, 14-23.
367. Kambam, S.; Ren, X.; Zheng, C.; Wang, F.; Wang, Y.; Chen, H.; Yin, J.; Xie, J.; Chen, X., *Bioorg. Med. Chem. Lett.* 2015, **25**, 262-265.
368. Mathur, D.; Rana, N.; Olsen, C. E.; Parmar, V. S.; Prasad, A. K., *J. Heterocycl. Chem.* 2015, **52**, 701-710.
369. Brundin, P.; Melki, R.; Kopito, R., *Nat. Rev. Mol. Cell Biol.* 2010, **11**, 301-307.
370. Geschwind, M. D., *Continuum (Minneap. Minn.)* 2015, **21**, 1612-1638.
371. Knowles, T. P. J.; Vendruscolo, M.; Dobson, C. M., *Nat. Rev. Mol. Cell Biol.* 2014, **15**, 384-396.
372. Chiti, F.; Dobson, C. M., *Annu. Rev. Biochem.* 2017, **86**, 27-68.
373. DeToma, A. S.; Salamekh, S.; Ramamoorthy, A.; Lim, M. H., *Chem. Soc. Rev.* 2012, **41**, 608-621.
374. Eisenberg, D.; Jucker, M., *Cell* 2012, **148**, 1188-1203.
375. Chen, Y.-R., *Alzheimers Dement.* 2010, **6**, e44-e44.
376. Jucker, M.; Walker, L. C., *Nature* 2013, **501**, 45-51.
377. Sowade, R. F.; Jahn, T. R., *Nat. Commun.* 2017, **8**, 512-524.
378. Hao, G.; Xin, Y.; Yudan, Z.; Robert, B. P.; Xinran, L.; Yang, L.; Kun, H., *Curr. Protein Pept. Sci* 2015, **16**, 135-146.

379. Ishimaru, D.; Andrade, L. R.; Teixeira, L. S. P.; Quesado, P. A.; Maiolino, L. M.; Lopez, P. M.; Cordeiro, Y.; Costa, L. T.; Heckl, W. M.; Weissmüller, G.; Foguel, D.; Silva, J. L., *Biochemistry* 2003, **42**, 9022-9027.
380. Lasagna-Reeves, C. A.; Clos, A. L.; Castillo-Carranza, D.; Sengupta, U.; Guerrero-Muñoz, M.; Kelly, B.; Wagner, R.; Kaye, R., *Biochem. Biophys. Res. Commun.* 2013, **430**, 963-968.
381. Kehrloesser, S.; Osterburg, C.; Tuppi, M.; Schäfer, B.; Vousden, K. H.; Dötsch, V., *Cell Death Differ.* 2016, **23**, 1952-1960.
382. Cino, E. A.; Soares, I. N.; Pedrote, M. M.; de Oliveira, G. A. P.; Silva, J. L., *Sci. Rep.* 2016, **6**, 32535-32547.
383. Lavin, M. F.; Gueven, N., *Cell Death Differ.* 2006, **13**, 941-950.
384. Chuikov, S.; Kurash, J. K.; Wilson, J. R.; Xiao, B.; Justin, N.; Ivanov, G. S.; McKinney, K.; Tempst, P.; Prives, C.; Gambin, S. J.; Barlev, N. A.; Reinberg, D., *Nature* 2004, **432**, 353-360.
385. Joerger, A. C.; Bauer, M. R.; Wilcken, R.; Baud, M. G. J.; Harbrecht, H.; Exner, T. E.; Boeckler, F. M.; Spencer, J.; Fersht, A. R., *Structure* 2015, **23**, 2246-2255.
386. Doveston, R. G.; Kuusk, A.; Andrei, S. A.; Leysen, S.; Cao, Q.; Castaldi, M. P.; Hendricks, A.; Brunsveld, L.; Chen, H.; Boyd, H.; Ottmann, C., *FEBS Lett.* 2017, **591**, 2449-2457.
387. Amaral, J. D.; Silva, D.; Rodrigues, C. M. P.; Solá, S.; Santos, M. M. M., *Front. Chem.* 2019, **7**, 1-14.
388. Hietanen, S.; Lain, S.; Krausz, E.; Blattner, C.; Lane, D. P., *Proc. Natl. Acad. Sci. U. S. A.* 2000, **97**, 8501-8506.
389. Rangel, L. P.; Ferretti, G. D. S.; Costa, C. L.; Andrade, S. M. M. V.; Carvalho, R. S.; Costa, D. C. F.; Silva, J. L., *J. Biol. Chem.* 2019, **294**, 3670-3682.
390. Kanapathipillai, M., *Cancers* 2018, **10**, 154-161.
391. Zhaolin, C.; Mathumai, K., *Protein Pept. Lett.* 2017, **24**, 353-357.
392. Chen, Z.; Chen, J.; Keshamouni, V. G.; Kanapathipillai, M., *Biochem. Biophys. Res. Commun.* 2017, **489**, 130-134.
393. Sharma, A.; Pachauri, V.; Flora, S. J. S., *Front. Pharmacol.* 2018, **9**, 1247-1247.
394. Savelieff, M. G.; Nam, G.; Kang, J.; Lee, H. J.; Lee, M.; Lim, M. H., *Chem. Rev.* 2019, **119**, 1221-1322.
395. Cirone, M.; Garufi, A.; Renzo, L.; Granato, M.; Faggioni, A.; D'Orazi, G., *Oncoimmunology* 2013, **2**, 1-9.
396. Garufi, A.; D'Orazi, V.; Crispini, A.; D'Orazi, G., *Int. J. Oncol.* 2015, **47**, 1241-1248.

397. Garufi, A.; Pucci, D.; D'Orazi, V.; Cirone, M.; Bossi, G.; Avantaggiati, M. L.; D'Orazi, G., *Cell Death Dis.* 2014, **5**, 1-9.
398. Carraway, R. E.; Dobner, P. R., *Biochim. Biophys. Acta* 2012, **1823**, 544-557.
399. Ami, D.; Natalello, A.; Lotti, M.; Doglia, S. M., *Microb. Cell Fact.* 2013, **12**, 17-17.
400. Lukashchuk, N.; Vousden, K. H., *Mol. Cell. Biol.* 2007, **27**, 8284-8295.
401. Rodrigues, N. R.; Rowan, A.; Smith, M. E.; Kerr, I. B.; Bodmer, W. F.; Gannon, J. V.; Lane, D. P., *Proc. Natl. Acad. Sci. U. S. A.* 1990, **87**, 7555-7559.
402. Lane, D. P.; Benchimol, S., *Genes Dev.* 1990, **4**, 1-8.
403. Oren, M.; Rotter, V., *Cold Spring Harb. Perspect. Biol.* 2010, **2**, a001107-a001107.
404. Rotter, V., *Proc. Natl. Acad. Sci. U. S. A.* 1983, **80**, 2613-2617.
405. Kaye, R.; Head, E.; Thompson, J. L.; McIntire, T. M.; Milton, S. C.; Cotman, C. W.; Glabe, C. G., *Science* 2003, **300**, 486-489.
406. Fine, G.; Saeed, S. M., *Am. J. Clin. Pathol.* 1967, **47**, 588-593.
407. Xu, J.; Reumers, J.; Couceiro, J. R.; De Smet, F.; Gallardo, R.; Rudyak, S.; Cornelis, A.; Rozenski, J.; Zwolinska, A.; Marine, J.-C.; Lambrechts, D.; Suh, Y.-A.; Rousseau, F.; Schymkowitz, J., *Nat. Chem. Biol.* 2011, **7**, 285-295.
408. Holbeck, S. L.; Collins, J. M.; Doroshow, J. H., *Mol. Cancer Ther.* 2010, **9**, 1451-1460.
409. Fenoglio-Preiser, C. M.; Wang, J.; Stemmermann, G. N.; Noffsinger, A., *Hum. Mutat.* 2003, **21**, 258-270.
410. Zhu, H.-B.; Yang, K.; Xie, Y.-Q.; Lin, Y.-W.; Mao, Q.-Q.; Xie, L.-P., *World J. Surg. Oncol.* 2013, **11**, 22-22.
411. Sayan, A. E.; Sayan, B. S.; Gogvadze, V.; Dinsdale, D.; Nyman, U.; Hansen, T. M.; Zhivotovsky, B.; Cohen, G. M.; Knight, R. A.; Melino, G., *Oncogene* 2008, **27**, 4363-4372.
412. Liu, J.; Uematsu, H.; Tsuchida, N.; Ikeda, M.-A., *Mol. Cancer* 2011, **10**, 95-95.
413. Frank, A. K.; Pietsch, E. C.; Dumont, P.; Tao, J.; Murphy, M. E., *Cancer Biol. Ther.* 2011, **11**, 740-745.
414. Bergamaschi, D.; Gasco, M.; Hiller, L.; Sullivan, A.; Syed, N.; Trigiante, G.; Yulug, I.; Merlano, M.; Numico, G.; Comino, A.; Attard, M.; Reelfs, O.; Gusterson, B.; Bell, A. K.; Heath, V.; Tavassoli, M.; Farrell, P. J.; Smith, P.; Lu, X.; Crook, T., *Cancer Cell* 2003, **3**, 387-402.
415. Marin, M. C.; Jost, C. A.; Brooks, L. A.; Irwin, M. S.; O'Nions, J.; Tidy, J. A.; James, N.; McGregor, J. M.; Harwood, C. A.; Yulug, I. G.; Vousden, K. H.; Allday, M. J.;

- Gusterson, B.; Ikawa, S.; Hinds, P. W.; Crook, T.; Kaelin Jr, W. G., *Nat. Genet.* 2000, **25**, 47-54.
416. Candé, C.; Vahsen, N.; Garrido, C.; Kroemer, G., *Cell Death Differ.* 2004, **11**, 591-595.
417. Stambolsky, P.; Weisz, L.; Shats, I.; Klein, Y.; Goldfinger, N.; Oren, M.; Rotter, V., *Cell Death Differ.* 2006, **13**, 2140-2149.
418. Shen, L.; Sun, X.; Fu, Z.; Yang, G.; Li, J.; Yao, L., *Clinical Cancer Res.* 2012, **18**, 1561-1567.
419. Perlman, H.; Zhang, X.; Chen, M. W.; Walsh, K.; Buttyan, R., *Cell Death Differ.* 1999, **6**, 48-54.
420. Walensky, L. D., *Nat. Chem. Biol.* 2019, **15**, 657-665.
421. Pearce, A.; Haas, M.; Viney, R.; Pearson, S.-A.; Haywood, P.; Brown, C.; Ward, R., *PloS one* 2017, **12**, e0184360-e0184360.
422. Cheek, C. F., *Cell cycle* 2012, **11**, 2227-2228.
423. van Leeuwen, I. M. M.; Rao, B.; Sachweh, M. C. C.; Laín, S., *Cell cycle* 2012, **11**, 1851-1861.
424. Lane, D. P.; Cheek, C. F.; Lain, S., *Cold Spring Harb. Perspect. Biol.* 2010, **2**, a001222-a001222.
425. Wallach, T. E.; Bayrer, J. R., *J. Pediatr. Gastroenterol. Nutr.* 2017, **64**, 180-185.
426. Fatehullah, A.; Tan, S. H.; Barker, N., *Nat. Cell Biol.* 2016, **18**, 246-254.
427. Fatfat, M.; Merhi, R. A.; Rahal, O.; Stoyanovsky, D. A.; Zaki, A.; Haidar, H.; Kagan, V. E.; Gali-Muhtasib, H.; Machaca, K., *BMC Cancer* 2014, **14**, 527-539.
428. Gupte, A.; Mumper, R. J., *Free Rad. Biol. Med.* 2007, **43**, 1271-1278.
429. Gaur, K.; Vázquez-Salgado, A. M.; Duran-Camacho, G.; Dominguez-Martinez, I.; Benjamín-Rivera, J. A.; Fernández-Vega, L.; Carmona Sarabia, L.; Cruz García, A.; Pérez-Deliz, F.; Méndez Román, J. A.; Vega-Cartagena, M.; Loza-Rosas, S. A.; Rodríguez Acevedo, X.; Tinoco, A. D., *Inorganics* 2018, **6**, 126-164.
430. Gupte, A.; Mumper, R. J., *Cancer Treat. Rev.* 2009, **35**, 32-46.
431. Niwa-Kawakita, M.; Ferhi, O.; Soilihi, H.; Le Bras, M.; Lallemand-Breitenbach, V.; de Thé, H., *J. Exp. Med.* 2017, **214**, 3197-3206.
432. Malarz, K.; Mrozek-Wilczkiewicz, A.; Serda, M.; Rejmund, M.; Polanski, J.; Musiol, R., *Oncotarget* 2018, **9**, 17689-17710.
433. Bellazzo, A.; Di Minin, G.; Collavin, L., *Mol. Cell. Oncol.* 2015, **2**, e1002719-e1002719.

434. Chen, K.; Xu, L.; Wiest, O., *J. Org. Chem.* 2013, **78**, 5051-5055.
435. Jacobsen, J. A.; Major Jourden, J. L.; Miller, M. T.; Cohen, S. M., *Biochim. Biophys. Acta* 2010, **1803**, 72-94.
436. Rao, B. G., *Curr. Pharm.* 2005, **11**, 295-322.
437. Augé, F.; Hornebeck, W.; Decarme, M.; Laronze, J.-Y., *Bioorg. Med. Chem. Lett.* 2003, **13**, 1783-1786.
438. Stewart, A. O.; Bhatia, P. A.; Martin, J. G.; Summers, J. B.; Rodrigues, K. E.; Martin, M. B.; Holms, J. H.; Moore, J. L.; Craig, R. A.; Kolasa, T.; Ratajczyk, J. D.; Mazdiyasn, H.; Kerdesky, F. A. J.; DeNinno, S. L.; Maki, R. G.; Bouska, J. B.; Young, P. R.; Lanni, C.; Bell, R. L.; Carter, G. W.; Brooks, C. D. W., *J. Med. Chem.* 1997, **40**, 1955-1968.
439. Hoffman, A.; Qadri, B.; Frant, J.; Katz, Y.; Bhusare, S. R.; Breuer, E.; Hadar, R.; Reich, R., *J. Med. Chem.* 2008, **51**, 1406-1414.
440. Grams, F.; Brandstetter, H.; Simonetta, D. A.; Geppert, D.; Krell, H.-W.; Leinert, H.; Livi, V.; Menta, E.; Oliva, A.; Zimmermann, G., Pyrimidine-2,4,6-Triones: A New Effective and Selective Class of Matrix Metalloproteinase Inhibitors. In *Biological Chemistry*, 2001; Vol. 382, p 1277.
441. Schaffhausen, J., *Trends Pharmacol. Sci.* 2015, **36**, 1.
442. Groves, J. T., *Developmental Cell* 2019, **48**, 15-16.
443. Habault, J.; Poyet, J.-L., *Molecules* 2019, **24**, 927-944.
444. Borrelli, A.; Tornesello, A. L.; Tornesello, M. L.; Buonaguro, F. M., *Molecules* 2018, **23**, 295-323.
445. Regberg, J.; Srimanee, A.; Langel, U., *Pharmaceuticals (Basel)* 2012, **5**, 991-1007.
446. Guidotti, G.; Brambilla, L.; Rossi, D., *Trends Pharmacol. Sci.* 2017, **38**, 406-424.
447. Mingeun, K.; Juhye, K.; Misun, L.; Jiyeon, H.; Geewoo, N.; Eunyong, T.; Min Sun, K.; Hyuck Jin, L.; Eunju, N.; Joo-Yong, L.; Mi Hee, L., *Minimalistic Design Approach for Multi-Reactivity against Free Radicals and Metal-Free and Metal-Bound Amyloid- β Peptides: Redox-Based Substitutions of Benzene*. 2019.
448. Thomas-Chollier, M.; Darbo, E.; Herrmann, C.; Defrance, M.; Thieffry, D.; van Helden, J., *Nature Protocols* 2012, **7**, 1551-1568.
449. Vaughan, C. A.; Singh, S.; Grossman, S. R.; Windle, B.; Deb, S. P.; Deb, S., *Mol. Oncol.* 2017, **11**, 696-711.
450. Burley, S. K.; Petsko, G. A., *Science* 1985, **229**, 23-28.
451. Ryan, D. M.; Anderson, S. B.; Nilsson, B. L., *Soft Matter* 2010, **6**, 3220-3231.

452. Bertolani, A.; Pirrie, L.; Stefan, L.; Houbenov, N.; Haataja, J. S.; Catalano, L.; Terraneo, G.; Giancane, G.; Valli, L.; Milani, R.; Ikkala, O.; Resnati, G.; Metrangolo, P., *Nat. Commun.* 2015, **6**, 7574-7583.
453. Pizzi, A.; Pigliacelli, C.; Gori, A.; Nonappa; Ikkala, O.; Demitri, N.; Terraneo, G.; Castelletto, V.; Hamley, I. W.; Baldelli Bombelli, F.; Metrangolo, P., *Nanoscale* 2017, **9**, 9805-9810.
454. Pizzi, A.; Dichiarante, V.; Terraneo, G.; Metrangolo, P., *Pept. Sci.* 2018, **110**, e23088-e23098.
455. Wong, H. E.; Irwin, J. A.; Kwon, I., *PLOS ONE* 2013, **8**, e57288-e57299.
456. Huang, L.; Liao, M.; Yang, X.; Gong, H.; Ma, L.; Zhao, Y.; Huang, K., *RSC Advances* 2016, **6**, 7239-7248.
457. Ng, J. W. K.; Lama, D.; Lukman, S.; Lane, D. P.; Verma, C. S.; Sim, A. Y. L., *Proteins.* 2015, **83**, 2240-2250.

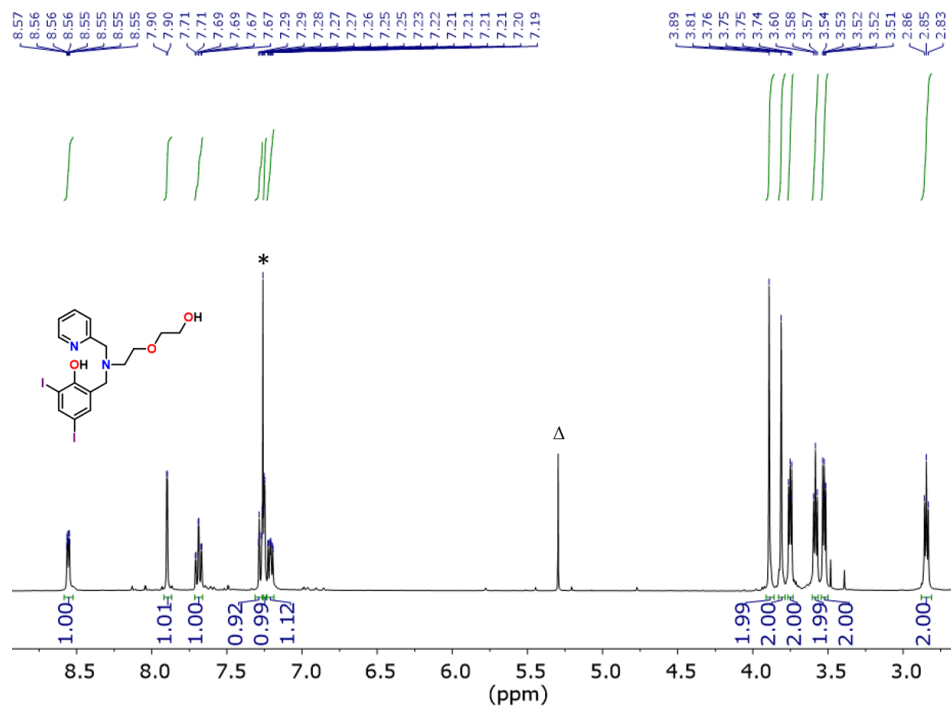


Figure A3. ^1H NMR of L3 in CDCl_3 (400 MHz). Asterisk denotes residual solvent peak. Δ denotes CH_2Cl_2 solvent peak.

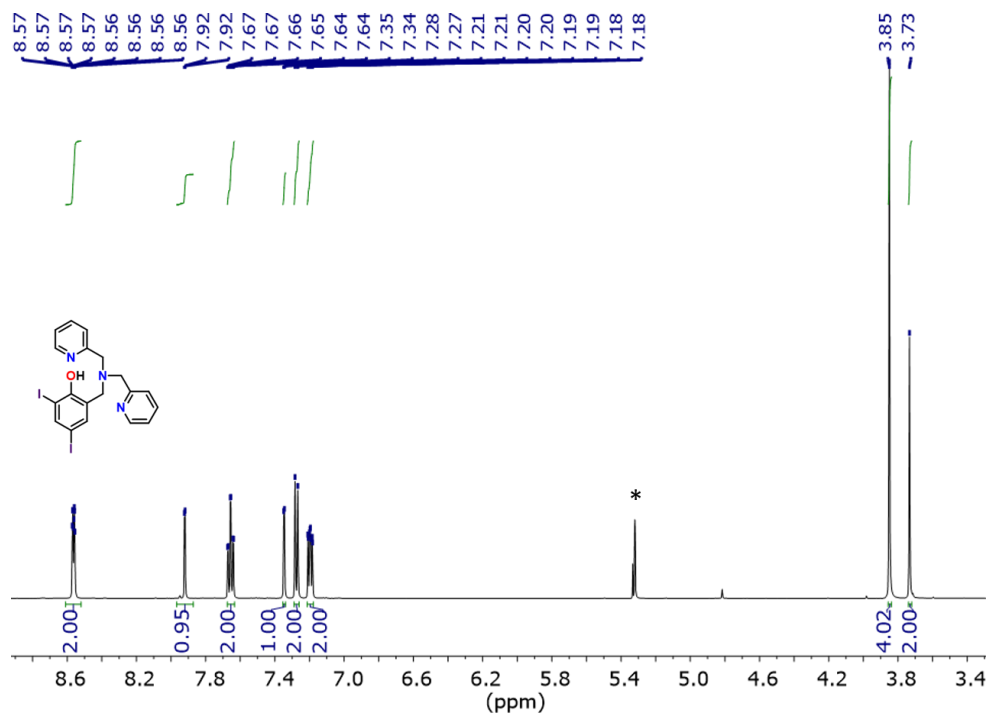


Figure A4. ^1H NMR of L4 in CD_2Cl_2 (500 MHz). Asterisk denotes residual solvent peak.

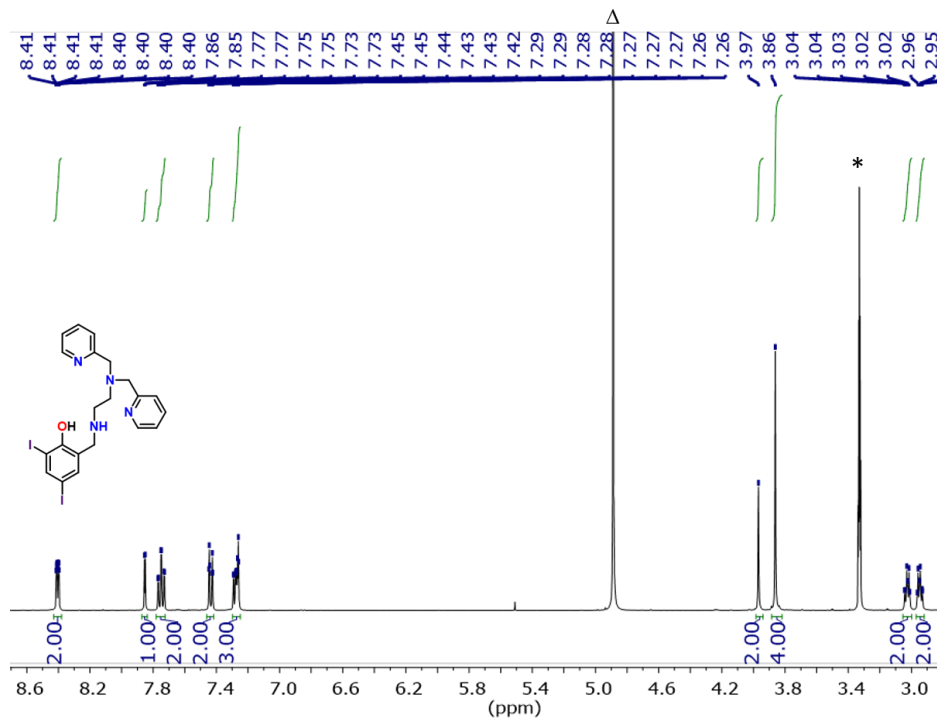


Figure A5. ^1H NMR of **L5** in CD_3OD (400 MHz). Asterisk denotes residual solvent peak. Δ denotes CH_2Cl_2 solvent peak.

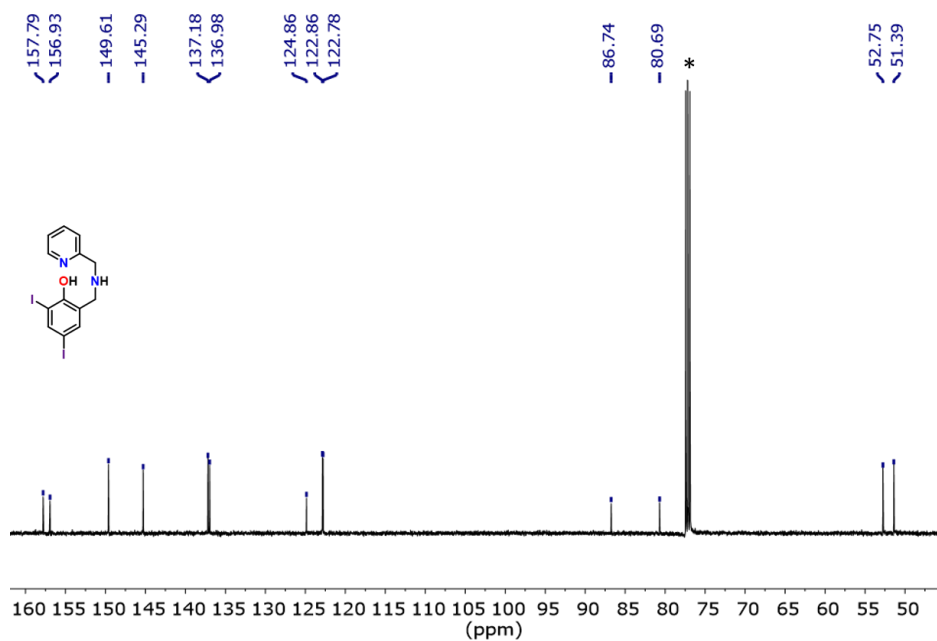


Figure A6. $^{13}\text{C}\{^1\text{H}\}$ NMR of **L1** in CDCl_3 (100.6 MHz). Asterisk denotes residual solvent peak.

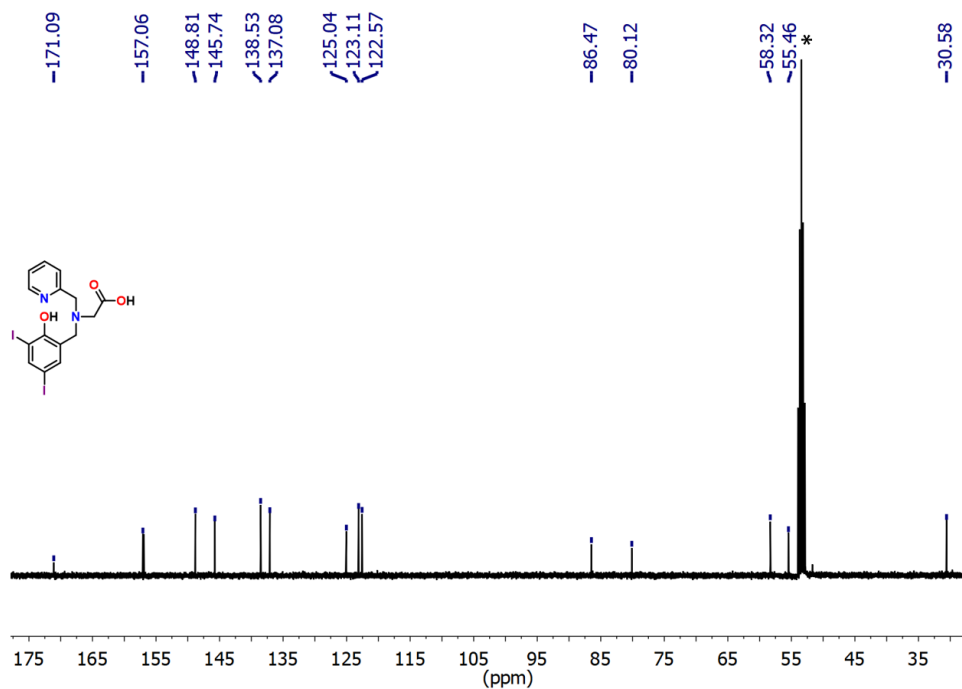


Figure A7. $^{13}\text{C}\{^1\text{H}\}$ NMR of **L2** in CD_2Cl_2 (100.6 MHz). Asterisk denotes residual solvent peak.

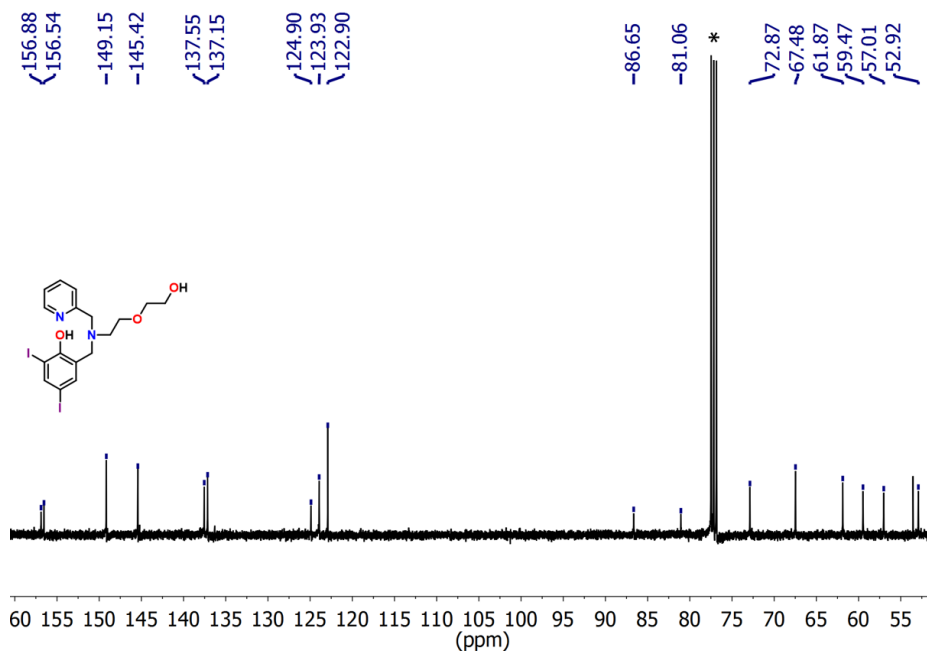


Figure A8. $^{13}\text{C}\{^1\text{H}\}$ NMR of **L3** in CDCl_3 (125.8 MHz). Asterisk denotes residual solvent peak.

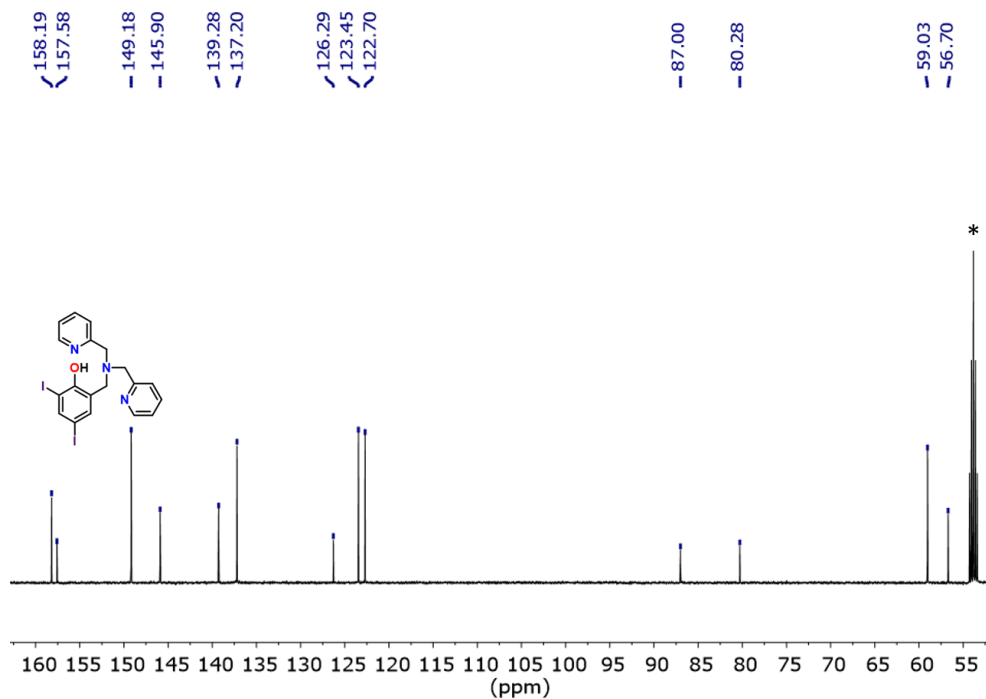


Figure A9. $^{13}\text{C}\{^1\text{H}\}$ NMR of **L4** in CD_2Cl_2 (125.8 MHz). Asterisk denotes residual solvent peak.

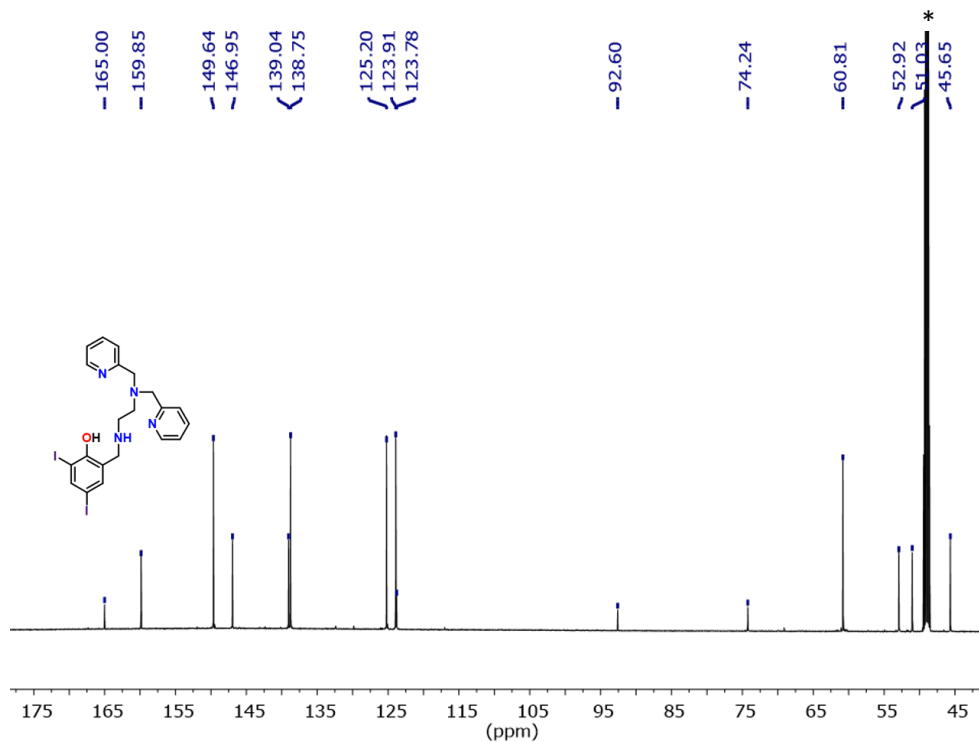


Figure A10. $^{13}\text{C}\{^1\text{H}\}$ NMR of **L5** in CD_3OD (150.9 MHz). Asterisk denotes residual solvent peak.

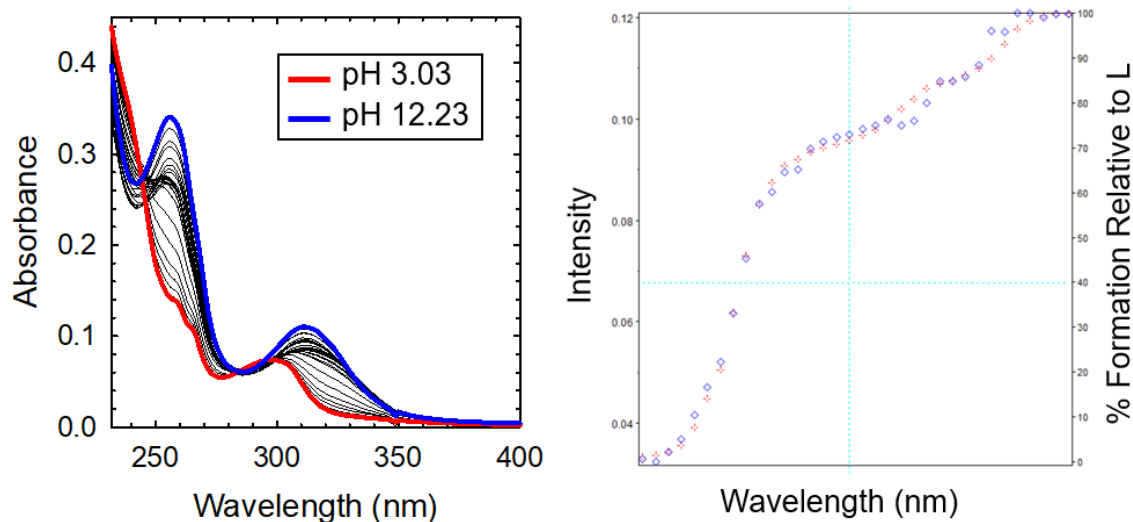


Figure A11. (left) Variable pH UV-vis titration of 12.5 μM **L1** ranging from pH 3.03-12.23 in 0.1 M NaCl. (right) Absorbance trace as a function of wavelength at pH 7.4. Observed absorbance values are shown in red, calculated absorbance values are in blue.

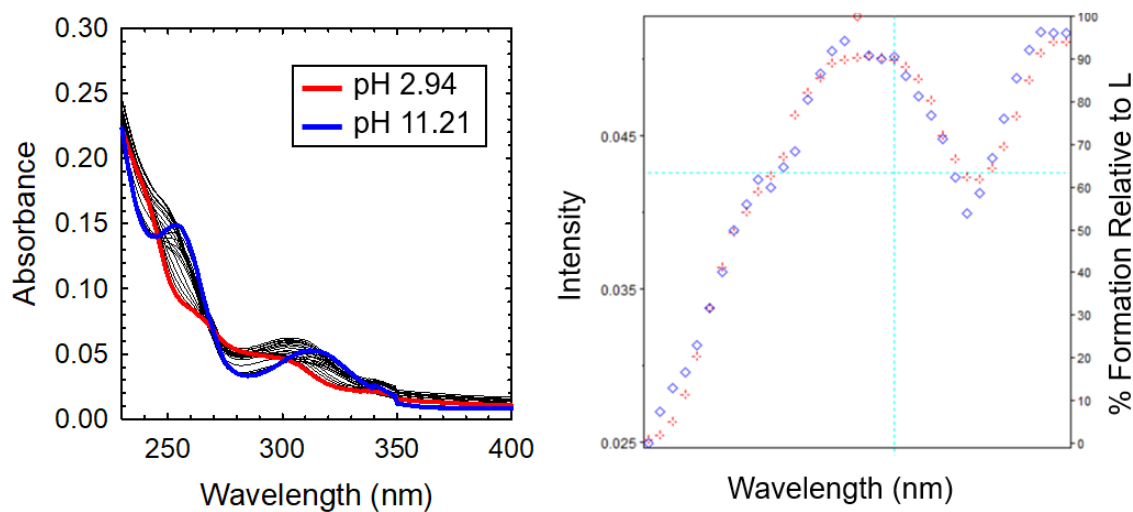


Figure A12. (left) Variable pH UV-vis titration of 12.5 μM **L2** ranging from pH 2.94-11.21 in 0.1 M NaCl. (right) Absorbance trace as a function of wavelength at pH 7.4. Observed absorbance values are shown in red, calculated absorbance values are in blue.

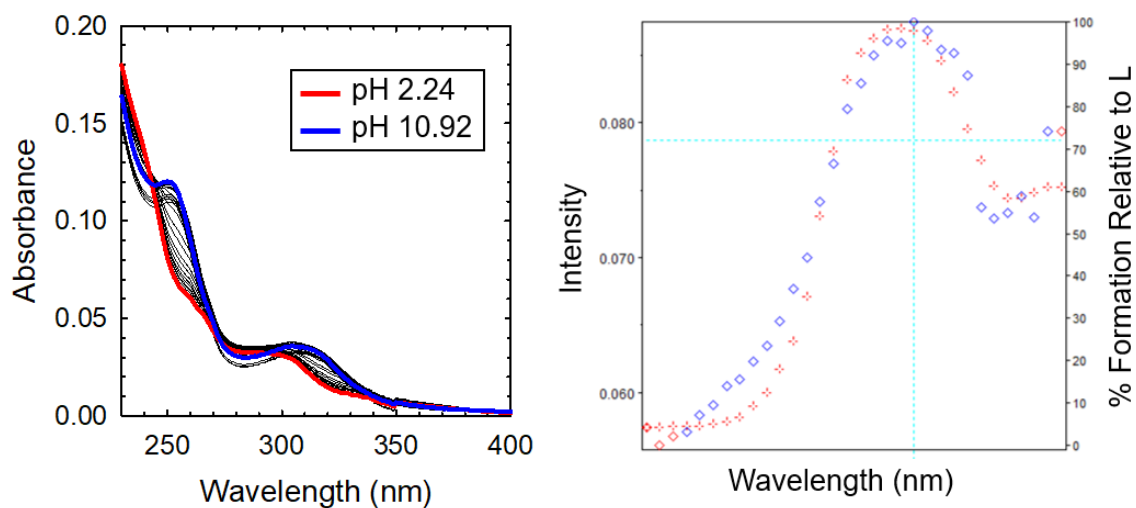


Figure A13. (left) Variable pH UV-vis titration of 12.5 μM **L3** ranging from pH 2.24-10.92 in 0.1 M NaCl. (right) Absorbance trace as a function of wavelength at pH 7.4. Observed absorbance values are shown in red, calculated absorbance values are in blue.

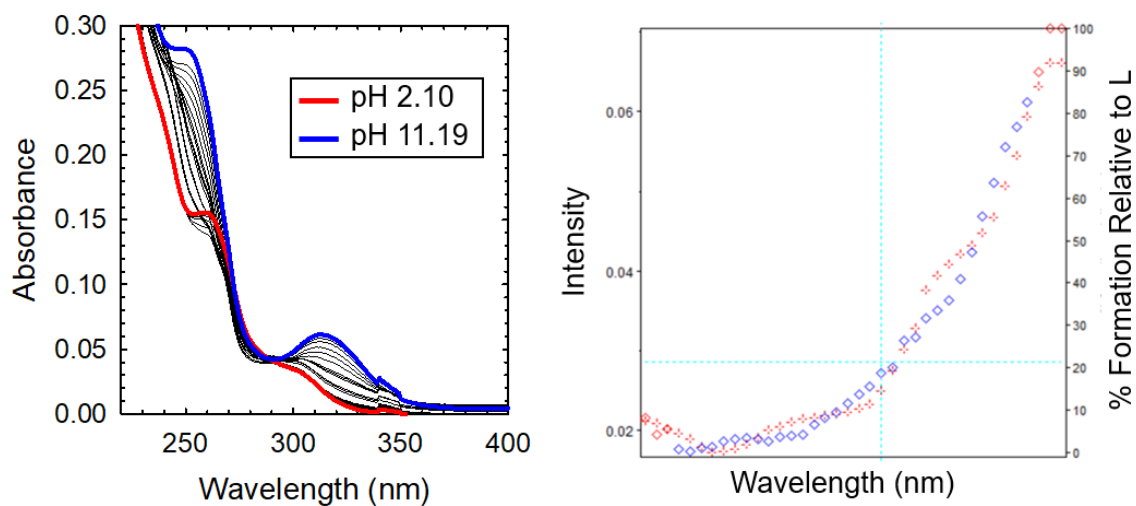


Figure A14. (left) Variable pH UV-vis titration of 12.5 μM **L4** ranging from pH 2.10-11.19 in 0.1 M NaCl. (right) Absorbance trace as a function of wavelength at pH 7.4. Observed absorbance values are shown in red, calculated absorbance values are in blue.

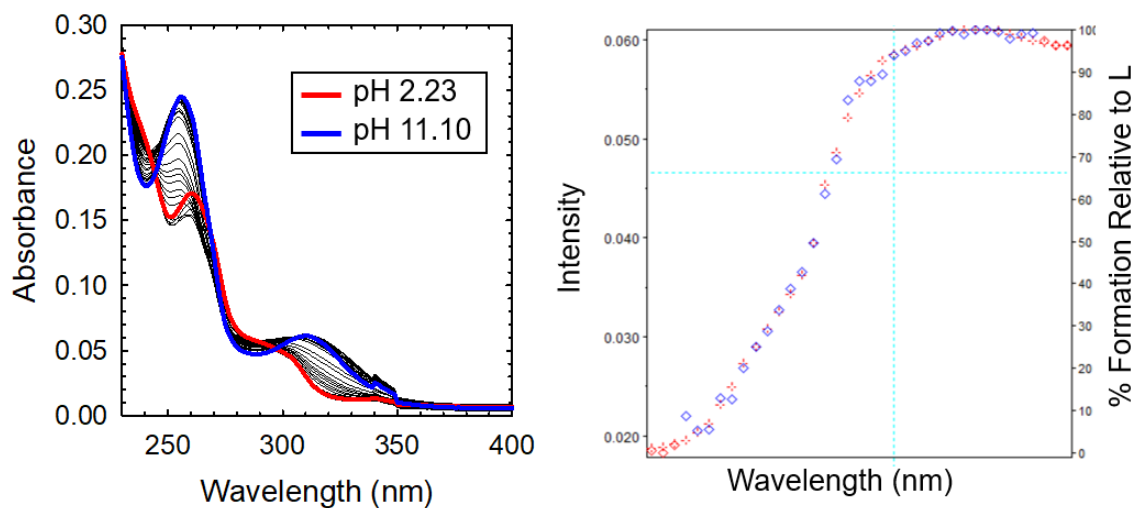


Figure A15. (left) Variable pH UV-vis titration of 12.5 μM **L5** ranging from pH 2.23-11.10 in 0.1 M NaCl. (right) Absorbance trace as a function of wavelength at pH 7.4. Observed absorbance values are shown in red, calculated absorbance values are in blue.

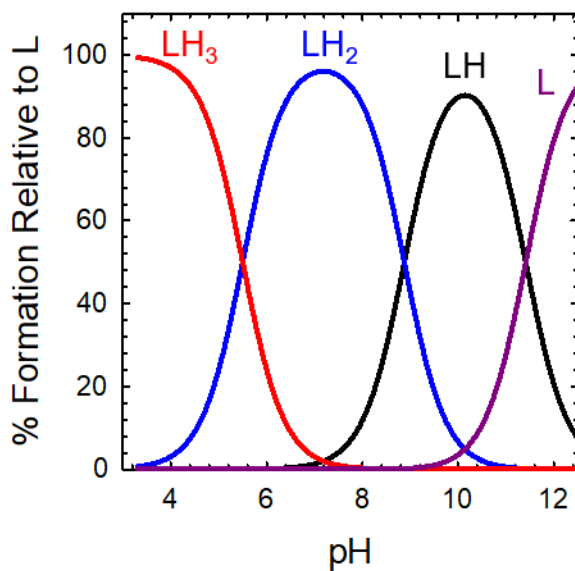


Figure A16. Simulated species distribution plot for **L1** using HypSpec and HySS2009.

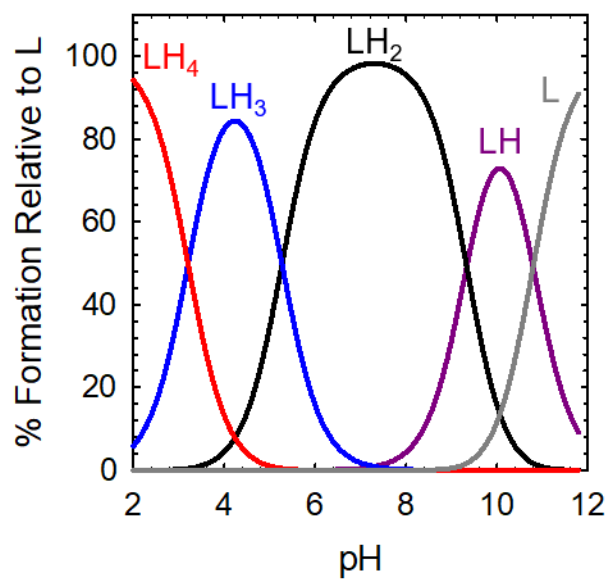


Figure A17. Simulated species distribution plot for **L2** using HypSpec and HySS2009.

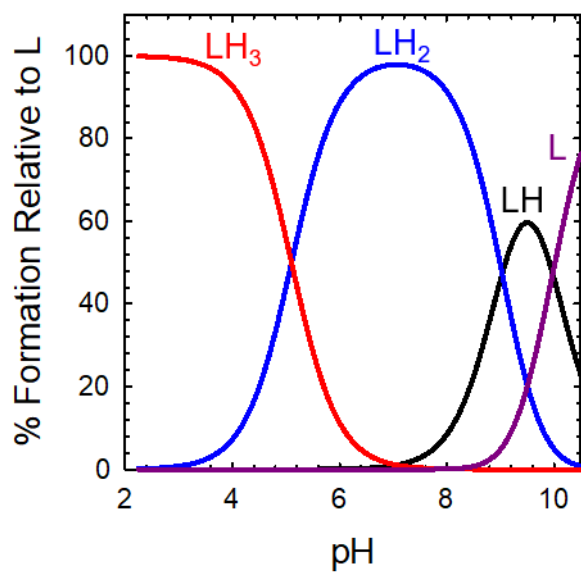


Figure A18. Simulated species distribution plot for **L3** using HypSpec and HySS2009.

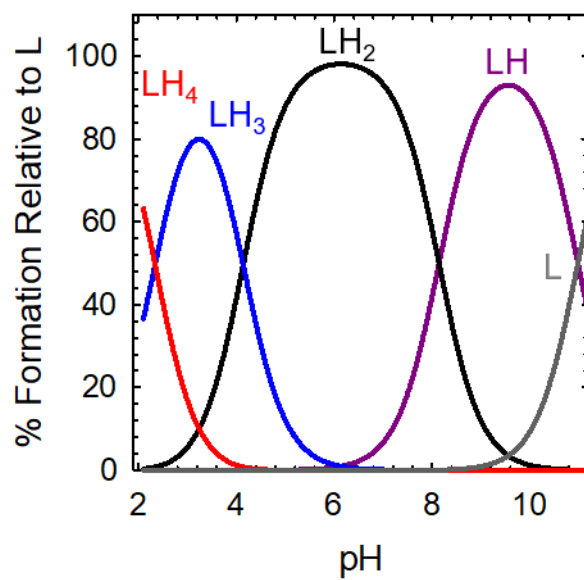


Figure A19. Simulated species distribution plot for **L4** using HypSpec and HySS2009.

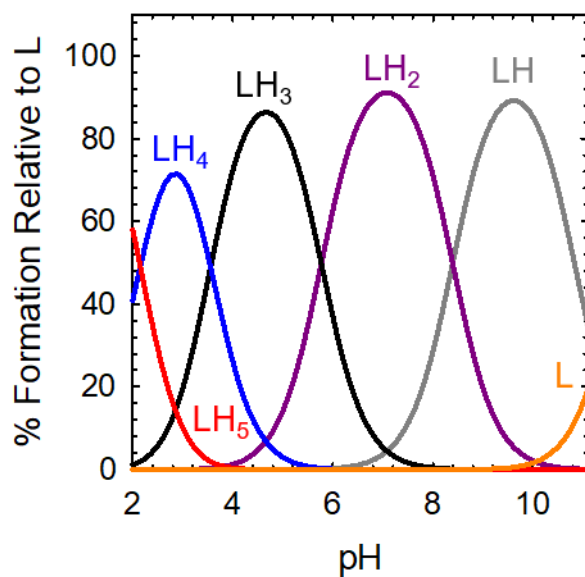


Figure A20. Simulated species distribution plot for **L5** using HypSpec and HySS2009.

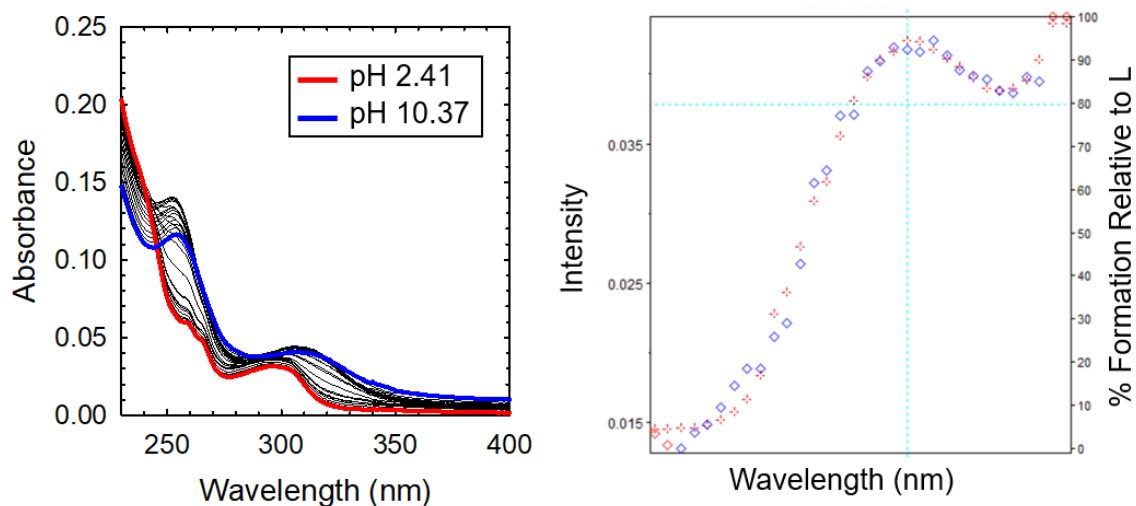


Figure A21. (left) Variable pH UV-vis titration of $6.25 \mu\text{M Zn}^{2+}$ and $12.5 \mu\text{M L1}$ ranging from pH 2.41-10.37 in 0.1 M NaCl. (right) Absorbance trace as a function of wavelength at pH 7.4. Observed absorbance values are shown in red, calculated absorbance values are in blue.

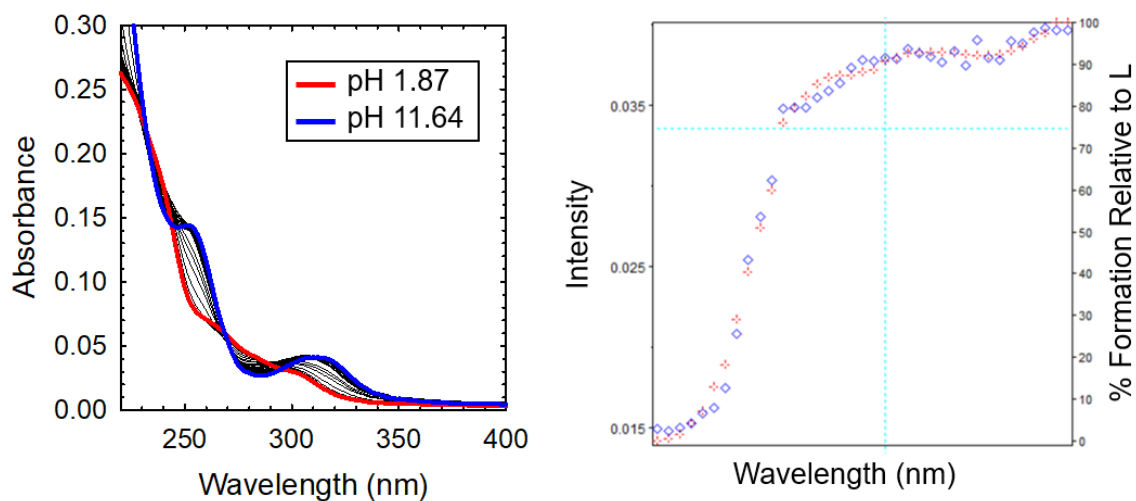


Figure A22. (left) Variable pH UV-vis titration of $6.25 \mu\text{M Zn}^{2+}$ and $12.5 \mu\text{M L2}$ ranging from pH 1.87-11.64 in 0.1 M NaCl. (right) Absorbance trace as a function of wavelength at pH 7.4. Observed absorbance values are shown in red, calculated absorbance values are in blue.

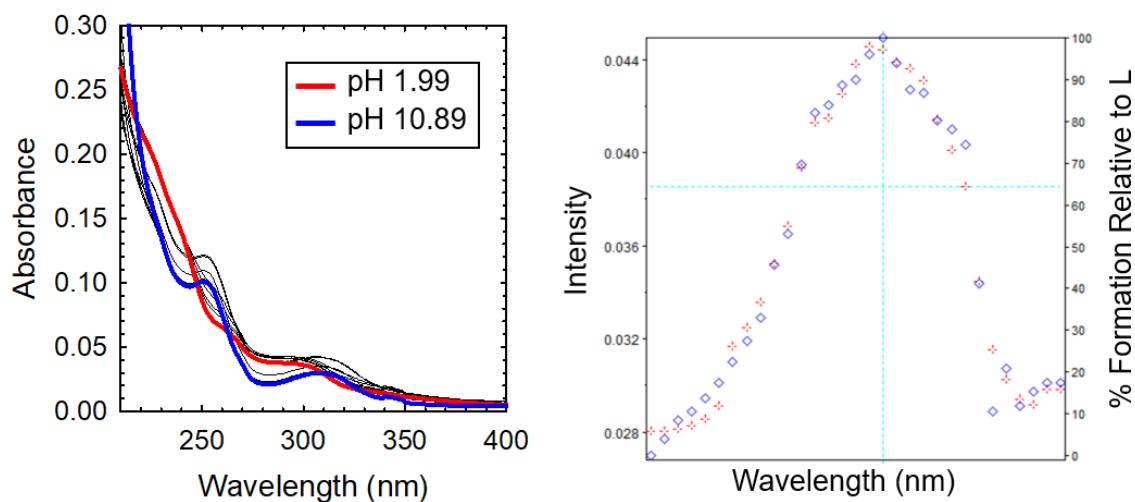


Figure A23. (left) Variable pH UV-vis titration of $6.25 \mu\text{M Zn}^{2+}$ and $12.5 \mu\text{M L3}$ ranging from pH 1.99-10.89 in 0.1 M NaCl. (right) Absorbance trace as a function of wavelength at pH 7.4. Observed absorbance values are shown in red, calculated absorbance values are in blue.

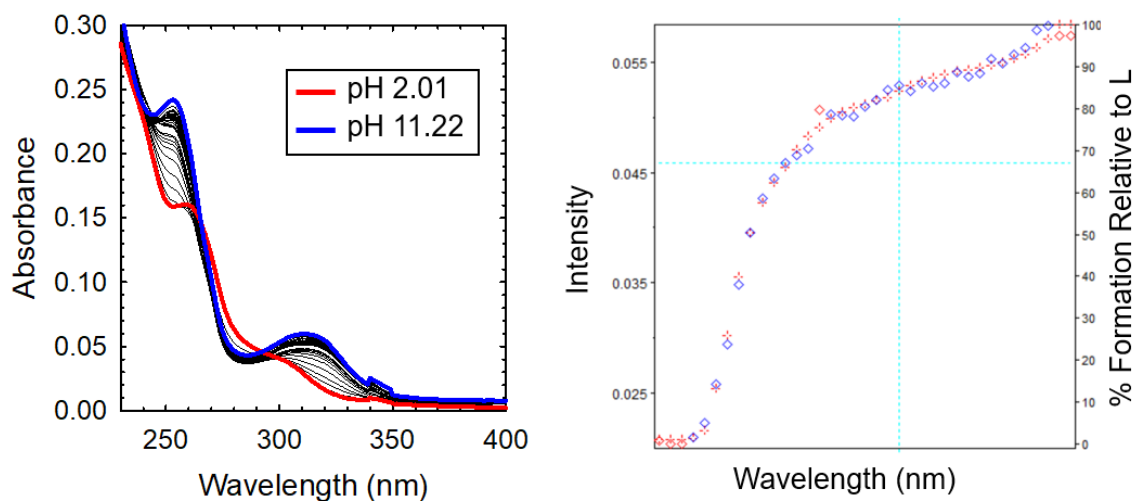


Figure A24. (left) Variable pH UV-vis titration of $12.5 \mu\text{M Zn}^{2+}$ and $12.5 \mu\text{M L4}$ ranging from pH 2.01-11.22 in 0.1 M NaCl. (right) Absorbance trace as a function of wavelength at pH 7.4. Observed absorbance values are shown in red, calculated absorbance values are in blue.

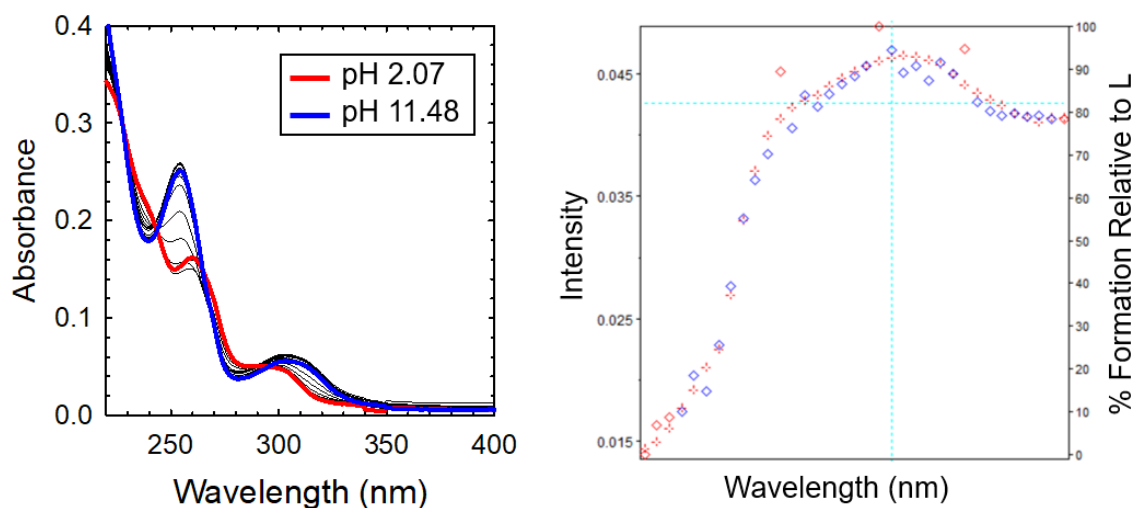


Figure A25. (left) Variable pH UV-vis titration of $12.5 \mu\text{M Zn}^{2+}$ and $12.5 \mu\text{M L5}$ ranging from pH 2.07-11.48 in 0.1 M NaCl. (right) Absorbance trace as a function of wavelength at pH 7.4. Observed absorbance values are shown in red, calculated absorbance values are in blue.

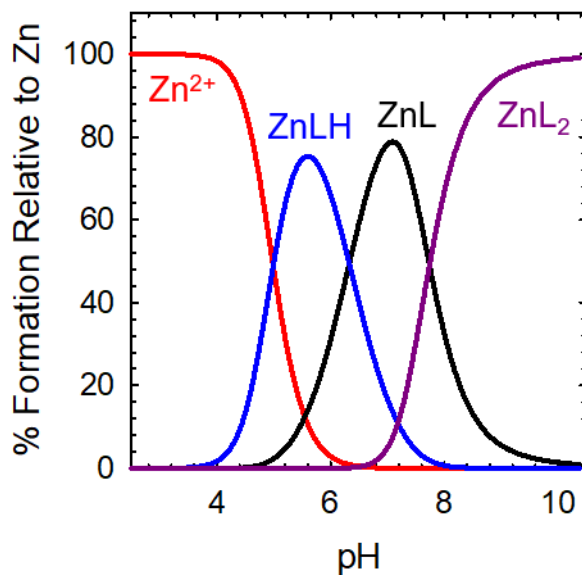


Figure A26. Simulated species distribution plot for $\text{Zn}^{2+} + \text{L1}$ using HypSpec and HySS2009.

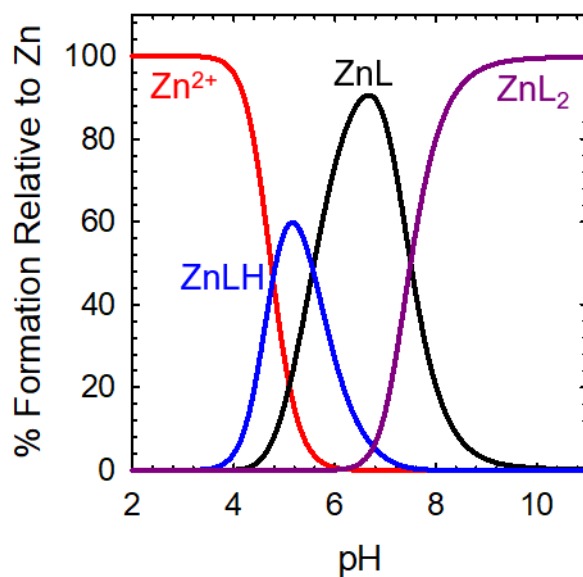


Figure A27. Simulated species distribution plot for Zn^{2+} + L2 using HypSpec and HySS2009.

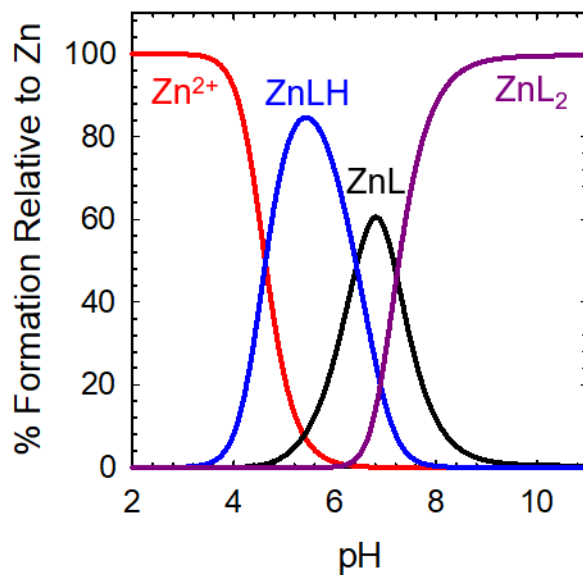


Figure A28. Simulated species distribution plot for Zn^{2+} + L3 using HypSpec and HySS2009.

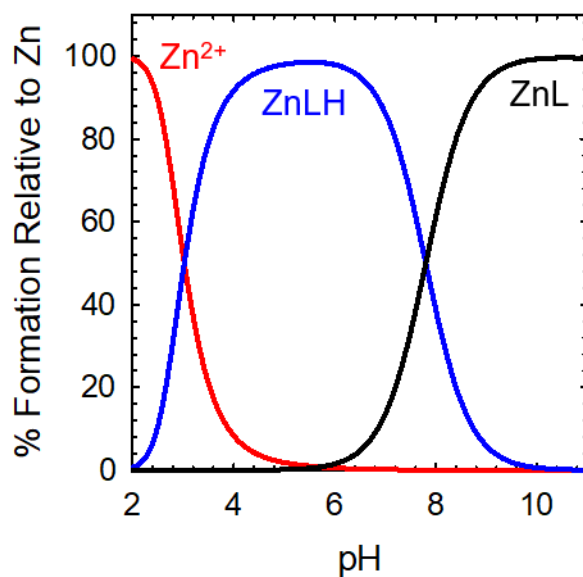


Figure A29. Simulated species distribution plot for Zn²⁺ + L4 using HypSpec and HySS2009.

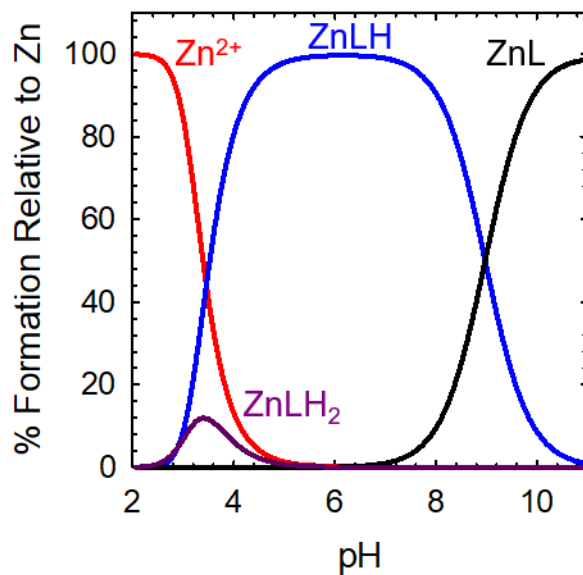


Figure A30. Simulated species distribution plot for Zn²⁺ + L5 using HypSpec and HySS2009.

Appendix B. Supplementary Information for Chapter 3

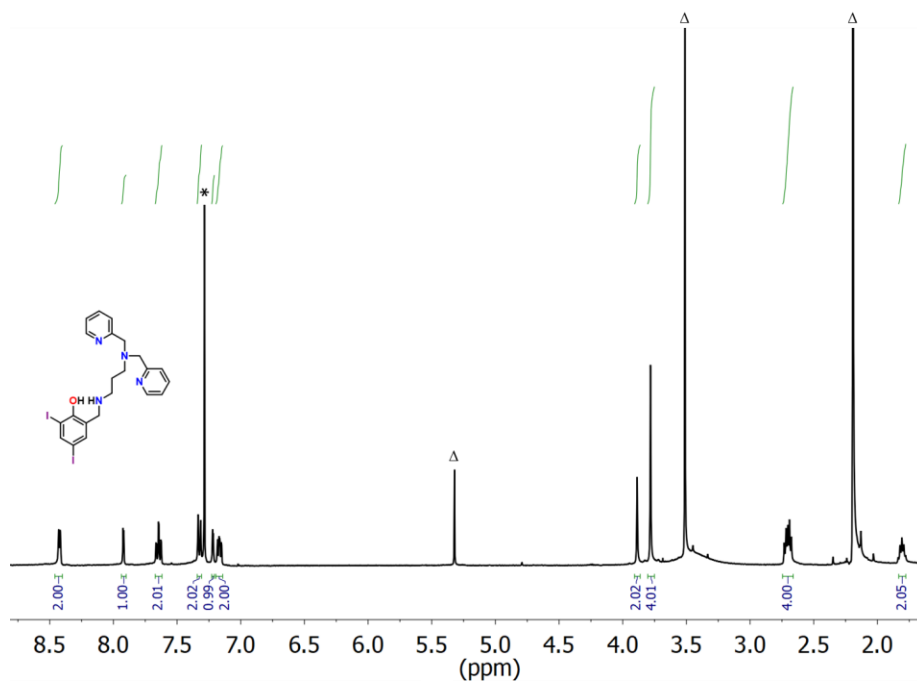


Figure B1. ^1H NMR of **L5-P** in CDCl_3 (400 MHz). Asterisk denotes residual solvent peak. Δ denotes solvent peaks.

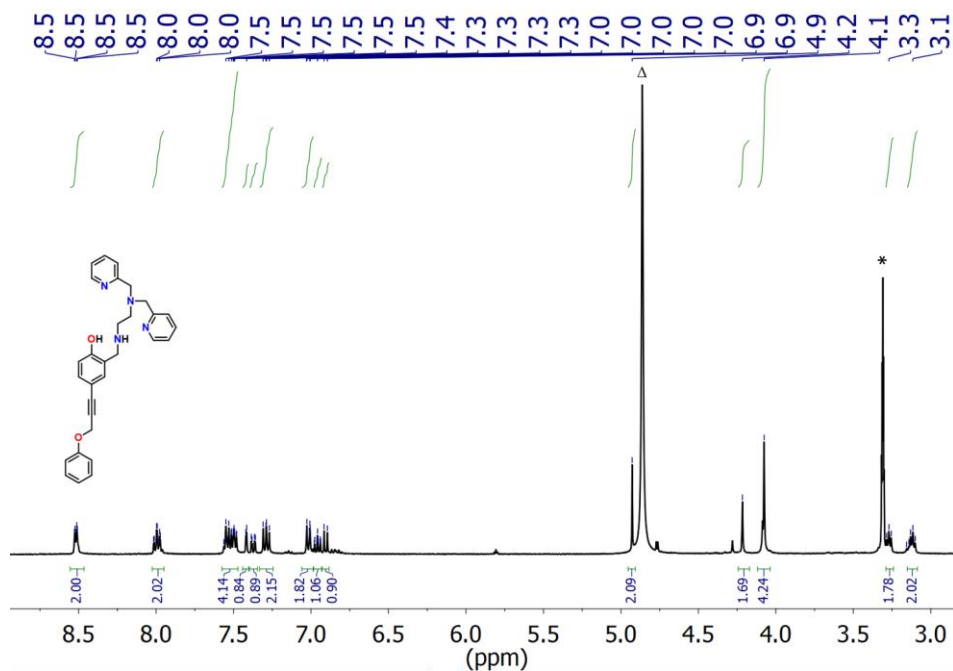


Figure B2. ^1H NMR of **L5-O** in CD_3OD (400 MHz). Asterisk denotes residual solvent peak. Δ denotes CH_2Cl_2 solvent peak.

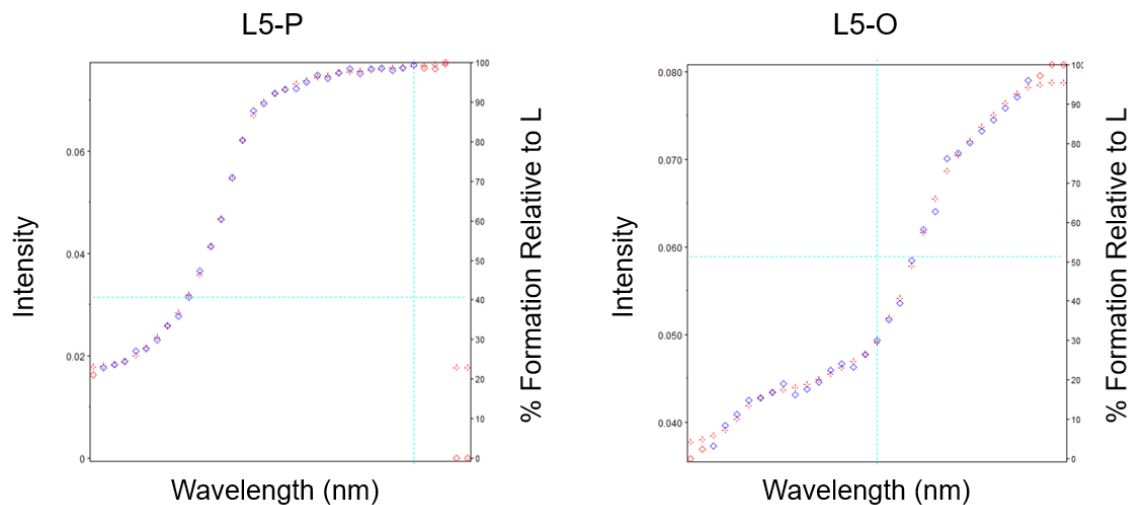


Figure B5. Absorbance trace as a function of wavelength at pH 7.4 (**L5-P** – left, **L5-O**, right). Observed absorbance values are shown in red, calculated absorbance values are in blue.

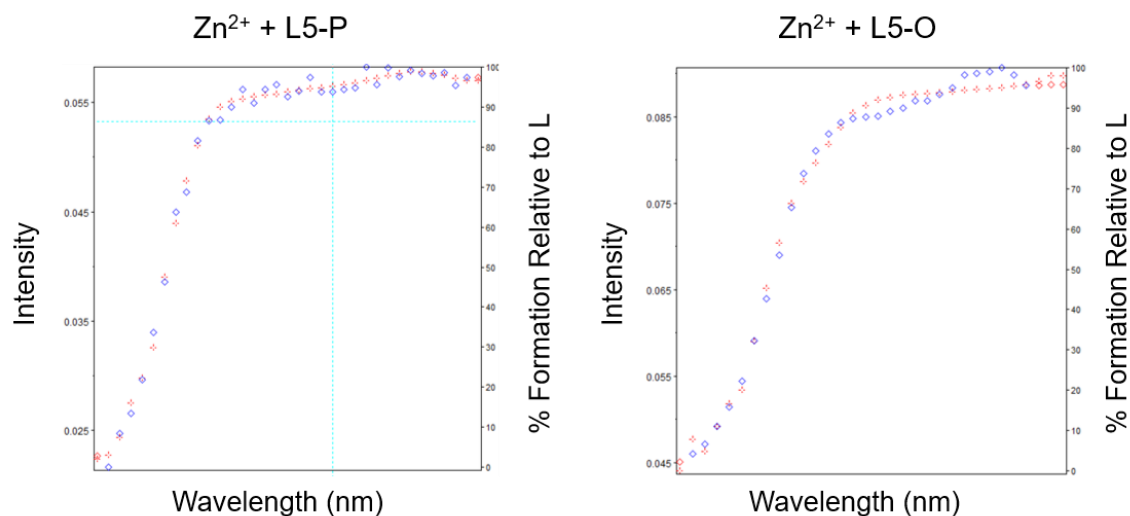


Figure B6. Absorbance trace as a function of wavelength at pH 7.4 (**Zn²⁺ + L5-P** – left, **Zn²⁺ + L5-O**, right). Observed absorbance values are shown in red, calculated absorbance values are in blue.

Appendix C. Supplementary Information for Chapter 4

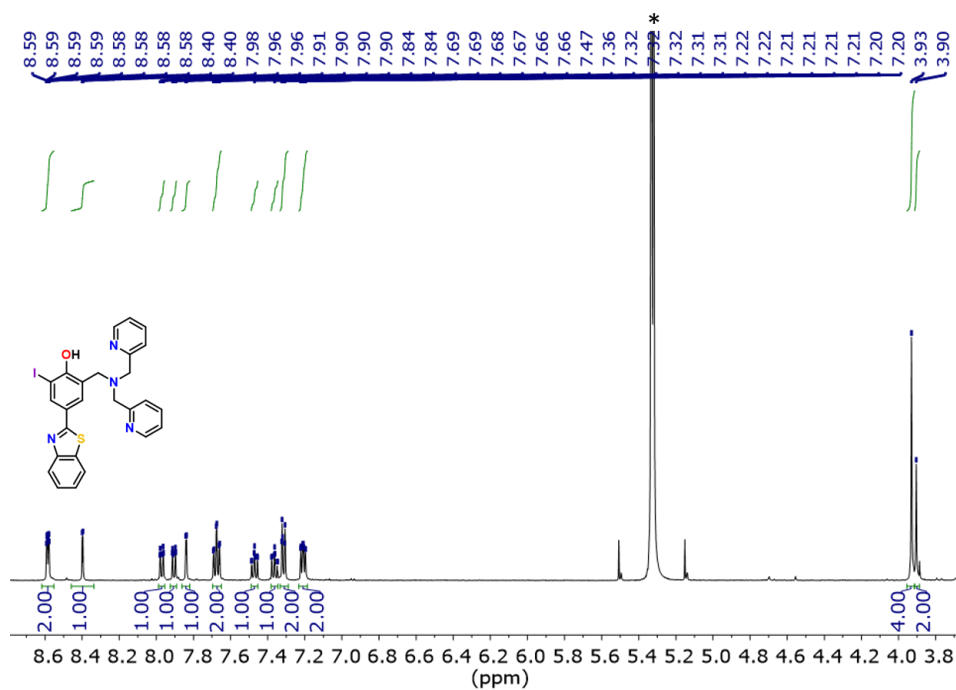


Figure C1. ^1H NMR of **L6** in CD_2Cl_2 (500 MHz). Asterisk denotes residual solvent peak.

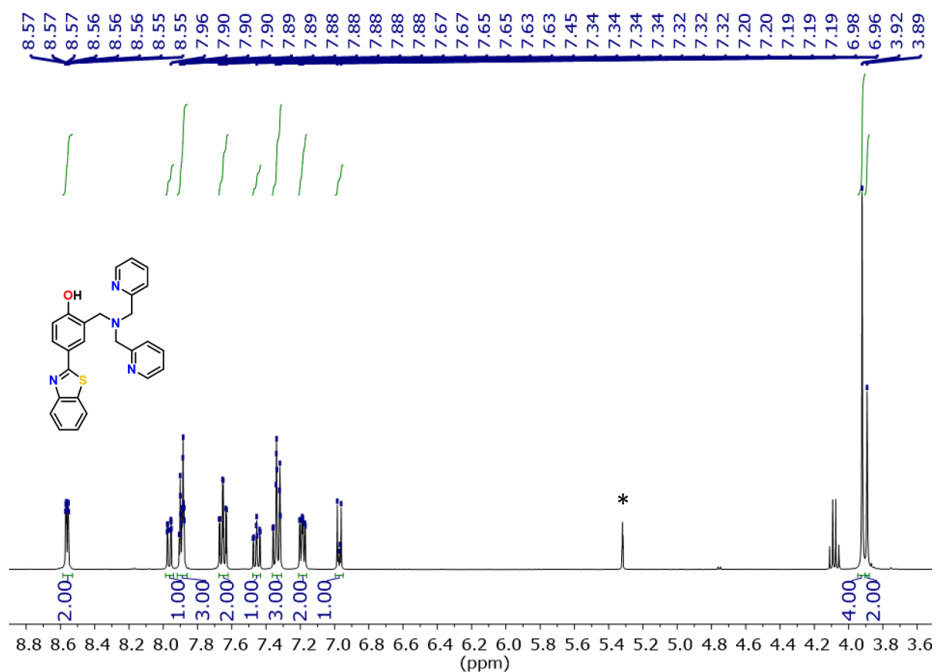


Figure C2. ^1H NMR of **L7** in CD_2Cl_2 (400 MHz). Asterisk denotes residual solvent peak.

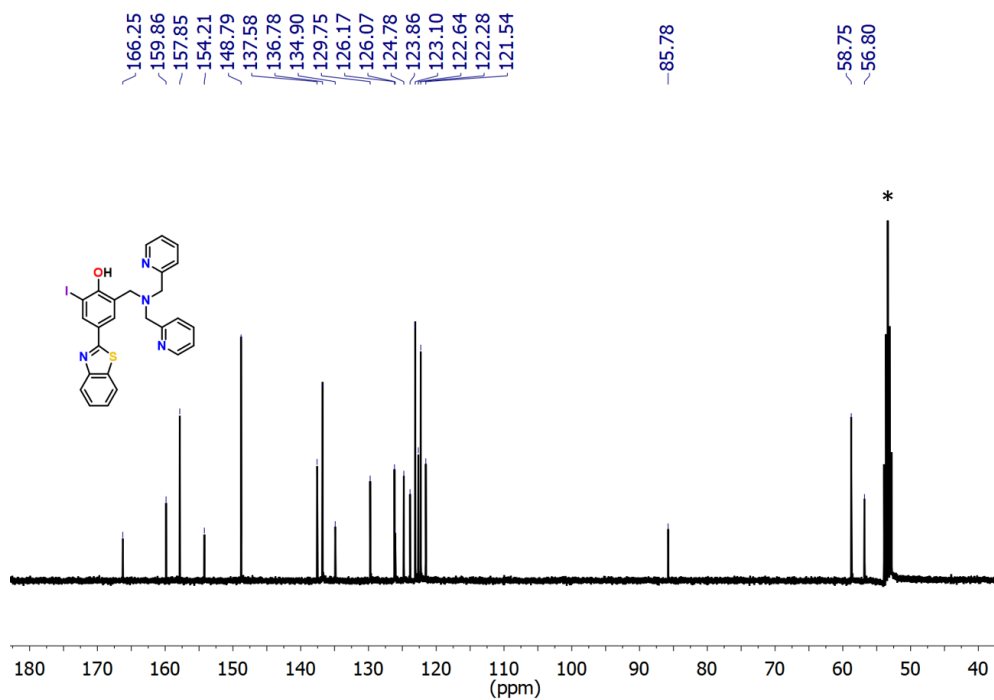


Figure C3. $^{13}\text{C}\{^1\text{H}\}$ NMR of **L6** in CD_2Cl_2 (125.8 MHz). Asterisk denotes residual solvent peak.

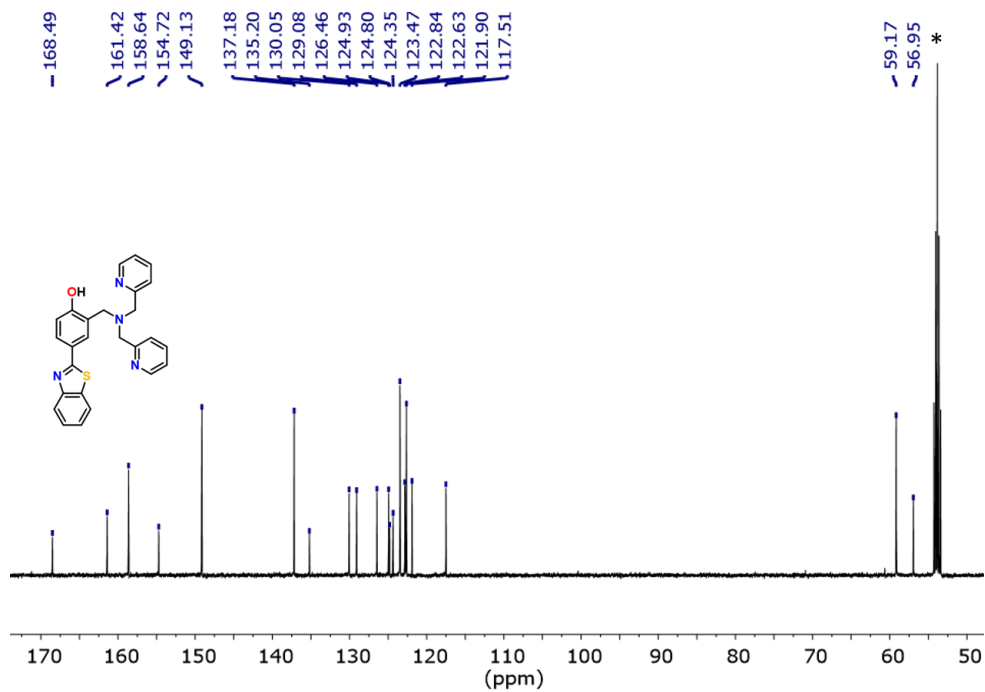


Figure C4. $^{13}\text{C}\{^1\text{H}\}$ NMR of **L7** in CD_2Cl_2 (125.8 MHz). Asterisk denotes residual solvent peak.

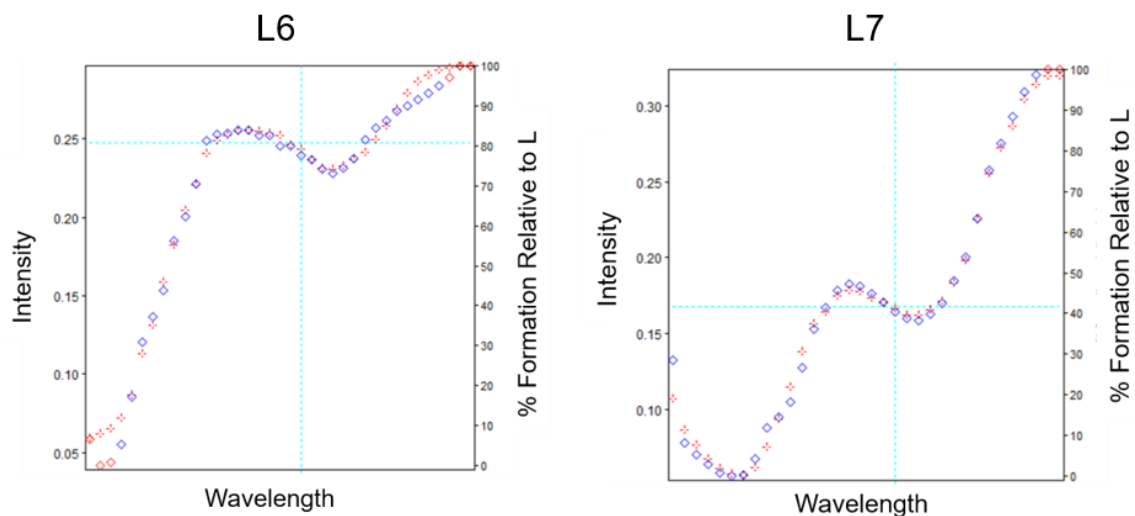


Figure C5. Absorbance trace as a function of wavelength at pH 7.4 (**L6** – left, **L7**, right). Observed absorbance values are shown in red, calculated absorbance values are in blue.

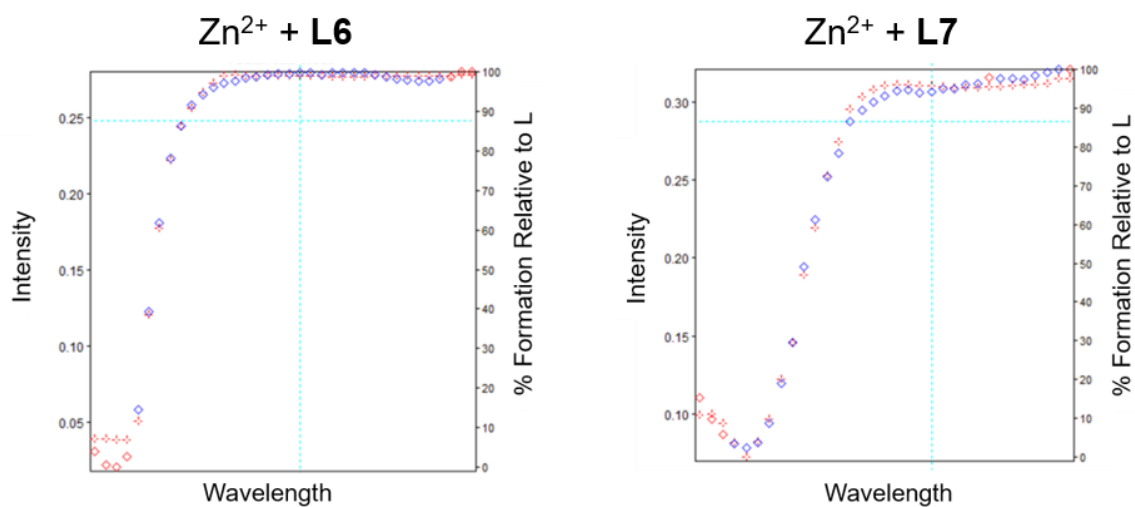


Figure C6. Absorbance trace as a function of wavelength at pH 7.4 (**Zn²⁺ + L6** – left, **Zn²⁺ + L7**, right). Observed absorbance values are shown in red, calculated absorbance values are in blue.

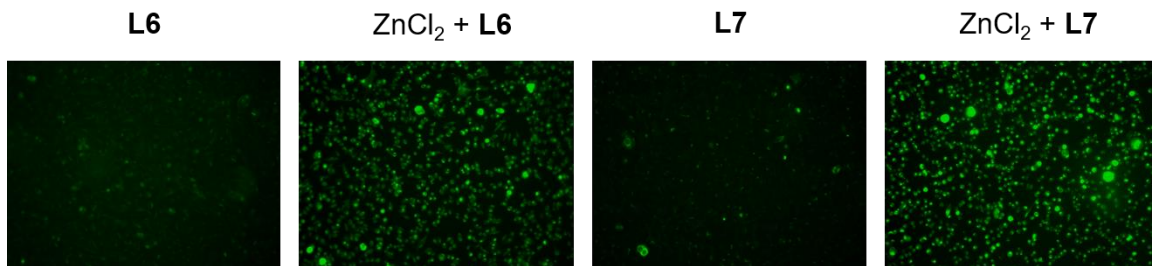


Figure C7. Imaging of intracellular Zn²⁺ levels in complete serum-free media. NUGC3 cells were incubated with 1 μ M FluoZin-3 for 20 minutes at 37°C, followed by incubation with 50 μ M **L6** and **L7** for 2 hours. Cells were imaged using a fluorescence microscope and fluorescence-quantified using ImageJ.